UNIVERSITY OF SOUTHAMPTON

Environments of powerful radio galaxies through the cosmic ages

Julie-Ann Goodlet

Submitted for the degree of Doctor of Philosophy

DEPARTMENT OF PHYSICS AND ASTRONOMY
FACULTY OF SCIENCE

October 14, 2004

UNIVERSITY OF SOUTHAMPTON

ABSTRACT

FACULTY OF SCIENCE

DEPARTMENT OF PHYSICS AND ASTRONOMY

Doctor of Philosophy

Environments of powerful radio galaxies through the cosmic ages

by Julie-Ann Goodlet

I define 3 samples of extragalactic radio sources of type FRII, containing 26 objects in total. The control sample consists of 6C and 7C sources with radio–luminosities of around $10^{27}\,\mathrm{W\,Hz^{-1}}$ at 151 MHz and redshifts of $z \sim 1$. The other samples contain 3CRR sources with either comparable redshifts but radio luminosities about a decade larger or with comparable radio–luminosities but redshifts around $z \sim 0.4$. These samples are used to investigate the possible evolution of depolarisation and rotation measure properties with redshift and radio luminosity independently. All sources show evidence for an external Faraday screen. Depolarisation and variations in the rotation measure of a source increase with redshift, only the depolarisation measure shows any trend with radio-luminosity. There are no strong trends with spectral index.

I use the Kaiser et al. (1997) model with 3 flux measurements to estimate the density of the source environment, source age and jet power. Depolarisation and variations in the rotation measure were found to be insensitive to changes in the density of the source environment. This indicates that depolarisation and variations in the rotation measure are not density indicators but map how the disorder in the magnetic field changes with redshift.

The model is then used on a larger set of FRII sources taken from the complete 3CRR, 6CE and 7C III samples. I find that the density of the source environment is a strong function of the source radio–luminosity but is insensitive to changes in redshift. The jet power is also a strong function of radio-luminosity but also a weak function of redshift. This indicates that the mass of the black–hole powering FRII sources is epoch dependent. In general, I find that the source environment is dominated by changes in the radio–luminosity but is relatively unaffected by changes in cosmic epoch.

Contents

List of Figures

List of Tables

Preface

All work presented here has been carried out by the author, in collaboration with others, at Southampton University between October 2001 and August 2004. The results presented in chapters 2 and 3 have been published by Goodlet, Kaiser, Best & Dennett-Thorpe (2004) in MNRAS.

The data used in chapters 2 and 3 uses archival observations provided by the National Radio Astronomy Observatory, details of which can be found in Tables 2.2 to 2.4. AD429 uses observations taken by J. Dennett-Thorpe and AD444 uses observations taken by P. Best. All observations used in this body of work were re-reduced and calibrated by the author.

The author uses models of the Faraday screen presented by Burn (1966) and Tribble (1991). The author also uses a model for the evolution of FRII sources presented by Kaiser & Alexander (1997) and Kaiser, Dennett-Thorpe & Alexander (1997).

JAG 23/08/04

Acknowledgements

I would like to thank PPARC for their financial support in the form of a PPARC studentship.

Above all I would like to thank my supervisor Christian Kaiser for his support and advice throughout my three years. I would also like to extend my thanks to Philip Best at the University of Edinburgh. His advice on the use of AIPS was essential. I also would like to thank the NRAO VLA facility for providing me with all the archival data I needed.

I would also like to thank my fiance, David for all his love and laughter. I would never have got to the end with out you. I would also like to thank my family especially my Nan, my Mum and my Dad for their support during the dark days.

This thesis is dedicated to my grandfather, Kenneth Tennant Goodlet, who sadly passed away this year before I could finish and who would have been very proud.

I miss you..

"In the beginning, the Universe was created. This has made a lot of people very angry, and is generally considered to have been a bad move."

- Douglas Adams

Chapter 1

Introduction

The formation of all massive galaxies and also understanding their evolution is a vital component in understanding how the Universe evolved. Some of the most extreme, distant and powerful sources in the Universe have been observed in the radio band. AGN and radio galaxies were first solidly detected in radio in the 1950's using large aperture radio telescopes such as the Cambridge University and Sydney University radio telescopes (Krolik, 1999). The publication of the 3$^{\rm rd}$ Cambridge survey (3C) in 1962 (Bennett, 1962) represented the first comprehensive list of radio sources in the northern hemisphere. Unfortunately it was not the first complete survey using the Cambridge telescope. Embarrassingly the 1$^{\rm st}$ and 2$^{\rm nd}$ Cambridge surveys were found to be highly confusion limited and had to be abandoned (Mills & Slee, 1957). The Cambridge telescope was later upgraded and the well known 3C survey was produced. The revised 3C sample (3CR) is flux-limited, only sources brighter than 12 Jy at 178 MHz are included and hence only contains sources out to $z \sim 2$. Current technology has vastly improved on this limit, the new Texas - Oxford Survey (TOOT) (Hill & Rawlings, 2003) has a flux limit 100 times fainter than the 3CR sample and reaches as far back as $z \sim 4$.

Radio sources are visible in all wavebands ranging from X-ray, through the optical and into the radio. The Cosmic Microwave Background radiation scatters off the radio synchrotron emitting electrons into the X-ray band and 3C 273 was the first radio source to be found in X-rays (Bowyer et al., 1970). The Compton scattered emission from radio jets emits in the X-ray but AGN also emit X-rays directly. It was not until the late 1970's that the *Ariel V* survey found a sub-class of radio galaxies that were strong X-ray emitters (Elvis et al., 1978). Radio sources often have optical counterparts that have been observed with the large optical telescopes such as Keck and the Hubble Space Telescope. By observing these sources in the optical, observers can determine the host galaxy properties. For many sources this is the only way to determine where the nucleus of the radio source should lie as it may be too faint to be present at radio wavelengths. Recent studies by Stevens et al.

(2003) using SCUBA in the sub-mm have found that AGN may be present in many if not *all* large elliptical galaxies. Radio galaxies have been found to contain some of the most massive and distant black holes observed (Willott et al., 2003; Almaini et al., 1999).

Observing in the radio offers an unique opportunity that is absent from any other waveband. Radio observations are not limited by obscuration of dust such as in the UV and soft X-ray. Radio observations also do not depend on the time of day and only the most extreme of weather conditions can disrupt observations. Telescopes can be built near cities, e.g. Jodrell Bank, and do not need to be built on high mountain tops. Radio astronomy is often connected to the large impressive arrays of dish antennas that span many kilometres such as the Very Large Array (VLA) or the globe with Very Long Baseline Interferometry (VLBI). However, radio astronomy can and is being done on much smaller and simpler scales. LOFAR (low frequency array) for example is currently being built and will use 10,000 wire antennas, spread out across the Netherlands and Germany.

It is perhaps the high redshift Universe that is best suited to radio observations and by studying how the environments of populations of radio galaxies evolve we can begin to understand how the Universe itself evolved and also understand how the properties of the host galaxy are affected by changes in the source environment.

1.1 Classifying radio galaxies

Fanaroff & Riley (1974) were the first to suggest that radio galaxies could be effectively split into two distinct classifications, the so called FRI's and FRII's. FRI's are bright near their centers and fade out towards the edge whereas FRII's are brightest at their edges and fainter towards the center. Around $P_{178\mathrm{MHz}} \sim 10^{25}$ Hz^{-1} there is a break between the two classifications, all FRI's, in general, lie below this break and all FRII's above. Owen & Ledlow (1994) found that the break in radio luminosity extends into the optical and that FRIIs reside in the more optically-luminous galaxies.

The distinction between the two classifications becomes even more complicated when their morphologies are considered: FRI's generally have both jet and counter-jet structures visible and exhibit complicated non-uniform structure (e.g. 3C 48 Leahy et al., 2000). FRII's on the other-hand have very rarely been observed to have both jet and counter-jet structures. FRII jets are well confined and their lobe structure can be seen to extend up to several Mpc (e.g. 3C 236 and 3C 326). The luminosity break and the associated change in the source morphology has been suggested to be due to magnetohydrodynamical properties of the jet flow which determine the stability of the jet (Rawlings, 2002; Kaiser & Alexander, 1997).

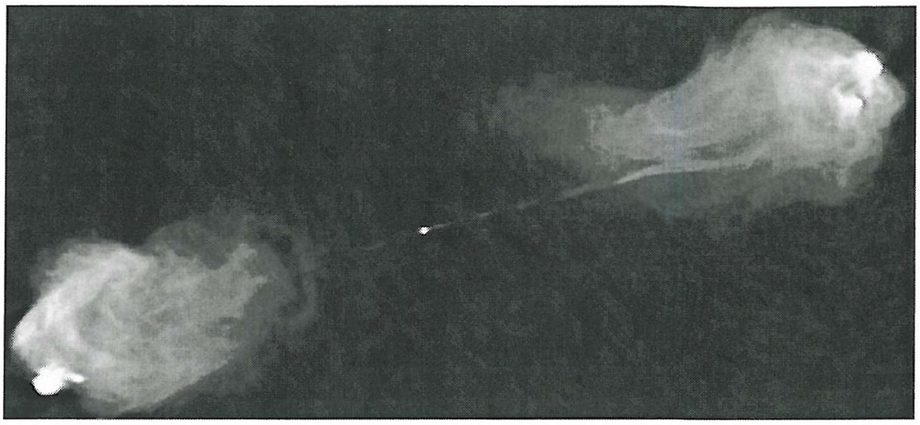

Figure 1.1: High resolution image of Cygnus A by Carilli & Barthel (1996). This image was generated with data from telescopes of the National Radio Astronomy Observatory, a National Science Foundation Facility, managed by Associated Universities. Inc.

The most famous example of a FRII is 3C 405, otherwise known as Cygnus A (see Carilli & Barthel (1996) for a good overview on this source). Figure 1.1 shows a high resolution image of Cygnus A, a "Classical Double" source. The low redshift ($z \sim 0.06$, Owen et al., 1997) of this object means that its radio structure has been well studied. At the top-right and bottom-left of Figure 1.1 there are two large diffuse structures known as the radio lobes. Within each lobe is a bright locale, known as the radio hotspot. Cygnus A is atypical in the fact that it shows a strong core (near the center) with both jet and counter-jet structures propagating outward. Both lobes show extensive filamentary structure, see Fomalont et al. (1989) for a discussion on the nature of these filaments. Cygnus A is often said to be overluminous (Carilli & Barthel, 1996) compared to most sources at this redshift. The relationship between redshift and radio-luminosity is discussed later in this chapter. In this thesis I concentrate on FRII objects only.

1.2 Environment or Orientation?

Many authors have used polarisation and flux measurements of powerful radio sources to argue that any observed asymmetries in these measurements are caused by orientation and/or environmental differences. Observing in different wavebands gives an insight into different regions of the source. In the optical, emission line properties of a source can give an indication of the richness of the source environment. X-ray observations sample the hot gas around a source and can determine how this gas influences the radio source. In the following sections I review the evidence for the interaction of powerful radio sources with their environment and explain how orientation effects also have a strong impact on what is observed at radio and other wavebands. I will then outline my own approach for determining the relationship between the observed source properties and the source environment.

1.2.1 The Laing-Garrington effect

Garrington et al. (1988) and Laing (1988) defined a sample of FRII sources with well defined jets. Both studies found that depolarisation, which is defined as the ratio of percentage polarisation at two separate frequencies, was almost always larger on the counter-jet side. This was deemed to be a simple orientation effect. The emission from the counter-jet, which is pointing away from an observer, has to travel along a longer path through the magnetised plasma in the vicinity of the source, causing it to appear more depolarised due to an inhomogeneous Faraday rotation (see chapters 4 and 5). This is known as the Laing-Garrington effect. Gregory & Condon (1991) proved that depolarisation by gas in the lobes themselves was unlikely to cause the observed asymmetry. This is now the common assumption: the depolarising medium in radio galaxies is external to the lobes and any internal component will not significantly contribute to the overall depolarisation.

1.2.2 Liu-Pooley effect

Liu & Pooley (1991a,b) found that the least depolarised lobe in a source also has the flatter spectral index. General arguments for the asymmetry of the spectral index in the lobes can be attributed to Doppler beaming of the hotspots. However, Liu & Pooley (1991a,b) found that the entire lobe shows a flatter spectral index, and thus the observed spectral asymmetry must be due to some intrinsic difference of the source environments. Later studies by Ishwara-Chandra et al. (2001) and Dennett-Thorpe et al. (1999) found that the Liu-Pooley effect was preferentially stronger for smaller sources and was independent of whether the sample comprised of radio galaxies, quasars or a mixture of both, see chapter 4 for a more detailed discussion.

1.2.3 Evidence for a non uniform medium around radio galaxies

Many authors have tried to determine if the so called Faraday screen around powerful radio sources is uniform or clumpy. The Faraday screen can cause the intrinsic polarisation vector of a source to rotate. It also causes a drop in the observed percentage polarisation if the structure of the magnetic field, within the Faraday screen, varies on scales smaller than the size of the beam of the telescope used in the observations. Both effects are highly wavelength dependent. The angle over which the polarisation vector rotates is directly related to the line–of–sight strength of the magnetic field and the column density of electrons surrounding a source. Carilli & Barthel (1996) found that Cygnus A showed a magnetic field structure that was uniform over $\sim$ 10 kpc.

Pedelty et al. (1989) found that the lobe length directly related to the strength of the depolarisation. Almost all of their high redshift, high radio-luminosity sources showed a preference for the smaller lobe to be more depolarised. This was explained as an environmental difference between the two lobes of an individual source and Pedelty et al. (1989) concluded that the Faraday medium around their radio galaxies was distinctly clumpy. If one lobe was embedded in a denser environment, it would not be able to expand as freely as the other lobe and the denser environment would cause a larger degree of depolarisation. This trend with size has also been found in many other studies (e.g. Strom, 1973; Strom & Jägers, 1988; Best et al., 1997). Strom (1973) also concluded that the depolarisation-size trend could be explained by the presence of a large gaseous halo around a source. Small sources would be deeply embedded in this Faraday screen and would be expected to show more depolarisation than a source that was only partially embedded. This is consistent with observations that there is a distinct lack of linear polarisation at long wavelengths ($\lambda >$ 49cm), which can be explained as a result of a large halo of gas around the source, generally associated with the host galaxy (Strom & Jägers, 1988). This halo then creates a large Faraday rotation, vastly reducing the degree of polarisation observed.

The extent to which the Faraday screen affects the observed radio properties of a source was first investigated by Burn (1966). More recent and perhaps realistic interpretations have been suggested by Tribble (1991) and Enßlin & Vogt (2003).

1.2.4 X-ray

A radio emitting source is generally assumed to be surrounded by a halo of hot, diffuse X-ray emitting material. Gregory & Condon (1991) found that the X-ray emission from elliptical galaxies was comprised of a symmetric halo, independent of whether the galaxy was in a group or a cluster. By combining X-ray observations with radio observations it is possible to show that in at least some sources, the diffuse halo of material is associated with the Faraday medium causing significant depolarisation (Gregory & Condon, 1991; Carilli & Barthel, 1996).

Observations of radio sources using ROSAT and CHANDRA have shown that FRII sources have a strong effect on the material surrounding them. A good example of this interaction is Cygnus A where the radio lobes are seen to forcibly expand into the X-ray emitting material (Carilli & Barthel, 1996). Young et al. (2001) also found this effect in their CHANDRA observations of M87. X-ray observations can be used to directly determine the gas density in the source environment. In a recent study by Hardcastle & Worrall (2000), it was found that low redshift FRII's do not reside in dense environments which is consistent with the results using galaxy correlation methods.

1.2.5 Galaxy correlation methods

Galaxy-correlation methods are an indirect method of sampling the environment around powerful radio galaxies. We expect that the density of the gas in-between galaxies is higher in 'rich' environments, e.g. galaxy clusters, compared to 'poorer' environments, e.g. isolated galaxies. The extent to which galaxies cluster around each other can be analysed using cross-correlation methods (Longair & Seldner, 1979; Prestage & Peacock, 1988; Yates et al., 1989; Yee & Green, 1987). This method is independent of any other observational method for sampling the source environment and only depends on how accurate galaxies can be correlated with each other.

Longair & Seldner (1979) were among the first to try and determine the extent to which radio sources in the 3CR and 4C samples (with $z < 0.1$), associated with the Zwicky galaxies (Zwicky et al., 1968), are clustered. Longair & Seldner (1979) found that extended powerful radio galaxies were in richer regions of space than galaxies selected at random. However, they also found that the sources with the strongest emission line spectra were isolated and very massive. This indicated that some sources could be massive enough to provide their own atmospheres and did not need to be within clusters or groups of galaxies. A later study by Prestage & Peacock (1988) using a much larger sample of galaxies out to $z < 0.25$, did not find this tendency for strong emission galaxies to be isolated, but did find that the most powerful galaxies were in rich clusters.

The conflicting results lead to the question as to whether the difference in the richness of the environment that surrounded a source was due to the differences in the redshift or radio-luminosity of the samples used. To try to overcome this degeneracy in redshift and radio-luminosity Yates et al. (1989) studied yet a larger volume of space with $0.15 < z < 0.82$. Yates et al. (1989) found that it was probably the differing radio-luminosity of the sources indicating differences in the richness of the environment, but they still could not rule out the possibility that there was some residual cosmic epoch effect.

1.2.6 Alignment effect

Powerful radio sources are often found to be located in giant elliptical galaxies and also to contain extended regions producing strong emission lines (e.g Inskip et al., 2002; Best et al., 2000a,b; Tadhunter et al., 1998; McCarthy et al., 1991; Ridgway et al., 2004; Inskip et al., 2003). These regions producing optical emission lines have often been found to align closely to the radio emission. A striking case is the aligned radio galaxy 3C 280 (Ridgway et al., 2004), which displays a tight correlation between its rest frame UV line emission and its radio emission. An expansion of a radio source into the surrounding medium can trigger star-formation (Storrie-Lombardi et al., 1996; Dey et al., 1997). 4C 41.17 at $z \sim 3.8$ is perhaps the strongest case for triggered star-formation. Optical measurements of the stellar population show a striking correlation with the position of the radio lobes. Chambers et al. (1987) also found that higher redshift sources displayed a stronger alignment effect, with very little alignment present in lower redshift sources (Inskip et al., 2002). Interestingly Inskip et al. (2003) found that the strength of the alignment effect was also dependent on the radio-luminosity of the sample, with the strength of the correlation weakening in the fainter 6C sample compared to the 3CR sample.

The observed alignment effect has also been found to depend on size, (Best et al., 1996) and the wavelength at which the observations were taken (Inskip et al., 2003). Inskip et al. (2003) found that the alignment effect was non-existent in their infrared observations of the 6C and 3CR sources at $z \sim 1$. McCarthy et al. (1991) found that there was more emission-line gas present in the near side of a source compared to the far side which argues for an orientation dependence of the emission-line gas.

1.2.7 Spectral Ageing

The spectral index of a source has been found, in general, to be flatter in the vicinity of the hotspot and steeper nearer the core regions (e.g Alexander & Leahy, 1987). This can be explained through energy losses of the electrons due to synchrotron radiation. The electrons towards the core are older than those closer to the hotspot and so have undergone more spectral ageing. Spectral ageing thus offers a unique way to determine the ages of radio sources. There are three main assumptions in this method:

i.) The main site of particle acceleration is the hotspot at the end of the jet,

ii.) The magnetic field is constant through-out the source,

iii.) The distribution of electrons can be described as a power-law.

Blundell & Rawlings (2001) argue against spectral ageing in radio sources, suggesting that the observed trend could be caused by a gradient in the magnetic field combined with a curved power-law distribution. Spectral ageing also assumes that there is no mixing between different populations of particles and that the radiative lifetime of synchrotron electrons is longer than the spectral age. Blundell & Rawlings (2001) suggest that both assumptions may be unrealistic.

Although the spectral ageing method may be too simplistic it is interesting to note that Alexander & Leahy (1987) find that the environmental effects on a source only become important around the FRI/FRII break. In other words, more luminous sources do not show spectral signatures caused by environmental effects.

1.2.8 Unified Model

There are many sub-classes within the FRII definition. Perhaps the most well known are the terms, radio galaxy, quasar and blazar. Originally these sources were thought to be separate and independent populations. It was proposed (e.g Barthel, 1989a) that the difference between these three populations was simply the angle at which the source was viewed, see Figure 1.2. At large angles to the line-of-sight an observer would simply see a radio galaxy with narrow line emission properties. As the angle decreases, the flux ratio of the lobes increases and the emission becomes dominated by the lobe pointing towards the observer. The narrow-line emission can no longer be seen and only broad line regions are visible, which is known as a broad line quasar. At very small angles to the line-of-sight the emission is completely swamped by the highly polarised jet emission. The separate FRII sub-classes can be simply stated a function of orientation angle (Scheuer, 1987; Peacock, 1987; Barthel, 1989a).

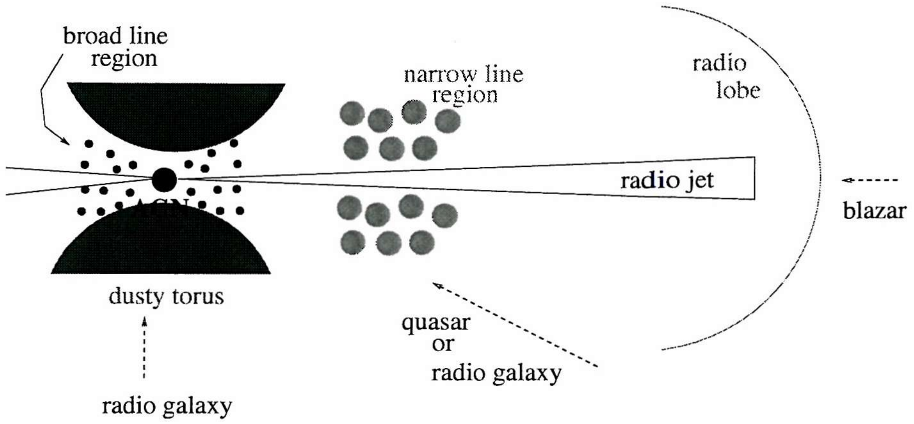

Figure 1.2: Simple cartoon picture of the unified model. The line-of-sight orientation determines if a source is observed to be a radio galaxy, quasar or blazar.

If the orientation angle was a factor in whether of not a source was observed to be a quasar or a 'normal' radio galaxy would expect all quasars and blazars to show evidence of beaming. Barthel (1989b) did indeed find that all the quasars in his sample showed some evidence of beaming.

1.2.9 Source or environment?

Sections 1.2.1 to 1.2.8 indicate that it is very hard to disentangle whether or not the gaseous environments of FRII radio sources change systematically as a function of redshift and/or radio luminosity. This is further complicated by orientation effects (e.g. Garrington et al., 1988), Doppler boosting (e.g. Leahy & Perley, 1991; Liu & Pooley, 1991a), size (Best et al., 1996) and wavelength (Inskip et al., 2003).

Studies are further complicated by the use of flux-limited samples and the resulting degeneracy between redshift and radio-luminosity.

1.3 Flux limited samples

A purely observational effect hampering the study of source environments is the Malmquist bias inherent in any flux-limited sample. Figure 1.3 demonstrates how severe this problem is in the case of the 3CRR sample by Laing et al. (1983). All complete surveys in the radio are flux-limited thus any analysis of the environments of these sources with respect to cosmic epoch or radio-luminosity will be greatly limited. To overcome the degeneracy between redshift and radio-luminosity it is possible to use sources taken from several samples, generally with different flux-limits, e.g. combining the 3CRR, 6CE and 7CRS samples (Blundell et al., 1999).

Figure 1.3 shows that there is a distinct lack of high radio-luminosity sources at lower redshifts. In fact, all low redshift sources (albeit a few over-luminous sources like Cygnus A) are at much lower luminosities than their high redshift cousins. As we observe at higher redshifts we are observing larger volumes of space. At low redshift the chance of finding a relatively powerful source is small because the radio luminosity function is steep. As the sampled volume of space increases, the probability of finding a rare high-luminosity source naturally increases. One of the aims of radio astronomy is to 'fill in' the z-P plane and remove the strong bias that is present in all surveys, even when using several complete samples, at different flux limits. Hill & Rawlings (2003) gives a concise review of the flux-limit problem.

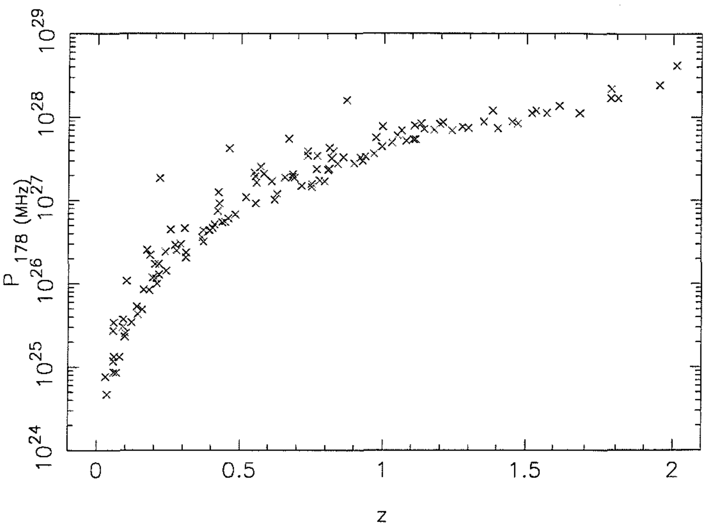

Figure 1.3: A radio luminosity-redshift plot for the 3CRR sample.

1.4 Modelling FRII's and their environment

In the previous sections I have reviewed observational techniques to test the environments of powerful radio sources. However, we can also attempt to model these sources and try to gain insights into their environments from a more theoretical point of view.

Scheuer (1974) and Blandford & Rees (1974) were the first to explain the double-lobed structure. In the simplest model, energy is transported from the nucleus of the source to the radio lobes by a relativistic beam, more commonly known as the radio-jet. Scheuer (1974) predicted that only a small fraction of the energy in the jet would be radiated away from the tip of the beam, known as the hotspot. The jet terminates at the hotspot and creates a jet shock. The lobe is generally assumed to be over-pressured and expands supersonically into the external medium, creating a bow shock (Alexander, 2002). A simple picture of the dynamics of a radio source is presented in Figure 1.4.

FRII's are generally assumed to expand with time along the jet axis and the pressure exerted by the jet is balanced by the ram pressure of the external gas (e.g Scheuer, 1974; Kaiser & Alexander, 1997; Kaiser et al., 1997; Hardcastle & Worrall, 2000). The jet must have enough ram pressure to overcome the external gas pressure, otherwise the source will not have a well defined hotspot (Prestage & Peacock, 1988). The rate of expansion of the lobe is highly dependent on the strength of the jet and the density of the source environment (Kaiser & Alexander, 1997). If a source was strongly constrained perpendicular to the jet axis, then there would be a tendency for sources to be long and thin which has not been observed

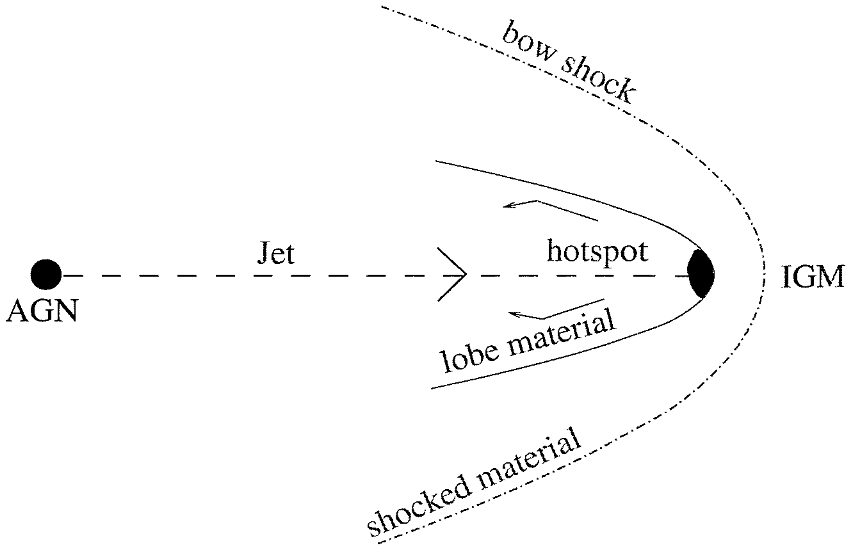

Figure 1.4: A simple impression of a FRII source.

(Miller et al., 1985).

In this thesis I apply the model of Kaiser & Alexander (1997) and Kaiser, Dennett-Thorpe & Alexander (1997) to the radio observations of FRII radio galaxies and quasars. Using this model I obtain estimates for the gas density in the environment of these sources. I then compare these model-dependent estimates with my observational results on the depolarisation of the radio emission.

1.5 This work

It is often difficult to obtain information on the properties of the black holes at the centres of active galaxies, their jets and their large scale environments from direct observations. As I have demonstrated, many studies to try and disentangle the source/environment interaction suffer from the redshift-radio luminosity degeneracy present in all flux-limited samples.

To break the degeneracy between redshift and radio luminosity I chose 3 subsamples of sources from the 3CRR and 6C/7C catalogues. The control sample consists of 6C and 7C sources at $z \sim 1$ with radio luminosities of around 10^{27} $\mathrm{WHz^{-1}}$ at 151 MHz. Another sample at the same redshift consists of 3CRR sources with radio luminosities around a magnitude higher at 151 MHz. The final sample consists of 3CRR sources at $z \sim 0.4$, again with radio luminosities of around 10^{27} $\mathrm{WHz^{-1}}$ at 151 MHz. The observations of these sources can then be used to study the source properties and the medium around the source, thus discovering which correlate with redshift and which correlate with radio luminosity enabling the following questions to be answered:

i.) Does a relationship exist between radio luminosity and the environment in which a given radio source lives?

ii.) Do the source environments evolve with redshift?

To arrive at answers to these questions I investigate in detail the depolarisation properties of my sample. I also apply the models of source evolution mentioned above to my observational results. Finally, I apply the later technique to a much larger sample.

As previously stated depolarisation and Faraday rotation are wavelength dependent. At low frequencies the degree of polarisation would be too low for an in-depth analysis of the environment and at high frequencies some of my sources would have too low signal-to-noise. Thus an intermediate frequency range of 1.4 GHz to 4.8 GHz was chosen.

The body of this work is dedicated to answering the question as to whether it is the redshift or the radio-luminosity of powerful radio sources that is the dominant factor in determining their observed characteristics.

1.6 Synopsis

In *chapter 2* I give a detailed description of the sample selection and subsequent methods used in the data reduction. I also present individual notes for each source used in the sample. All sources which have pre-published maps between 1.4 GHz and 4.8 GHz are detailed in Table 2.6.

In *chapter 3* I present the polarisation and flux properties for each source present in my sample and analyse the bulk trends present between my sub-samples. I also present the results of correcting the depolarisation measurements to a common redshift, $z = 1$, using the Burn (1966) law.

In *chapter 4* I present a more detailed analysis of the results presented in chapter 3. I use the Spearman Rank, Partial Spearman Rank and Principal Component Analysis tests to determine how the rotation measure and polarisation parameters relate to the fundamental parameters of redshift, radio-luminosity and radio size. I also analyse the asymmetries present in the flux and polarisation results to determine how the environments of these 26 sources differ and if these differences can be related to the fundamental parameters.

In *chapter 5* I present the results of using the Tribble (1991) models to correct the depolarisation measurements to a common redshift, $z = 1$, and the results are compared with those from chapter 3 using the simpler Burn (1966) prescription. I then use the Tribble (1991) models to determine if there is any evolution in the Faraday screen with respect to redshift or radio-luminosity.

In *chapter 6* I use the Kaiser & Alexander (1997) and Kaiser et al. (1997) models to estimate the density of the source environment and lobe pressure for each source described in chapter 2. I compare the density of the source environment and the lobe pressure, from the model, with the observed depolarisation and variations in the rotation measure to determine if the polarisation parameters are affected by the source environment. I then apply the models to the FRII sources from the combined 3CRR, 6CE and 7C III samples to estimate the density of the source environment, lobe pressure, jet-power and lobe age for each source. This allows a global approach to determine how the environments of powerful radio sources evolve with cosmological epoch and also with radio-luminosity.

Chapter 7 details the conclusions drawn from my findings and gives possible avenues for an extension to this study.

In appendices A to C I present the radio maps of all 26 sources from the small sample. Each source has an associated polarisation intensity and polarisation angle map at 4.8 GHz and 1.4 GHz, a spectral index and depolarisation map between 1.4 GHz and 4.8 GHz and a rotation measure and magnetic field angle map between 1.4 GHz and 4.8 GHz. 3C 457 is the exception as this source does not have any rotation measure or magnetic field maps associated with it. All chapters use a cosmology which assumes $H_o = 75$ kms^{-1}Mpc^{-1}, and $\Omega_m = 0.35$ $(\Lambda = 0.65)$. For full details of the cosmology used see appendix D. Finally, appendices E to G detail the archive information used in the modelling of the 3CRR, 6CE and 7C III samples.

Chapter 2

Observations and Data Analysis

Observations of the polarisation properties of extragalactic radio sources can provide information on the relationships between the radio source properties and their environments as well as the evolution of both with redshift. Many previous studies of variations in polarisation properties have suffered from a degeneracy between radio luminosity and redshift due to a Malmquist bias, present in all flux-limited samples. A good example of this effect is the depolarisation correlations (i.e. the ratio of percentage polarised flux at two frequencies) found independently by Kronberg et al. (1972) and Morris & Tabara (1973).

Kronberg et al. (1972) found that depolarisation of the radio lobes generally increased with redshift whereas Morris & Tabara (1973) found depolarisation to increase with radio luminosity. Due to the flux-limited samples (PKS and 3C) used by both authors it is difficult to distinguish which is the fundamental correlation, or whether some combination of the two occurs. Both suggestions have ready explanations: (i) If radio sources are confined by a dense medium then synchrotron losses due to adiabatic expansion are reduced, the internal magnetic field is stronger and a more luminous radio source results; if this confining medium also acts as a Faraday medium, more luminous sources will tend to be more depolarised. (ii) Sources at different cosmological epochs may reside in different environments and/or their intrinsic properties may change with redshift.

Hill & Lilly (1991) observed that galaxy densities around FRII radio sources increased with redshift out to $z \sim 0.5$ and beyond, but Wold et al. (2001) did not find this trend in a recent study. Welter et al. (1984) argued that the increase in rotation measure with redshift is primarily attributable to an increasing contribution of intervening matter. However, depolarisation asymmetries within a source, e.g the Laing-Garrington effect, increase with redshift which imply an origin local to the host galaxy (Garrington & Conway, 1991; Laing, 1980; Laing & Peacock, 1980).

2.1 Observational program

2.1.1 Sample selection

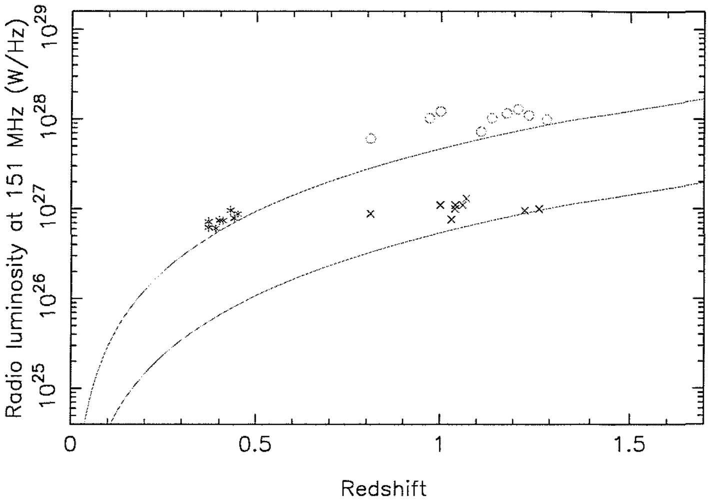

Figure 2.1: A radio luminosity-redshift plot showing the 3 subsamples used in the observations. Sample A is represented by '×', sample B by 'o' and sample C by '*'. The lines mark the flux limits for the 3CRR and 6C samples. A spectral index of -0.75 was used to shift the 3CRR data, originally observed at 178 MHz to 151 MHz.

Sample A was defined as a subsample chosen from the 6CE (Eales et al., 1997) subregion of the 6C survey (Hales et al., 1990), and the 7C III subsample (Lacy et al., 1999), drawn from the 7C and 8C surveys (Pooley et al., 1998). The selected sources have redshifts $0.8 < z < 1.3$, and radio luminosities at 151 MHz between $6.5 \times 10^{26}\,\mathrm{WHz}^{-1} < P_{151\,\mathrm{MHz}} < 1.35 \times 10^{27}\,\mathrm{WHz}^{-1}$. Sample B was defined as a subsample from the revised 3CR survey by Laing et al. (1983) containing sources within the same redshift range, but with luminosities in the range $6.5\times10^{27}\,\mathrm{WHz}^{-1} < P_{151\,\mathrm{MHz}} < 1.35 \times 10^{28}\,\mathrm{WHz}^{-1}$. Sample C is also from the 3CRR catalogue; it has the same radio luminosity distribution as the control sample, sample A, but with $0.3 < z < 0.5$. I only include sources that are more luminous than the flux limits of the original samples at 151 MHz (Figure 2.1). In all samples only sources with angular sizes $\theta \geq 10''$ (corresponding to $\sim$ 90 kpc at z=1) were included, see Table 2.1. This angular size limit is imposed by the depolarisation measurements. I required a minimum of ten independent telescope beams (1" per beam) over the entire source to ensure sufficient signal–to–noise. The distributions of linear sizes of the radio lobes are reasonably matched across all the samples (Figure 2.2), but note the two 'giant' sources in sample B.

Each sample initially contained 9 sources. The source 3C 109 was subsequently excluded from sample C as the VLA data for that source was of much poorer quality

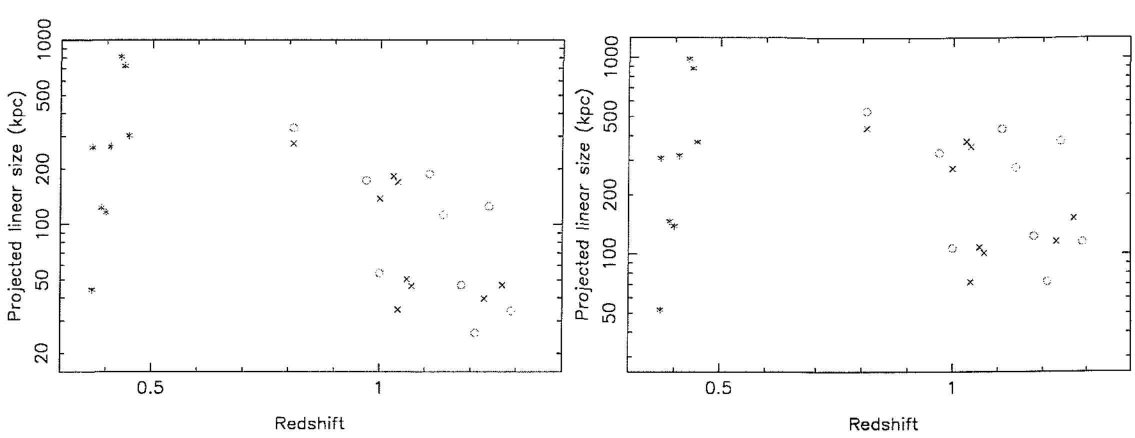

Figure 2.2: Linear size-redshift plots of the 3 subsamples used in the observations. Symbols as in Figure 2.1. Figure (a) assumes $H_o = 75$ kms^{-1}Mpc^{-1}, and $\Omega_m = 0.5$, $\Omega_\Lambda = 0$. Figure (b) assumes $H_o = 75$ kms^{-1}Mpc^{-1}, and $\Omega_m = 0.35$, $\Omega_\Lambda = 0.65$.

than that for the rest of the sample. The sources in the 3 subsamples are representative of sources with similar redshifts, radio-luminosities and sizes. However, the samples are not statistically complete because of observing time limitations. Sources that were fairly well observed at 4.8 GHz at B array (and C array if needed) were selected from the archives, this ensured that only a minimum of new observations were needed.

The ratio of angular to physical size varies only by a factor 1.3 between $z = 0.4$ and $z = 1.4$. This ensured that all the sources were observed at similar physical resolutions. All redshift values for 6C sources were taken from Eales et al. (1997) except for 6C 1018+37 which was taken from Rawlings et al. (2001). Redshifts for the 7C sources were taken from Lacy et al. (1999). Redshifts for the 3CRR sources were taken from Spinrad et al. (1985), 4C 16.49 was taken from Barkhouse & Hall (2001), 4C 14.27 was taken from Herbig & Readhead (1992) and 3C 457 was taken from Hewitt & Burbidge (1991).

2.1.2 Very Large Array observations

Observations of all 26 radio galaxies were made close to 1.4 GHz using the A-array configuration and a 25-MHz bandwidth. This bandwidth was used instead of 50 MHz to reduce the effect of bandwidth depolarisation which occurs when there are large changes in the rotation measure on the same scale as the beam size. The maximum angular size that can be successfully imaged using A array at 1.4 GHz is 38″. 12 sources were larger than this and were observed additionally with B array. Observations were also made at 4.8 GHz using a 50 MHz bandwidth. The maximum observable angular size in B array at 4.8 GHz is 36″. The same 12 sources as before,

Source	z	$P_{151\,\mathrm{MHz}}$ (W/Hz)	Angular size (arcsec)	$\sigma_{4.8\,\mathrm{GHz}}$ (μ Jy)	$\sigma_{1.4\,\mathrm{GHz}}$ (μ Jy)
6C 0943+39	1.04	1.0×10^{27}	10	20	55
6C 1011+36	1.04	1.1×10^{27}	49	15	65
6C 1018+37	0.81	8.8×10^{26}	64	24	50
6C 1129+37	1.06	1.1×10^{27}	15	21	60
6C 1256+36	1.07	1.3×10^{27}	14	18	70
6C 1257+36	1.00	1.1×10^{27}	38	33	100
7C 1745+642	1.23	9.5×10^{26}	16	30	60
7C 1801+690	1.27	1.0×10^{27}	21	24	75
7C 1813+684	1.03	7.1×10^{26}	52	23	47
3C 65	1.18	1.0×10^{28}	17	22	61
3C 68.1	1.24	1.1×10^{28}	52	41	100
3C 252	1.11	7.2×10^{27}	60	23	100
3C 265	0.81	6.5×10^{27}	78	32	70
3C 268.1	0.97	1.0×10^{28}	46	32	68
3C 267	1.14	1.0×10^{28}	38	25	61
3C 280	1.00	1.2×10^{28}	15	33	75
3C 324	1.21	1.3×10^{28}	10	26	70
4C 16.49	1.29	9.9×10^{27}	16	25	81
3C 16	0.41	7.4×10^{26}	63	36	80
3C 42	0.40	7.5×10^{26}	28	29	70
3C 46	0.44	7.9×10^{27}	168	20	53
3C 299	0.37	6.9×10^{26}	11	39	77
3C 341	0.45	8.8×10^{26}	70	26	88
3C 351	0.37	7.6×10^{26}	65	31	100
3C 457	0.43	9.6×10^{27}	190	18	80
4C 14.27	0.39	8.8×10^{26}	30	30	90

Table 2.1: Details of the sources in sample A, B & C. Sources in italics are quasars. σ_ν gives the 1σ noise level in the final total flux maps at frequency ν.

were then observed at 4.8 GHz with C array. This ensured that both 1.4 GHz and 4.8 GHz observations were equally matched in sensitivity and resolution. Details of the observations are given in Tables 2.2 to 2.4.

Sources in the 6C and 7C samples have a typical bridge surface brightness of $\sim 70\mu$ Jy beam^{-1} in 4.8 GHz A-array observations (Best et al., 1999). In order to detect 10% polarisation at 3σ in B-array observations I required an rms noise level of 20μ Jy beam^{-1}, corresponding to 70 mins of integration time. At 1.4 GHz, assuming $\alpha = -1.3$, bridges will be a factor of 4 more luminous. At this frequency, the integration time is set by the requirement to have an adequate amount of *uv*-coverage to map the bridge structures. 20 minute observations were split into 4×5 minute intervals. This observation splitting to improve *uv*-coverage was also done for the 4.8 GHz data.

As Table 2.2 demonstrates, for many of my sources the integration times at 4.8 GHz are considerably less than the 70 min requirement, due to telescope time constraints. At 1.4 GHz the integration time on all the sources is above the minimum required for good signal–to–noise. This is not the case at 4.8 GHz. Many of the observed properties that depend on polarisation observations (e.g depolarisation and rotation measure), are therefore poorly measured in the fainter components at 4.8 GHz. The values obtained are then only representative of the small region detected and not the entire component. Spectral index is independent of the polarisation measurements and so it is relatively unaffected by the short integration times.

The 3CRR sources are more luminous but much of this is due to the increase in the luminosity of their hotspots; their bridge structures are only a few times brighter than those of the 6C/7C III sources. To reach a 3σ detection of 7% polarisation on the bridge structures, a total integration time of 30 mins was required at 4.8 GHz and 20 mins at 1.4 GHz, split into 3-4 minute intervals to improve *uv*-coverage. The vast majority of the sources in sample B and C had at least this minimum amount of time on source at each frequency (see Tables 2.3 and 2.4).

2.1.3 Observational Programs

AD429 Most observations at 1.4 GHz in A array were obtained on 31/07/99 with the observing program AD429. The data from this day is strongly affected by a thunderstorm at the telescope site during most of the observations. Even after removal of bad baselines and antennas the noise level in this data remained at least twice the theoretical value. However, careful calibration and CLEANing reduced this effect to a minimum. Sample A was most affected by the thunderstorm and the lack of observing time at all frequencies. However, I find that the results obtained by Best et al. (1999) for some of the sources in sample A are in good agreement with my results. I am confident that my data is reliable for fluxes above the $3\sigma_{\rm noise}$ level. The polarisation calibration of AD429 was compared to the B–array data at 1.4 GHz (for the 12 sources that had B–array data). This confirmed that the position angle (PA) of the polarisation vector in both data sets agreed to within 15 degrees in all sources. This additional check was used to ensure that the 1.4 GHz polarisation angle calibration was accurate. AD429 also contains observations of sources in C array at 4.8 GHz. As these observations were taken on 12/06/00, these observations are obviously not affected by the thunderstorm that affects the 1.4 GHz data.

AD444 Tables 2.2 to 2.4 show that AD444 was used to observe some of the sources in B array at 4.8 GHz and also to complement the AD429 1.4 GHz observations in

Source	Array configuration	Frequency (MHz)	Bandwidth (MHz)	Observing program (dd/mm/yy)	Int. (min)
6C 0943+39	A	1465,1665	25	31/07/99 (AD429)	16
	B	4885,4535	50	20/05/01 (AD444)	31
6C 1011+36	A	1465,1665	25	31/07/99 (AD429)	16
	B	1452,1652	25	20/05/01 (AD444)	17
	B	4885,4535	50	25/02/97 (AL397)	21
		4885,4535	50	20/05/01 (AD444)	30
	C	4885,4535	50	12/06/00 (AD429)	20
6C 1018+37	A	1465,1665	25	31/07/99 (AD429)	16
	B	1452,1652	25	20/05/01 (AD444)	17
	B	4885,4535	50	20/05/01 (AD444)	31
	C	4885,4535	50	12/06/00(AD429)	20
6C 1129+37	A	1465,1665	25	31/07/99 (AD429)	16
	B	4885,4535	50	20/05/01 (AD444)	17
		4885,4535	50	25/02/97 (AL397)	21
6C 1256+36	A	1465,1665	25	31/07/99 (AD429)	16
	B	4885,4535	50	27/02/93 (AR287)	15
6C 1257+36	A	1465,1665	25	31/07/99 (AD429)	16
	B	4885,4535	50	20/05/01 (AD444)	16
		4885,4535	50	25/02/97 (AL397)	22
7C 1745+642	A	1465,1665	25	31/07/99 (AD429)	16
	B	4885,4535	50	20/05/01 (AD444)	11
		4885,4535	50	23/11/97 (AL401)	31
7C 1801+690	A	1465,1665	25	31/07/99 (AD429)	16
	B	4885,4535	50	26/03/96 (AB978)	29
		4885,4535	50	23/11/97 (AL401)	17
7C 1813+684	A	1465,1665	25	31/07/99 (AD429)	16
	B	1452,1652	25	20/05/01 (AD444)	16
	B	4885,4535	50	20/05/01 (AD444)	39
		4885,4535	50	23/11/97 (AL401)	19
	C	4885,4535	50	12/06/00 (AD429)	20

Table 2.2: Details of the VLA observations for sample A with the integration times included. See Tables 2.3 and 2.4 for samples B and C respectively.

Source	Array configuration	Frequency (MHz)	Bandwidth (MHz)	Observing program (dd/mm/yy)	Int. (min)
3C 65	A	1465,1665	25	31/07/99 (AD429)	16
	B	4885,4535	50	20/05/01 (AD444)	20
3C 68.1	A	1417,1652	25	31/07/99 (AD429)	16
	B	1417,1652	25	13/07/86 (AL113)	20
	B	4885,4535	50	19/07/86 (AB369)	300
	C	4885,4535	50	12/06/00 (AD429)	20
3C 252	A	1465,1665	25	31/07/99 (AD429)	16
	B	1465,1665	25	20/05/01 (AD444)	27
	B	4885,4535	50	19/07/86 (AB369)	97
	C	4885,4535	50	12/06/00 (AD429)	20
3C 265	A	1417,1652	25	31/07/99 (AD429)	16
	B	1417,1652	25	13/07/86 (AL113)	30
	B	4873,4823	50	17/12/83 (AM224)	238
	C	4873,4823	50	12/06/00 (AD429)	20
3C 267	A	1465,1665	25	31/07/99 (AD429)	16
	B	4873,4823	50	17/12/83 (AM224)	56
3C 268.1	A	1417,1652	25	31/07/99 (AD429)	16
	B	1417,1652	25	13/07/86 (AL113)	30
	B	4885,4835	50	15/08/88 (AR166)	20
		4885,4835	50	01/06/85 (AR123)	21
	C	4885,4835	50	06/11/86 (AL124)	102
3C 280	A	1465,1665	25	31/07/99 (AD429)	16
	B	4873,4823	50	17/12/83 (AM224)	46
3C 324	A	1465,1665	25	31/07/99 (AD429)	16
	B	4873,4823	50	17/12/83 (AM224)	51
4C 16.49	A	1465,1652	25	31/07/99 (AD429)	16
	B	4885,4535	50	04/03/97 (AB796)	30

Table 2.3: Details of the VLA observations for sample B

Source	Array configuration	Frequency (MHz)	Bandwidth (MHz)	Observing prog. (dd/mm/yy)	Int. (min)
3C 16	A	1452,1502	25	14/09/87 (AL146)	59
	B	1452,1502	25	25/11/87 (AL146)	39
	B	4885,4535	50	20/05/01 (AD444)	20
		4885,4535	50	17/11/87 (AH271)	10
	C	4885,4535	50	12/06/00 (AD429)	20
3C 42	A	1452,1502	25	14/09/87 (AL146)	40
	B	4885,4535	50	23/12/91 (AF213)	67
3C 46	A	1452,1502	25	31/07/99 (AD429)	16
	B	1452,1502	25	25/11/87 (AL146)	35
	B	4885,4535	50	20/05/01 (AD444)	20
	C	4885,4535	50	12/06/00 (AD429)	20
3C 299	A	1452,1502	25	31/07/99 (AD429)	16
	B	4835,4535	50	20/05/01 (AD444)	15
		4885,4835	50	28/01/98 (AP331)	15
3C 341	A	1452,1502	25	14/09/87 (AL146)	38
	B	1452,1502	25	25/11/87 (AL146)	47
	B	4885,4535	50	20/05/01 (AD444)	11
		4935,4535	50	26/10/92 (AA133)	25
	C	4885,4535	50	12/06/00 (AD429)	20
3C 351	A	1452,1502	25	31/07/99 (AD429)	16
	B	1452,1502	25	25/11/87 (AL146)	56
	B	4885,4835	50	19/07/86 (AB369)	12
		4885,4535	50	20/5/01 (AD444)	16
	C	4885,4835	50	09/10/87 (AA64)	22
3C 457	A	1452,1502	25	31/07/99 (AD429)	16
	B	1452,1502	25	25/11/87 (AL146)	30
	B	4885,4535	50	20/05/01 (AD444)	50
	C	4885,4535	50	12/06/00 (AD429)	20
4C 14.27	A	1452,1502	25	14/09/87 (AL146)	28
	B	4885,4535	50	20/05/01 (AD444)	17

Table 2.4: Details of the VLA observations for sample C

B array. The observations were all taken on the 20/05/01 and were not affected by any serious problems.

Archival Data For most sources some archival data has been used to supplement AD429 and AD444. Tables 2.2 to 2.4 detail which archival programs were used and the dates on which the sources were observed.

2.2 Data Reduction

The data reduction of the VLA data was done using the National Radio Astronomy Observatory's **A**stronomical **I**maging **P**rocessing **S**ystem or AIPS. All data from the archives was re-reduced to maintain consistency of data reduction methods when analysing the results.

2.2.1 Flux calibration.

The first step in the data reduction process involves removing the first 10s (usually) of each observation in the data set. This process is used to remove any residual errors from antenna tracking problems after moving to the target source. Once these initial scans are removed then the data is 'flagged' to remove any further errors in the data. Data is usually flagged for many reasons, such as interference from terrestrial sources (e.g mobile phones), errors with the antenna and receivers and bad weather. If a thunderstorm is present during an observing run, then this will cause large errors in the data due to the highly ionised clouds. This was unfortunately the case for most of the data set AD429 at 1.4 GHz and results in a higher noise level for the sources, see section 2.1.3. All scans flagged are entered into a 'FG' table within AIPS and are no longer used in the rest of the data reduction process.

A good example of where flagging is essential can be seen in the source 7C 1745+642 as observed as part of AD429. Figure 2.3(a) shows the effect of the thunderstorm on 7C 1745+642. The usual flux of this source is $\sim$ 80 mJy, but in several timesteps the flux jumps to more than 700 Jy, completely swamping the weak source underneath. By careful flagging of the bad timesteps I was able to retrieve the flux from the source which can be seen in Figure 2.3(b). Although this is an extreme case, it does demonstrate the need for flagging. After all the corrupted data has been removed the observations are ready to be calibrated.

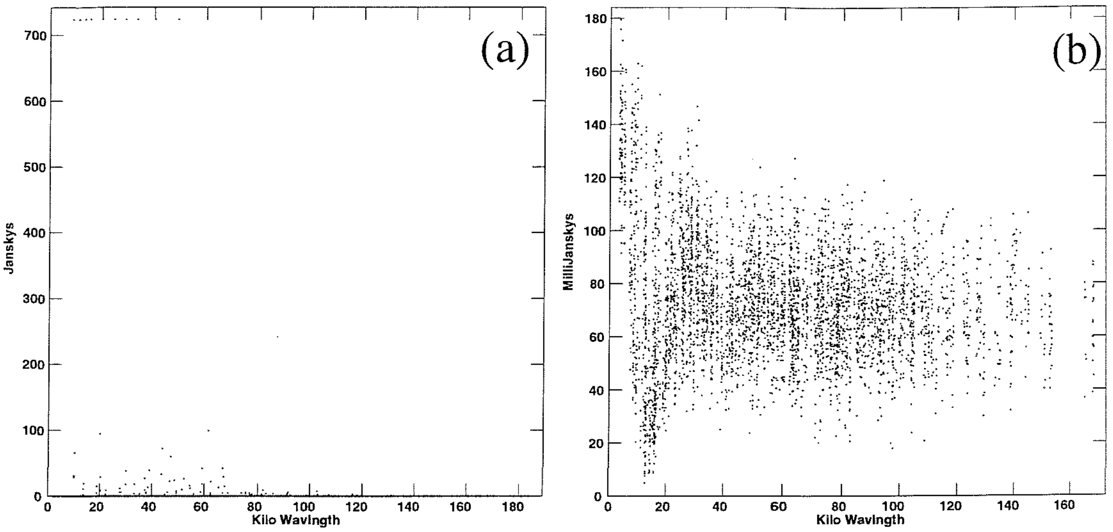

Figure 2.3: (a) A plot of the flux against u-v for the source 7C 1745+642. The radio flux of this source lies in the mJy range indicating that the burst exceeding 700 Jy is from a lightning bolt near the array. The lightning bolt affected 20 seconds of the data. (b) Removal of the affected 20 seconds results in a realistic UV spectrum. Only every 10th visibility is plotted.

2.2.1.1 Calibrating the primary calibrator.

The AIPS task SETJY uses a primary flux calibrator such as 3C 286 or 3C 48 to determine the absolute flux density scale on which all other calibrations are based. 3C 286 and 3C 48 are observed every few years with the VLA in D–configuration. Their flux density are recalculated accordingly using the modified Baars scale (Baars et al., 1977),

$$\log S = A + B \log \nu + C(\log \nu)^2 + D(\log \nu)^3 \tag{2.1}$$

where S is in Jansky, ν is in MHz and Table 2.5 gives the values of the constants A, B, C and D for 3C 286 and 3C 48 which I used here. SETJY uses the calculated flux densities of these primary calibrators to set the absolute flux calibration.

Source	A	B	C	D
3C 48	1.31572	-0.74090	-0.16708	0.01525
3C 286	1.23734	-0.43276	-0.14223	0.00345

Table 2.5: The constants for equation 2.1 with the 1999.2 values.

The task VLACALIB was then used to determine the antenna based calibration for the primary calibrator. Ideally the primary calibrators should be point sources that do not have any time variability. However, 3C 286 is partially resolved with most array combinations of the VLA and most wave bands. It is resolved on two scale lengths, it has a small secondary core located 2.5" from the central core and the core itself is partially resolved at longer baselines. To over come this it is possible to restrict the *uv*-range and (if necessary) the number of inner antennas used in the calibration fit. 3C 48 is also resolved with some array configurations and thus it also has some restrictions on its use. It also shows some time variability on the time scale of years. However, both calibrators are still the preferred primary calibrators and the restrictions do not adversely affect the flux calibration. For full details see the AIPS calibrator manual.

2.2.1.2 Calibrating the secondary

The primary calibrator sets the absolute flux density of the observations. Several secondary calibrators that lie as close to the target sources as possible are observed as frequently as the target sources. These secondary calibrators are essential in the phase calibration of the sources. The secondary calibrators are calibrated using the task GETJY which calculates the flux density of the secondaries with respect to the primary, thus 'bootstrapping' the initial calibration on to the secondaries. VLACLCAL then interpolates between individual observations of the secondary calibrator, thus applying the calibration to the entire data set. The last step in the flux calibration is to self-calibrate all the calibrators, still using VLACLCAL. This ensures that the flux calibration is complete. A final check on the flux density calibration is done using the task LISTR with OPTYPE='MATRIX' and DPARM = 3 1 0. This displays all the rms noise values for the calibrators. A high value of the rms noise indicates a bad calibration. In this case the calibration process was repeated until a satisfactory rms value was achieved.

2.2.2 Polarisation calibration.

Polarisation calibration is more straight forward than the flux density calibration. However, the range of polarisation angles (PA) must be known for the calibrators as a successful calibration requires a polarisation angle change of more than 90 degrees over the course of individual observing programmes. PCAL reads in the *uv*-data and determines the effective feed parameters for each antenna and also for each IF (intermediate frequency)*. All corrections are then applied to the 'AN' (antenna) table. PCAL removes the parallactic angle from the phase of the visibility data and applies the corrections to the instrumental corrections that are placed in 'AN'.

---

*The IF is the frequency that comes from mixing the local oscillator (LO) frequency with the radio frequency (RF). The RF is the incoming frequency of the observations and the LO is a sinusoidal signal that converts the RF to an IF.

2.2.3 Calibration of source files

The flux calibration and the polarisation calibration is now complete for the observations as a whole, but the sources must be individually 'cleaned'. There are several calibration methods that can be used, the main two used are CLEAN and the Maximum Entropy Method (MEM). The CLEAN method by Högbom (1974) represents a radio source as a collection of point sources in an empty field. An iterative process is used to find the flux and position of these point sources, removing 10% from the flux of the point sources, with the maximum flux, in each iteration. It then selects the most probable image from a set of images. MEM is not a procedural method, it selects the image with the largest entropy that fits the data and lies within the noise level. For full details of both methods see Cornwell et al. (1999). I use CLEAN to calibrate all my sources, but in order to check the quality of my maps I also use MEM, implemented in the AIPS task VTESS, instead of the CLEAN algorithm. The resulting maps are not significantly different from those produced by the CLEAN algorithm. In fact, despite common opinion VTESS is not necessarily superior to CLEAN in producing accurate maps of extended low surface brightness regions (Rupen, 1997).

2.2.3.1 Clean

Before the maps of individual sources can be cleaned they are first split off from the entire data set using the task SPLIT. The source is then loaded into IMAGR and the number of CLEAN iterations set via NITER. NITER determines the number of times IMAGR will subtract 10% from the current peak flux. By choosing too small a value of NITER the task IMAGR will not reach the noise level. By choosing too large an NITER the CLEAN algorithm will clean past the noise level, i.e. it will assume that the noise is part of the source structure and will try to incorporate it into a model of the source. This 'over–cleaning' can lead to errors in the final source map. Thus it is a sensitive balance and a conservative value for NITER is usually the best option for the first round of cleaning. When IMAGR is finished it produces a set of clean components (CC's). The CC's are essentially a representation of a map of the source including the noise. Selecting a set of CC's excluding the noise provides a template map for the observed source. This subset corresponds to a specific *uv*–range of the source and this range must be used in CALIB for self–calibration. The sub-set of the CC's and their corresponding *uv*–range are used in conjunction with SOLMODE='p' which means that the initial calibration is only concerned with the phase of the source. The template map of the source is used in self–calibration to reduce the residual noise, in other words, the template is used to modify the *uv* data to more closely fit the template. The new *uv* data set is then run through IMAGR again and the whole process is repeated. In general the self–calibration is used with SOLMODE='p' for two iterations and then SOLMODE='a&p' (i.e. both amplitude and phase) for all remaining iterations. After the final self-cleaning step the *uv* data set is ran through IMAGR with NITER set to a much higher value to remove the last remnants of any remaining noise from the stokes 'I' image, i.e. the total intensity image. IMAGR is then run on a reduced number of NITER with stokes 'Q' and then 'U'[†] to produce the raw maps that can be combined to produce polarisation maps described below.

2.3 Map production

Total intensity maps were made from the Stokes I parameters at each frequency. Polarisation maps were also made at all frequencies by combining the Stokes Q and U polarisation parameters. A map was then produced that contained the polarised flux, $P = (Q^2 + U^2)^{1/2}$, and the electric field position angle, $PA = 0.5\tan^{-1}(\frac{U}{Q})$, at a given frequency. The AIPS task POLCO was used to correct for Ricean bias, which arises when the Stokes Q and U maps are combined without removing noise-dominated pixels. By careful setting of the PCUT parameter this bias is removed. All maps only contain pixels where the polarised flux and the total intensity flux are above $5\sigma_{\rm noise}$ at 4.8 GHz and $3\sigma_{\rm noise}$ at 1.4 GHz. The lower threshold at 1.4 GHz was necessary because the 1.4 GHz data had a higher noise level, so blanking flux below 5σ resulted in large regions of polarised flux being lost.

At all frequencies the individual maps were made such that the beam size, the cell size of the image and the coordinates of the observations were exactly the same. If any of these properties of the map differed between frequencies, then the resultant multi-frequency map would contain false structures that would be directly related to the mis-alignment of the maps. To make sure that the coordinates (and cell size) were always within acceptable tolerances the AIPS task HGEOM was used to realign maps at one frequency to maps at another frequency. In sources where an identifiable core exists at both frequencies, the core positions were used as a check on the alignment from HGEOM. In general HGEOM is adequate in aligning the multi-frequency data. Sources with a distinct core at all frequencies were aligned within 0.03", where no core existed the hotspots were aligned within 0.045". In 4 sources this was not sufficient. 3C 68.1 had to be shifted 0.05" east and 0.07" north, 3C 265 had to be shifted 0.04" west and 0.02" north, 3C 299 had to be shifted 0.1" east and 0.03" north and finally 3C 16 had to be shifted 0.1" east and 0.1" north. All shifts were applied to the 4.8 GHz observations.

Spectral index maps were made between 4.8 GHz and 1.4 GHz, where the spectral index, α, is defined by $S_\nu \propto \nu^\alpha$. Depolarisation maps were made by dividing the map of the percentage polarised flux at 4.8 GHz by the corresponding map at 1.4

[†] $Q = (RL + LR)/2$ and $U = \mathrm{i}(RL - LR)/2$, where R is the right circular polarisation and L is the left circular polarisation (Fomalont & Perley, 1999).

GHz. Rotation measure maps were made using the polarisation angle maps at three frequencies,

$$PA(\lambda) = PA_\circ + RM\lambda^2, \tag{2.2}$$

where PA is the observed polarisation position angle of a source, $PA_\circ$ is the initial polarisation angle before any Faraday rotation, RM is the rotation measure and λ is the wavelength of the observations. Clearly, polarisation angle measurements are ambiguous by $\pm n\pi$ and this can introduce ambiguities in the rotation measure maps. A change of π between 1.4 GHz and 4.8 GHz introduced by the used fitting algorithm will cause a change of $\approx$ 80 rad m^{-2} in rotation measure. To determine if any strong rotation measure change is real within a rotation measure map a plot of the polarisation angle (measured on both sides of the observed jump) against λ^2, including $n\pi$ ambiguities can be produced. The best fit from AIPS is then overlayed. Any true feature will not show any ambiguities in $n\pi$. This has been done for two sources: 4C 16.49 and 6C 1256+36. The resulting fits are presented in Figures 2.4 to 2.5 and their corresponding χ^2 values for the fits are discussed in the relevant notes on these sources below. Another test that a feature is real is that a true jump in rotation measure causes depolarisation near the jump, but the magnetic field map shows no corresponding jump in the region.

The rotation measure maps of 7C 1813+684, 3C 65 and 3C 268.1 contained obvious jumps in position angle which I was not able to remove. Plots analogous to Figures 2.4 to 2.5 indicated that there were regions that obviously contained errors caused by $n\pi$ ambiguities. As previously noted the A array AD429 data was problematic and this was found to be the cause of the jumps. To overcome this problem I artificially shifted the position angles at 1.4 GHz data down by 10 to 15 degrees before the PA maps were produced. This shift is within the position angle error and resolved any ambiguities.

Table 2.4 shows that all sources in sample C were observed with IFs separated by only 50 MHz or less at around 1.4 GHz. This means that they were not well enough separated at 1.4 GHz to overcome the $n\pi$ ambiguities. To compensate for this lack of separation the 4.8 GHz observations were split into their two component frequencies, 4885 MHz and 4535 MHz. I then used 4 frequencies for the fit instead of 3, but the sources in sample C are still only marginally sensitive to $n\pi$ jumps. The resulting rotation measure maps cover the same frequency range as samples A and B, but use different frequencies for the fit. This was not possible in the case of 3C 351 and 3C 299, resulting in larger uncertainties in the rotation measurements for these sources.

In the case of sample C any source that has a large range of rotation measures ($>$ 80 rad m^{-2}), the AIPS task RM will force the rotation measure into a range $\pm$40 rad m^{-2} around the mean rotation measure. This is due to the lack of frequency separation at 1.4 GHz and it can cause jumps. In the case of 3C 457 these jumps were severe and I was unable to resolve them. The rotation measure and magnetic field maps for this source are not included in the analysis. The rotation measure varies smoothly over all other sources in this sample. The error affects the absolute value of the rotation measure for each source and therefore it does not affect the difference in the rotation measure between the two lobes of a given source, dRM or the rms variation in the rotation measure.

Depolarisation and rotation measure properties are discussed in more detail in chapter 3.

2.3.1 Notes on individual sources

In appendices A to C (Figures A.1 to C.8) I present the maps of the radio properties discussed above for all the sources from the 3 samples. Each figure shows the depolarisation map (where the polarisation was detected at all frequencies), the spectral index map, the rotation measure map and the magnetic field direction map (when a rotation measure is detected). Table 2.6 contains a listing of previously published maps for all sources, for completeness I have included all my reduced maps in the appendices but these maps are not published in Goodlet et al.(2004). In all cases only regions from the top end of the grey–scales saturate, as I have always kept the lowest values well inside the grey–scales, to ensure that no information has been lost.

2.3.1.1 Sample A:

6C 0943+39: (Figure A.1) No core is detected in my observations. Best et al. (1999) detected a core at 8.2 GHz and minimally at 4.8 GHz. My non-detection is probably due to the different resolution of the two data sets. The value of the rotation measure in the Eastern lobe must be considered with caution as it is based on only a few pixels.

6C 1011+36: (Figure A.2) This is a classic double-lobed structure, showing a strong core at both 4.7 GHz and 1.4 GHz with an inverted spectrum.

6C 1018+37: (Figure A.3) The maps were made with the smaller arrays only at each frequency. In the 1.4 GHz A-array data set the lower lobe was partially resolved out, but this was compounded by the high noise. So no feasible combination of the A and B array was possible. To maintain consistency the B-array 4.7 GHz data was also excluded.

Source	Map	Frequency (GHz)	Reference
6C 0943+39	P	4.8	Best et al. (1999)
6C 1011+36	P	4.8	Best et al. (1999)
	TI	1.4	Law-Green et al. (1995)
6C 1129+37	P	4.8	Best et al. (1999)
	TI	1.4	Law-Green et al. (1995)
6C 1256+36	P	4.8	Best et al. (1999)
	TI	1.4	Law-Green et al. (1995)
6C 1257+36	P	4.8	Best et al. (1999)
	TI	1.4	Law-Green et al. (1995)
3C 65	TI	1.4, 4.8	Polatidis et al. (1995)
3C 68.1	P	4.8	Bridle et al. (1994)
	TI	1.4	Leahy et al. (1989)
3C 252	P	4.8	Fernini et al. (1993)
3C 265	P	4.8	Fernini et al. (1993)
3C 267	TI	4.8	Best et al. (1997)
		1.4	Leahy et al. (1989)
3C 268.1	P	4.8	Laing (1981)
	TI	1.4	Leahy et al. (1989)
3C 280	P	1.4, 4.8	Liu & Pooley (1991b)
	S, D	1.4, 4.8	Liu & Pooley (1991b)
3C 324	TI	4.8	Best et al. (1998)
	P	1.4	Fernini et al. (1993)
4C 16.49	P	4.8	Lonsdale et al. (1993)
3C 16	TI	4.8	Giovannini et al. (1988)
	P	1.4	Leahy & Perley (1991)
3C 42	P	4.8	Fernini et al. (1997)
3C 46	TI	4.8	Giovannini et al. (1988)
		1.4	Gregorini et al. (1988)
3C 299	P	1.4, 4.8	Liu & Pooley (1991b)
	S, D	1.4, 4.8	Liu & Pooley (1991a)
3C 341	P	1.4	Leahy & Perley (1991)
3C 351	TI	4.8	Bridle et al. (1994)
	P	1.4	Leahy & Perley (1991)
3C 457	P	1.4	Leahy & Perley (1991)
4C 14.27	P	1.4	Leahy & Perley (1991)

Table 2.6: Details of previously published maps. TI = total intensity, P = polarisation, S = spectral index & D = depolarisation

6C 1129+37: (Figure A.4) The SE lobe contains two distinct hotspots, Best et al. (1999) found 3 hotspots. This discrepancy is probably due to the different resolutions of the two observations. The source shows distinct regions of very strong depolarisation, however these regions are slightly smaller than the beam size.

6C 1256+36: (Figure A.5) The rotation measure map shows distinct changes in the values of the rotation measure. Figure 2.4 shows that although the jump in RM, in the southern lobe, does not correspond to a jump in depolarisation, it is not due to any error in the fitting program. The corresponding reduced χ^2 values for the fits are given in Table 2.7.

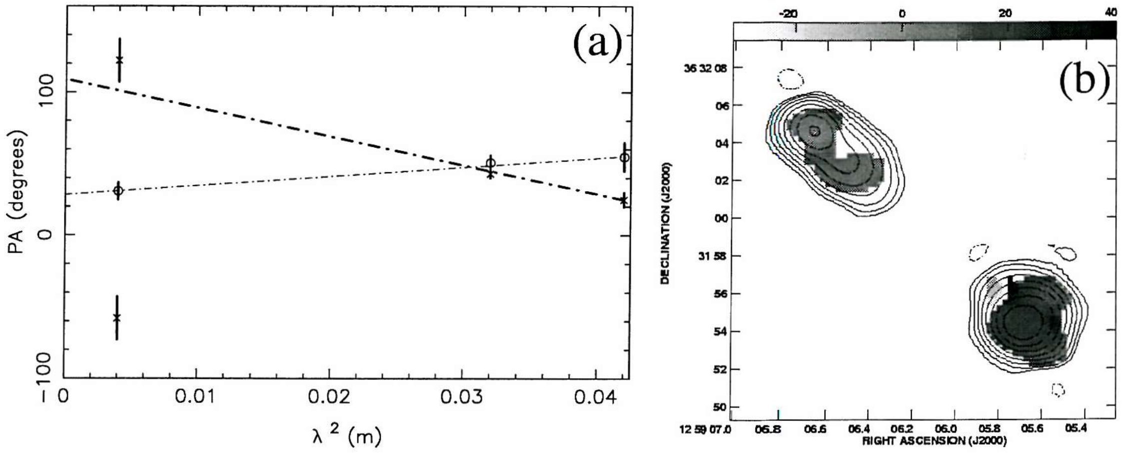

Figure 2.4: (a) A plot of the polarisation angle against λ^2, allowing for nπ variations, for the southern lobe of 6C 1256+36 with the dashed lines showing the best fit models. All reasonable nπ solutions for the 4.7 GHz data are considered and plotted. Both sides of the jump are plotted with 'o' indicating one side of the jump and '×' the other. (b) The rotation measure map for 6C 1256+36 (rad m^{-2}) between 4710 MHz, 1665 MHz and 1465 MHz. All contours are at 5σ at 4710 MHz (0.25 mJy beam^{-1})×(-1, 1, 2, 4...,1024) with a beam size of 2.5" × 1.4".

Source	Lobe	$n=-1$	$n=0$	$n=1$	Symbol
6C 1256+36	S	382.0	51.0	1.9	×
		981.6	1.2	976.5	o

Table 2.7: Reduced χ^2 values for the rotation measure fits for 6C 1256+36.

6C 1257+37: (Figure A.6) A core was detected at 4.7 GHz but was absent from the 1.4 GHz data. The high noise level and short observation time meant that the S lobe had very little polarised flux above the noise level. Reliable values for the rotation measure were found in only a few pixels around the hotspots.

7C 1745+642: (Figure A.7) This is a highly core dominated source, with the northern lobe appearing faintly. There is an indication of a jet-like structure leading down from the core into the southern, highly extended, off-axis, lobe. The source is a weak core dominated quasar (Barkhouse & Hall, 2001).

7C 1813+684: (Figure A.9) This is the faintest of the sources in sample A and is also a quasar (Barkhouse & Hall, 2001). The source shows a compact core that is present at all observing frequencies, but it is too faint to detect any reliable polarisation properties.

2.3.1.2 Sample B:

3C 65: (Figure B.1) The W lobe shows a strong depolarisation shadow that is smaller than the beam size. Best (2000) found the source to lie in a cluster which might account for the presence of the depolarisation shadow and the large depolarisation overall.

3C 68.1: (Figure B.2) The source is a quasar (Bridle et al., 1994). A core has been detected by Bridle et al. (1994) in deeper observations.

3C 252: (Figure B.3) The SE lobe shows a sharp drop in the polarisation between the 4.7 GHz and 1.4 GHz observations.

3C 265: (Figure B.4) The NW lobe shows evidence of a compact, bright region with a highly ordered magnetic field which at higher resolutions Fernini et al. (1993) show is the primary hotspot.

3C 267: (Figure B.5) The E lobe is highly extended, reaching to the core position, which can be seen in the 1.4 GHz image. The large depolarisation region in the W lobe coincides with a region with no observed rotation measure. The core is strongly inverted with $\alpha = 0.48$.

3C268.1: (Figure B.6) This is a classic double–lobed source but there is no core detected at either 1.4 GHz or 4.8 GHz.

3C 280: (Figure B.7) The value of the rotation measure and the magnetic field direction in the E lobe must be treated with caution as it is based on only a small region of the entire lobe. The sharp changes in the rotation measure map are not seen in the magnetic field map and the depolarisation map shows a similar structure suggesting that is not due a fitting error.

3C 324: (Figure B.8) The NE lobe shows evidence of a depolarisation shadow. Best (2000) found the source to lie in a cluster which may explain the faint shadow.

4C 16.49: (Figure B.9) The source is a quasar (Barkhouse & Hall, 2001), that shows a strong radio core, jet structure and possibly a small counter-jet. The source is highly asymmetric with the southern lobe almost appearing to connect to the core. It has a very steep spectral index, $\alpha < -1.0$ making it an atypical source. Figures 2.5(b) and 2.5(c) demonstrates that the sharp changes in the rotation measure map, see Figure 2.5(a), are not due to any fitting errors. The corresponding reduced χ^2 values for the fits are given in Table 2.8.

Source	Lobe	$n=-1$	$n=0$	$n=1$	Symbol
4C 16.49	N (b)	1.6	669.0	2917.0	○
		2772.0	90.1	1.7	×
4C 16.49	S (c)	151.9	0.9	62.0	○
		45.4	0.4	34.8	×

Table 2.8: Reduced χ^2 values for the rotation measure fits for Figure 2.5.

2.3.1.3 Sample C:

3C 16: (Figure C.1) The source shows a strong SW lobe, with a relaxed NE lobe. The SW lobe shows a strong depolarisation feature that is narrower than the beam size. The strong rotation measure feature is evident in the depolarisation map, but not the magnetic field map, indicating that it is not an error in the fitting program. No value for the rotation measure was obtained for the NE lobe because the polarisation observed was too weak.

3C 42: (Figure C.2) The core was detected at 4.7 GHz, but was absent at the lower frequencies. The source has been observed to lie in a small cluster by de Vries et al. (2000). Fernini et al. (1997) observed that the N hotspot was double, but this is not evident in my observations which can be attributed to the differences in the resolutions of the two observations.

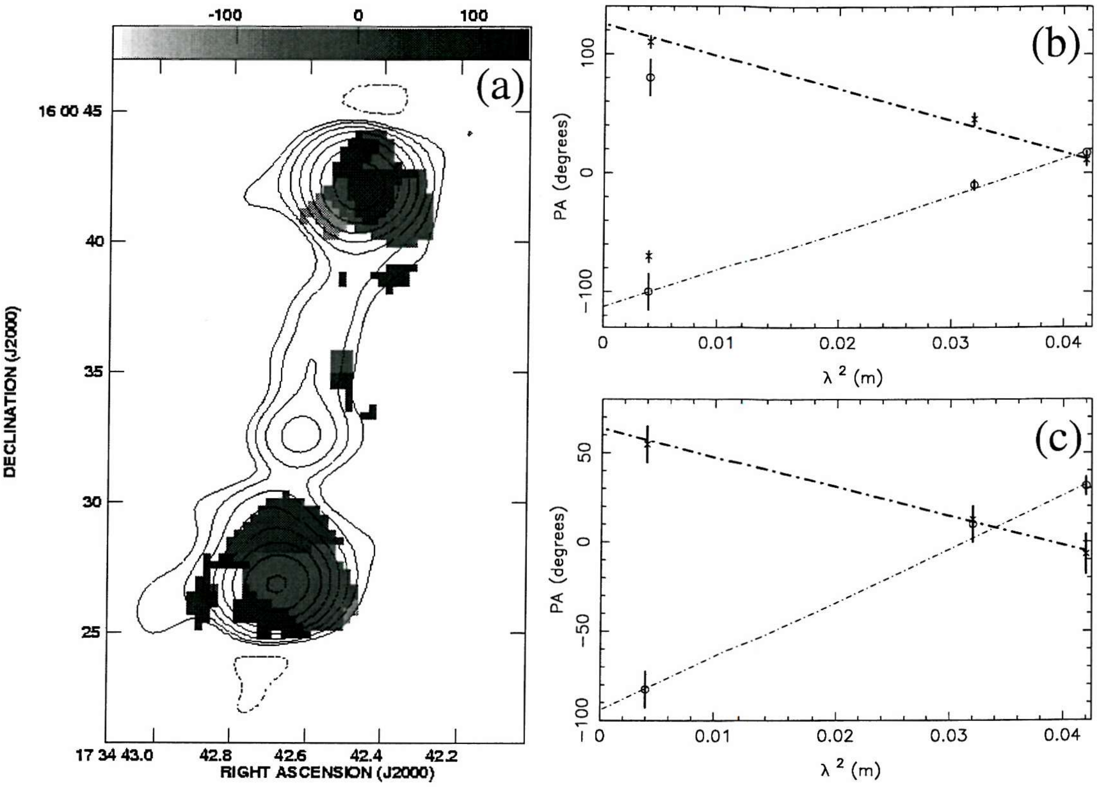

Figure 2.5: (a) Map of the rotation measure of the radio source 4C 16.49 (rad m^{-2}) between 4710 MHz, 1665 MHz and 1465 MHz. All contours are at 5σ at 4710 MHz (0.8 mJy beam^{-1})×(-1, 1, 2, 4...,1024) with a beam size of 2.2" × 1.8". (b) A plot of the polarisation angle against λ^2, allowing for nπ, for the northern lobe of 4C 16.49 with the dashed lines showing the best fit models. All reasonable nπ solutions for the 4.7 GHz data are considered and plotted. Data for two small regions, one on each side of the jump are plotted with 'o' indicating one side of the jump and '×' the other. The jump plotted lies SW of the central intensity contour. (c) Same as (b) but for the southern lobe, the region plotted lie either side of the jump south of the peak intensity contour.

3C 46: (Figure C.5) The source has a prominent core at 4710 MHz, but it is indistinguishable from the extended lobe at 1452 MHz.

3C 341: (Figure C.3) The source is a classic double with a resolved jet-like structure running into the SW lobe. The jet is more prominent in the higher frequency observations than at the lower frequencies.

3C 351: (Figure C.4) The source is an extended and distorted quasar (Bridle et al., 1994). Both lobes expand out to envelope the core. The NE lobe is highly extended, off-axis and shows two very distinct hotspots. The depolarisation increases towards the more compact SW lobe supporting the idea that the environment around the SW lobe is denser, stopping the expansion seen in the NE lobe. There is evidence of a rotation measure ridge in the NE hotspots which corresponds to a narrow ridge of depolarisation, but there is no corresponding shift in the magnetic field map.

3C 457: (Figure C.6) The SW lobe shows a prominent double hotspot. The small compact object just south of the SW hotspots is most likely an unrelated background object. The inverted core was observed to be present at all frequencies. This source has no rotation measure map or magnetic field measure map as I was unable to remove all $n\pi$ ambiguities from this source. This was due to the small separation of observing frequencies around 1.4 GHz and 4.8 GHz, see section 2.3.

3C 299: (Figure C.7) The source is the least luminous of all the sample members. The source shows a large change in rotation measure between the lobes but the difference is probably due to the small number of pixels with rotation measure information in the NE lobe.

4C 14.27: (Figure C.8) There is no core detected at any frequency even in a better quality map by Leahy & Perley (1991).

Chapter 3

Source properties and trends

The average spectral index, average depolarisation and average rotation measure are given by α, DM and RM respectively. Each of these parameters are the average over each individual lobe of a source. α is calculated using $S_{\nu} \propto \nu^{\alpha}$ between 1.4 GHz and 4.8 GHz, where the S_{ν} are the Total Intensity Flux values given in Tables 3.1 to 3.3. The average DM is calculated using the percentage polarised flux measurements given in Tables 3.1 to 3.3. The average RM is measured directly from the rotation measure maps (see appendix A to C) using the AIPS task IMEAN.

The differential spectral index, differential depolarisation and differential rotation measure over the lobe of an individual source are given by dα, dDM and dRM respectively. All differential properties are taken to be the difference of the averages over individual lobes of a source e.g. dDM = DM_{lobe_1} - DM_{lobe_2}. The rms variation of the rotation measure is defined by σ_{RM}.

To test if any property is varying between samples I compare the average of the property over a *sample* with the average taken from the other two samples. This allows a simple statistical test to be applied to the data. I also average properties over samples with equal distributions in redshift (A+B) and equal distributions in radio-luminosity (A+C). For example, if depolarisation increases with redshift but not with radio-luminosity I would expect samples A and B to show similar averages (within errors) but to be statistically greater than sample C. In this case I would also expect to see the average of sample A+C (low radio luminosity sources) to be statistically similar to the average of sample B (high radio luminosity sources). A more thorough statistical approach using Spearman Rank, Partial Spearman Rank and Principal Component Analysis is presented in chapter 4.

3.1 Polarised Flux and Spectral Index.

The flux observed from both lobes of all sources was found to be polarised at levels greater than 1%, the only exceptions being 6C 0943+39 and 3C 299, see Tables 3.1 to 3.3. At lower redshifts the polarisation exhibits the largest range from 0.8% in 3C 299 to 28.0% in 3C 341. This range is not evident in either of the other two samples. Statistically the sources at low redshift (sample C) are slightly more polarised than those at high redshift, both at 1.4 GHz (sample A: 2.1σ, sample B: 2.3σ) and at 4.8 GHz (sample A: 1.8σ, sample B: 1.8σ). There is no difference between the low radio luminosity sources (sample A) and the high luminosity objects (sample B). This suggests that percentage polarisation decreases for increasing redshift but is less dependent on radio luminosity.

Table 3.4 shows that there are no significant correlations between spectral index, α, and redshift or radio luminosity as suggested by Onuora (1989), Veron et al. (1972) and Athreya & Kapahi (1999), which use much larger samples. This suggests the trend may be present, but may be masked by my small sample size. However, there are trends found with the difference in spectral index between the two lobes. Sample B shows a larger average difference in the spectral indices, $d\alpha$ between the two lobes of a given source than the other samples (sample A: 2.5σ, sample C: 3.3σ). Sample B contains the sources with the highest radio luminosity and so I find that in my samples the difference in spectral index, $d\alpha$ increases with radio luminosity rather than with redshift. The trend of the difference in the spectral index between the two lobes may be related to the extra luminosity of the 3CRR hotspots compared to the 6C/7C hotspots (see section 2.1.2). On average I find that the hotspots of my sources have shallower spectral indices. The average spectral index integrated over the entire sources will therefore depend on the fraction of emission from the hotspots compared to the extended lobe, thus creating the observed trend.

3.2 Rotation measure

Faraday rotation occurs when polarised light passes through a plasma. AGN's emit synchrotron radiation which is almost completely linearly polarised, this can be separated into right-handed (RH) and left-handed (LH) circular polarisation which have different phase velocities. At a distance dl from a source the two circular polarisations will be out of phase by $\Delta\theta$, which is given by:

$$\Delta\theta = \frac{\phi_{RH} - \phi_{LH}}{2} = \left(\sqrt{(}\epsilon_{RH}) - \sqrt{(}\epsilon_{LH})\right)\frac{\omega dl}{2c} \tag{3.1}$$

$$\text{where} \quad \sqrt{(}\epsilon) = 1 - \frac{\omega_p^2}{2\omega^2}\left(1 - \pm\frac{\omega_g}{\omega}\right) \tag{3.2}$$

		4800 MHz		1465 MHz		
Source	Comp.	Total Flux (mJy)	Polarisation %	Total Flux (mJy)	Polarisation %	α
6C 0943+37	W	31.0	11.8	71.7	5.4	-0.72
	E	42.0	2.7	136.4	0.7	-1.01
6C 1011+36	N	44.3	7.8	119.6	5.1	-0.88
	S	18.7	12.2	50.9	11.5	-0.89
	Core	3.2	–	0.7 ±0.5	–	1.35
6C 1018+37	NE	46.4	10.0	125.8	8.1	-0.85
	SW	28.7	7.0	76.3	2.9	-0.84
	Core	0.63 ±0.2	–	–	–	–
6C 1129+37	NW	46.5	7.3	129.1	2.9	-0.85
	SE	73.2	16.3	215.0	3.2	-0.90
6C 1256+36	NE	57.8	10.4	148.9	7.7	-0.79
	SW	101.4	8.9	288.5	8.8	-0.87
6C 1257+36	NW	43.5	17.0	102.2	13.4	-0.71
	SE	20.5	9.8	73.0	5.2	-1.06
	Core	0.29 ±0.1	–	–	–	–
7C 1745+642	N	23.5	9.6	64.5	5.2	-0.86
	Core	84.1	4.9	69.4	2.9	0.16 ±0.1
	S	33.8	8.6	98.5	9.5	-0.91
7C 1801+690	N	8.80 ±3.0	3.0	28.2	2.7	-0.97
	Core	79.1	1.8	78.4	4.0	0.007
	S	28.7	10.0	75.8	7.2	-0.81
7C 1813+684	NE	15.0	7.7	44.8	9.5	-0.92
	SW	30.2	8.4	78.1	7.4	-0.79
	Core	3.3	–	2.65	–	–

Table 3.1: Properties of the sample A radio source components. Errors are 5% or less unless stated otherwise. The spectral indices are the mean values for each component, calculated between approximately 4800 MHz and 1465 MHz.

Source	Comp.	4800 MHz Total Flux (mJy)	4800 MHz Polarisation %	1465 MHz Total Flux (mJy)	1465 MHz Polarisation %	α
3C 65	W	524.0	19.3	1683.1	5.4	-1.00
	E	240.9	9.2	800.4	7.2	-1.03
3C 252	NW	178.7	6.4	592.2	5.9	-1.00
	SE	80.0	14.1	300.5	6.8	-1.10
	Core	1.98	–	1.33	–	0.33
3C 267	E	184.0	8.9	745.7	6.8	-1.17
	Core	1.87 ±1	–	1.05 ±2	–	0.48
	W	479.2	3.5	1294.6	3.3	-0.83
3C 280	E	326.0	8.0	1219.2	4.4	-1.01
	W	1289.2	10.0	3191.6	6.5	-0.76
3C 324	NE	432.6	9.3	1525.2	5.6	-1.05
	SW	166.0	7.8	651.8	4.0	-1.14
4C 16.49	N	107.2	8.3	307.2	13.0	-0.88
	Jet	8.5 ±4	14.5	45.9	7.2	-1.41
	Core	9.64 ±2	2.7	58.2	3.5	-1.50
	S	142.3	7.0	695.3	6.4	-1.32
3C 68.1	N	667.2	8.6	1767.4	7.0	-0.82
	S	36.8	11.4	134.6	6.6	-1.08
3C 265	NW	224.0	10.0	478.7	5.8	-0.62
	SE	318.9	6.2	835.0	4.2	-0.78
3C 268.1	E	262.3	5.0	816.4	3.4	-0.92
	W	2296.6	4.7	4699.0	2.7	-0.58

Table 3.2: Properties of the sample B radio source components. Errors are 5% or less unless stated otherwise. The spectral indices are the mean values for each component, calculated between approximately 4800 MHz and 1465 MHz.

		4800 MHz		1452 MHz		
Source	Comp.	Total Flux (mJy)	Polarisation %	Total Flux (mJy)	Polarisation %	α
3C 42	NW	353.9	12.5	999.7	12.3	-0.87
	SE	450.6	7.5	1266.3	7.4	-0.86
4C 14.27	NW	107.0	12.4	368.2	8.8	-1.06
	SE	124.8	9.6	489.3	9.3	-1.17
3C 46	NE	162.7	16.2	488.0	12.8	-0.94
	SW	173.7	13.7	506.4	12.0	-0.91
	Core	2.54	–	7.94	–	-0.97
3C 457	NE	208.6	15.8	692.0	15.7	-1.02
	SW	290.5	11.9	898.9	10.0	-0.94
	Core	3.03	–	2.63	–	0.12
3C 351	NE	971.7	6.8	2327.9	8.1	-0.73
	Diffuse	122.2	26.4	421.3	13.7	-1.03
	Core	18.3	18.6	46.2	8.2	-0.77
	SW	77.1	22.8	235.7	8.9	-0.93
3C 341	NE	123.8	28.0	336.4	19.6	-0.85
	SW	265.9	26.4	862.6	17.2	-1.00
3C 299	NE	876.5	0.79±0.5	2592.4	0.43 ±0.3	-0.93
	SW	53.7	3.1	122.6	2.6	-0.71
3C 16	NE	22.1 ±3	10.8	60.9	4.9	-0.87
	SW	484.9	14.7	1510.9	8.2	-0.97

Table 3.3: Properties of the sample C radio source components. Errors are 5% or less unless stated otherwise. The spectral indices are the mean values for each component, calculated between approximately 4800 MHz and 1452 MHz.

Average Prop.	Sample A	B	C
z	1.06 ± 0.04	1.11 ± 0.05	0.41 ± 0.01
P_{151}	$(1.02 \pm 0.06)\times10^{27}$	$(1.01 \pm 0.07)\times10^{28}$	$(8.02 \pm 0.40)\times10^{26}$
D	220.34 ± 46.40	262.69 ± 55.41	399.57 ± 122.50
α	-0.87 ± 0.01	-0.92 ± 0.06	-0.94 ± 0.03
dα	0.13 ± 0.04	0.23 ± 0.04	0.10 ± 0.03
$PF_{1.4}$	6.29 ± 0.86	5.88 ± 0.64	9.89 ± 1.75
$PF_{4.8}$	8.91 ± 1.03	8.76 ± 0.89	13.31 ± 2.48

Average Prop.	Sample A+B	A+C
z	1.08 ± 0.03	0.75 ± 0.08
P_{151}	$(5.57 \pm 1.16)\times10^{27}$	$(8.97 \pm 0.77)\times10^{26}$
D	241.51 ± 35.43	304.69 ± 64.50
α	-0.90 ± 0.03	-0.90 ± 0.02
dα	0.18 ± 0.01	0.12 ± 0.02
$PF_{1.4}$	6.08 ± 0.52	7.98 ± 1.01
$PF_{4.8}$	8.83 ± 0.66	10.98 ± 1.36

Table 3.4: Mean properties of the sources averaged over each sample with the associated error. Differential spectral index (dα) is derived by taking the difference in the spectral index between the two lobes of each source and then averaging this difference over each sample. Source size is in kpc and radio-luminosity is in W/Hz.

where ω_p is the phase velocity of the polarisation, ω_g is the non relativistic gyrofrequency of the electrons in a magnetic field, $\omega = 2\pi\nu$ where ν is the frequency of the observations and c is the speed of light. The total phase difference is then

$$\Delta\theta = \frac{e^3}{2\omega^2 m_e^2 c\epsilon_0}\int_0^z n_e B_{||}\,dl \tag{3.3}$$

where $B_{||}$ is the line-of-sight component of the magnetic field, n_e, the column density around the source, dl is the path length to the source, e is charge on the electron, m_e is the mass of an electron and ϵ_o is the electric constant. From section 2.3 the observed rotation measure, RM, of a source depends on the frequency of the observations, $RM = \Delta\theta/\lambda^2$, hence equation 3.3 becomes:

$$RM = \frac{e^3}{8\pi^2 m_e^2 c^3 \epsilon_o}\int_0^z n_e B_{||}\,dl \tag{3.4}$$

where RM is in rad m^{-2}.

Observationally it is not possible to measure the electron density or the magnetic field strength without some prior assumptions, thus the rotation measure must be calculated from the observed polarisation angle. The rotation measure a source displays is related to the degree of rotation of the polarisation position angle over a set frequency range, see equation 2.2. To gain an accurate value of the rotation measure three frequencies (1.4 GHz, 1.6 GHz and 4.8 GHz) are used to overcome the $n\pi$ ambiguities discussed in chapter 2.3 that arise when fitting to the observed polarisation angles (Simard-Normandin et al., 1981; Rudnick et al., 1983).

The observed RM and the degree of polarisation in a source may be caused by the presence of plasma either inside the radio source itself (internal depolarisation) or by a Faraday screen in between the source and the observer (external depolarisation). In the latter case the screen may be local to the radio source or within the Galaxy, or both. Only in the case of an external Faraday screen *local* to the radio source do the measurements contain any information on the source environment.

The average RM observed in my sources is consistent with a Galactic origin (Leahy, 1987). This is also consistent with the absence of any significant differences of RM between the samples (see Table 3.5). However, large variations of RM are observed within individual lobes on small angular scales, e.g. dRM and σ_{RM}, are probably caused by a Faraday screen local to the source (Leahy, 1987) and therefore must be corrected for the source redshift by multiplying by a factor $(1+z)^2$. This allows a valid comparison between sources. The variation of RM on angular scales of order 10s of arcseconds, i.e. between the two lobes of a source, dRM, may still be somewhat influenced by the Galactic Faraday screen. Nevertheless, the large variations of RM found on arcsecond scales measured by σ_{RM} suggest an origin local to the source. There is no statistically significant trend of dRM with respect to redshift or radio luminosity as is seen in Table 3.5. This is again consistent with a Galactic origin of the RM properties of the sources on large scales. On small angular scales the variation of RM as measured by its rms variation, σ_{RM}, shows a significant trend between the low redshift sample (C) and the high redshift samples (A: 2.6σ, B: 3.3σ). The exclusion of 3C 457 due to $n\pi$-ambiguities in the rotation measure (see Section 2.3) from the rotation measure averages could bias the sample C results towards a small value of σ_{RM}. In principle, similar ambiguities could also affect other sources in sample C. However, as stated above the rotation measure is found to vary smoothly across the other sources in this sample. The exclusion of one source will not remove the trend found here. There is no significant difference between the low and high radio luminosity samples A and B, suggesting that at least the range of rotation measures on small angular scales in a source *does* depend on the source redshift and not the source radio luminosity.

3.3 Depolarisation

The observed depolarisation depends on the amount of polarised flux at two frequencies but also on the total intensity flux at the same two frequencies. It is defined

Average	Sample				
Prop.	A	B	C	A+B	A+C
z	1.06 ± 0.04	1.11 ± 0.05	0.41 ± 0.01	1.08 ± 0.03	0.75 ± 0.08
P_{151}	(1.02 ± 0.06)×10^{27}	(1.01 ± 0.07)×10^{28}	(8.02 ± 0.40)×10^{26}	(5.57 ± 1.16)×10^{27}	(8.97 ± 0.77)×10^{26}
D	220.34 ± 46.40	262.69 ± 55.41	399.57 ± 122.50	241.51 ± 35.43	304.69 ± 64.50
RM	29.03 ± 12.81	26.41 ± 7.74	16.24 ± 8.33	27.64 ± 7.05	23.55 ± 8.07
dRM	97.85 ± 36.41	115.96 ± 42.81	50.77 ± 43.29	107.44 ± 27.62	77.68 ± 27.54
σ_{RM}	115.62 ± 33.43	122.94 ± 28.48	29.45 ± 9.98	119.49 ± 21.11	78.69 ± 22.36

Table 3.5: Mean properties of the sources averaged over each sample with the associated error. Differential rotation measure (dRM) is derived by taking the difference of the rotation measure between the two lobes of each source and then averaging this difference over each sample. σ_{RM} is the variation of the RM over the source. Properties in italics are in the source frame of reference.

as:

$$DM^{4.8\,\mathrm{GHz}}_{1.4\,\mathrm{GHz}} = \frac{PF_{4.8\,\mathrm{GHz}}}{PF_{1.4\,\mathrm{GHz}}} = \frac{m_{6\,\mathrm{cm}}}{m_{20\,\mathrm{cm}}}, \tag{3.5}$$

where the PF_ν is the fractional polarisation, (polarised flux)/(total intensity flux), at a given frequency, ν, and m_λ is the percentage polarisation at an observed wavelength λ.

The observed depolarisation also depends on the distribution of the Faraday depths covered by the projected area of the telescope beam, i.e. the variation of RM on the smallest angular scales. If the depolarisation is caused by a local but external Faraday screen and the distribution of Faraday depths in this screen is Gaussian with standard deviation Δ, then (e.g. Burn, 1966)

$$m_\lambda = m_0 \exp\left\{-2\Delta^2 \left[\lambda/\left(1+z\right)\right]^4\right\}, \tag{3.6}$$

where, m_0 is the initial percentage polarisation before any depolarisation and z is the redshift of the source. Since I measure m_λ at two observing frequencies (1.4 GHz and 4.8 GHz), equation (3.6) can be solved for Δ as a function of the depolarisation measure,

$$\Delta = \sqrt{\frac{(1+z)^4 \ln DM_{1.4\,\mathrm{GHz}}^{4.8\,\mathrm{GHz}}}{2(\lambda_{1.4\,\mathrm{GHz}}^4 - \lambda_{4.8\,\mathrm{GHz}}^4)}} \quad \mathrm{rad\,m^{-2}}. \tag{3.7}$$

I now drop the GHz subscript.

For each source, it is possible to compare the value of Δ as derived from the measured depolarisation with the observed rms of the rotation measure, σ_{RM}. If the Faraday dispersion is less than σ_{RM}, then the observations are consistent with an external Faraday screen (Garrington & Conway, 1991). Figure 3.1 displays the Faraday dispersion, Δ, for each lobe of the sources against the rms of the rotation measures observed. It is evident from the plot that the value of $\sigma_{RM} > \Delta$ for most components, see Tables 3.6 to 3.8 but there are a few sources where this is not the case. However, these components belong to sources where the depolarisation or rotation measure is only determined reliably for a few pixels so an accurate value is not obtainable for σ_{RM} or Δ. There is little correlation between Δ and σ_{RM}. This is a strong indicator that the Faraday medium responsible for variations of RM on small angular scales, and thus for the polarisation properties of the sources, is consistent with being external but local to the sources'.

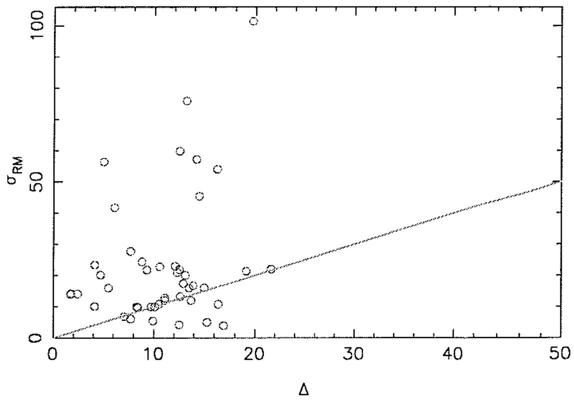

Figure 3.1: Plot of the Faraday dispersion, Δ, against the rms of the rotation measure for each source.

Comparing the average depolarisation of individual samples with each other I find only very weak trends with redshift or radio luminosity. When the samples are averaged together I find a trend in depolarisation with redshift but none with radio luminosity. Samples A+C (low radio luminosity) are statistically identical to sample B (high radio luminosity), suggesting that there is no trend with radio luminosity in my sources. By considering the averaged depolarisation of samples A+B (high redshift) compared with that of sample C (low redshift) there is a weak trend, 1.7σ, with redshift. This trend is echoed in the dDM values (1.9σ). This may confirm the results of Kronberg et al. (1972): redshift is the dominant factor compared to

Source	Component	RM (rad m^{-2})	DM$^{4.8}_{1.4}$	Average Δ (rad m^{-2})	σ_{RM} (rad m^{-2})
6C 0943+37	W	1.6 ± 2	2.19	15.01	16.1
	E	-19.1 ± 6	3.86	19.7	101.4
6C 1011+36	N	30.8 ± 5	1.53	11.1	12.8
	S	12.6 ± 4	1.06	4.1	10.1
6C 1018+37	NE	0.85± 3	1.23	7.71	6.1
	SW	11.2 ± 2	2.41	15.9	2.9
6C 1129+37	NW	-19.3 ± 4	2.51	16.3	54.0
	SE	0.08± 3	5.09	21.61	22.0
6C 1256+36	NE	5.9 ± 3	1.35	9.3	21.8
	SW	15.4 ± 3	1.01	1.7	14.0
6C 1257+36	NW	-115.3 ± 9	1.27	8.3	10.0
	SE	-115.6 ±10	1.88	13.5	16.0
7C 1745+642	N	–	1.85	13.3	–
	Core	65.4 ± 4	1.69	12.3	20.9
	S	12.8 ± 3	0.91	-	3.1
7C 1801+690	N	44.8 ± 3	1.11	5.5	16.0
	Core	30.3 ± 3	0.45	–	1.80
	S	20.8 ± 2	1.39	9.7	10.0
7C 1813+684	NE	13.9 ± 3	0.81	–	85.0
	SW	-68.4 ± 7	1.14	6.1	41.7

Table 3.6: Properties of the sample A radio source components. Errors are 5% or less unless stated otherwise. The depolarisation measures are the mean values of the ratio of the fractional polarisation between approximately 4800 MHz and 1465 MHz for each component. The rotation measures are the mean values between approximately 4800 MHz, 1665 MHz and 1465 MHz and are quoted in the observer's frame of reference. The Faraday dispersion, Δ, is given in equation 3.7. σ_{RM} is the rms in the rotation measure. All mean values take into account pixels above $5\sigma_{rms}$ at 4.8 GHz and above $3\sigma_{rms}$ at 1.4 GHz.

Source	Component	RM (rad m^{-2})	DM$_{1.4}^{4.8}$	Average Δ (rad m^{-2})	σ_{RM} (rad m^{-2})
3C 65	W	-82.6± 7	3.57	19.1	21.4
	E	-86.1± 6	1.28	8.4	9.7
3C 252	NW	15.7± 6	1.08	4.7	20.2
	SE	58.5± 6	2.07	14.5	45.4
3C 267	E	-9.6± 3	1.31	8.8	24.4
	W	-21.5± 3	1.06	4.1	23.4
3C 280	E	-37.7± 8	1.82	13.1	20.1
	W	-7.5± 4	1.54	11.1	1.5
3C 324	NE	22.1± 4	1.66	12.1	23.0
	SW	43.0± 5	1.95	13.9	16.8
4C 16.49	N	-4.3± 5	0.64	–	56.4
	Jet	30.1± 4	2.01	14.2	57.2
	Core	–	0.77	–	–
	S	0.9± 3	1.09	5.0	56.4
3C 68.1	N	-26.6± 5	1.23	7.7	27.7
	S	57.9± 2	1.73	12.5	59.8
3C 265	NW	42.2± 6	1.72	12.5	21.9
	SE	32.8± 3	1.48	10.6	22.8
3C 268.1	E	21.7± 5	1.47	10.5	10.8
	W	26.8± 6	1.74	12.6	13.3

Table 3.7: As Table 3.6 but for sample B.

Source	Component	RM (rad m^{-2})	$\mathrm{DM}^{4.8}_{1.4}$	Average Δ (rad m^{-2})	σ_{RM} (rad m^{-2})
3C 42	NW	-2.4 ±5	1.02	2.4	14.1
	SE	5.0 ±5	1.01	1.7	14.2
4C 14.27	NW	-13.0 ±4	1.41	9.9	5.4
	SE	-17.3 ±5	1.03	2.9	4.8
3C 46	NE	-4.8 ±5	1.27	16.9	3.9
	SW	-2.9 ±1	1.14	12.5	4.
3C 457	NE	–	1.01	2.1	–
	SW	–	1.19	5.6	–
3C 351	NE	1.00±5	0.84	–	13.
	Diffuse	-8.7 ±1	1.93	13.7	12.
	Core	-0.53±2	2.27	15.3	5.
	SW	4.4 ±3	2.56	16.4	10.8
3C 341	NE	20.3 ±5	1.43	10.1	10.0
	SW	18.2 ±5	1.53	11.1	12.0
3C 299	NE	-126.3 ±8	1.84	13.2	75.9
	SW	16.0 ±5	1.19	7.10	6.9
3C 16	NE	–	2.20	15.0	–
	SW	-4.3 ±3	1.79	12.9	17.4

Table 3.8: As Table 3.6 but for sample C.

radio luminosity in determining the depolarisation properties of a source but since the significance levels are low it is not possible to say with any confidence.

Average Prop.	Sample A	Sample B	Sample C
z	1.06 ± 0.04	1.11 ± 0.05	0.41 ± 0.01
P_{151}	$(1.02 \pm 0.06)\times10^{27}$	$(1.01 \pm 0.07)\times10^{28}$	$(8.02 \pm 0.40)\times10^{26}$
D	220.34 ± 46.40	262.69 ± 55.41	399.57 ± 122.50
DM	1.82 ± 0.32	1.61 ± 0.13	1.42 ± 0.12
dDM	0.93 ± 0.26	0.61 ± 0.22	0.43 ± 0.18

Average Prop.	Sample A+B	Sample A+C
z	1.08 ± 0.03	0.75 ± 0.08
P_{151}	$(5.57 \pm 1.16)\times10^{27}$	$(8.97 \pm 0.77)\times10^{26}$
D	241.51 ± 35.43	304.69 ± 64.50
DM	1.71 ± 0.17	1.63 ± 0.18
dDM	0.77 ± 0.17	0.69 ± 0.17

Table 3.9: Mean properties of the sources averaged over each sample with the associated error. Differential depolarisation (dDM) is derived by taking the difference of the depolarisation between the two lobes of each source and then averaging this difference over each sample.

Strom (1973); Strom & Jägers (1988); Pedelty et al. (1989); Ishwara-Chandra et al. (1998) find an anti-correlation of depolarisation with linear size. Figure 3.2 shows that there is a weak anti-correlation between physical source size and depolarisation. However, this trend is due to the two largest sources in sample C, 3C 46 and 3C 457. Removing these sources yields an average depolarisation measure of 1.50 ± 0.15 for sample C, which is not significantly different from the average with these two sources included. So I can rule out the possibility that the larger depolarisation at high redshift is caused by selecting preferentially smaller sources at high redshift.

3.3.1 Laing–Garrington effect

Assuming that a radio source does not lie flat to the observers line–of–sight and that both lobes are embedded in the same Faraday medium then one lobe will lie further away. The polarised flux from this lobe will have to travel through a larger path length and will become more depolarised than the nearer lobe. This creates an asymmetry in the depolarisation that is known as the Laing–Garrington effect. 8 sources show $\mathrm{dDM} \geq 1$ over the source and a further 6 show $0.5 \leq \mathrm{dDM} < 1$. This implies that 14 sources out of 26 sources show a significant asymmetry in the depolarisation of their lobes. I would expect a proportion of the sources to be

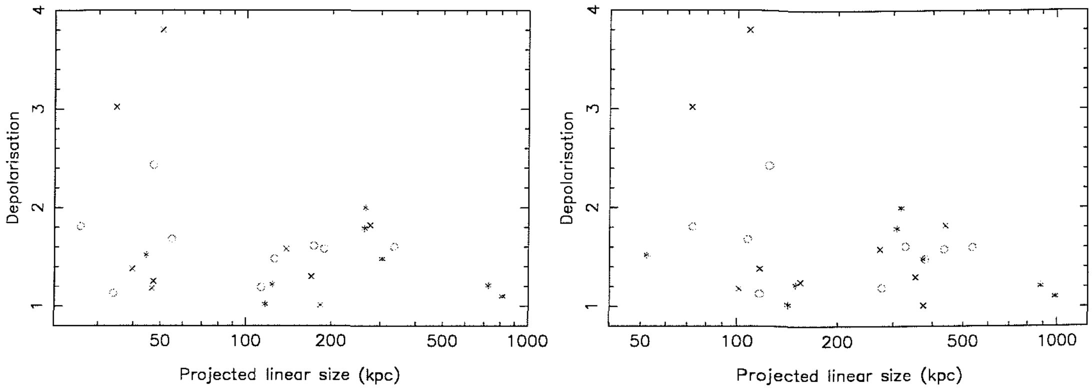

Figure 3.2: Average depolarisation against projected linear size (kpc) for all 3 samples. Symbols as in Figure 2.1. Figure (a) assumes H_o = 75 kms^{-1}Mpc^{-1}, and $\Omega_m = 0.5$, $\Omega_\Lambda = 0$. Figure (b) assumes H_o = 75 kms^{-1}Mpc^{-1}, and $\Omega_m = 0.35$, $\Omega_\Lambda = 0.65$.

observed at angles considerably smaller than 90° to my line-of-sight. Therefore it is not surprising that so many sources are found to be candidates for the Laing-Garrington effect.

3.3.2 Depolarisation shadows

Depolarisation shadows (regions where the depolarisation is appreciably greater than in the surrounding area) are seen in a few sources, e.g. Figure 3.3, and may be real features. These were first found by Fomalont et al. (1989) in a study of Fornax A. Depolarisation shadows can be caused by the parent galaxy as in the case of 3C 324 or by an external galaxy in the foreground of the source, causing a depolarising silhouette (Best et al., 1997). Several sources show signs of depolarisation shadows in at least one of the lobes. Of these, 6C 1256+36 was observed to lie in a cluster by Roche et al. (1998), as were 3C 65 and 3C 324 (Best, 2000). 3C 324 has been observed by Best et al. (1998) in the sub-mm (850μm) and found a large dust mass centred around 3C 324. The host galaxy was shown to be the cause of the very strong depolarisation, (Best et al., 1998).

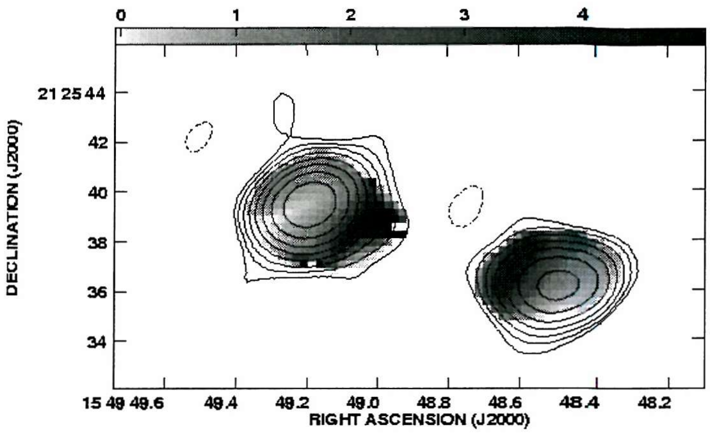

Figure 3.3: Depolarisation map of the radio source 3C 324 between 4848 MHz and 1465 MHz. All contours are at 5σ at 4848 MHz (1.5 mJy beam^{-1})$\times$(-1, 1, 2, 4...,1024) with a beam size of 2.2" × 1.6".

3.4 Using Burn's law

3.4.1 Polarisation

So far I have only considered the percentage polarisations of a source measured in the observing frame. Variations of the RM on small angular scales which determine the degree of polarisation are caused in Faraday screens local to the sources. The trend with redshift may therefore simply reflect the different shifts of the observing frequency in the source rest-frame for sources at low and high redshift. Using Burn's law in the form of equations (3.6) and (3.7) it is possible to determine, for each source, the percentage polarisation expected to be observable at a frequency corresponding to a wavelength of 5 cm in its rest-frame. This wavelength was chosen as it lies close to the wavelengths already observed in all the sources. The results for individual sources are presented in Table 3.10 and the sample averages are summarised in Table 3.11. Again sources at low redshift (sample C) are slightly more polarised than sources at high redshift (sample A: 1.9σ, sample B: 2.1σ). As before, there is no trend with radio luminosity, indicating that the trend with redshift is dominant. This is not caused by pure Doppler shifts of the observing frequencies.

3.4.2 Depolarisation

Cosmological Doppler shifts of the observing frequencies influence the trend of DM with redshift, and in fact the true trend is stronger than that naively observed. To demonstrate this equation (3.7) can be used to derive the standard deviation of

Source	z	Δ_z	$DM_{z=1}$	$dDM_{z=1}$	Polarisation $\lambda_{rest} = 5\,cm$
6C 0943+37	1.04	74.12	3.31	1.98	3.10
6C 1018+37	0.81	42.95	1.49	0.52	8.32
6C 1011+36	1.04	36.11	1.33	0.66	5.63
6C 1129+37	1.06	83.07	4.49	3.43	3.09
6C 1256+36	1.07	29.53	1.21	0.40	8.26
6C 1257+36	1.00	45.51	1.58	0.61	9.39
7C 1801+690	1.27	41.24	1.45	0.54	3.33
7C 1813+684	1.03	6.96	1.01	0.25	8.47
7C 1745+642	1.23	47.81	1.65	1.36	7.32
3C 65	1.18	75.33	3.50	4.61	6.26
3C 252	1.11	50.66	1.76	1.36	6.36
3C 267	1.14	32.34	1.26	0.35	5.04
3C 280	1.00	48.79	1.68	0.28	5.48
3C 324	1.21	54.34	2.42	0.58	4.74
3C 265	0.81	35.56	1.37	0.14	5.05
3C 268.1	0.97	42.13	1.57	0.25	3.07
3C 68.1	1.24	45.11	1.85	0.98	10.20
4C 16.49	1.29	31.04	1.23	0.47	6.76
3C 42	0.40	4.59	1.00	0.01	9.85
4C 14.27	0.39	14.34	1.05	0.08	9.08
3C 46	0.44	15.06	1.05	0.03	12.45
3C 457	0.43	10.50	1.03	0.04	12.88
3C 351	0.37	23.82	1.14	0.15	8.59
3C 341	0.45	21.91	1.11	0.02	18.57
3C 16	0.41	27.54	1.19	0.06	6.64
3C 299	0.37	20.20	1.10	0.10	1.52

Table 3.10: Recalculated average depolarisation and dDM for each source if it was located at $z = 1$ and average percentage polarisation of all sources if it was emitted at 5 cm in the rest frame.

Faraday depths, Δ, for each source. By setting $z = 1$ it is possible to then rescale all the depolarisations, $DM^{4.8}_{1.4}$, to the same redshift. This allows all 3 samples to be compared without any bias due to pure redshift effects (see Tables 3.10 and 3.11). If there was no intrinsic difference between the high-redshift and low-redshift samples then I would expect these values to be consistent with each other. This is evidently not the case. The high redshift samples are, on average, significantly more depolarised (sample A: 2.2σ, sample B: 3.2σ) than their low-redshift counterparts (sample C). Comparing sample A with sample B I find no trend with radio luminosity. However, a note of caution must be issued as the corrections applied use Burn's law and may actually be too large. Considering the precorrected and the corrected values together it is obvious that there is a connection between redshift and depolarisation but there is no significant trend of depolarisation with radio luminosity. There is also a connection between the difference in the depolarisation, dDM, and the redshift of the source, but no significant trend of the difference in the depolarisation with the radio luminosity of the source. As noted in section 2.3 regions with signal-to-noise $< 3\sigma$ were blanked in the map production. In individual sources blanking of low S/N regions in the polarisation maps will cause the measured depolarisation to be underestimated. Sources in sample A are more affected by this problem than objects in the other samples. Therefore I probably underestimate the average depolarisation in sample A implying that the trend with redshift could be even stronger than my findings suggest.

Average Prop.	Sample A	 B	 C	 A+B	 A+C
$\mathrm{DM}_{z=1}$	1.95 ± 0.39	1.85 ± 0.24	1.08 ± 0.02	1.90 ± 0.22	1.54 ± 0.23
$\mathrm{dDM}_{z=1}$	1.08 ± 0.34	1.00 ± 0.47	0.06 ± 0.02	1.04 ± 0.28	0.60 ± 0.22
$\mathrm{PF}_{\lambda_{rest}=5\,\mathrm{cm}}$	6.32 ± 0.86	5.88 ± 0.65	9.82 ± 1.85	6.10 ± 0.53	7.97 ± 1.04

Table 3.11: Average DM and dDM now shifted so that all the measurements are taken at $z = 1$. Average polarisation of all the sources, shifted to a common rest frame wavelength of 5 cm using equation 3.7.

The trends of percentage polarisation and of depolarisation with redshift are probably related in the sense that a lower degree of depolarisation at low redshift also leads to a higher observed degree of polarisation. Clearly a variation of the initial polarisation, m_0, with redshift would lead to variations of the observed m_λ independent of the properties of any external Faraday screen. Therefore both trends could also be caused by a significantly higher level of m_0 for sources at low redshift (sample C). Using equation (3.6) I find $m_0 = 9.3 \pm 1.1$ for sample A, $m_0 = 9.1 \pm 1.0$ for sample B and $m_0 = 13.5 \pm 2.5$ for sample C. The uncertainties associated with the use of Burn's law in extrapolating from my observations to $\lambda = 0$ are large. There is no difference between the average initial polarisation of the sources in samples A and B. The difference found for m_0 at low redshift (sample C) compared to high redshift (samples A and B) is small compared to the difference found for the depolarisation comparing the same samples. This suggests that the differences in percentage polarisation and depolarisation are due to variation with redshift of the Faraday screens local to the sources rather than to differences in the initial degree of polarisation. However note, that the variation of m_0 is not significantly smaller than the trend of percentage polarisation with redshift.

Burn's law predicts a steep decrease of percentage polarisation with increasing observing frequency. Although the decrease may well be 'softened' by geometrical and other effects in more realistic source models (Laing, 1984), the value of DM may be small for sources in which the observing frequencies are lower than the frequency at which strong depolarisation occurs. For such sources I would expect to measure a low value of DM associated with a low percentage polarisation. Akujor & Garrington (1995) show that one of my sources, 3C 299 (sample C), is strongly depolarised between 1.6 GHz and 8.4 GHz with almost all of the depolarisation taking place between 4.8 GHz and 8.4 GHz. I measure only a very low percentage polarisation for this source and the average value of $\mathrm{DM}^{4.8}_{1.4} = 1.5$ is also lower than $\mathrm{DM}^{8.4}_{1.6} \sim 4$ as measured by Akujor & Garrington (1995). If many of the sources at low redshift are affected by strong depolarisation at frequencies higher than 4.8 GHz, then this may cause the trend of DM with redshift noted above. The absence of any other sources with very low degrees of polarisation combined with a low value for DM, at least in the low redshift sample C, argues against this bias. In fact, Tabara & Inoue (1980) show that the sources 3C 42, 3C 46, 3C 68.1, 3C 265, 3C 267, 3C 324 and 3C 341 depolarise strongly only at frequencies lower than my observing frequencies. 3C 16, 3C 65, 3C 252, 3C 268.1 and 3C 280 do depolarise strongly between 1.4 GHz and 4.8 GHz. In all the sources mentioned in Tabara & Inoue (1980) none have strong depolarisation at frequencies higher than 4.8 GHz. There is no information for 4C 14.27, 4C 16.49, 3C 351 and 3C 457. Those sources which do depolarise strongly between my observing frequencies, 1.4 and 4.8 GHz, could in principle have inaccurate values of the rotation measure because of this. However, the pixels containing most depolarised regions of the source are likely to have been blanked because of insufficient signal–to–noise in their polarisation at 1.4 GHz; the rotation measure is determined from the unblanked (less depolarised) regions of the source, and will therefore be reliable.

3.5 Discussion

In this chapter I present the complete data set of the three samples of radio galaxies and radio-loud quasars. The three samples were defined such that two of them overlap in redshift and two have similar radio luminosities. Allowing the effects of redshift and radio luminosity on various source properties to be analysed.

There is little correlation between Δ and σ_{RM}, suggesting that the Faraday medium responsible for variations of RM on small angular scales, is consistent with being external but local to the sources. This implies that any trends with radio luminosity and/or redshift reflect changes of the source environment depending on these quantities. There is also little correlation between rotation measure and redshift or radio luminosity which is consistent with a Galactic origin of the RM properties of the sources on large scales. However, I find that the rms fluctuations of the rotation measure correlate with redshift but not radio luminosity to a confidence level of $> 99.9\%$, determined in the sources' frame of reference.

I find that the polarisation of a source anti-correlates with its redshift but is independent of its radio luminosity, resulting in the low redshift sample having much higher degrees of polarisation, in general. I also detect higher degrees of depolarisation in the high redshift samples (A and B) compared to sources at lower redshift (sample C). This suggests that depolarisation is correlated with redshift. These two results are probably related in that lower depolarisation at low redshift leads to both lower depolarisation measurements and also higher degrees of observed polarisation. According to Burn's law (Burn, 1966), this implies an increase in the source environments of either the plasma density or the magnetic field strength or both with redshift. Such an interpretation is also supported by the increased depolarisation asymmetry of sources at high redshift compared with their low redshift counterparts.

The findings on the rotation measurements and polarisation properties of my sources are indicative of an increase of the density and/or the strength of the magnetic field in the source environments with increasing redshift.

I do not find a strong correlation between the projected sizes of the sources and their depolarisation measure as found by Strom (1973); Strom & Jägers (1988); Pedelty et al. (1989); Ishwara-Chandra et al. (1998).

I find no correlation between the spectral index and redshift or radio luminosity. However, I do find the difference in the spectral index, across individual sources, increases for increasing radio luminosity of the source.

The correlations found are only general trends within the samples. To completely break the z-P degeneracy a much more rigorous and detailed approach to the statistical analysis is needed. In the next chapter I will investigate the observational properties using Principal Component Analysis and Spearman Rank and determine the significance of the results presented here.

Chapter 4

Analysing the observations

In this chapter I investigate the trends and correlations of a number of observational parameters (spectral index, rotation measure and depolarisation measure) with the 'fundamental' parameters, low frequency radio luminosity, redshift and the physical size of the radio structure. The observational parameters mainly constrain the properties of the gas in the vicinity of the radio structure which acts as a Faraday screen, see sections 3.2 and 3.3.

In my statistical analysis I use Spearman Rank as well as Partial Spearman Rank and Principal Component Analysis techniques. Thus I am able to assess whether any observed correlations of parameters with redshift and radio luminosity are significant in their own right or whether they simply arise from a Malmquist bias.

The 3 samples can also be used to determine if there are any asymmetries present between the lobes of sources and if so, what causes these asymmetries. Traditionally this has been done with sources in which jets are detected so that the asymmetries between the jet side and counter–jet side can be studied, (e.g. Garrington & Conway, 1991; Dennett-Thorpe et al., 1997; Leahy, 1987). This type of study allows a direct insight into the orientation of a source. In my sample only a few sources have a well defined jet at either 4.8 GHz or 1.4 GHz, so this type of analysis is not possible. However, I compare the brighter lobe to the fainter lobe to determine if there are any asymmetries present in the samples and if possible, explain the underlying physical cause(s) of the asymmetries.

4.1 Statistics

4.1.1 Spearman Rank

The Spearman Rank test is a non-parametric correlation test assigning a rank to given source properties, X and Y and then performing a correlation on the rank. The statistic is given by

$$\begin{aligned} r_{\mathrm{XY}} &= \frac{\Sigma x_i^r y_i^r}{\sqrt{\Sigma x_i^{r2} \Sigma y_i^{r2}}} \\ &= 1 - \frac{6\Sigma d^2}{n^3 - n} \end{aligned} \tag{4.1}$$

where d is the difference between the rank in the X direction and the rank in the Y direction and r_{XY} has a Student–t distribution:

$$D_{\mathrm{XY}} = \frac{r_{\mathrm{XY}}\sqrt{n-2}}{\sqrt{1 - r_{\mathrm{XY}}^2}} \tag{4.2}$$

where n is the number of sources.

The null hypothesis states that no correlation is present between two properties X and Y, corresponding to r_{XY}=0 and a (anti–) correlation corresponds to (-)1. A correlation with a confidence level above 95% will show a Student-t value greater than 2 for my sample size (Riley et al., 1997).

Partial Spearman Rank is used to determine if a correlation between two variables (X, Y) depends on the presence of a third, A (Macklin, 1982). The null hypotheses are:

- the A-X correlation is entirely due to the X-Y and the Y-A independent correlations, and
- the Y-A correlation is entirely due to the X-Y and the X-A independent correlations

The Partial Spearman Rank correlation coefficient is given by:

$$r_{\mathrm{AX,Y}} = \frac{r_{\mathrm{AX}} - r_{\mathrm{XY}} r_{\mathrm{AY}}}{\sqrt{[(1 - r_{\mathrm{XY}}^2)(1 - r_{\mathrm{AY}}^2)]}} \tag{4.3}$$

where r_{AX} is the normal Spearman Rank correlation coefficient described above. The significance level for the A-X correlation, independent of Y is

$$D_{\mathrm{AX,Y}} = \frac{1}{2}(n-4)^{\frac{1}{2}} ln \left(\frac{1 + r_{\mathrm{AX,Y}}}{1 - r_{\mathrm{AX,Y}}} \right). \tag{4.4}$$

To fully determine the relationships between X,Y and A, the triplet $r_{\mathrm{AX,Y}}$, $r_{\mathrm{AY,X}}$ and $r_{\mathrm{XY,A}}$ must be calculated and their corresponding significance levels found. By comparing this triplet it is possible to determine which relationship, if any, between X, Y and A dominates.

4.1.2 Principal Component Analysis, PCA

Principal Component Analysis, PCA, is a multi-variate statistical test which is described in detail by Deeming (1964) and Efstathiou & Fall (1984). PCA is a linear self–orthogonal transformation from an original set of n objects and m attributes forming a $n \times m$ matrix, with zero mean and unit variance, to a new set of parameters, known as principal components. The principal components of the new dataset are all independent of each other and hence orthogonal. The first component describes the largest variation in the data and has, by definition, the largest eigenvalue of the $n \times m$ matrix. In physical terms the magnitude of the eigenvalue determines what fraction of the variance in the data any correlation describes. Thus a strong correlation will be present in the first eigenvector and will only strongly reverse in the last. PCA in its simplest terms is an eigenvector–eigenvalue problem on a transformed, diagonalised and standardised set of variables. n objects will create an eigenvector–eigenvalue problem in $n-1$ dimensions. To avoid problems with the interpretation of my results I do not use more than 4 parameters in any part of the analysis.

4.2 Fundamental Parameters

In the following I investigate the relationship of the observational properties of my sources with the 'fundamental' properties redshift, z, radio luminosity at 151 MHz, P_{151}, and physical size, D_{source}. For this I first need to understand the relations between these three fundamental parameters. Table 4.1 contains the associated Spearman Rank results. Redshift and radio luminosity are highly correlated, to a significance of $\approx$ 99.9% but this is simply due to the way the samples were selected. Using the statistical techniques described above this correlation can be isolated from other correlations. In fact, it provides a 'bench mark' for other correlations.

Parameters	rs value	t value
z P_{151}	0.69846	4.78
z D_{source}	-0.22940	-1.15
P_{151} D_{source}	-0.13026	-0.64

Table 4.1: Spearman rank values for z, P_{151} and D_{source}.

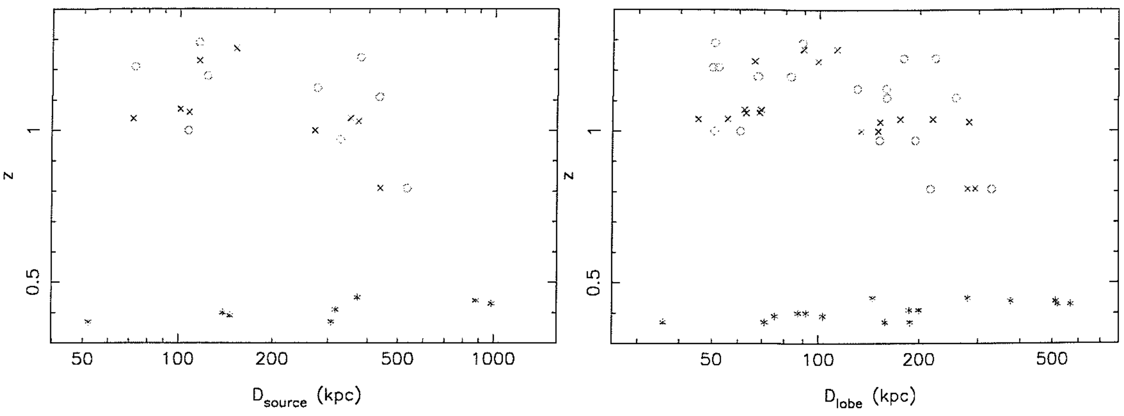

Figure 4.1: (a - left) Redshift against average source sizes in kpc and (b - right) with individual lobe sizes in kpc. Sample A is represented by '×', sample B by 'o' and sample C by '*'.

There is also a weak z - D_{source} anti-correlation, but as Table 4.1 demonstrates this anti-correlation is not significant. Figure 4.1(a) shows how the source size is distributed over the redshift range of my samples. The presence of the two low redshift giants, 3C 46 and 3C 457 are the cause of the weak correlation. By removing these two giants the anti-correlation completely disappears. However, as the anti-correlation is below 95% significant, even with the two giants included in the sample, any correlations found with size will not be biased towards lower redshift sources. Figure 4.1(b) demonstrates that the sizes of individual lobes are evenly distributed over the redshift range of the three samples and is also not unduly affected by the presence of the two giants.

Partial Spearman Rank was used to determine the dependencies between z, P_{151} and D_{source}.

$$\begin{aligned} r_{zD_{source},P_{151}} &= 0.04, & D &= 0.20 \\ r_{zP_{151},D_{source}} &= 0.69, & D &= 4.00 \\ r_{P_{151}D_{source},z} &= -0.20, & D &= 0.93 \end{aligned}$$

Using Partial Spearman Rank I find no independent z - D_{source} anti-correlation, proving that my sample is not biased towards larger sources at lower redshifts, allowing a fair comparison with higher redshift sources. Interestingly Table 4.1 indicates that there is no relationship between a sources' radio-luminosity and its size and this result is confirmed by the Partial Spearman Rank results at any fixed redshift. In a study by Kapahi (1989) it was found that $D_{source} \propto (1+z)^{-3\pm0.5}$ using $\Omega = 1$, but at constant redshift it was found that $D_{source} \propto P^{0.3\pm0.1}$. Singal (1993) also found that for his sample of 789 sources, size predominantly correlated with radio-luminosity and was only a very weak function of redshift. However it is interesting to note that Barthel & Miley (1988) found that $D \propto (1+z)^{-1.5\pm1.4}P^{-0.03\pm0.3}$ using a sample of steep spectrum radio quasars. My results are consistent with the results from Barthel & Miley (1988). These results demonstrate that it is very complicated to disentangle the redshift, radio-luminosity and size correlation and my sample is simply too small to add anything significant to this well studied field.

In Tables 4.2 to 4.7 the relationships between the observational parameters with the fundamental parameters are given.

4.3 Observational Parameters

In order to compare the differential observational parameters e.g. dDM_z* with averaged properties like DM, all averaged properties are taken over the entire source as opposed to individual lobes. This is the only method possible as for each source I only have one measurement of the differential properties and two measurements of the average properties (taken from each lobe). In the case of the RM properties (RM, dRM_z & σ_{RM_z}) I only use 23 of the 26 sources in the analysis. This is simply due to the fact that 7C 1745+642, 3C 16 and 3C 457 do not have reliable RM information in at least one of their lobes.

4.3.1 Spectral index

Parameters	rs value	t value	Parameters	rs value	t value
α_s z	-0.12615	-0.62	dα z	0.15487	0.77
α_s D_{source}	0.20889	1.05	dα D_{source}	-0.20957	-1.05
α_s P_{151}	0.03932	0.19	dα P_{151}	0.26632	1.35

Table 4.2: Spearman rank values for all spectral index parameters where the subscript s indicates that the spectral index is averaged over both lobes in a source.

There are no strong correlations between spectral index, α_s, and any of the fundamental parameters as the Spearman Rank results in Table 4.2 demonstrates. The PCA analysis confirms these findings (Table 4.3). The difference in the spectral index between the lobes, dα, also shows little correlation with any of the fundamental parameters. Veron et al. (1972) and Onuora (1989) find a strong spectral index–radio luminosity correlation, but no corresponding correlation with redshift. Interestingly Athreya & Kapahi (1999) find a strong correlation of spectral index with redshift, but no significant correlation with radio luminosity when they analysed the MRC/ 1Jy sample. Although I do not find strong support for either trend, this could simply be due to my small sample size.

---

*$\mathrm{dDM}_z = |DM_{z_{lobe1}} - DM_{z_{lobe2}}|$, see also the previous chapter.

Parameter	1	2	3	4
z	0.6354	-0.2475	0.0568	-0.7292
P	0.5781	-0.1595	0.5304	0.5992
D	-0.4690	-0.1168	0.8206	-0.3051
α_s	-0.2053	-0.9485	-0.2050	0.1271
Eigenvalue	44.6%	24.6%	20.5%	10.2 %
z	0.5565	-0.0810	0.5422	-0.6243
P	0.5487	0.4404	0.2629	0.6602
D	-0.4038	0.8418	0.1920	-0.3024
dα	0.4756	0.3014	-0.7746	-0.2879
Eigenvalue	51.4%	21.3%	17.7%	9.5 %

Table 4.3: Eigenvectors and Eigenvalues for spectral index.

A recent study by Blundell, Rawlings & Willott (1999) using the 3CRR, 6CE and 7C samples found that α anti-correlated not only with radio-luminosity, but also with source size. They found that in general, larger sources had a steeper spectral index. Again the fact that I do not find this trend could simply be due to my much smaller sample size.

4.3.2 Depolarisation

In the previous chapter I motivated the adjustment of the measured depolarisation to a common redshift, $z = 1$, using the Burn[†] theory of depolarisation (Burn, 1966), for all sources. There is little difference between the redshift and the radio luminosity correlations with the average adjusted depolarisation, taken over the source as a whole, DM_z, (see Table 4.4) as both correlations show significance levels greater than 99.9%. There is also an indication of a DM_z-D_{source} anti-correlation, but this is found not to be significant. The Partial Spearman Rank test is used to determine if the P_{151}-DM_z correlation can be explained by the independent z-DM_z and z-P_{151} correlations.

$$\begin{aligned} r_{zDM_z,P_{151}} &= 0.40, & D &= 2.00 \\ r_{zP_{151},DM_z} &= 0.44, & D &= 2.21 \\ r_{P_{151}DM_z,z} &= 0.41, & D &= 2.04 \end{aligned}$$

It is evident that there is still little difference between the redshift and radio-luminosity correlations. This is confirmed using the PCA results in Table 4.5(top).

[†] As noted in the previous chapter the Burn method for shifting the depolarisation may result in an over-estimation of the depolarisation. In the next chapter I discuss other methods for shifting the depolarisation and determine what effect this has on the correlations presented here.

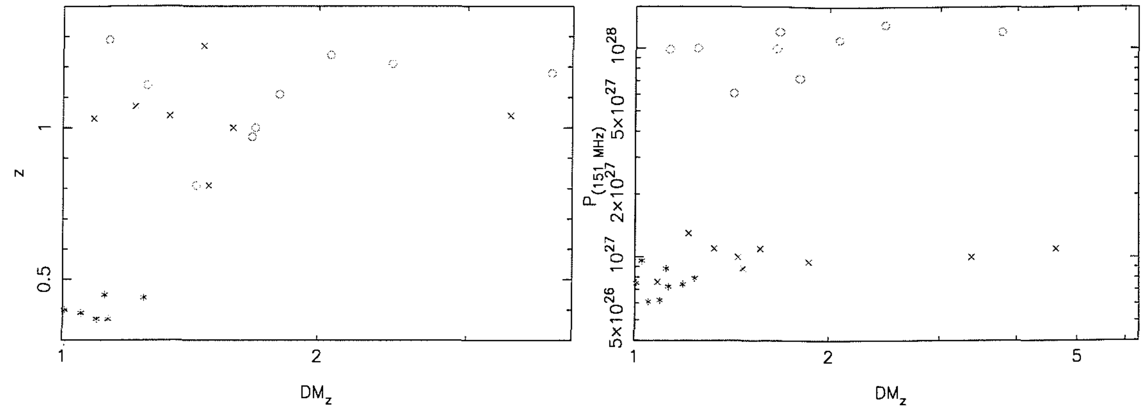

Figure 4.2: (a - left) Redshift against the average depolarisation of a source. (b - right) Radio-luminosity against the average depolarisation. The depolarisation has been shifted to a common redshift, z=1. Symbols are as in Figure 4.1.

Parameters	rs value	t value	Parameters	rs value	t value
DM_z z	0.68955	4.66	dDM_z z	0.74017	5.39
DM_z P_{151}	0.68821	4.65	dDM_z P_{151}	0.54462	3.18
DM_z D_{source}	-0.31145	-1.61	dDM_z D_{source}	-0.31009	-1.60
DM_z σ_{RM_z}	0.45257	2.33	dDM_z σ_{RM_z}	0.55929	3.09
DM_z dDM_z	0.89197	9.67	dDM_z dRM_z	0.40514	2.03

Table 4.4: Spearman rank values for all shifted depolarisation parameters.

Figure 4.2(a) shows that the higher redshift sources display, on average, a larger degree of depolarisation and also a much larger spread of depolarisation at any given redshift compared to their low redshift counterparts. There is also very little difference between the two high redshift samples indicating that the difference in the radio-luminosity of the two samples is unimportant, see Figure 4.2(b). Interestingly Morris & Tabara (1973) found depolarisation to correlate with radio–luminosity whereas Kronberg et al. (1972) found the correlation was predominantly with redshift. My results support the findings of both groups.

The trend with redshift is more pronounced when the difference in the depolarisation over the source, dDM_z, is considered (Tables 4.4 and 4.5(bottom)). Using Partial Spearman Rank I find

$$r_{zdDM_z,P_{151}} = 0.60, \qquad D = 3.25$$

$$r_{zP_{151},dDM_z} = 0.53, \qquad D = 2.77$$

$$r_{P_{151}dDM_z,z} = 0.05, \qquad D = 0.23$$

This shows a definite correlation between redshift and dDM_z at any given radio luminosity, but the corresponding P_{151}-dDM_z correlation is considerably weaker at

Parameter	1	2	3	4
z	0.5837	0.2185	-0.0001	-0.7820
P	0.4699	0.6727	-0.1909	0.5387
D	-0.4397	0.6135	0.6368	-0.1570
DM_z	0.4951	-0.3511	0.7470	0.2713
Eigenvalue	52.7%	22.0%	15.5%	9.8 %
z	0.5957	0.1851	0.0132	0.7815
P	0.4760	0.6755	-0.2183	-0.5192
D	-0.4281	0.6314	0.6249	0.1662
dDM_z	0.4851	-0.3329	0.7495	-0.3036
Eigenvalue	52.0%	21.6%	16.9%	9.5 %

Table 4.5: Eigenvectors and Eigenvalues for depolarisation

a given redshift.

It is not surprising that DM_z and dDM_z are highly correlated, with a significance greater than 99.9% (Figure 4.3). A source with a high average DM_z will be located in a region with a dense Faraday medium, which also causes a significant difference between the lobes and hence the correlation. The Laing Garrington effect discussed in section 3.3.1 could also cause the observed correlation between DM_z and dDM_z, assuming that the sources are not angled flat to the line-of-sight.

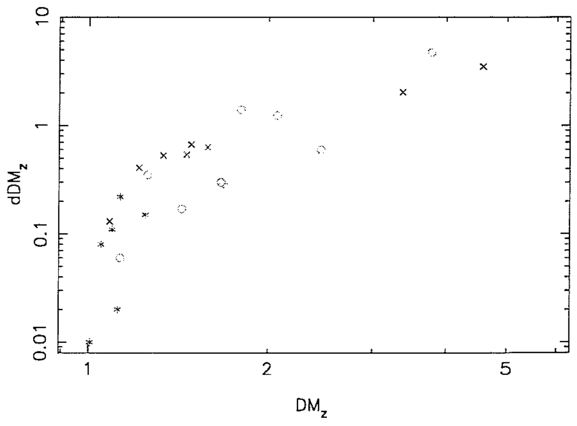

Figure 4.3: DM_z against the difference in depolarisation, dDM_z. dDM_z is the difference in the average depolarisation of each lobe. The depolarisation has been shifted to a common redshift, $z = 1$. Symbols are as in Figure 4.1.

Table 4.4 shows a very weak DM_z-D_{source} anti-correlation. This detection is marginal and as the PCA results in Table 4.5(top) demonstrate this anti-correlation is not very significant. Interestingly this trend has been found by Strom (1973); Strom & Jägers (1988); Pedelty et al. (1989); Best et al. (1999) and Ishwara-Chandra et al. (1998), but was not found by Dennett-Thorpe (1996)[DT96]. The observations by Strom (1973), Strom & Jägers (1988) and Ishwara-Chandra et al. (1998) are at a lower resolution than my measurements and thus their depolarisation measurements may be affected by this resolution difference. The observations by Best et al. (1999) are at a higher resolution, but also at higher frequencies (4.8 GHz to 8.4 GHz) and so I would expect any depolarisation trends to be stronger in this sample. Pedelty et al. (1989)(P89) however observe at the same frequency range and resolution as my samples and they find an anti-correlation with size. DT96 also observes at the same frequency and resolution as P89, but also does not find any trend with size. Even when my results from sample B, which are taken at the most similar redshift and radio-luminosity range to those of P89, are analysed separately, I still find no trend with size. There is no difference in the selection of the P89 sample and my sample B except that P89 chose their sample from sources which had strong emission lines. By preferentially selecting sources with strong emission lines P89 has chosen sources that would have strong depolarisation asymmetries and hence large depolarisation measurements overall. This could strengthen any D_{source}-DM correlation found. However, there does not seem to be any convincing physical explanation why one set of sources should show such a strong size-depolarisation anti-correlation and another set of sources should show no trend.

It is usually assumed that radio sources are located in stratified atmospheres. Therefore a small source will be embedded in denser gas which acts as a more efficient Faraday screen. As the source expands the lobes have a higher probability of extending beyond the denser inner atmosphere, thus reducing the amount of depolarisation observed. In section 4.2 it was shown that there is no significant z-D_{source} anti-correlation in my sample. Therefore a lack of any DM_z-D_{source} anti-correlation suggests that there is no significant difference in the source environments at any redshift, of my samples, as the sources become larger. This may be evidence that on scales of up to a Mpc the environment is relatively homogeneous and does not show evidence of stratification. The lack of any D_{source}-dDM_z could simply be caused by the Laing-Garrington effect (see section 3.3.1).

4.3.3 Rotation measure

The Spearman Rank results in Table 4.6 show that there are no strong correlations of the fundamental parameters with rotation measure, RM. In every case the correlation is below 95% significant. The PCA results in Table 4.7(top) also demonstrate that the RM of a source does not depend on the size, redshift or the radio luminosity of the source. This is consistent with the idea that the observed RM is due to Galactic variations and not to a local Faraday screen (see section 3.3) and would not be expected to vary in response to any change in the source properties.

The difference in the rotation measure, dRM_z, between the two lobes of a given source and the rms variation in the rotation measure, σ_{RM_z}, are local to the source

Parameters	rs value	t value
RM_a z	0.16996	0.79
RM_a P_{151}	0.27470	1.31
RM_a D_{source}	-0.05040	-0.23
dRM_z z	0.50000	2.65
dRM_z P_{151}	0.22530	1.06
dRM_z D_{source}	-0.22332	-1.05
dRM_z dDM_z	0.40514	2.03

Parameters	rs value	t value
σ_{RM_z} z	0.67885	4.24
σ_{RM_z} P_{151}	0.34881	1.71
σ_{RM_z} D_{source}	-0.30435	-1.46
σ_{RM_z} dDM_z	0.55929	3.09
σ_{RM_z} DM_z	0.45257	2.33
σ_{RM_z} dRM_z	0.68874	4.35

Table 4.6: Spearman rank values for all rotation measure parameters. The subscript *a* indicates that the RM has not been shifted to the sources' frame of reference.

and have been corrected to the sources' frame of reference. There is a dRM_z-z correlation present in the Spearman Rank results, (see Table 4.6), but it is weaker in the PCA results where the correlation is strongly reversed in the 3rd eigenvector, see Table 4.7 (middle). Figure 4.4 shows that in principal I should find a strong dRM_z-z correlation. However, the presence of the low redshift - high dRM_z source (3C 299) weakens this trend. 3C 299 has a large dRM_z produced by a lack of polarisation information in one lobe. Removing this source strengthens the correlation giving $r_{dRM_z,z} = 0.632$ which corresponds to a significance of 99.98%.

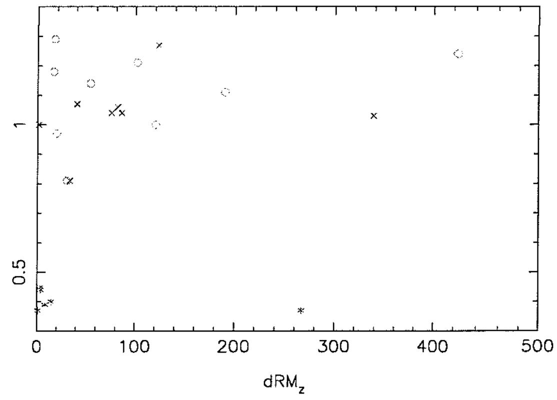

Figure 4.4: Redshift against difference in rotation measure, dRM_z across the lobes of a source. dRM_z has been shifted to the sources' frame of reference. Symbols are as in Figure 4.1.

As previously noted, σ_{RM_z} measures variations of the Faraday screen on scales smaller than dRM_z, which may still be influenced by the Galactic Faraday screen. However, it is interesting to note that dRM_z correlates strongly with σ_{RM_z}, see Figure 4.5. So the two parameters may sample the same, local Faraday screen even if dRM_z may still contain some Galactic contribution. σ_{RM_z} shows a strong correlation with redshift, > 99.9% significance, and a weak anti-correlation with D_{source}. The σ_{RM_z}–z correlation also strengthens with the removal of 3C 299, becoming $r_{\sigma_{RM_z},z} = 0.767$ which corresponds to a significance exceeding 99.99%. These correlations are more obvious when the PCA results are considered, see Table 4.7

Parameter	1	2	3	4
z	0.6398	0.2390	-0.0491	0.7288
P	0.5968	0.4094	-0.1678	-0.6694
D	-0.3781	0.4402	-0.8034	0.1335
RM	0.3026	-0.7625	-0.5693	-0.0540
Eigenvalue	43.8%	24.1 %	21.5%	10.6%
z	0.6293	-0.0201	0.2213	0.7447
P	0.5820	-0.1197	0.4874	-0.6399
D	-0.3224	-0.8641	0.3594	0.1423
dRM$_z$	0.4017	-0.4885	-0.7644	-0.1255
Eigenvalue	45.9%	23.3%	20.3%	10.5 %
z	0.6215	0.1765	0.0623	0.7607
P	0.4923	0.4210	-0.6151	-0.4495
D	-0.3212	0.8876	0.3288	0.0296
σ_{RM_z}	0.5178	-0.0615	0.7139	-0.4673
Eigenvalue	51.3%	22.4%	18.6%	7.6 %

Table 4.7: Eigenvectors and Eigenvalues for rotation measure.

(bottom). The first eigenvector contains 51.3% of the variation in the data and shows a strong z-σ_{RM_z} correlation and a weaker D$_{source}$-σ_{RM_z} anti-correlation. The D$_{source}$-σ_{RM_z} anticorrelation reverses in the third eigenvector indicating that it is a considerably weaker trend compared to the z-σ_{RM_z} correlation which only reverses in the last eigenvector. The Partial Spearman Rank results below confirm that there are no significant correlations with radio–luminosity for both dRM$_z$ and σ_{RM_z},

$$\begin{aligned} r_{zdRM_zP_{151}} &= 0.49, & D = 2.40 \\ r_{zP_{151},dRM_z} &= 0.69, & D = 3.79 \\ r_{P_{151}dRM_z,z} &= -0.19, & D = 0.86 \end{aligned}$$

$$\begin{aligned} r_{z\sigma_{RM_z}P_{151}} &= 0.65, & D = 3.47 \\ r_{zP_{151},\sigma_{RM_z}} &= 0.67, & D = 3.63 \\ r_{P_{151}\sigma_{RM_z},z} &= -0.24, & D = 1.09 \end{aligned}$$

In a survey of 27 high redshift sources Pentericci et al. (2000)[P02] found that the Faraday rotation was independent of size or radio–luminosity but they also found that the number of sources with high levels of Faraday rotation increased with redshift. The results from P02 use the RM of a source in the sources' frame of reference. As noted in section 3.2 the RM from my sources is taken to be dominated by contributions from the Galaxy thus I use σ_{RM_z} and dRM$_z$ as indicators of the environment instead of RM. σ_{RM_z}, dRM$_z$ and RM sample the same medium and both sets of results find a trend with redshift. The P02 trend indicates that the strength of

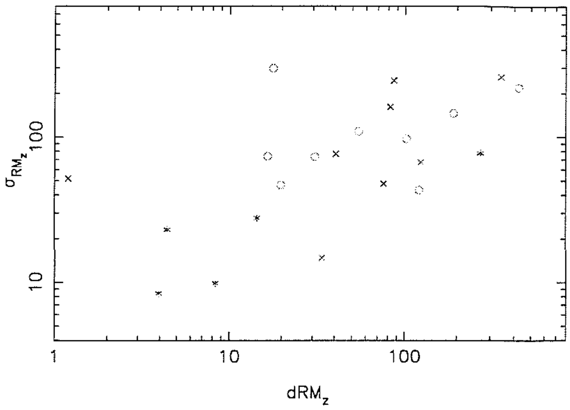

Figure 4.5: The rms variation in the rotation measure,σ_{RM_z} against the difference in rotation measure across the lobes of a source. Symbols are as in Figure 4.1.

the magnetic field or the density of the environment (or both) is increasing with redshift but by using only RM they are unable to determine how the disorder of the environment changes with redshift. Conversely by using only σ_{RM_z} and dRM_z I have no information on the density of the environment or the magnetic field but I find that the disorder in the environment increases with redshift.

The Spearman Rank results in Table 4.6 show that there is a strong σ_{RM_z}-DM_z correlation, indicating that σ_{RM_z} is sampling the same medium as the depolarisation measurements and thus either parameter can be used as a test of the Faraday screen.

4.3.4 Summary

Depolarisation, DM_z, and the differential rotation measure properties, dRM_z and σ_{RM_z}, correlate with redshift, indicating that there is a change in the source environments as redshift increases. Only depolarisation shows a trend with radio–luminosity. By analysing the rotation measure down to its rms variations (σ_{RM_z}) and the depolarisation measure, I am probing smaller and smaller variations in the Faraday screen. I find that there is an increasingly strong correlation with redshift over radio–luminosity which suggests that the environment has no direct link to the radio–luminosity of a source. The fact that there are no spectral index correlations found also corroborates this view.

4.4 Source asymmetries

The previous sections have allowed me to analyse the bulk trends of the source properties with the fundamental properties, but also with themselves. However, it is also interesting to look at the asymmetries of the sources and to determine their underlying physical cause.

The angle at which a source is orientated to the line–of–sight, θ, can affect the projected lobe length. Sources orientated at a small angle will have lobes that appear more asymmetrical than sources at a large angle, assuming there are no environmental differences between the lobes. The orientation of a source will also affect the observed depolarisation (Garrington & Conway, 1991), the spectral index (Liu & Pooley, 1991b) and the rotation measure. In a simple orientation model emission from the lobe pointing away from the observer will have a longer path length through the local Faraday screen and thus any depolarisation measurements of this lobe would be larger than the lobe pointing towards the observer. This is known as the Laing-Garrington effect, see section 3.3.1. Liu & Pooley (1991b) also find that the least depolarised lobe has a flatter spectrum.

Beaming can also cause asymmetries in a source, independent of path length through the Faraday screen. Assuming a source is angled at θ to the line–of–sight, then the ratio of lobe lengths, D_1/D_2, is given by (Longair & Riley, 1979)

$$\frac{D_1}{D_2} = \frac{1 + v_{\circ}/c \cos\theta}{1 - v_{\circ}/c \cos\theta} \tag{4.5}$$

where $v_{\circ}$ is the velocity at which the hotspot (Longair & Riley, 1979) is moving away from the nucleus and c is the speed of light. As the hotspot becomes increasingly more beamed (i.e. $\theta \to 0$) the lobe ratio increases. The hotspot will begin to dominate the flux and spectral index in the beamed lobe. Thus as beaming becomes more dominant in a source, the beamed lobe will become brighter, longer and its spectrum flatter than the receding lobe.

Half of my sources do not contain any detection of a core at either 4.8 GHz or 1.4 GHz. This was a problem as I needed to define where the core was located to determine an accurate estimation of the lobe length. In the cases were there was no core detection I used previously published maps to determine where a core is likely to be located. However in several cases, most notably 3C 16, there was no core to be found. In these cases I estimated the location of the core position by using the most likely core position from the literature (Leahy & Perley, 1991). This may seem a rather drastic approach, but as the maps are not of very high resolution, the values calculated for the lobe length can only be an approximation to the true length. The lobe volume is calculated by assuming cylindrical symmetry and using the measured lobe length, D_{lobe}, but also the parameter R, which determines the ratio of the lobe length to the width at half the lobe length,

$$V_{lobe} = \frac{\pi D_{lobe}^3}{4R^2} \tag{4.6}$$

In most cases R > 1 but in extreme cases like the southern lobe of 7C 1745+642 (see Figure A.7) R is less than unity, which causes the large volume ratio (> 10) for this source apparent in Figure 4.18(a).

In the following sections the subscripts *b* and *f* are used to denote the value from the brighter lobe and the fainter lobe of an individual source, respectively.

In the previous section I used the corrected $z = 1$ depolarisation in my analysis of the trend of depolarisation with the fundamental parameters. However, by correcting the depolarisation to a common redshift I am assuming a specific underlying structure to the Faraday screen which may mask any underlying asymmetries between lobes. In previous studies (e.g. Pedelty et al., 1989; Liu & Pooley, 1991a; Gregory & Condon, 1991, etc.) the observed depolarisation is used as an asymmetry indicator. To ensure my results are comparable to those published I use only the *observed* depolarisation values given in Tables 3.1 to 3.3 in my analysis of any depolarisation asymmetries.

4.4.1 Flux asymmetries

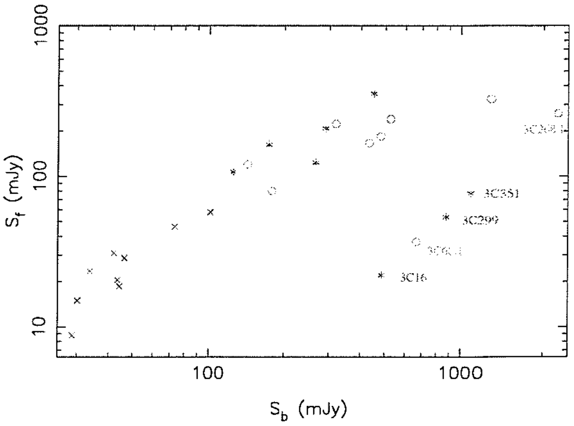

Figure 4.6: Plot of the flux of the brighter lobe against the fainter lobe at 4.8 GHz. Symbols are as in Figure 4.1.

Figures 4.6 to 4.8 use the 4.8 GHz flux data as a test for flux asymmetry over the source. Tables 3.1 to 3.3 show that the 1.4 GHz flux is much larger compared to the 4.8 GHz flux for each source. Although this suggests that the 1.4 GHz flux data would be a better indicator of any source asymmetries than the 4.8 GHz flux data, since fainter lobes such as the northern lobe of 7C 1745+642 are much more prominent, but the noise level in each source is also much higher. To ensure that my analysis was not unduly affected by high noise levels I chose to use the 4.8 GHz flux instead of the 1.4 GHz flux, in my analysis of the asymmetries.

Figure 4.6 demonstrates that in all my sources there is a tight correlation between the flux of the brightest lobe when compared to the flux of the fainter lobe. In several cases the fainter flux is much smaller than the brighter flux. 3 of these sources are quasars, 3C 351, 3C 68.1 and 3C 16 but interestingly 3C 299 and 3C 268.1 also display this atypical behaviour. McCarthy et al. (1995) noted that 3C 299 showed a strong asymmetry and was more similar to a high redshift (z >1) radio galaxy than a low redshift galaxy. Harvanek & Stocke (2002) also noted that this source has lobes of very different lengths. I find 3C 299 to have a σ_{RM_z} comparable to the high redshift samples.

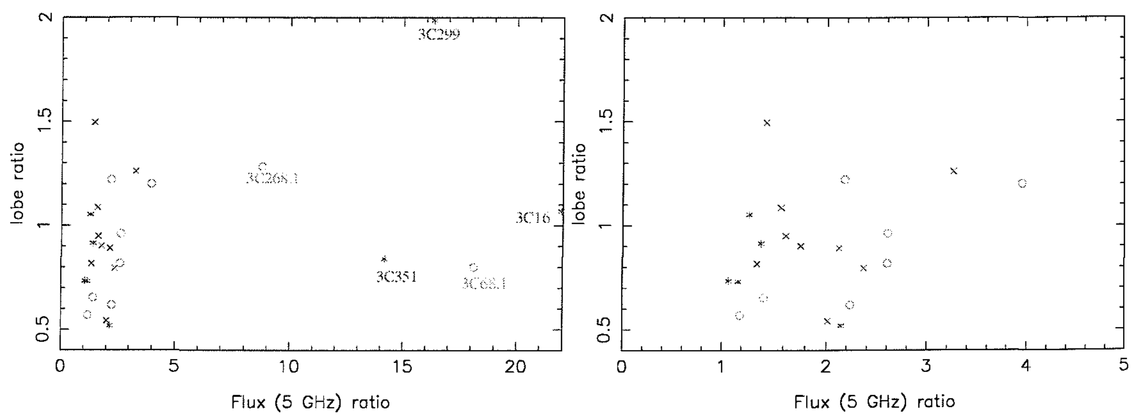

Figure 4.7: Plot of the flux ratio at 4.8 GHz against the lobe ratio, (a - left) with all sources and (b - right) zoomed in on the more 'normal' sources. Symbols are as in Figure 4.1.

Figure 4.7(a) shows that 3C 299, 3C 268.1 and 3C 16 do show larger (>1) lobe ratios but 3C 351 and 3C 68.1 do not. However 3C 351's position in this plot is uncertain. The estimation of the lobe length requires an estimation of where the lobe terminates but in the case of 3C 351's northern lobe it extends far to the west of the hotspots whereas the southern lobe is much more well defined (see Figure C.4). Thus the estimation of the length of the northern lobe may be incorrect and hence the calculated lobe ratio may be smaller than it really is. 3C 68.1 and 3C 16 have no detected cores either by me or previously published data[‡]. This means that the lobe length estimation in these sources may also be flawed. To further aggravate this problem both of these sources have very faint lobes (see Figures B.2 & C.1) and so it is hard to determine where exactly the lobe terminates. However, it is worth noting that when these 5 sources are removed from the analysis (Figure 4.7(b)) there is no significant trend for the brighter flux ratio sources to have a larger lobe ratio.

[‡] Bridle et al. (1994) do marginally detect a core in deeper observations of 3C 68.1.

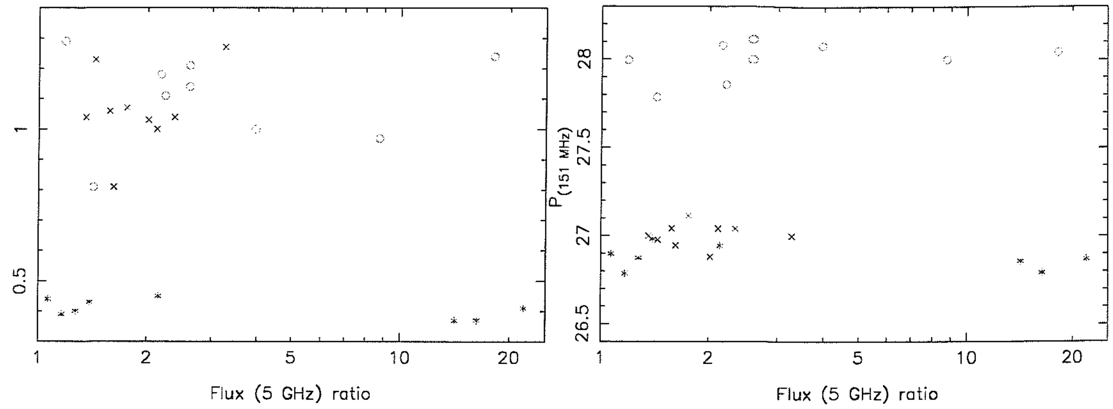

Figure 4.8: (a - left) Plot of the flux ratio at 4.8 GHz against redshift, (b - right) and against radio-luminosity. Symbols are as in Figure 4.1.

Figures 4.8(a) and 4.8(b) show that the trends noted are intrinsic to the sources and not due to any redshift and radio-luminosity differences in the samples. It is worth noting that sources in the high-redshift, low radio-luminosity sample, sample A ('×'), always seem to have a smaller flux ratio than sources in the other two samples.

4.4.2 Asymmetries in spectral index

4.4.2.1 Liu-Pooley effect

The Liu-Pooley (LP) effect predicts that the lobe with the flatter spectrum in a source is also the least depolarised lobe (Liu & Pooley, 1991a; Ishwara-Chandra et al., 2001). Liu & Pooley (1991a) found that 12 out of their 13 sources demonstrated this effect. As noted in section 4.4, to allow a fair comparison between my results and those of Liu & Pooley (1991a) I use only the *observed* depolarisation in the following analysis.

As Figure 4.9 shows I find no significant Liu-Pooley (LP) effect in my sample. As another comparison I used the rms variations in the rotation measure in the sources' reference frame, σ_{RM_z}, instead of depolarisation measure. Clearly Figure 4.10 shows that with σ_{RM_z} I find no significant evidence of any LP effect. Even by plotting the difference in depolarisation or the difference in σ_{RM_z} against the spectral index difference, insuring that the difference in DM or σ_{RM_z} were always positive, there was no significant LP effect. In all cases I find only a maximum of 14 sources out of the 26 sources (12 out of 23 in the case of σ_{RM_z}) to show definite signs of the LP effect.

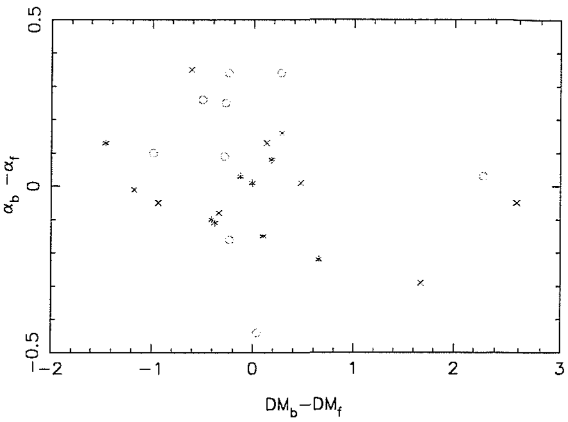

Figure 4.9: The difference in the spectral index of the bright lobe to the faint lobe against the difference in the depolarisation of the bright lobe to the faint lobe. Depolarisation is taken to be the observed (unshifted) value. Symbols are as in Figure 4.1.

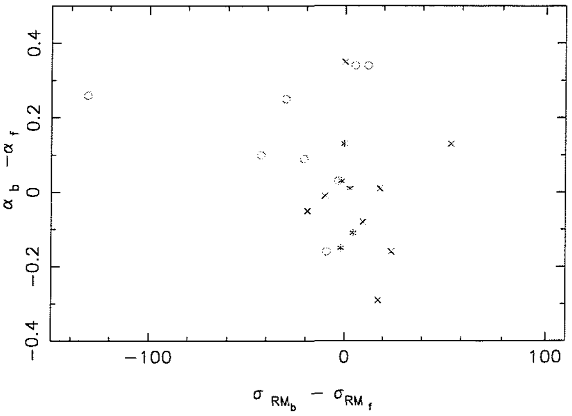

Figure 4.10: The difference in the spectral index of the bright lobe to the faint lobe against the difference in the σ_{RM_z} of the bright lobe to the faint lobe. σ_{RM_z} is the value *local* to the source. Symbols are as in Figure 4.1.

Ishwara-Chandra et al. (2001)[IC0] have shown that the LP effect is stronger for smaller sources and shows no dependence on redshift. They also find that the LP effect is not affected by the choice of quasars or radio galaxies in a sample and is equally significant in both species. They also find that for their large sample (comprised of the Liu & Pooley (1991a); Pedelty et al. (1989); Garrington et al. (1991) samples and the Molongo Reference Catalogue/1 Jy sample) only 58% of radio galaxies and 59% of quasars show the LP effect which is consistent with my results. The inherent difference between sources chosen in samples as well as orientation effects has been suggested by IC0 as an explanation to the number of sources showing the LP effect, in any given sample.

4.4.2.2 Effect of changes in the lobe length

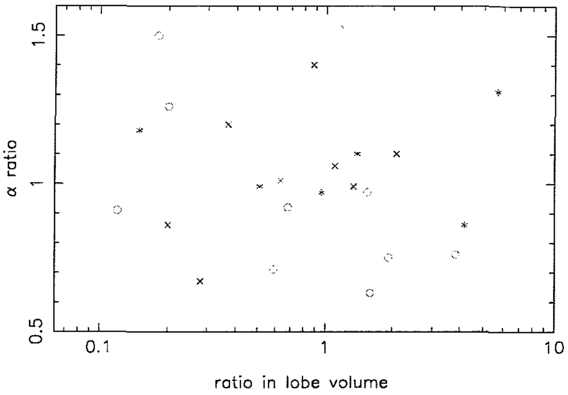

Figure 4.11: The ratio of spectral indices against the lobe ratio. Symbols are as in Figure 4.1.

Figure 4.11 shows that the ratio of spectral indices of the sources' lobes is insensitive to changes in the lobe volume. A source with a large lobe volume ratio (> 1) is equally likely to have a low spectral index ratio as a high spectral index ratio. This suggests that the environment, which affects how large a volume a source can grow to, has no direct effect on the spectral index of a lobe. Thus spectral index should not be used as a tracer for the environment.

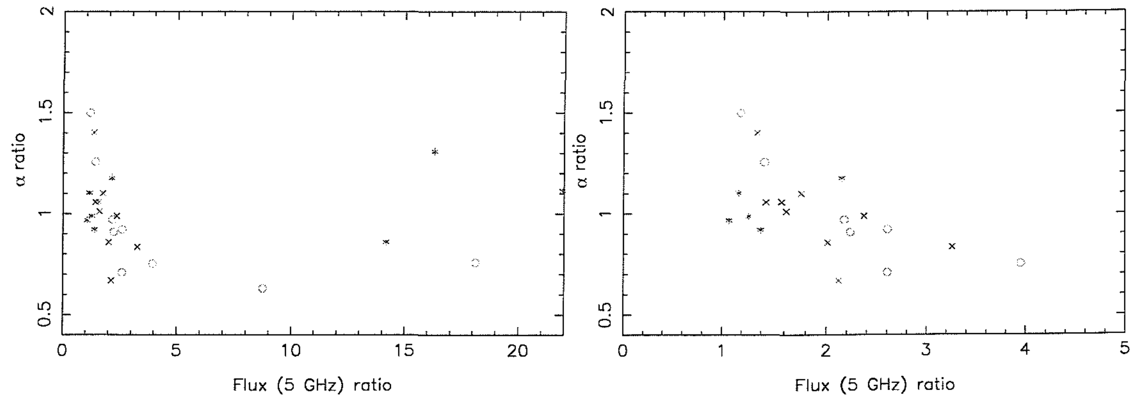

Figure 4.12: The spectral index ratio against the flux ratio, (a - left) all sources and (b - right) zoomed in on sources with a flux ratio < 5. Symbols are as in Figure 4.1.

Figure 4.12(a) shows that in general, a source with a higher flux ratio has a smaller spectral index ratio. This means that the brighter lobe becomes progressively flatter (i.e. $\alpha_b/\alpha_f \rightarrow 0$) as the difference in the flux ratio's increases. This is consistent with the theory that beaming is present in these sources. 3C 16 and 3C 299 are notable exceptions to this trend. 3C 299 has already been discussed above and possess exceptional properties when compared to other radio galaxies. 3C 16 is a quasar and I would expect this source to have shown more evidence for beaming but it has almost similar spectral indices in both lobes. Harvanck & Hardcastle (1998) found evidence that 3C 16 maybe a radio source that is just beginning to restart and hence the fainter lobe will not have a well defined hotspot, therefore beaming is currently not important in this source. Figure 4.12(b) shows that when the more extreme sources are removed the anti-correlation is even more evident.

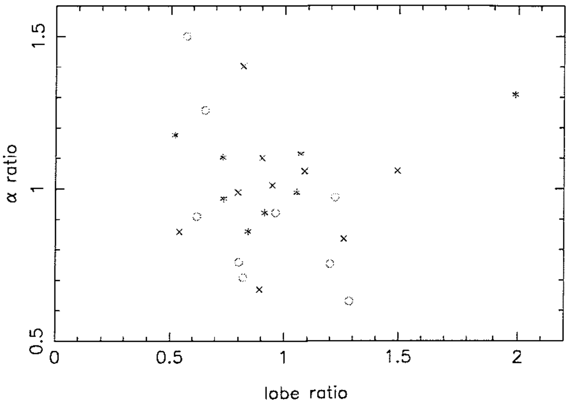

Figure 4.13: The ratio of spectral indices against the lobe ratio. Symbols are as in Figure 4.1.

Figure 4.13 shows that as the lobe length ratio increases the spectral index ratio decreases. This means that in the more length asymmetric sources the larger lobe has the flatter spectral index. Once again 3C 299 again contradicts this result. It has a high ratio of spectral indices and a high lobe length ratio. The trend between lobe ratio and the spectral index ratio adds further evidence to the presence of beaming in many of my sources.

Although Figures 4.12 and 4.13 show evidence for beaming, another possibility would be that the observed asymmetries are caused by a difference in the density of the environment between both lobes. A denser environment would mean that the lobe has a higher minimum magnetic field. Thus any asymmetries in the minimum energy magnetic field would indicate that it is the environment and not beaming that is causing the observed asymmetries with spectral index.

4.4.2.3 Minimum energy of the magnetic field

A simple method to estimate the magnetic field of a radio source is to use the minimum energy argument (e.g Longair, 1994). For any given radio source of a given volume and radio-luminosity the minimum energy magnetic field argument calculates the minimum energy that must be present in the emitting volume. The minimum energy argument assumes that $W_{\rm mag} = \frac{4}{3} W_{\rm particles}$, i.e. a source has approximately equal energy in its relativistic particles as it has in its magnetic field.

The minimum energy approach assumes a perfectly uniform magnetic field throughout the lobe. There are no energy losses from the electrons. Therefore, the energy distribution of the relativistic electrons is a perfect power–law throughout the lifetime of the source. This is a simplistic model but it can be used to model the magnetic field, B$_{min}$, in the lobe with few assumptions required. For full details see Longair (1994) which gives,

$$B_{min} = \left(\frac{9\sqrt{3}c\mu_0^2 L_\nu \bar{\nu}^{-\frac{1}{2}} e^{\frac{1}{2}} m_e^{\frac{1}{2}} \kappa}{2^3\sqrt{\pi}\sigma_T V}\right)^{\frac{2}{7}}, \qquad \text{(Tesla)} \qquad (4.7)$$

where

$$\bar{\nu}^{-\frac{1}{2}} = \left[\left(\frac{3-x}{2-x}\right)\left(\frac{\nu_1^{\frac{2-x}{2}} - \nu_2^{\frac{2-x}{2}}}{\nu_1^{\frac{3-x}{2}} - \nu_2^{\frac{3-x}{2}}}\right)\right] \qquad (4.8)$$

and $x = 1 - 2\alpha$. The volume of a lobe, V, is assumed to be cylindrical with $V = \frac{\pi}{4}D_{lobe}^3/R^2$ as before. $\nu_1 = 10$ MHz and $\nu_2 = 100$ GHz are taken to be the lower and upper limits of the synchrotron spectrum and the luminosity, L$_\nu$, is calculated using the 4.8 GHz flux of each lobe.

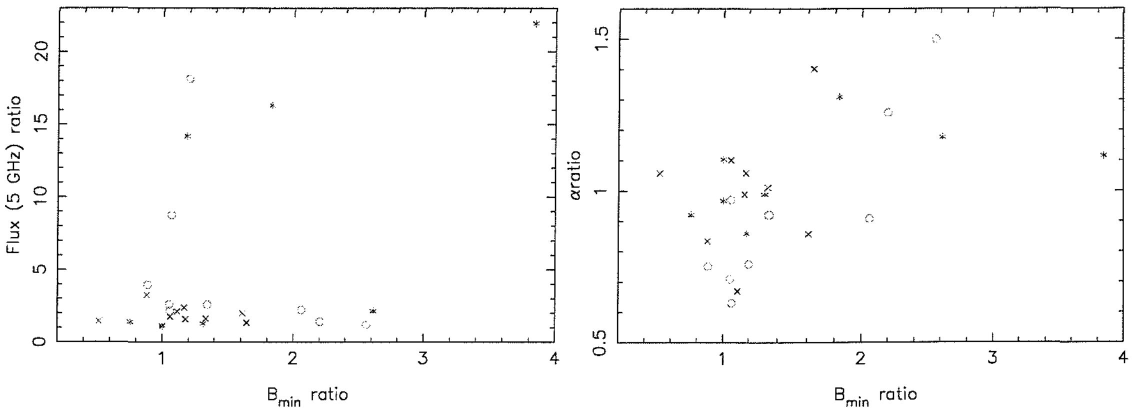

Figure 4.14: (a - left) The minimum energy magnetic field ratio against the flux ratio and (b - right) against the spectral index ratio. Symbols are as in Figure 4.1.

As Figure 4.14(a) demonstrates, there is no relationship between the minimum energy magnetic field ratio and the flux ratio. This indicates that there is no significant environmental difference causing the flux differences between two lobes of a source.

Correspondingly Figure 4.14(b) shows that there is a weak correlation in the minimum energy magnetic field ratio when compared with the spectral index ratio. A beamed, flat spectrum hotspot will have a stronger magnetic field which could explain the weak trend in Figure 4.14(b). However, the asymmetries in the minimum energy magnetic field could also be caused by differences in the density of the environment across the lobes. Figure 4.15 shows that there is no trend with redshift and so the minimum energy magnetic field- α ratio is intrinsic to the local source environment and is not affected by the redshift of a source.

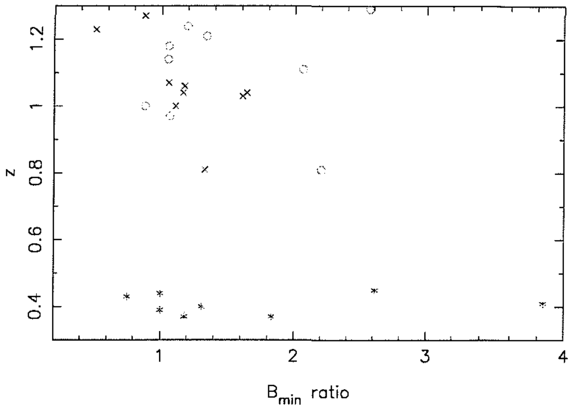

Figure 4.15: The minimum energy magnetic field ratio against the redshift of the source. Symbols are as in Figure 4.1.

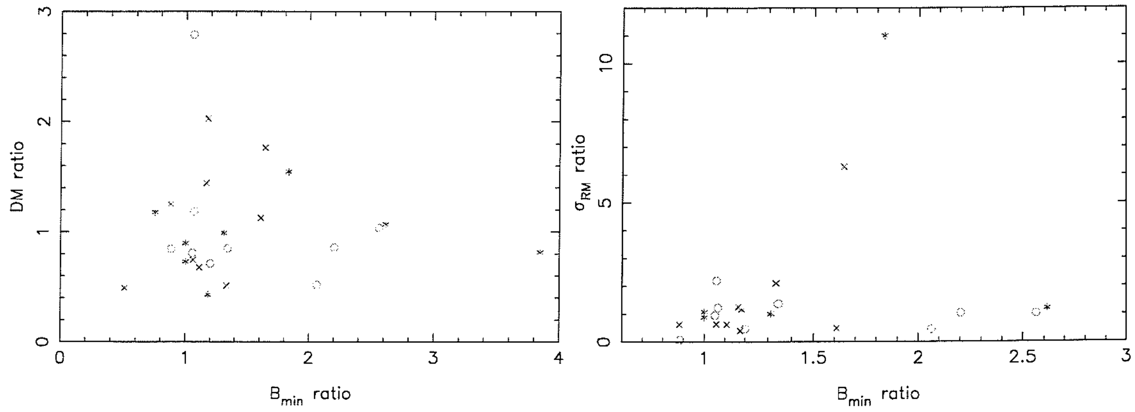

Figure 4.16: The minimum energy magnetic field ratio against (a - left) the depolarisation ratio and (b - right) σ_{RM_z} ratio. Symbols are as in Figure 4.1.

It is interesting to note that the asymmetries in depolarisation and σ_{RM_z} are not related to asymmetries in the minimum energy magnetic field (see Figure 4.16). Depolarisation and σ_{RM_z} are both thought to be observational indicators of density[§], in the source environment but neither show any relationship with the minimum

---

[§] Rotation measure is a direct function of density and the magnetic field of a source (section 3.2) and since σ_{RM_z} and the shifted depolarisation have been shown to be correlated (section 4.3.3) then both can be said to be tracers of the density of the environment.

energy magnetic field ratio. This suggests that the environment has no direct impact on either depolarisation or σ_{RM_z} asymmetries.

4.4.3 Asymmetries in depolarisation

Unlike the flux asymmetry (Figure 4.6) the depolarisation shows no obvious correlation between the depolarisation of the brighter and fainter lobes, see Figure 4.17. It is worth noting that in most cases the depolarisation of the brighter lobe is smaller than the depolarisation of the fainter lobe. This is again indicative of beaming in these sources. In the case of beaming, the fainter lobe is assumed to be pointing away from the observer. The radiation of the fainter lobe will then have a larger path length to traverse through the local Faraday screen compared to the radiation of the brighter lobe and will appear more depolarised.

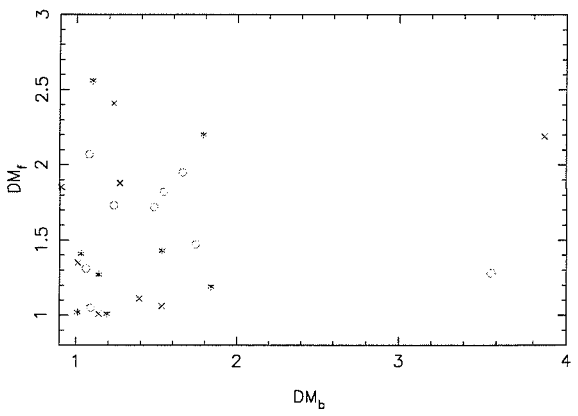

Figure 4.17: Depolarisation of the brighter lobe against the fainter lobe. Symbols are as in Figure 4.1.

The flux asymmetry is independent of any depolarisation asymmetry as 3C 299, 3C 16, 3C 68.1, 3C 351 and 3C 268.1 (the high flux ratio sources) show similar spreads in their depolarisation ratios when compared to all the other sources. Figure 4.18(a) at first sight indicates that the volume of the lobe also plays no part in the magnitude of the depolarisation ratio. However, on closer inspection it is worth noting that in 16 out of the 26 sources, the lobe with the larger volume is the more depolarised. In fact, only 4C 14.27, 3C 68.1, 3C 351, 6C 1256+36 and 7C 1745+642 vary significantly from this trend.

By plotting the depolarisation ratio against the lobe volume ratio in Figure 4.18(a) I assume that all the lobes in the three samples can be described by a cylinder. This is not a good approximation for extremely distorted sources like 3C 351 and 7C 1745+642. As Figure 4.18(b) shows the trend still exists when the dif-

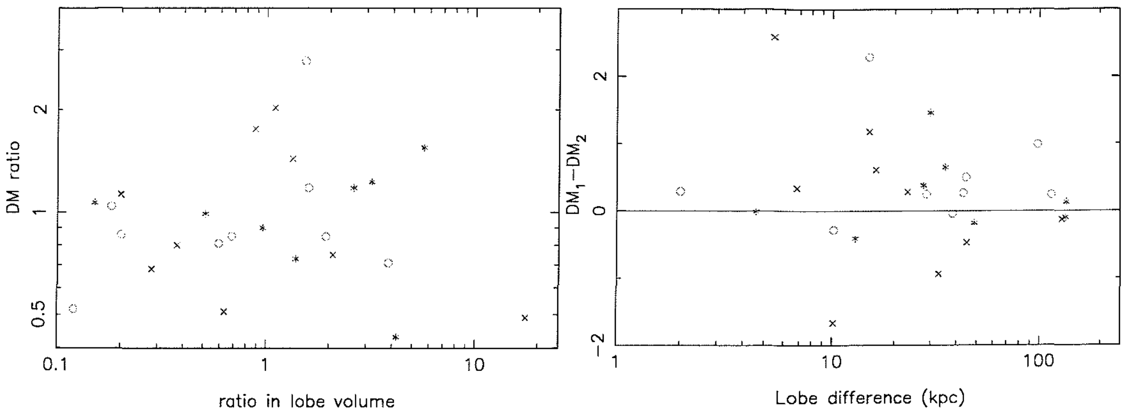

Figure 4.18: (a - left) Depolarisation ratio against the lobe volume ratio. (b - right) Difference in depolarisation against the difference in size of the lobes. Plotted so that D_{lobe_1}-D_{lobe_2}> 1 in all cases. Symbols are as in Figure 4.1.

ference in the lobe lengths is compared with the difference in the depolarisations of each lobe. In this case the trend is much more pronounced with only 6C 0943+39 and 7C 1745+642 showing significant disagreement with the findings. Both of these sources show the same trends in (a) and (b). This disagrees with the results of Pedelty et al. (1989) and Liu & Pooley (1991a), who find that the shorter lobe is the more depolarised lobe. However DT96 also finds this reverse correlation with only 3C 351 in common between her sample and my sample. The DT96 correlation was found to be strong in the quasars, but the depolarisation of the radio galaxies was too low to be able to determine if the correlation was significant. This may indicate that there is an inherent difference in the Pedelty et al. (1989) and Liu & Pooley (1991a) samples and the DT96 sample and mine. This may be due to the fact that the Pedelty et al. (1989) sample was selected from sources with strong emission lines and the Liu & Pooley (1991a) sample only contains sources smaller than 23″.

4.4.4 Asymmetries in σ_{RM_z}

Figure 4.19 shows there is no relationship between σ_{RM_z} of the brighter lobe when compared to the fainter lobe. I find that only half the sources show that the fainter lobe has the larger σ_{RM_z}. This is unlike the depolarisation result where in almost all cases the fainter lobe was more depolarised. However, the depolarisation is affected by changes in the path length through the Faraday screen but σ_{RM_z} is insensitive to these changes and so would not be expected to show any trend with the lobe asymmetries.

As with depolarisation there is little trend with lobe volume (Figure 4.20(a)).

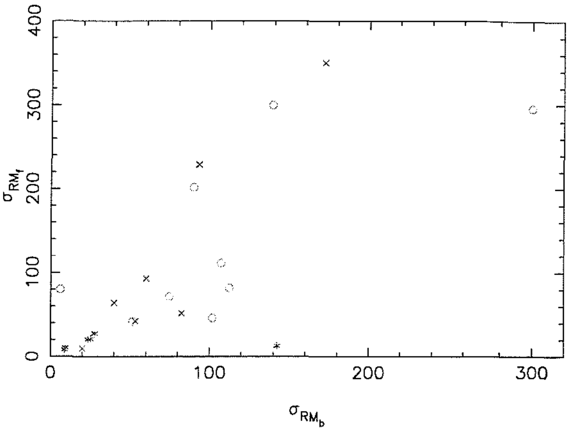

Figure 4.19: σ_{RM_z} of the bright lobe against the fainter lobe. Symbols are as in Figure 4.1.

This confirms the idea that the extent that a lobe can grow to (i.e the volume) has little effect on the measured parameters such as spectral index, depolarisation and σ_{RM_z}. Most of the sources show that the larger σ_{RM_z} is in the longer lobe. In only 3 out of the 23 sources is this not the case (6C 1129+37, 6C 0943+39 and 3C 280) which is similar to the trend noted with depolarisation.

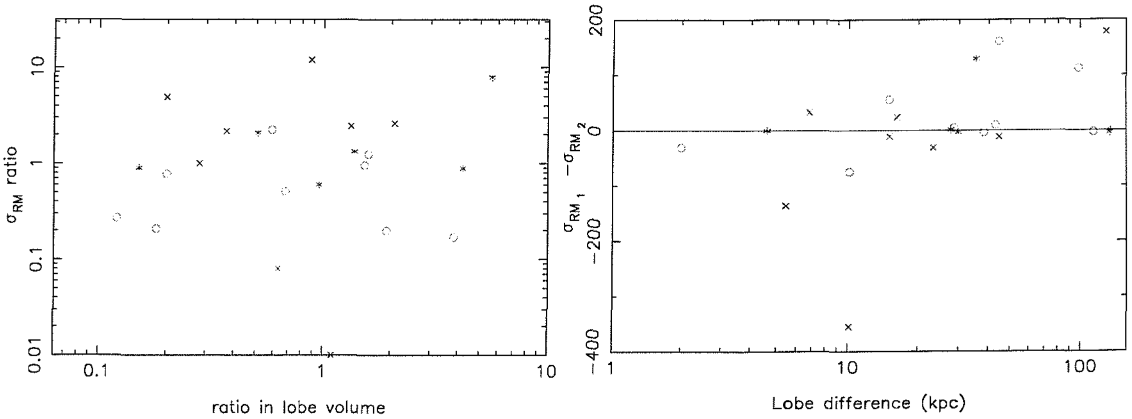

Figure 4.20: (a - left) σ_{RM_z} ratio against the lobe volume ratio. (b - right) Difference in σ_{RM_z} against the difference in size of the lobes. Plotted so that D_{lobe_1}-D_{lobe_2}> 1 in all cases. Symbols are as in Figure 4.1.

4.4.5 Summary

I found that there is no significant LP effect, but this lack of trend could be attributed to the larger size distribution of my sample compared to the sample of Liu & Pooley

(1991a). This dependence on size has also been noted by IC01. From the spectral and depolarisation asymmetries I found evidence that many of the sources were beamed. The minimum energy magnetic field asymmetry results could be explained by both a change in the environment or by the presence of beaming. The minimum energy magnetic field model is not an accurate picture of the magnetic field of a source but does give a rough estimate of the size of the field.

The depolarisation and σ_{RM_z} asymmetries are similar, confirming the assumption that they sample similar regions of the Faraday screen. In general, the depolarisation and σ_{RM_z} are smaller in the shorter lobe and almost all the fainter lobes show larger depolarisations. The σ_{RM_z} variations are insensitive to which lobe is brighter.

4.5 Conclusions

A number of source properties are derived directly from the radio observations. These include the spectral index, the rotation measure and the depolarisation measure. I find no correlation of spectral index with any of the fundamental parameters (redshift, radio-luminosity and radio-size). I can therefore not confirm previous findings of a correlation of spectral index with redshift (Athreya & Kapahi, 1999), a trend of spectral index with radio luminosity (Veron et al., 1972; Onuora, 1989) nor a trend of spectral index with size (Blundell et al., 1999).

In the previous chapter I argued that the overall rotation measure for a given source is mainly Galactic in origin. This interpretation is consistent with the absence of any correlation of rotation measure with the fundamental parameters. Variations in the rotation measure are quantified in order of decreasing angular scales by dRM_z (difference of rotation measure between the two lobes of an individual source), σ_{RM_z} (rms variation of rotation measure) and DM_z (depolarisation measure). I find that the significance of a correlation with redshift increases from dRM_z to DM_z. Therefore I can conclude that the variation of the rotation measure on small angular scales is caused by a Faraday screen local to the sources. Furthermore, these Faraday screens give rise to greater variation of the rotation measure for sources at higher redshift compared to their low redshift counterparts.

I have also studied the asymmetries of these derived properties with the fundamental properties, but I have also looked at the asymmetries in the 4.8 GHz flux data, S, and the minimum energy magnetic field, B_{min}. By definition, $S_b/S_f > 1$ but several sources, of which 3 are quasars, show a much larger flux ratio. I find evidence from spectral asymmetries that many of the sources show indications of beaming. However, the results from the B_{min} asymmetries are inconclusive and could also explain the asymmetries by implying a more environmental based explanation. In general all asymmetries were found to be insensitive to changes in the source redshift, or low frequency radio luminosity; suggesting that the environments of the high redshift and low redshift samples are similar and any asymmetries caused are due to localised changes in the environment.

This interpretation is confirmed in the analysis of the depolarisation and σ_{RM_z} asymmetries with B_{min}. I suggest that it is not the environment that is causing the depolarisation and σ_{RM_z} asymmetries but is actually the degree of disorder in the sources that is causing a change. This fits with my findings that the shifted depolarisation, DM_z, dRM_z and σ_{RM_z} show trends with redshift but no trend with the minimum energy magnetic field. Thus it is the degree of disorder in the magnetic field that is changing with redshift and not the density of the source environment.

Chapter 5

Modelling of the Faraday screen

To sample the environment around radio sources I use the observed polarisation and the observed RM variations. These parameters are used to determine how the environment evolves with redshift, radio-luminosity and radio size*. However, the observed polarisation, the observed RM variations and hence the observed depolarisation measure are also effected by source based variations in the structure of the Faraday screen. The structure of the Faraday screen combined with the limited spatial resolution of any radio observation lead to the observed depolarisation of the synchrotron emission.

A uniform Faraday screen comprised of large (> 50 kpc) cells will have little effect on the underlying polarisation and RM structure. A cell is defined as a region in the Faraday screen where the magnetic field has almost uniform strength and orientation. As these cells shrink (i.e the cells size becomes smaller than the size of the telescope beam) and the Faraday screen becomes increasingly non-uniform the effects of the underlying structure can become more pronounced. The effect of the Faraday screen on a source was first investigated by Burn (1966). I use the Tribble (1991), hereafter T91, models as a modern alternative to Burn's theory. The T91 models assume a specific structure to the RM variations and calculate the effect of the structure function on the underlying RM distribution and hence the overall polarisation of a source at any given wavelength. These models can be used to correct the observed depolarisation of my sample sources to a common redshift and the results can be compared with the Burn shifted depolarisation, DM_z, in section 3.3. If the depolarisation measure is found to be correlated with redshift and radio-luminosity using the T91, models then this will confirm the findings in section 4.3.2 where DM_z is found to be a function of both redshift and radio-luminosity.

---

*The relationship between the environment and the depolarisation measure and σ_{RM_z} are discussed in detail in the previous chapters.

5.1 Critique of Burn's model

The polarisation, p, at a given point in a radio map can be defined as a function of position within the source, $\vec{x_\circ}$, and wavelength, λ,

$$p(\vec{x_\circ}, \lambda) = \int \mathrm{W}(\vec{x_\circ} - \vec{x}) e^{2iRM(\vec{x})\lambda^2} d^2\vec{x} \tag{5.1}$$

where W is the restoring beam of the telescope and RM[†] is the intrinsic rotation measure of the Faraday screen in front of the source.

By assuming that the RM can be defined as a Gaussian distribution with a dispersion σ (T91), equation 5.1 reduces to $< p(\lambda) >= e^{-2\sigma^2\lambda^4}$ which is more commonly known as Burn's law for a foreground depolarisation screen (Burn, 1966).

Burn noted that this law only applies when the scale of the Faraday screen fluctuations are much smaller than the physical size of the source. Observations of Cygnus A by Carilli & Barthel (1996) found that their RM fluctuations were coherent over scales of order 10 kpc. This scale length is comparable to the results found by Pedelty et al. (1989), who find scale lengths between 10-50 kpc, using a sample of high redshift, high radio-luminosity sources. These coherence lengths are not significantly smaller than the source size, violating one of the main assumptions of Burns' theory.

This is not the only problem associated with Burn's theory. In his analysis of the polarisation properties of a source, Burn used the vector $< p(\lambda) >$ as a test for the polarisation which falls off rapidly to zero as the direction of the polarisation field randomises. Burn also predicts that the observed polarisation decreases steeply as a function of wavelength, which is very rarely observed. Table 5.1 demonstrates than even in a small sample of radio galaxies the decrease of the polarisation fraction with wavelength varies widely from the Burn relationship, $p \sim \lambda^{-4}$. This confirms the assumption that by using Burn's theory to shift the depolarisation to a common redshift in section 3.4.2 I am almost certainly over-estimating the depolarisation. Any observations of the polarisation of radio emission measures the length of the polarisation vector, thus $< |p(\lambda)|^2 >$ is a better indicator of the polarisation compared to Burn's $< p(\lambda) >$. In the next section I explain the main points of the T91 models which use $< |p(\lambda)|^2 >$ to test the Faraday medium around a source. For full details see T91.

[†] See section 3.2 for a full explanation of the rotation measure of a source.

5.2 The Tribble models

The polarisation distribution as a function of wavelength, independent of any source model, is given by,

$$< |p\,(\lambda)\,|^2 >= \int R(\vec{s})\,\xi_p(\vec{s})\,d^2\vec{s} \tag{5.2}$$

where $R(\vec{s})$ is determined by the size of the telescope beam W on the sky and $\xi_p(\vec{s}) = \xi_f(\vec{s},\lambda)\,\xi_\varepsilon(\vec{s})\,\xi_\theta(\vec{s})$. $\xi_\varepsilon(\vec{s})$ determines how the emissivity of neighbouring regions interact and becomes important when a radio source has prominent filamentary structures (Fomalont et al., 1989). $\xi_\theta(\vec{s})$ determines how the intrinsic polarisation angle of neighbouring regions interact. For a uniform source both the emissivity, $\xi_\varepsilon(\vec{s})$, and the angle, $\xi_\theta(\vec{s})$, are unity, therefore $\xi_p(\vec{s})$ depends only on the distribution of the external Faraday screen, $\xi_f(\vec{s},\lambda)$.

$\xi_f(\vec{s},\lambda)$ is the critical component in the determination of the polarisation as this relates directly to the structure function of the RM fluctuations, $D(\vec{s})$.

$$\xi_f(\vec{s},\lambda) = e^{-2\lambda^4 D(\vec{s})} \tag{5.3}$$

where $D(\vec{s})$ determines the RM distribution in a source and how neighbouring regions of local RM are correlated, i.e. $D(\vec{s}) =< [RM(\vec{x}+\vec{s}) - RM(\vec{x})]^2 >$. The exact form of the structure function depends on whether or not the RM field is assumed to be dominated by Quadratic fluctuations, Gaussian auto-correlation fluctuations or Power-law fluctuations.

The exact form of $R(\vec{s})$ is dependent on the structure of the telescope beam,

$$R(\vec{s}) = \int W(\vec{x})\,W(\vec{x}+\vec{s})\,d^2\vec{x} \tag{5.4}$$

assuming a Gaussian beam this reduces to,

$$R(\vec{s}) = \frac{1}{2\pi t^2}\,e^{-|s|^2/t^2} \tag{5.5}$$

where t is the physical size of the telescope beam. The Tribble models are calculated in the restframe of the source. The size of the RM fluctuations, $s_\circ$, t and the observing wavelength, λ must all be calculated in the source frame of reference.

5.2.1 Quadratic model

For the quadratic model the structure function is given by,

$$\begin{aligned} D(s) = &\quad 2\sigma^2(s/s_\circ)^2 \quad s < s_\circ \\ D(s) = &\quad 2\sigma^2 \qquad\qquad\ s > s_\circ \end{aligned} \tag{5.6}$$

where $s_\circ$ is the size of the RM fluctuations within the telescope beam, t. The number of independent RM cells within a telescope beam is given by $N = (t/s_\circ)^2$. A completely unresolved source has $s_\circ \ll t$ whereas a completely resolved source has $s_\circ \gg t$.

The structure function can be substituted into equation 5.2 to give an expression for the polarisation,

$$< |p(\lambda)|^2 >= \frac{1 - e^{-\alpha-\beta}}{1 + 2\beta/\alpha} + e^{-\alpha-\beta} \tag{5.7}$$

where $\alpha = \mathrm{s}_\circ^2/2t^2$ and $\beta = 4\sigma^2\,\lambda^4$

However, to calculate the observed polarisation at any given wavelength the intrinsic σ of the source must also be known and this is affected by the choice of the structure function.

For the quadratic model,

$$\sigma^2_{\mathrm{observed}} = \sigma^2_{\mathrm{RM}}[1 - (1 - e^{-\alpha})/\alpha] \tag{5.8}$$

where $\sigma_{\mathrm{observed}}$ is taken from the observations of the RM variations but the exact value of $\mathrm{s}_\circ$ is not known. In theory it should be possible to estimate the value of $\mathrm{s}_\circ$ from high resolution RM maps as $\mathrm{s}_\circ$ should be comparable to the scale length over which the RM is roughly constant. This would require higher resolution maps than those presented here, thus it is not possible to directly estimate the value of $\mathrm{s}_\circ$ from my observations. In section 5.3 I discuss the effects of varying $\mathrm{s}_\circ$ on the observed polarisation and the RM variations.

5.2.2 Gaussian auto-correlation model

The Gaussian auto-correlation structure function is given by,

$$D(s) = 2\sigma^2[1 - e^{-s^2/s_\circ^2}] \tag{5.9}$$

Again substituting the structure function into equation 5.2 gives,

$$< |p(\lambda)|^2 >= \alpha e^{-\beta} \int_0^1 t^{\alpha-1}\, e^{\beta t} dt \tag{5.10}$$

and the dispersion in the RM is given by,

$$\sigma^2_{\mathrm{observed}} = \frac{\sigma^2_{\mathrm{RM}}}{1 + 1/\alpha}. \tag{5.11}$$

5.2.3 Power-law model

The power law model is slightly more complicated and depends on the choice of m, the power-law exponent. The structure function is given by,

$$D(s) = 2\sigma^2\,[1 - (1 + 2s^2/ms_\circ^2)]^{-m/2} \tag{5.12}$$

which using equation 5.2 gives,

$$< |p\,(\lambda\,)|^2 >= (m/2)\,\alpha\,e^{\alpha-\beta} \int_1^\infty e^{-m\alpha\nu/2}\,e^{\beta\nu^{-m/2}}d\nu. \tag{5.13}$$

This form of the structure function results in the relation $p \sim \lambda^{-4/m}$.

The dispersion of RM in this model is much more complex than either of the previous models and is given by,

$$\begin{aligned} \sigma^2_{\rm observed} &= \sigma^2_{\rm RM}[m\alpha/2]^{m/2}\,\Gamma(1 - m/2, m\alpha/2)\,e^{m\alpha/2} && (5.14)\\ \text{where} \quad \Gamma(a,x) &= \int_x^\infty e^{-t}\,t^{a-1}dt. \end{aligned}$$

In all 3 models when the source is completely resolved $\sigma^2_{\rm observed} = \sigma^2_{\rm RM}$.

5.2.3.1 Power law exponent

T91 uses $m = 2$ in his analysis, but a sample of radio galaxies may show a range of exponents. The only way to determine how polarisation decreases with wavelength is to take a sample of sources with at least 3 sets of polarisation information widely separated in frequency, but also at high enough resolution that the polarisation measurements are not affected by beam depolarisation. The sample must also be observed at the same resolution at all three frequencies. Although there is a large volume of polarisation information in the archives, it proved to be difficult to find a large enough sample of sources with these requirements. Table 5.1 shows the best fit to p $\sim \lambda^{-4/m}$ using sources taken from Akujor & Garrington (1995) with observations at 1.4, 4.8 and 8.4 GHz. In general I find that the polarisation decreases with $1 \lesssim$m$\lesssim$ 4. The north lobe of 3C 266 shows a much steeper decrease in its polarisation, but as Figure 5.3 demonstrates the effects of changing m are small. I use $m = 2$ and $m = 4$ in the following sections as limiting cases.

5.3 Fitting the T91 models to the observations

The T91 models have 2 free parameters, s$_\circ$ and σ_{RM} and two parameters taken from observations, t and the observed variations in the RM, $\sigma_{observed}$, plus a third

Source	Component	$-4/m$
3C 67	T	1.03
3C 173	T	1.79
3C 213.1	T	1.72
3C 266	N	0.26
3C 266	S	1.72
3C 299	S	2.34
3C 305.1	T	3.17
3C 309.1	T	1.29
3C 346	E	3.94
3C 380	E	3.16
3C 380	W	1.62
3C 455	T	2.56

Table 5.1: Calculating the range of exponents ,m, seen in sources observed by Akujor & Garrington (1995)

parameter, m, for the power-law model. There are three basic assumptions that can be made about the values of s_o and σ_{RM}:

i.) The observations of $\sigma_{\rm observed}$ and z can be fitted assuming a constant s_o and a constant σ_{RM} with respect to redshift. If s_o is constant at all redshifts then this assumes that cells in the Faraday screen are always the same size independent of the source morphology or location and will have the same effect on the underlying RM distribution independent of redshift. By also setting σ_{RM} to be constant with redshift I am assuming that all sources have the same underlying RM distribution. This is a rather naive picture as Table 4.6 shows a strong evolution in the observed variations in the RM with redshift.

ii.) A more realistic assumption is that the observations of $\sigma_{\rm observed}$ and z can be fitted assuming a constant σ_{RM} and varying s_o as a function of redshift i.e. $s_o = \gamma(1+z)^{\mu}$.

iii.) Conversely, the observations may also be fitted assuming a constant s_o and varying σ_{RM} as a function of redshift, i.e. $\sigma_{RM} = \gamma(1+z)^{\mu}$.

I use the Numerical Recipes subroutine AMOEBA (Press et al., 1997) to estimate the best fits for the three assumptions presented above. This is done by calculating the least squares difference between the predicted $\sigma_{\rm observed}$ and the true $\sigma_{\rm observed}$ for each source. The best-fit is then given by the values of s_o and σ_{RM} which gives the smallest least squares value[‡]. These results are presented in Table 5.2. Unfortunately, no best-fit solutions can be given for either Power-law model when both free parameters are constant with redshift. This is simply due to the fact that

---

[‡] Least squares value = (model - observed)^2

the Gamma function in equation 5.14 is very sensitive to the exact choice of s_o and σ_{RM} and no reasonable fit can be achieved.

	constant σ_{RM}, constant s_o	
Gaussian	$\sigma_{RM} = 89.1$	$s_o = 15.9$
Quadratic	$\sigma_{RM} = 85.2$	$s_o = 3.5\times10^3$
	constant σ_{RM}, varying s_o	
Gaussian	$\sigma_{RM} = 523.4$	$s_o = 0.03(1+z)^{5.5}$
Quadratic	$\sigma_{RM} = 173.3$	$s_o = 1.20(1+z)^{3.2}$
Power-law with $m = 2$	$\sigma_{RM} = 529.6$	$s_o = 0.01(1+z)^{6.1}$
Power-law with $m = 4$	$\sigma_{RM} = 504.6$	$s_o = 0.03(1+z)^{5.2}$
	constant s_o, varying σ_{RM}	
Gaussian	$\sigma_{RM} = 6.1(1+z)^{4.7}$	$s_o = 5.5$
Quadratic	$\sigma_{RM} = 4.9(1+z)^{4.6}$	$s_o = 2.0$
Power-law with $m = 2$	$\sigma_{RM} = 6.9(1+z)^{4.8}$	$s_o = 2.4$
Power-law with $m = 4$	$\sigma_{RM} = 5.4(1+z)^{4.4}$	$s_o = 12.0$

Table 5.2: Parameters of best fit. s_o in units of kpc and σ_{RM} in units of rad m^{-2}. All results are in the sources' frame of reference.

5.3.1 Constant s_o, constant σ_{RM}

Figure 5.1 demonstrates that the models with constant s_o and constant σ_{RM} do not adequately describe the data. Both models, despite having slightly different σ_{RM} and drastically different s_o, have similar solutions. The only discernible difference occurs at very low redshift where the Quadratic model quickly falls to zero. It is obvious then that there must be some evolution with redshift in either s_o or σ_{RM} to account for the observed correlation between σ_{observed} and redshift.

5.3.2 Varying s_o and σ_{RM}

Figure 5.2(a) and 5.2(b) present the best fit solutions to the Gaussian auto-correlation model and the Quadratic model when s_o is varied keeping σ_{RM} constant and also when σ_{RM} is varied keeping s_o constant. Figures 5.2(a) and 5.2(b) use the RM dispersion of the lobe and that averaged over the entire source, respectively when calculating the best-fit solutions. It is obvious that the solutions, although using subtly different data, produce almost identical fits. For this reason I use only the average source values in all further fits.

The best-fit solutions to the Power-law model with exponents $m = 2$ and $m = 4$ are shown in Figure 5.3. Comparing all 8 solutions presented in Figures 5.2(b) and

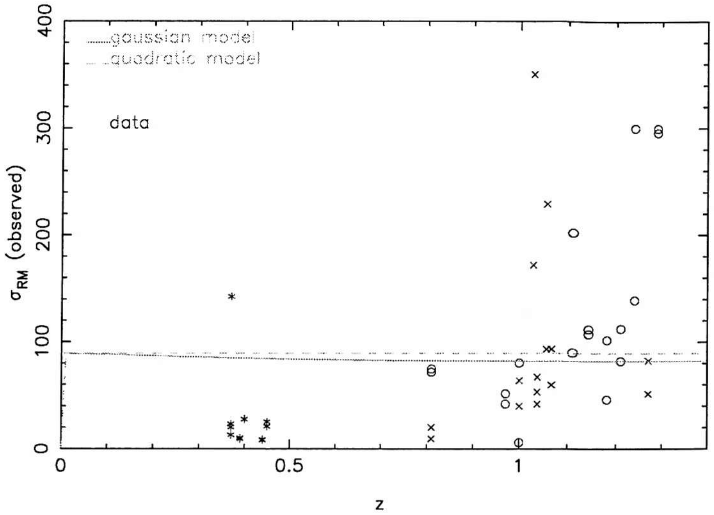

Figure 5.1: Best fit solution of the Faraday screen keeping s$_\circ$ and σ_{RM} fixed for the Quadratic and Gaussian models. The $\sigma_{\rm observed}$ values for all lobes are plotted as '×'.

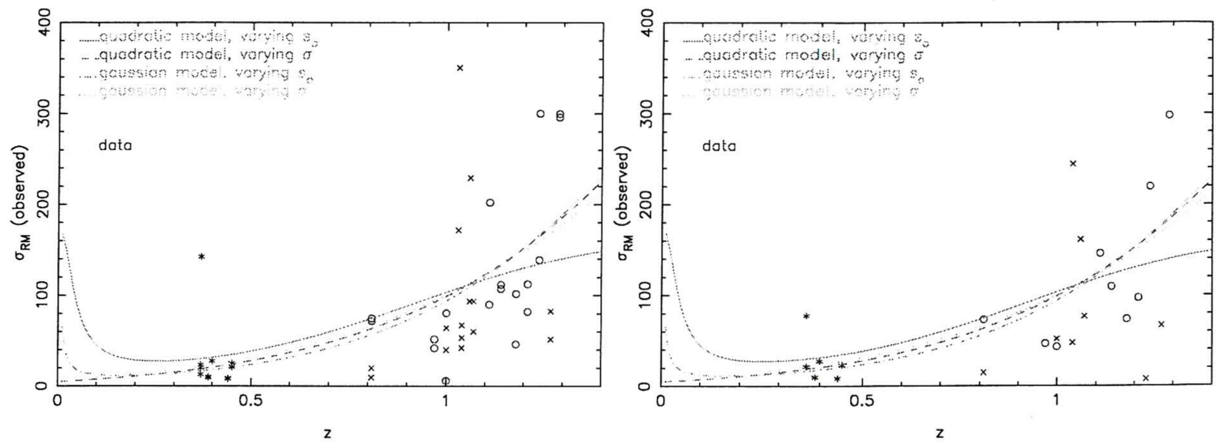

Figure 5.2: Best fit solutions of the Faraday screen for the Quadratic and Gaussian auto-correlation models. Line styles indicate whether s$_\circ$ or σ_{RM} are being varied as a function of (1+z). (a - left) Solution uses all lobe $\sigma_{\rm observed}$ values in the and all lobe $\sigma_{\rm observed}$ values are plotted. (b - right) Solution uses only the average $\sigma_{\rm observed}$ values for each source and the average source $\sigma_{\rm observed}$ values are plotted.

5.3 demonstrates that by using the $\sigma_{\rm observed}$ from observations it is impossible to determine whether or not it is s$_\circ$ varying with redshift or σ_{RM} varying with redshift that is causing the observed trend of $\sigma_{\rm observed}$ with redshift. All 8 solutions are statistically identical in terms of their least squares fit value. The only noticeable difference occurs at very low redshifts when s$_\circ$ varies as a function of redshift and σ_{RM} is kept constant. Each of the different models shows a slight upturn as $z \rightarrow 0$. This is simply due to the fact that as $z \rightarrow 0$, the beam size approaches zero and hence $\alpha \rightarrow \infty$ and so $\sigma^2_{\text{observed}} = \sigma^2_{\text{RM}}$. This is similar to the case when a source is completely resolved.

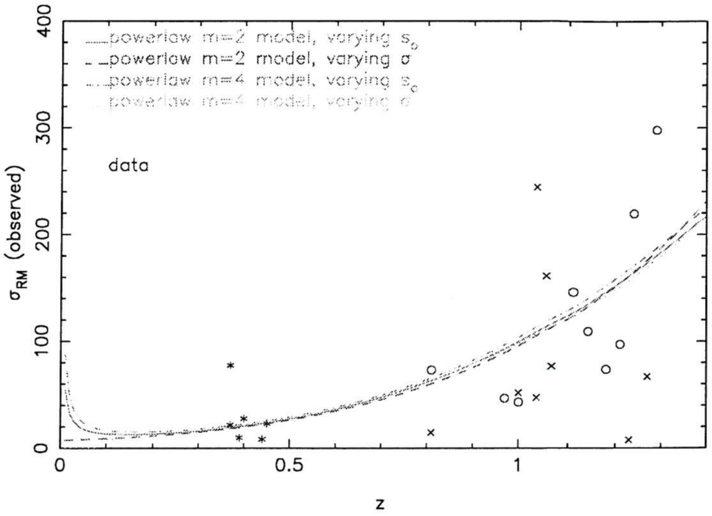

Figure 5.3: Best fit solutions of the Tribble models for the Faraday screen for a Power-law model with exponents $m = 2$ and $m = 4$ plotted against the average σ_{observed} values for each source.

5.3.3 Depolarisation

Although there is no significant difference between the solutions with varying s_o as a function of redshift compared to varying σ_{RM}, I folded the results presented in Table 5.2 into the corresponding expressions for polarisation given in equations 5.7 to 5.13. This allows the fractional polarisation that would be observed at 4.8 GHz and also at 1.4 GHz to be calculated. These values can then be used to calculate the depolarisation parameter $\text{DM}^{4.8}_{1.4}$ (see section 3.3).

5.3.3.1 Constant s_o, constant σ_{RM}

Figure 5.4 shows that the calculated Quadratic depolarisation keeping s_o and σ_{RM} constant with respect to redshift, is always 1. It is obvious that this model fails to describe the data. When the Gaussian auto-correlation model is used to calculate the depolarisation, it predicts more depolarisation at lower redshifts, underestimating the higher redshift depolarisation measurements. Both models fail to describe the data confirming my earlier finding that there must be some evolution in either s_o or σ_{RM}.

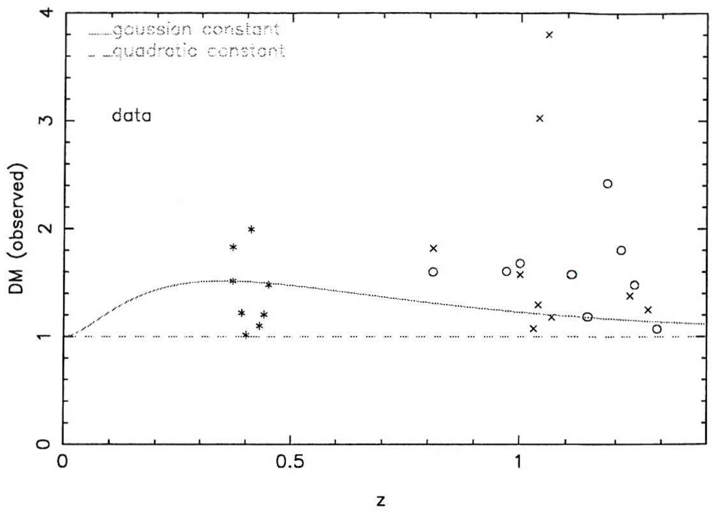

Figure 5.4: Model prediction for the depolarisation with constant s$_{\circ}$ and σ_{RM} obtained from the best-fit solutions using the Quadratic and Gaussian auto-correlation models. The data points represent the average observed source depolarisation.

5.3.3.2 Varying s$_{\circ}$ and σ_{RM}

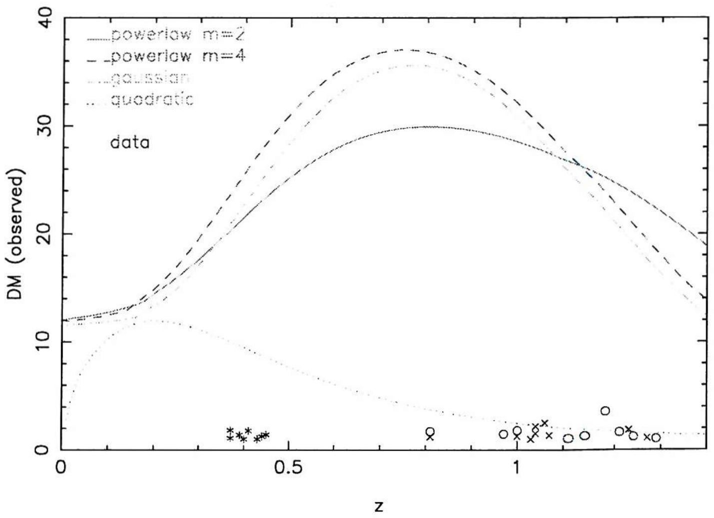

Figure 5.5: Model predictions for depolarisation using all models with a constant σ_{RM} and a varying s$_{\circ}$ with redshift, obtained from the best-fit solutions in Table 5.2. Data points are as in Figure 5.4.

All solutions presented in Figures 5.2 and 5.3 are equally significant independent of whether or not s$_{\circ}$ or σ_{RM} is varied. The solutions are also independent of which model is used to calculate the observed RM variations. However, there *is* considerable difference between the calculated depolarisations as shown in Figures 5.5 and

5.6. Figure 5.5 uses only the solutions which have a constant σ_{RM} and varying $s_\circ$. In all cases the depolarisation is widely over-estimated. In the most extreme cases predicting depolarisations in excess of 30. Such high depolarisations have never been observed, even at high resolution (e.g Best et al., 1997; Carilli & Barthel, 1996; Best et al., 1998; Dennett-Thorpe et al., 1997). In the case of the Quadratic model the solution even predicts a strong anti-correlation of depolarisation with redshift which has never been observed. In striking contrast Figure 5.6, which shows the results for constant $s_\circ$ and varying σ_{RM}, is a much better fit to the observations. At lower redshifts ($z < 0.5$) all models are equally likely and the scatter in the depolarisation encompasses all the solutions. It is only when the higher redshift ($z > 0.5$) sources are considered that I am able to determine a significant difference between the models. Both the Power-law model (with an exponent $m = 2$) and the Quadratic model overestimate the observed depolarisation. However, the $m = 4$ Power-law solution and the Gaussian auto-correlation solution give results that are consistent with the observations. The fact that there is some degree of scatter at all redshifts suggests that a fixed $s_\circ$ is a simplification and $s_\circ$ may vary slightly from source to source. However, the dominant effect is the variation of σ_{RM}.

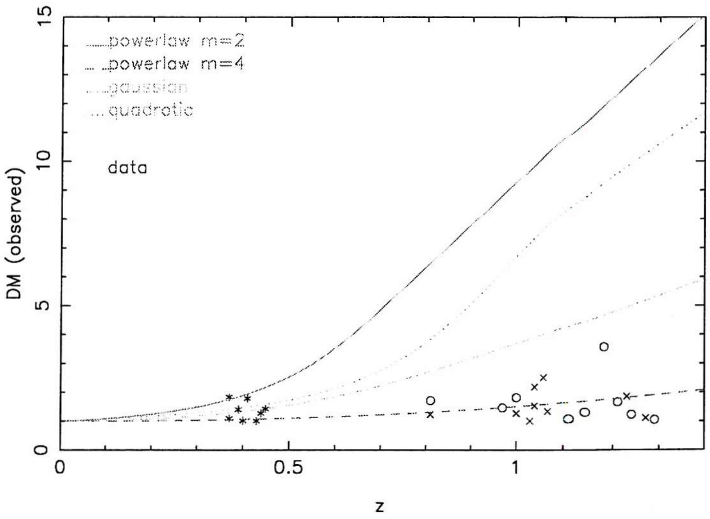

Figure 5.6: As Figure 5.5 but with a constant $s_\circ$ and varying σ_{RM} with redshift.

In the next section I consider the effects of varying $s_\circ$ slightly using the Gaussian auto-correlation model and the Power-law model with $m = 4$.

5.3.4 Scatter in $s_\circ$

Figure 5.7(a) shows the Gaussian auto-correlation model with $\sigma_{RM} = 6.1(1 + z)^{4.7}$ rad m^{-2} with $s_\circ$ varying around the best-fit value, $s_\circ$=5.5 kpc. By allowing $s_\circ$ to vary by a maximum of ±90% from the best fit value I can determine the effects of changes in s$_\circ$ on the data. Figure 5.7(b) is the $m = 4$ Power-law model with $\sigma_{RM} = 5.4(1+z)^{4.4}$ rad m^{-2}, again s$_\circ$ is allowed to vary around the corresponding best-fit value of s$_\circ$=12.0 kpc. In both cases the low redshift results (z <0.5) are largely insensitive to changes in s$_\circ$. This is not the case at the higher redshifts (z > 0.5). As s$_\circ$→ ±90%s$_\circ$ the depolarisation becomes increasingly unrealistic. In both models using s$_\circ$=0.1s$_\circ$ produces large over-estimates in the high redshift depolarisations. This is also true when s$_\circ$=0.5s$_\circ$ using the Gaussian auto-correlation model. This suggests that although s$_\circ$ doesn't vary with redshift, a small amount of variation can describe the scatter in the observed data seen in the DM-z plots of the previous chapters. Figure 5.7(b) is the best fit to the data suggesting that the Power-law model with $m = 4$ is perhaps the most accurate and the small variations in s$_\circ$ do aptly describe the data. This model predicts $p \sim \lambda^{-1}$ compared to the Burn-law $p \sim \lambda^{-4}$.

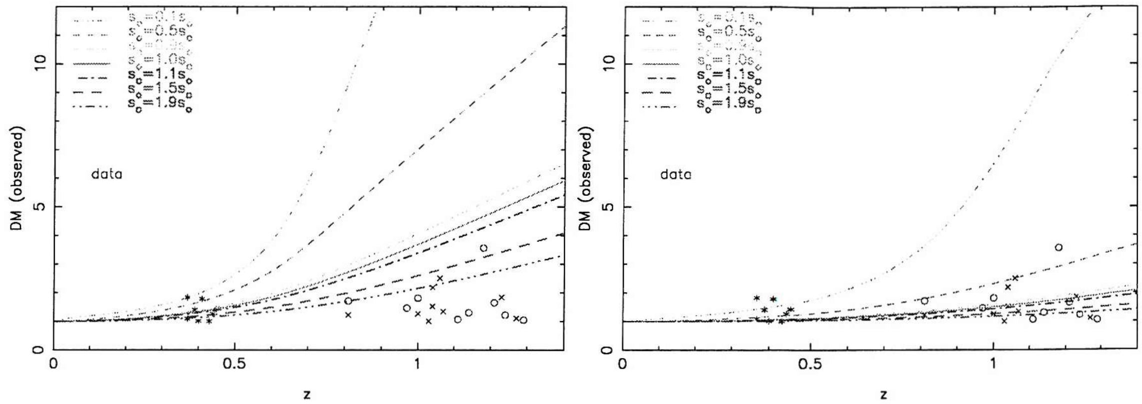

Figure 5.7: (a - left) Varying the value of s$_\circ$ using the Gaussian auto-correlation model and (b - right) the Power-law model with $m = 4$. In both plots the bold line indicates the initial s$_\circ$ taken from Table 5.2.

It must be noted that the fitting procedure only uses 23 out of a possible 26 sources[§]. To gain a better estimate of which model is the most accurate a much larger sample, preferably with higher resolution, would have to be used. By using a sample of radio galaxies at high resolution the variations in s$_\circ$ would be less significant and the sources would be well resolved and hence $\sigma_{RM} \approx \sigma_{\mathrm{observed}}$.

5.3.5 Using s$_\circ$=10 kpc

As I have already noted my RM maps are not of sufficient quality to determine how the RM structure changes over each lobe of a source. In several sources (e.g. 3C 299

[§] As noted in the previous chapters 3 sources have no RM information in at least one lobe.

and 6C 0943+39) I have only a few pixels of RM data in each lobe. In section 5.3.3 I demonstrated that keeping s_o constant and varying σ_{RM} as a function of redshift is the most realistic of all the solutions presented. In all cases s_o was found to be less than 12 kpc.

The method described in the previous sections does not include any information on how the depolarisation differs with changes in radio-luminosity. Figures 5.2 to 5.3 show that the two high redshift samples ('×' = low radio-luminosity sample A and 'o' = high radio-luminosity sample B) are equally distributed around the solutions. This method does not enable any determination of how depolarisation is affected by changes in P_{151} and D_{lobe}. To overcome this problem, I set s_o=10 kpc and calculate σ_{RM} using the observed rms variation in the rotation measure, $\sigma_{\mathrm{observed}}$, and the known beam size. This calculated σ_{RM} is then used to work out the depolarisation for the source if it was located at $z = 1$. Only by doing this can I determine if any depolarisation trends are really due to redshift effects and not simply due to the fact that a third of my sample is located at $z = 0.4$. This is the same method as used in section 3.4.2 to shift the depolarisation using Burn's law.

Quadratic model results

$r_{z,DM} = 0.67857$ $t = 6.13$
$r_{P,DM} = 0.49405$ $t = 3.77$
$r_{D,DM} = -0.21899$ $t = -1.49$

Gaussian model results

$r_{z,DM} = 0.67894$ $t = 6.13$
$r_{P,DM} = 0.49541$ $t = 3.78$
$r_{D,DM} = -0.22294$ $t = -1.52$

Power-law model results

$r_{z,DM} = 0.67771$ $t = 6.1$
$r_{P,DM} = 0.49171$ $t = 3.75$
$r_{D,DM} = -0.23059$ $t = -1.57$

Table 5.3: Spearman rank results for s_o=10 kpc

As Table 5.3 demonstrates, I always find a strong $DM_{z=1}$–z correlation with a weaker correlation with radio-luminosity, independent of the model used. There is never a significant anti-correlation with size. These results are consistent with the results found in the previous chapters, obtained from Burn's law.

5.4 Conclusions

I have used the T91 models to determine how the size of the cells in an external Faraday screen, s_o, varies with redshift and also to determine if there is any evolution in the intrinsic RM variations, σ_{RM}, with redshift.

I have compared the observed RM variations with the predicted RM variations using a constant s_o and σ_{RM} with redshift and I find that this model is inconsistent with the data. There is no statistical difference between the models when s_o is varied compared to when σ_{RM} is varied. Only by comparing the predicted depolarisation with the observed depolarisation is there any distinction between the models. In all cases when s_o is varied, keeping σ_{RM} constant, the predicted depolarisation is over-estimated. Only by keeping s_o constant and varying σ_{RM} is the predicted depolarisation similar to the observed depolarisation.

The Gaussian auto-correlation model and the Power-law model with exponent $m = 4$ are good fits to the data. When s_o is allowed to vary slightly in these models I find that it has little effect on the low redshift sources, but as redshift increases the size of s_o becomes important. A small amount of variation (typically $< 50\%$) can be introduced to the models to allow for the obvious scatter in the depolarisation-redshift plots. In all cases it is the higher redshift sources that constrain the models.

A fixed cell size and varying σ_{RM} with redshift gives further evidence that the observed depolarisation is due to the increasing disorder with redshift and not due changes in the density of the environment with redshift (see previous chapter).

By setting s_o=10 kpc and calculating σ_{RM} using the observed $\sigma_{\mathrm{observed}}$ and the known beam size I am able to determine how the depolarisation is affected by changes in radio-luminosity and radio-size. Irrespective of the model I use I always find that depolarisation correlates strongly with redshift and with radio-luminosity. In no cases do I find an anti-correlation with size. These findings agree with the results presented in sections 3.4.2 and 4.3.2. Although the Burn's law over-estimates the degree of depolarisation, I find similar results using the T91 models, which are more realistic than the Burn model. This proves that the simplistic Burn model can still be used to find general trends with depolarisation in a sample, irrespective of the fact that it may overestimate the depolarisation. Interestingly I find that $p \sim \lambda^{-1}$ best describes the data, compared to the widely used Burn $p \sim \lambda^{-4}$ result.

Chapter 6

Modelling FRII sources

In the previous chapters I have used depolarisation and the variations in the rotation measure to sample the environment around powerful FRII radio galaxies. However, In chapter 4 I found evidence that these quantities do not sample the density of the source environment (e.g. Gregory & Condon, 1991), but are indicators of the degree of disorder of the Faraday screen.

In the following I use the model for the evolution of the radio luminosity of FRII-type sources as a function of source age by Kaiser et al. (1997, hereafter KDA) to model the source spectra. This allows a more theoretical approach to determine source properties such as the age of the jets and their energy transport rate or jet power. The model also provides an estimate for the density of the gaseous source environment. By comparing observations of the source depolarisation and variations in the RM with model estimates of the density, jet-power and lobe pressure allows an independent check on the trends of the observational properties of the source environment derived in the previous chapters.

I have obtained depolarisation and rotation measure observations for only a small sample of 26 sources. Because the KDA model can be used to model the radio spectra of a source I can apply it to the complete 3CRR, 6CE and 7C III samples. In practice I use flux measurements at 3 different observing frequencies, for each source, to constrain the KDA model. I then analyse how the model parameters (jet power, density of the environment, source age and lobe pressure) evolve as a function of radio-luminosity, size and cosmological epoch. This gives a more statistically significant result on the overall evolution of the environments of powerful FRII sources.

6.1 The model for FRII sources

The large scale structure of FRII sources is formed from twin jets emerging from a central AGN buried inside the nucleus of the host galaxy. Each jet propagates outward from the core of the source and terminates in a strong shock giving rise to the so–called radio hotspots. The jet material inflates a lobe surrounding the jet, which drives a bow shock into the surrounding medium. This model was first proposed by Scheuer (1974). Kaiser & Alexander (1997), hereafter KA, showed that in a purely dynamical model of FRII evolution, the bow shock and lobe grow self–similarly, which has also been inferred from observations (e.g Leahy & Williams, 1984; Leahy et al., 1989).

The dynamical model of KA assumes a simple power–law for the external density distribution around the radio source, ρ_x,

$$\rho_x = \rho_\circ \left(\frac{d}{a_\circ} \right)^{-\beta} \tag{6.1}$$

where d is the distance from the central AGN, $a_\circ$ is a scale height, $\rho_\circ$ is the density at $d = a_\circ$ and $0 < \beta < 2$.

The KA model also assumes that the rate of injection of energy into the lobe, defined as the jet power, $Q_\circ$, is constant over the lifetime of the source. Due to the high sound speed in the lobes, the lobe pressure is uniform throughout except for the regions close to the hotspots. It is the lobe pressure, p_{lobe} , that confines the jets.

The KA model predicts that the length of a single jet, D_{lobe}, grows with time as

$$D_{lobe} = c_1 \left(\frac{t^3 Q_\circ}{a_\circ^\beta \rho_\circ} \right)^{\frac{1}{5-\beta}} \tag{6.2}$$

where c_1 is a constant which depends on the geometry of the lobe, the thermodynamic properties of the jet material and the gas in the source environment (see KA for details). t is the age of the source.

KDA added a prescription for calculating the synchrotron radio emission of the lobes to the dynamical model of KA. For this the lobe is split into small volume elements, δV. These are injected into the lobe at time t_i containing a population of relativistic electrons with a power–law energy distribution with exponent p ranging from $\gamma = 1$ to some γ_{max}. Here, γ is the Lorentz factor of the relativistic electrons. This electron distribution is then subject to energy losses due to adiabatic expansion, synchrotron radiation and inverse Compton scattering of the CMB. Since t_i will be different for different volume elements, the resulting energy distribution of the electrons in each δV at time t is a function of the injection time t_i.

The total radio emission of the lobe at a given frequency, ν, is the sum of all the contributions from the volume elements,

$$P_\nu = \int \frac{1}{6\pi} \sigma_T \, c \, u_B \, \frac{\gamma^3}{\nu} n(\gamma) \, \delta V(t) \tag{6.3}$$

where σ_T is the Thomson cross section, u_B is the energy density of the magnetic field and $n(\gamma)$ is the density of relativistic electrons with Lorentz factor γ.

In the model of KDA equation 6.3 becomes,

$$P_\nu = \int_0^t \frac{\sigma_T \, c \, r Q_\circ \, n_\circ}{6\pi \, \nu \, (r+1)} \frac{(2R)^{\frac{2(1-\Gamma_c)}{\Gamma_c}} \gamma^{3-p} \, t_i^{a_1 (p-2)/3}}{\left(t^{-a_1/3} - a_2(t, t_i)\gamma\right)^{2-p}} \left(\frac{t}{t_i}\right)^{-a_1 (1/3+\Gamma_B)} dt_i, \tag{6.4}$$

where $n_\circ$ is the normalisation of the electron energy distribution. r is the ratio of the energy density of the magnetic field and that of all particles at the time of injection, t_i. R is the ratio of the length of the lobe and its width at half the lobe length. The various Γ are the adiabatic indices of the material in the lobe, Γ_c, and the magnetic field, which is assumed to be tangled on small scales, Γ_B. $a_2(t, t_i) = (t^{-a_1/3})/\gamma - (t_i^{-a_1/3})/\gamma_i$ where a_1 is the exponent of the power-law time dependence of the volume elements, i.e. $\delta V \propto t^{a_1}$, which KDA find to be $a_1 = (4+\beta)/[\Gamma_c(5-\beta)]$. Finally, γ_i is the Lorentz factor at t_i of electrons which have a Lorentz factor of γ at the current time, t.

There is no analytical solution for equation 6.4 for general p. However, for $p = 2$ the integral simplifies considerably to give

$$P_\nu = G \frac{p_{lobe}^{7/4}}{s} \left[1 - \left(\frac{t_{min}}{t} \right)^s \right] \tag{6.5}$$

where $s = a_1 \left(\frac{1}{3} + \frac{3\Gamma_B}{4}\right) + \left(\frac{8-7\beta}{20-4\beta}\right)$, and

$$G = \frac{\sigma_T \, r^{3/4} \, (\Gamma_x + 1) \, (2R)^{2/\Gamma_c} \, D_{lobe}^3 \, [ln(\gamma_{i,max}) + \gamma_{i,max}^{-1} - 1]^{-1}}{108 \, \pi \, \nu^{1/2} \, c_1^{(5-\beta)} \, c \, m_e^{1/2} \, (\Gamma_c - 1)^{3/4} \, (k'+1) \, (r+1)^{7/4} \, (5-\beta)^{-2}} \left(\frac{2\pi^2}{e^2 \mu_\circ}\right)^{1/4}, \tag{6.6}$$

where p_{lobe} is the pressure in the lobe at the current time t. a_1 determines $a_3 = 1 - a_1(\Gamma_B + 1/3)$ and $a_4 = 1 - a_1/3$. Γ_x is the adiabatic index of the gas in the source environment. The lobe may contain non-relativistic particles, the ratio of their energy density and that of the relativistic electrons is given by k'. Finally, m_e is the electron mass and $\mu_\circ$ is the magnetic permeability of the vacuum.*

Older parts of the lobe will no longer radiate at the observing frequency ν due to severe radiative losses, so it is not realistic to integrate equation 6.4 over the entire age of the source. t_{min} is the minimum injection time for volume elements to still be

---

*In the derivation of equations 6.4 to 6.6 I have used the results of KA and KDA.

emitting radiation at the observing frequency ν. I assume that the electrons only emit at their critical frequency $\gamma^2(t, t_i)\nu_L(t, t_i)$ where ν_L is the Lamour frequency, and use the condition that $\nu = \gamma^2(t, t_{min})\nu_L(t, t_{min})$ to give an implicit equation for t_{min},

$$\nu = \frac{et^{-(2a_1/3)}}{2\pi m_e} \left\{ \frac{\sqrt{(2X\mu_o)}\, t_{min}^{-(a_1\Gamma_c/2)}\, (t_{min}/t)^{\Gamma_B a_1/2}(3m_e c)^2}{(4\sigma_T)^2 \left[X\, t_{min}^{a_1(\Gamma_B-\Gamma_c)}(t^{a_3} - t_{min}^{a_3})/a_3 + u_c(t^{a_4} - t_{min}^{a_4})/a_4\right]^2} \right\} \qquad (6.7)$$

where $X = (r\, p_{lobe}\, t^{\Gamma_c a_1})/[(r+1)\,(\Gamma_c - 1)]$, u_c is the energy density of the cosmic microwave background, $u_c \propto (1+z)^4$, (see also KDA). There is no analytical solution for t_{min}, but it is possible to numerically find a t_{min}, for any given source age and frequency, that solves equation 6.7 to a high degree of accuracy (i.e. within 1×10^{-4} or less.)

The model calculates all the properties in the sources' frame of reference. This means that the observing frequency and P_ν have to be transformed using the chosen cosmology, see appendix D for details.

6.1.1 Application of the model

The model for an individual radio lobe depends on a number of parameters, some of which are determined from the radio observations. These are the observing frequency, ν, the length of the lobe, D_{lobe}, the aspect ratio of the lobe, R, and the monochromatic radio luminosity, P_ν. The source redshift is taken from archival observations, see section 2.1 and appendices E to G. Another set of parameters are not directly accessible by observations, but their values are either well-constrained in general or are simply set to reasonable values. The adiabatic indices are set to $\Gamma_x = \Gamma_c = 5/3$, assuming that the material in the lobe is mainly non-relativistic. The magnetic field in the lobe is assumed to be tangled on scales much smaller than D_{lobe}, therefore $\Gamma_B = 4/3$. Any particles in the lobe other than the electrons responsible for the emission of synchrotron radiation are neglected, so $k' = 0$. I further assume that the relativistic electrons and the magnetic field are initially, at time t_i, given by their values appropriate for minimum energy conditions (e.g. Longair, 1994). Thus $r = 3/4$ for the chosen slope of the electron energy distribution with $p = 2$. I set the high-energy cut-off of this distribution to $\gamma_{i,max} = 10^{18}$ and $\gamma_{i,min} = 1$. It is clear from equation 6.6 that the exact value of $\gamma_{i,max}$ does not significantly influence the results. Finally, the gaseous atmospheres around powerful radio galaxies imply $1 \leq \beta \leq 2$ and so I set $\beta = 1.5$. This leaves three free model parameters: The current pressure in the lobe, p_{lobe}, the age of the source, t, and the minimum injection time, t_{min}.

D$_{lobe}$, the lobe ratio and the rest frame frequency of the observations are used to determine the constant G (equation 6.6). Although p$_{lobe}$ and t are the principal free parameters of the model, in the fitting process $a_\circ^\beta \rho_\circ$ is used instead of the lobe pressure. This is due to the fact that p$_{lobe}$ and ty (the age of a source in years) are highly anti-correlated, see Table 6.4, and applying the model using these parameters could create a bias in the data. As Table 6.2 shows there is no significant $a_\circ^\beta \rho_\circ$-ty correlation, making these two parameters a good choice for the input parameters for the fitting process. Initial 'guesses' for $a_\circ^\beta \rho_\circ$ and ty are used to calculate the lobe pressure, which depends on the jet length and the lobe ratio.

$$
\begin{aligned}
p_{lobe} &= \frac{18\, c_1^{2-\beta}\, t^{-a_1 \Gamma_c}}{4R^2(\Gamma_x + 1)(5-\beta)^2} \left(\frac{a_\circ^\beta \rho_\circ}{Q_\circ^{(\beta-2)/3}} \right)^{3/(5-\beta)} \qquad (6.8) \\
&= \frac{9 a_\circ^\beta \rho_\circ D_{lobe}^{2-\beta}}{2(\Gamma_c + 1)(5-\beta)^2 R^2 t y^2} \qquad (6.9)
\end{aligned}
$$

The age of a source and its density, $a_\circ^\beta \rho_\circ$, are used to calculate the minimum injection time, t_{min}, (equation 6.7) and the monochromatic luminosity, P_ν, using equation (6.5). This monochromatic luminosity is converted to a specific flux, S$_\nu$ using equation (D.4). Comparing S$_\nu$ with the observed flux it is possible to obtain a χ_ν^2 deviation of the model at frequency ν. This gives three measurements of χ_ν^2 at the three different frequencies. The Numerical Recipes subroutine AMOEBA (Press et al., 1997), is used to find the best estimate for ty and $a_\circ^\beta \rho_\circ$ for a lobe by minimising $\chi^2 = \chi_{\nu_1}^2 + \chi_{\nu_2}^2 + \chi_{\nu_3}^2$.

The jet power, Q$_\circ$, is then calculated from the final values of ty, $a_\circ^\beta \rho_\circ$ and hence p$_{lobe}$,

$$
Q_\circ = \frac{2 p_{lobe} (\Gamma_c + 1)(5-\beta)^2 D_{lobe}^3 R}{9 c_1^{5-\beta} t} \qquad (6.10)
$$

For full details of the above model see KA and KDA.

6.2 Modelling the small sample of 26 sources

The model uses the three flux measurements around 1.4 GHz, 1.6 GHz and 4.8 GHz and their corresponding errors to constrain the free parameters of the model. D$_{lobe}$, is calculated from the observed angle of the source on the sky, and the measured redshift using the chosen cosmology. The lobe ratio is taken from the total intensity maps.

6.2.1 Angle to the line of sight

It is not possible to determine from the radio data whether or not the jets in a given source lie in the plane of the sky or whether the measured length of the lobe is projected. The length of the jet and the lobe ratio are both affected by this angle dependence, however it is the jet–length that is most affected.

To test how sensitive the model is to a change of the viewing angle, each source is modelled with a number of viewing angles ranging from 10° to 90° to the line–of–sight. I found that in most cases the source is most probably angled around 57.3° to the line–of–sight, which is the average angle expected for a sample of randomly oriented sources. In these cases there is no significant difference in the results for any orientation unless the source is angled to less than 23° to the line–of–sight. These very small angles produced highly unlikely results, i.e. extremely large sizes, improbable jet–powers and/or extremely high densities. Sources which are already large, e.g. 3C 46, are unlikely to be orientated at angles much less than 57° as this makes the source larger than a few Mpc across. In several cases when the sources became large (small orientation angle) the source age was not consistent with the source size, i.e. less than 10^6 years for sources of order of a Mpc across.

There are a few sources that all angles seemed equally probable (e.g. 6C 0943+39 and 3C 280), but these are in the minority. To assume a different angle for each source is impractical, especially in section 6.4 where 211 sources taken from the combined 3CRR, 6CE and 7C III samples are modelled. The model does not directly depend on the line–of–sight so it is not possible to determine an orientation angle from the fitting procedure.

For a sample of randomly orientated sources the most likely orientation is 57.3° to the line–of–sight and only a few of the sources will be orientated at angles smaller than 23°. Thus these sources will not have a large effect on the statistics. In all the following sections the results have been calculated using an orientation angle of 57.3° for all sources.

6.3 Results

The KDA model provides an estimate for the jet-power, density, lobe pressure and source age for each lobe in the small sample. However, in the next section I only consider how the density parameter, $a_\circ^\beta \rho_\circ$, relates to changes in depolarisation and variations in the rotation measure. How the model parameters are affected by changes in the 'fundamental' parameters (i.e. redshift, radio-luminosity and source size) is presented in detail in section 6.4 using the combined 3CRR, 6CE and 7C III samples. By using a large sample any results found will be more significant than with only 26 sources. However, the large samples do not have depolarisation and rotation measure information for each source. Therefore I use my smaller sample to determine if depolarisation and density are related.

6.3.1 Comparing $a_o^\beta \rho_o$ with DM$_z$ and σ_{RM_z}

In section 4.3.2 I found that the Burn corrected depolarisation measure, DM$_z$, correlated strongly with redshift. By analysing the minimum energy magnetic field asymmetries in section 4.4.2.3 I found evidence that the observed depolarisation of a source was unaffected by changes in the density of the environment. The KDA model gives an estimate of the gas density around each lobe which can be compared with the source depolarisation.

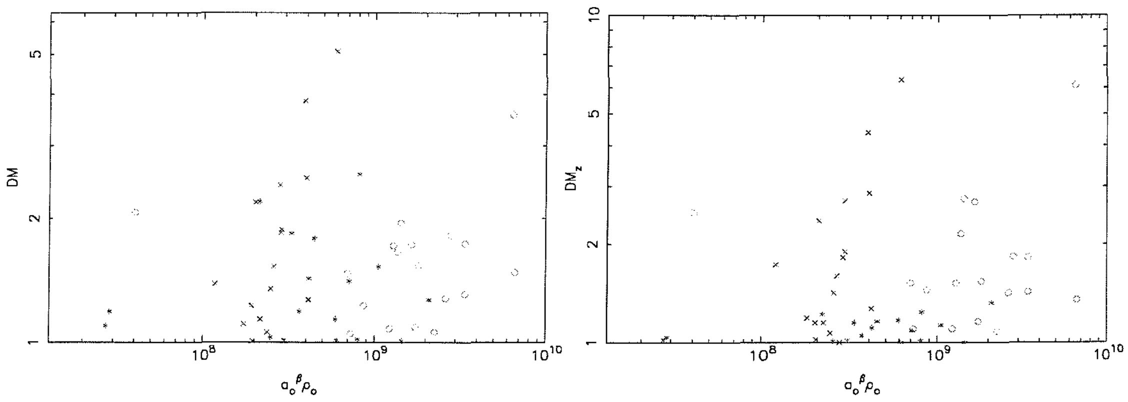

Figure 6.1: (a - left) Unshifted depolarisation against $a_o^\beta \rho_o$ and (b - right) depolarisation shifted using Burn's law. Symbols are as in Figure 4.1.

Figure 6.1 shows that there is no relationship between depolarisation and $a_o^\beta \rho_o$, independent of whether I use the observed depolarisation (Figure 6.1(a)) or I use the shifted depolarisation from section 3.3 (Figure 6.1(b)). Figure 6.2 shows that there is also no trend between the variations in the RM in the sources' frame of reference, σ_{RM_z}, and $a_o^\beta \rho_o$.

Figure 6.3 shows a weak correlation between radio luminosity and $a_o^\beta \rho_o$, but no corresponding correlation with redshift. The relationships between, z, P_{151} and $a_o^\beta \rho_o$ are discussed in detail in section 6.4.6 using the large sample. However, it is worth noting that in the small sample there is no indication of any evolution of the environment density with redshift. Thus the evolution of depolarisation with redshift cannot be attributed to changes in density. In section 4.3.2 I also found a strong P_{151}-DM$_z$ correlation that was comparable to the z-DM$_z$ correlation. As the Partial Spearman results show, at any given radio-luminosity there is still no

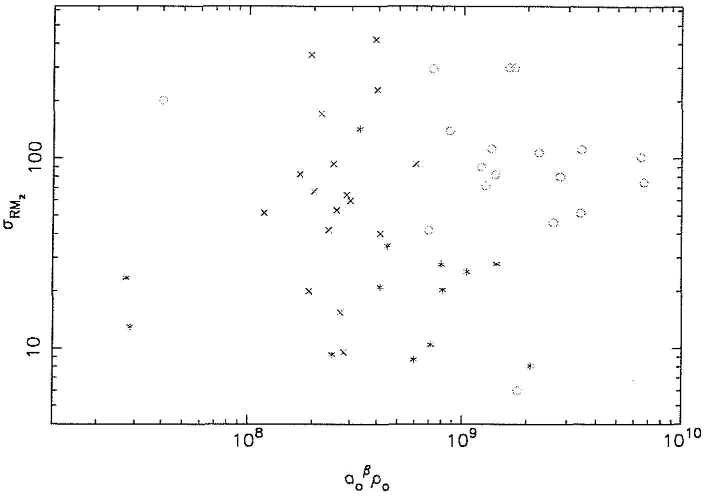

Figure 6.2: σ_{RM_z} against $a_\text{o}^\beta \rho_\text{o}$. Symbols are as in Figure 4.1.

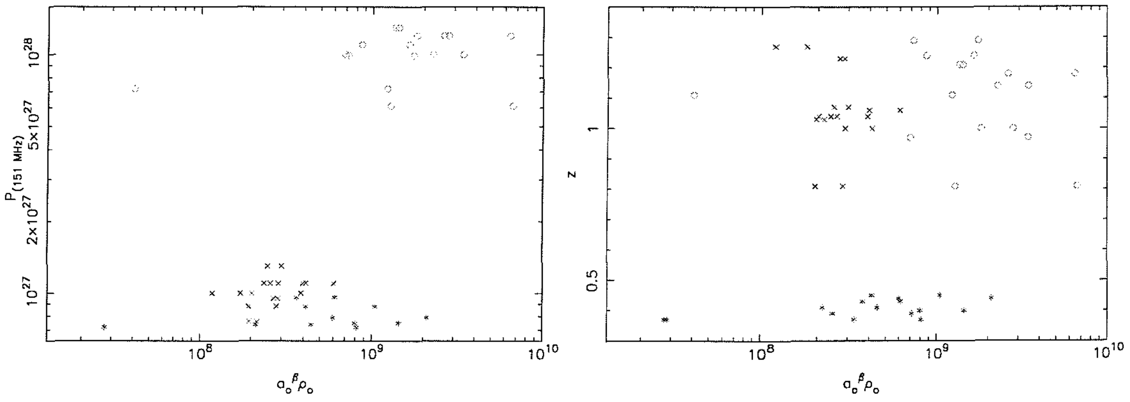

Figure 6.3: (a - left) Radio-luminosity against $a_\text{o}^\beta \rho_\text{o}$ and (b - right) redshift against $a_\text{o}^\beta \rho_\text{o}$. Symbols are as in Figure 4.1.

significant DM$_z$-$a_\text{o}^\beta \rho_\text{o}$ correlation.

$$\begin{array}{rclr} r_{a_\text{o}^\beta \rho_\text{o}\ DM_z,\ P_{151}} & = & -0.119 & D = 0.83 \\ r_{a_\text{o}^\beta \rho_\text{o}\ P_{151},\ DM_z} & = & 0.526 & D = 4.05 \\ r_{P_{151}\ DM_z,\ a_\text{o}^\beta \rho_\text{o}} & = & 0.504 & D = 3.84 \end{array}$$

At any given density the P$_{151}$-DM$_z$ correlation still exists, thus any changes in DM$_z$ with either z or P$_{151}$ are independent of changes in the density of the source environment. The lack of correlation between $a_\text{o}^\beta \rho_\text{o}$ and the observed polarisation parameters gives further evidence that depolarisation and σ_{RM_z} should *not* be used as tracers of the density of the environment (e.g Burn, 1966; Garrington & Conway, 1991; Blundell et al., 1999) and should only be used as a measure for the disorder in the environment.

6.3.2 Minimum energy, $a_\circ^\beta \rho_\circ$ and p_{lobe}

Figure 6.4(a) shows that there is a tight correlation between the ratio of pressures in the lobes of a given source and the minimum energy magnetic field ratio. The only notable exception being 3C 16, which has a high minimum energy magnetic field ratio, but a relatively low ratio of lobe pressures. This agrees with the suggestion that 3C 16 is in the process of switching back on (Harvanck & Hardcastle, 1998, also see section 4.4.2.2). Figure 6.4(a) demonstrates that the simple minimum energy magnetic field model can be used to give an estimate of the lobe pressure. For the sources in the large sample, discussed in section 6.4, there is no information on the individual lobes of each source so it is impossible to estimate the minimum energy magnetic field for individual lobes. However, as the minimum energy magnetic field and p_{lobe} are tightly correlated, I can be confident that the results using the KDA model give a good estimation of the magnetic field in a source.

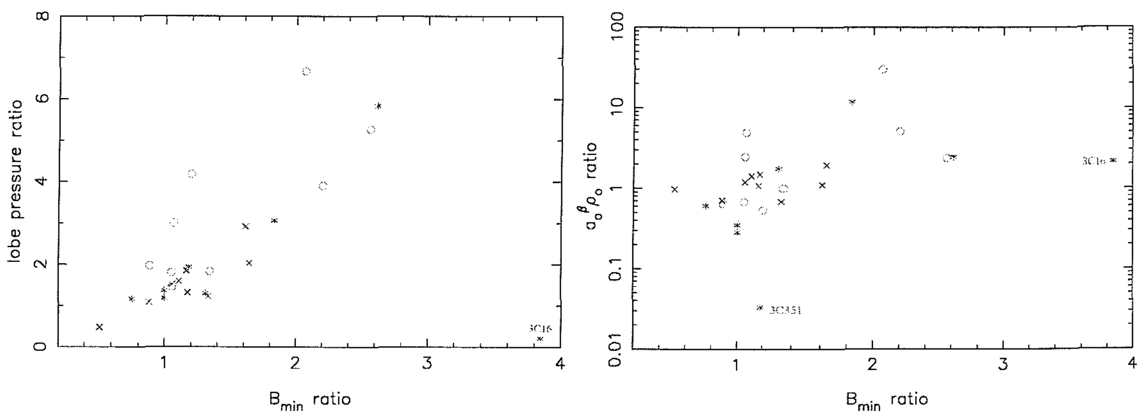

Figure 6.4: (a - left) Ratio of minimum energy magnetic field against the ratio of lobe pressures and (b - right) against the ratio in $a_\circ^\beta \rho_\circ$. Symbols are as in Figure 4.1.

Figure 6.4(b) shows that there is a weaker correlation between the density ratio and the minimum energy magnetic field ratio which corresponds to a significance of ~99.5%. By removing 3C 351 and 3C 16 the correlation becomes >99.9% significant. In section 4.4.1 I noted that 3C 351 has a very distorted northern lobe, significantly extending to the west of the double hotspots. This could be attributed to a very low density on the western side of the north lobe, allowing the source to propagate westward. The southern lobe is much more constrained, implying a larger density, which could be the cause of the large ratio of densities between the two lobes. The fact that the minimum energy magnetic field ratio and $a_\circ^\beta \rho_\circ$ ratio are correlated suggests that it is the difference in the environment of the two lobes of a source that is causing the difference in the minimum energy magnetic field and *not* beaming as suggested in section 4.4.2.3.

6.4 Modelling the complete 3CRR, 6CE and 7C III FRII samples

6.4.1 Observations

The large sample contains a sample of 211 FRII sources taken from the complete 3CRR, 6CE and 7C III samples, see Figure 6.5. Only sources larger than 10 kpc are included in the analysis as below this limit the model may not be applicable (Alexander, 2000). For consistency all sources smaller than 10 kpc are excluded using the stated cosmology.

Appendices E to G give the archival redshift, size, flux measurements, lobe ratio and their associated references for each source used in the analysis. In section 6.2 I stated that the model uses three flux measurements and their corresponding errors to constrain the free parameters. I apply the model to the flux measurements at 178 MHz[†], 365 MHz and 1400 MHz for the 3CRR sample; 151 MHz, 365 MHz and 1400 MHz for the 6CE sample and 151 MHz, 327 MHz and 1490 MHz for the 7C III sample. α_{low} is defined as the spectral index between the lower frequency and 365 MHz and α_{high} is defined as the spectral index between 365 MHz and 1400 MHz[‡].

In section 6.1 I use $p = 2$ in the determination of the monochromatic radio luminosity, P_ν. This means that only sources with a spectral index, $\alpha_{boundary} < -0.5$ (including errors) can be accurately modelled where $\alpha_{boundary}$ is determined by the choice of p, i.e. $p = -2\alpha+1$ (Longair, 1994). For this reason 3C 382 and 6C 0922+36 are excluded, since they have $\alpha_{high} = -0.22$ and $\alpha_{high} = -0.30$ respectively, which even when the errors are accounted for have $\alpha_{high} > \alpha_{boundary}$.

6.4.2 Application of the model to the combined sample

The source size, D_{source}, is calculated from the observed angle of the source on the sky, and the source redshift. The lobe ratio for each lobe ($R_{\rm lobe1}$ and $R_{\rm lobe2}$) is taken from high resolution maps, where they exist, in the literature (see appendices E to G). In the few cases where there are no high resolution maps, particularly the faint 7C III sources, the lobe ratio is set to be the average sample lobe ratio, using the sample that the source is taken from.

[†] The different lower frequency of the 3CRR sample is simply due to the fact that it is defined at 178 MHz instead of 151 MHz.

[‡] For the 7C III sample I use 327 MHz and 1490 MHz instead of 365 MHz and 1490 MHz. This is due to the fact that is only at 327 MHz and 1490 MHz that there is flux information for each source in the sample.

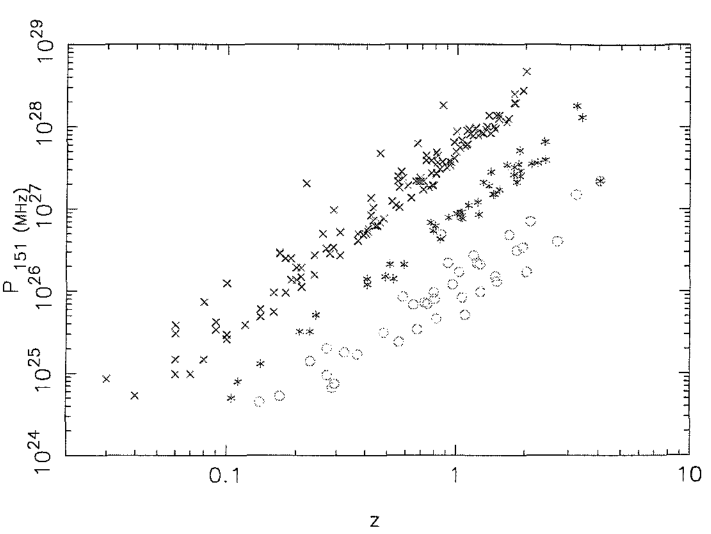

Figure 6.5: Redshift against the radio luminosity at 151 MHz. The 3CRR sample is represented by '×', the 6CE sample by 'o' and the 7C III sample by '*'. A spectral index of -0.75 is used to shift the 3CRR luminosity data at 178 MHz to 151 MHz.

For every source the flux of the lobe, at each frequency, is taken to be half the total flux. This a simplification, but there are no flux measurements for individual lobes, at all 3 frequencies, for each of the 211 sources in the literature. For this reason the lobe length is also taken to be $D_{lobe} = D_{source}/2$ and the lobe ratio is averaged over the source i.e. $R_{\mathrm{average}} = (R_{\mathrm{lobe1}} + R_{\mathrm{lobe2}})/2$. This ensured that the results are not biased towards sources that are well observed and have high resolution maps (e.g. the majority of the 3CRR sample). This is particularly important when dealing with the sources of the 7C III sample for which very little archival information exists.

6.4.3 Fundamental Parameters

In the following sections I investigate the relationship of the model properties of my sources with the 'fundamental' properties redshift, z, radio luminosity at 151 MHz, P_{151}, and physical size, D_{lobe}. Before I can understand how the model parameters evolve with the fundamental properties I need to understand the relationship between the fundamental properties. This is similar to the analysis in section 4.2. Table 6.1 contains the associated Spearman Rank results of the fundamental parameters. As expected, I find redshift and radio luminosity to be highly correlated (see Figure 6.5), to a significance of $> 99.99\%$, but this is simply due to the flux limits of the samples and cannot be avoided. Using the statistical techniques described in chapter 4.1 this correlation can be isolated from any other correlations.

By using the Partial Spearman Rank test I find that even with 3 large complete

Parameters	rs value	t value
z P_{151}	0.69302	13.93
z D_{lobe}	-0.40682	6.45
P_{151} D_{lobe}	-0.29855	4.53

Table 6.1: Spearman Rank values for z, P_{151} and D_{lobe} in the combined samples.

samples there is no significant P_{151}-D_{lobe} correlation and that the size-redshift anti-correlation is weak when it is compared to the strength of the redshift - radio luminosity correlation.

$$r_{z\ D_{lobe},\ P_{151}} = -0.288 \qquad D = 4.27$$
$$r_{z\ P_{151},\ D_{lobe}} = 0.655 \qquad D = 11.27$$
$$r_{P_{151}\ D_{lobe},\ z} = -0.019 \qquad D = 0.27$$

This is also evident in Figure 6.6(a), the weak P_{151}-D_{lobe} anti-correlation is almost indistinguishable from the scatter. This confirms that even with such a large sample of sources there is only a weak relationship between the low frequency radio-luminosity and lobe size and agrees with the findings of Barthel & Miley (1988).[§]

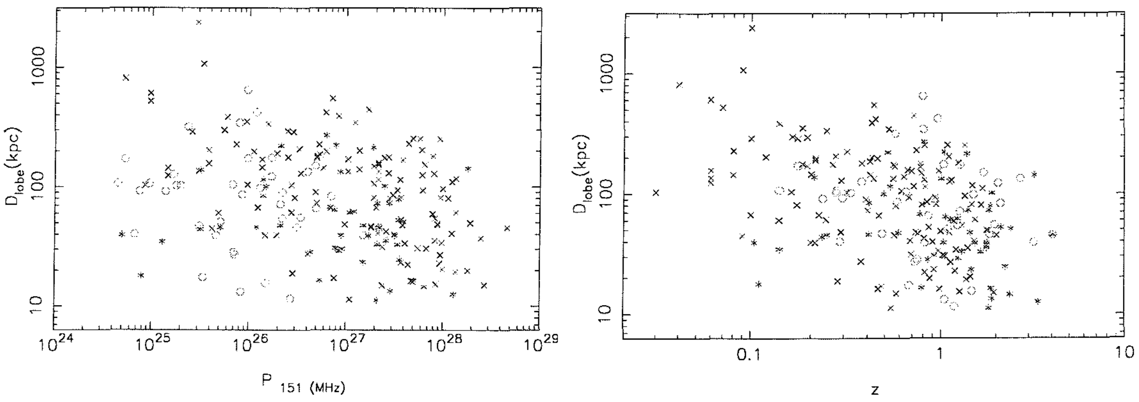

Figure 6.6: (a - left) Source size against radio-luminosity and (b - right) against redshift. Symbols are as in Figure 6.5.

As already noted, redshift and lobe size are only weakly related, see Figure 6.6(b). The weak correlation can be see in Table 6.1 and also in the Partial Spearman Rank results above. However the z-D_{lobe} correlation is much weaker than the z-P_{151} correlation and will have little effect on the model results.

[§] The P_{151}-D_{lobe} anti-correlation is discussed in detail in section 4.2.

6.4.4 Source age, ty

An important test of the model is to determine if the age of a lobe, ty, correlates with its size, D_{lobe}. Clearly larger sources should be older. As Table 6.2 and Figure 6.7 demonstrate, D_{lobe} and ty correlate to a high degree, > 99.99% significant. The PCA results shown in Table 6.3 are dominated by this strong correlation and do not show any other significant trends. A strong D_{lobe}-ty correlation is expected from the model, but it is the scatter caused by redshift and radio-luminosity that is important in determining how the source environment affects its age.

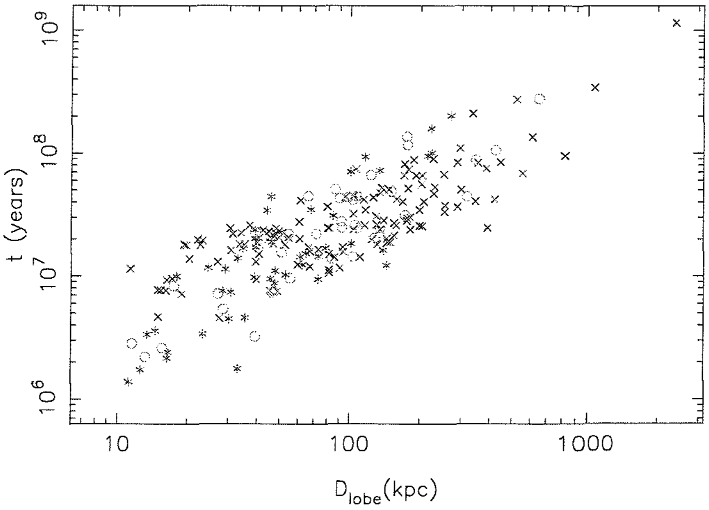

Figure 6.7: Source age against source size. Symbols are as in Figure 6.5.

Parameters	rs value	t value
ty D_{lobe}	0.80452	19.63
ty z	-0.40583	6.43
ty P_{151}	-0.29238	4.43
ty $a_o^{\beta}\rho_o$	0.01446	0.21
ty α_{low}	-0.24527	3.67

Table 6.2: Spearman Rank values for the age of a lobe

Table 6.2 shows an anti-correlation of the source age with redshift and also a slightly weaker anti-correlation with radio-luminosity. Figure 6.8(a) shows that the P_{151}-ty correlation is weak. The trend with redshift could be explained by the inclusion of low-redshift giants. In section 6.4.3 I have shown that there is a weak z-D_{lobe} anti-correlation which combined with the strong evolution of source size with age could cause the apparent z-ty anti-correlation seen in Figure 6.8(b).

The Partial Spearman Rank analysis shown below demonstrates, that for any given radio-size the z-ty correlation is barely significant. Interestingly at any given

Parameter	1	2	3	4
z	0.378	0.575	0.724	0.054
P_{151}	0.312	0.658	-0.685	0.001
D_{lobe}	-0.625	0.318	0.021	0.713
ty	-0.608	0.368	0.078	-0.699
Eigenvalue	53.09%	30.96 %	13.70%	2.25 %

Table 6.3: Eigenvectors and Eigenvalues for the age of the lobe

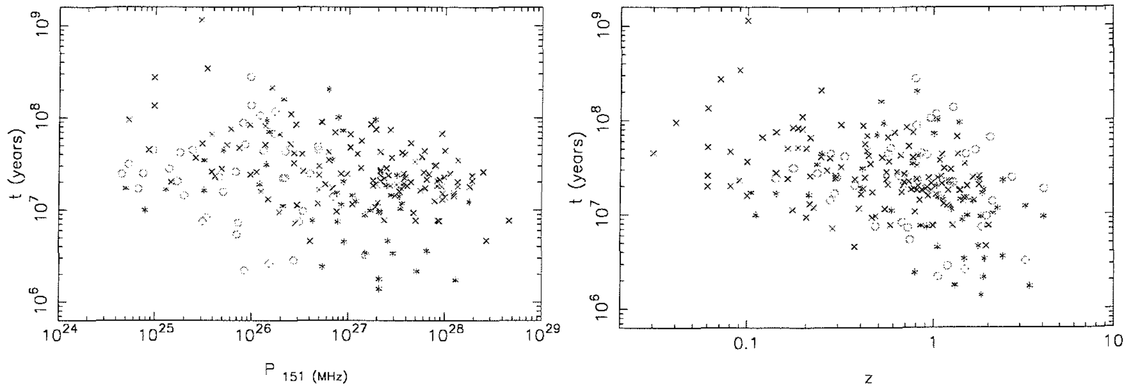

Figure 6.8: (a - left) Source age against radio-luminosity and (b - right) against redshift. Symbols are as in Figure 6.5.

source age, the z-D_{lobe} also becomes barely significant. This suggests that the observed z-D_{lobe} correlation (and hence also the z-ty correlation) is simply a by product of the Malmquist bias arising from the flux-limited nature of the samples. Only by observing at fainter flux-limits, e.g TOOT (Hill & Rawlings, 2003), can this observational bias be removed.

$$r_{z\ D_{lobe},\ ty} = -0.148 \qquad D = 2.15$$
$$r_{z\ ty,\ D_{lobe}} = -0.145 \qquad D = 2.10$$
$$r_{D_{lobe}\ ty,\ z} = 0.766 \qquad D = 14.57$$

It is also worth noting that when I use Partial Spearman rank to determine the relationship between redshift, radio-luminosity and age the P_{151}-ty anti-correlation vanishes at a fixed source age.

$$r_{z\ ty,\ P_{151}} = -0.295 \qquad D = 4.38$$
$$r_{z\ P_{151},\ ty} = 0.657 \qquad D = 11.36$$
$$r_{P_{151}\ ty,\ z} = -0.017 \qquad D = 0.24$$

This suggests that both the z-ty and P_{151}-ty anti-correlations are due to the strong D_{lobe}-ty and z-P_{151} correlations. Sources at higher redshifts and/or higher radio-luminosities are not younger than their lower redshifts/lower radio-luminosity cousins.

Table 6.2 also shows that there is a weak anti-correlation of the low-frequency spectral index with the age of the source. However, I would expect α_{high} to show the stronger correlation over α_{low} due to spectral ageing. Although Table 6.2 shows that there is a weak anti-correlation, Figure 6.9(a) indicates that the α_{low}-ty anti-correlation is insignificant. Figure 6.9(b) also shows that there is no α_{high}-ty anti-correlation. Thus, between 151 MHz and 1400 MHz spectral ageing appears to be insignificant.

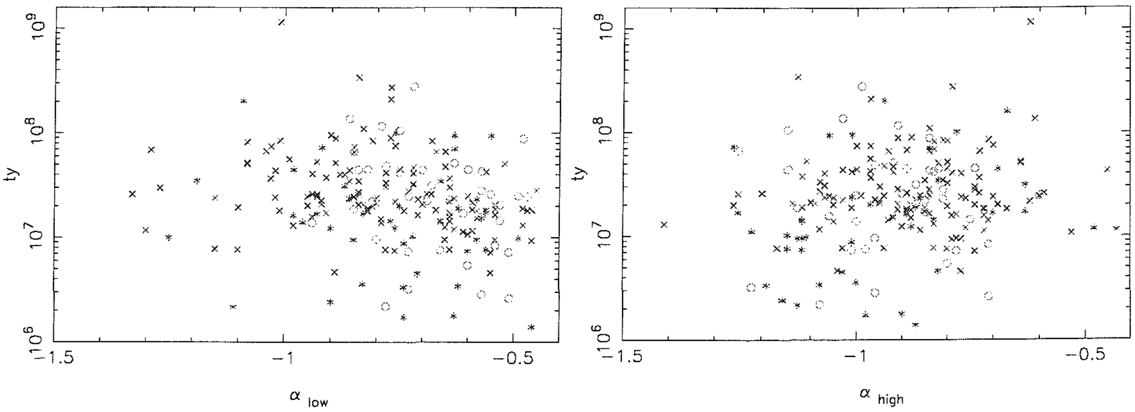

Figure 6.9: (a - left) Source age against α_{low} and (b - right) against α_{high}. Symbols are as in Figure 6.5.

6.4.5 Lobe pressure, p_{lobe}

Table 6.4 shows that there is a strong D_{lobe}-p_{lobe} anti-correlation, at a significance exceeding 99.99%. This is not surprising as a small source will have a high initial lobe pressure, driving the source to expand which in turn will cause the lobe pressure to fall. Table 6.4 also shows a somewhat weaker ty-p_{lobe} anti-correlation, but this is simply due to the strong D_{lobe}-ty correlation from section 6.4.4 and the strong D_{lobe}-p_{lobe} anti-correlation already discussed.

Parameters	rs value	t value
p_{lobe} z	0.70061	14.23
p_{lobe} P_{151}	0.75192	16.53
p_{lobe} D_{lobe}	-0.81074	-20.07
p_{lobe} ty	-0.64674	-12.29
p_{lobe} $a_o^\beta \rho_o$	0.67819	13.37
p_{lobe} α_{high}	-0.33934	-5.23

Table 6.4: Spearman Rank values for the lobe pressure.

Table 6.4 also reveals a strong P_{151}-p_{lobe} correlation and a slightly weaker p_{lobe}-z correlation. Both of these strong correlations can be seen in Figures 6.10(a) and 6.10(b) respectively. This suggests that the lobe pressure is dependent on both the redshift and radio-luminosity of a source. By using Partial Spearman Rank on p_{lobe}, P_{151} and z it is possible to disentangle the relationship with lobe pressure.

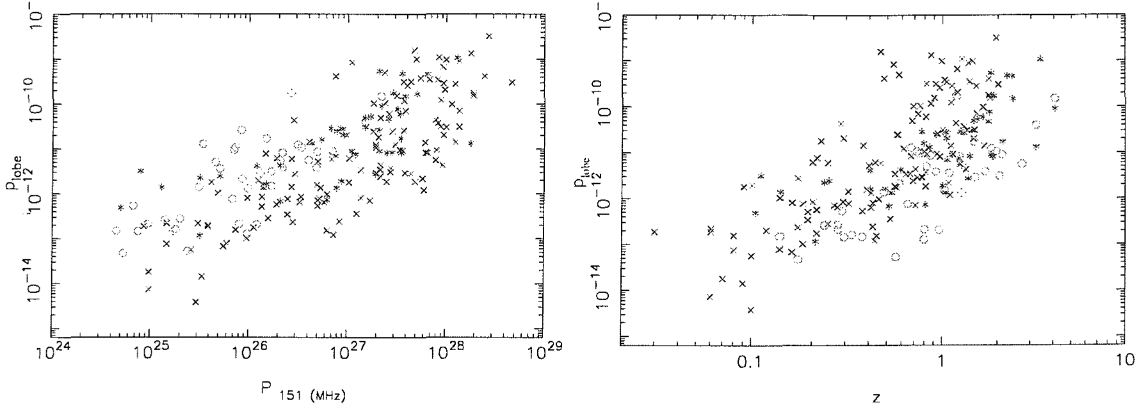

Figure 6.10: (a - left) Lobe pressure against radio-luminosity and (b - right) against redshift. Symbols are as in Figure 6.5.

$$\begin{array}{rcll}
r_{z\,p_{lobe},\,P_{151}} & = & 0.378 & D = 5.72 \\
r_{z\,P_{151},\,p_{lobe}} & = & 0.353 & D = 5.31 \\
r_{P_{151}\,p_{lobe},\,z} & = & 0.518 & D = 8.27
\end{array}$$

I find that neither the p_{lobe}-z nor the P_{151}-p_{lobe} correlation vanish at any given radio-luminosity or redshift, respectively. However, it is worth noting that in both the Spearman Rank results (Table 6.4) and the Partial Spearman Rank results the P_{151}-p_{lobe} correlation is always the stronger correlation.

The Partial Spearman Rank results below show that at any given radio-size, the redshift - lobe pressure correlation still exists and is not due to any other independent correlation with the fundamental parameters. This suggests that although the P_{151}-p_{lobe} correlation is stronger than the z-p_{lobe} correlation, the z-p_{lobe} correlation is significant and indicates that there is some evolution in the lobe pressure of a source with redshift.

$$\begin{array}{rcll}
r_{z\,D_{lobe},\,p_{lobe}} & = & 0.386 & D = 5.86 \\
r_{z\,p_{lobe},\,D_{lobe}} & = & 0.693 & D = 12.28 \\
r_{D_{lobe}\,p_{lobe},\,z} & = & -0.807 & D = 16.09
\end{array}$$

The result is consistent with Bremer et al. (1992) who find that the pressure around $z \sim 1$ radio-loud quasars is an order of magnitude higher than the pressures around a lower luminosity set of quasars at $z \sim 0.3$. Unfortunately the study by Bremer et al. (1992) cannot determine whether it is the redshift or the radio-luminosity of the quasars that is connected to the change in the lobe pressure.

The PCA results in Table 6.5 show that the first eigenvector holds 48.2% of the variation in the data. Suprisingly I find that this eigenvector is dominated by the P_{151}-p_{lobe} and z-p_{lobe} correlations, with D_{lobe}-p_{lobe} the weakest. In the second eigenvector, only the P_{151}-p_{lobe} correlation does not reverse. However, it is the D_{lobe}-p_{lobe} *correlation* that dominates this eigen-vector. The PCA results indicate that the P_{151}-p_{lobe} correlation is the dominant correlation and that the z-p_{lobe} is not highly significant.

Parameter	1	2	3	4
z	0.518	-0.182	0.716	-0.431
P_{151}	0.587	0.322	0.100	0.736
D_{lobe}	-0.347	0.845	0.380	-0.144
p_{lobe}	0.516	0.386	-0.577	-0.501
Eigenvalue	48.2%	22.9%	18.1%	10.8 %

Table 6.5: Eigenvectors and Eigenvalues for the lobe pressure

The complicated relationship between P_{151}, p_{lobe} and D_{lobe} is revealed by using the Partial Spearman Rank statistic. I find that the P_{151}-p_{lobe} correlation is almost as significant as the D_{lobe}-p_{lobe} anti-correlation. The fact that both relationships are almost equally significant means that PCA is unable to distinguish between the two separate relationships.

$$\begin{aligned} r_{P_{151}\,D_{lobe},\,p_{lobe}} &= 0.805 & D &= 16.06 \\ r_{P_{151}\,p_{lobe},\,D_{lobe}} &= 0.912 & D &= 22.22 \\ r_{D_{lobe}\,p_{lobe},\,P_{151}} &= -0.931 & D &= 24.08 \end{aligned}$$

Using the minimum energy magnetic field argument or the KDA model it is possible to show that the density of the lobe environment directly influences the lobe pressure of a source (e.g Longair, 1994). It is not surprising then that I find p_{lobe} and $a_o^{\beta}\rho_o$ to be correlated, see Table 6.4. The KDA model results demonstrate that by deriving the pressure in a lobe, we can obtain an accurate estimate of the gas density in the surroundings of a lobe.

Interestingly Table 6.4 shows a weak anti-correlation between α_{high} and p_{lobe} , but no corresponding relationship with α_{low}. In section 6.3.2 I stated that a stronger magnetic field should cause stronger radiative losses in a source and would lead to a steeper spectral index. This explains the weak α_{high}-p_{lobe} anti-correlation seen in Table 6.4. The fact that I do not find any relationship of α_{low} with p_{lobe} indicates a lower level of radiative losses between 151 MHz and 365 MHz.

6.4.6 Density of the source environment, $a_o^\beta \rho_o$

In section 6.3.1 I found that in the small sample of 26 sources there was a weak P_{151}-$a_o^\beta \rho_o$ correlation and no significant trend with redshift. Table 6.6 demonstrates that with the large sample containing 211 sources I find a much stronger P_{151}-$a_o^\beta \rho_o$ correlation (see Figure 6.5(a)) and a weak z-$a_o^\beta \rho_o$ correlation (see Figure 6.5(b)).

Parameters	rs value	t value
$a_o^\beta \rho_o$ z	0.47835	7.89
$a_o^\beta \rho_o$ P_{151}	0.66294	12.83
$a_o^\beta \rho_o$ D_{lobe}	-0.33283	-5.11
$a_o^\beta \rho_o$ α_{high}	-0.31872	-4.87

Table 6.6: Spearman Rank values for $a_o^\beta \rho_o$

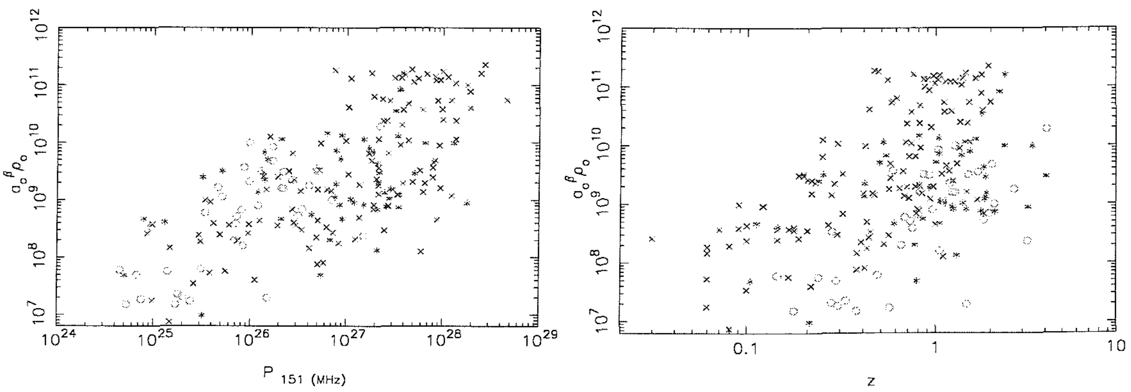

Figure 6.11: (a - left) Source density against radio-luminosity and (b- right) against redshift. Symbols are as in Figure 6.5.

However, as the Partial Spearman Rank results below show, the z-$a_o^\beta \rho_o$ correlation vanishes at any given radio-luminosity. This demonstrates that the apparent correlation of density with redshift is simply due to the strong z-P_{151} correlation and the independent $a_o^\beta \rho_o$-P_{151} correlation present in the samples.

$$r_{z\ a_o^\beta \rho_o,\ P_{151}} = 0.035 \qquad D = 0.51$$

$$r_{z\ P_{151},\ a_o^\beta \rho_o} = 0.572 \qquad D = 9.38$$

$$r_{P_{151}\ a_o^\beta \rho_o,\ z} = 0.524 \qquad D = 8.39$$

The PCA results in Table 6.7 shows only a weak z-$a_o^\beta \rho_o$ correlation which reverses in the second eigenvector. This adds further evidence to the lack of any significant evolution of the source density with redshift. The P_{151}-$a_o^\beta \rho_o$ correlation means that a more powerful source resides in a denser atmosphere. By comparing sources with a range of radio-luminosities, any bias with respect to density of the source environment in a sample is effectively removed. However, studies which only select

Parameter	1	2	3	4
z	0.515	-0.213	0.677	-0.481
P_{151}	0.587	0.349	0.168	0.711
D_{lobe}	-0.372	0.813	0.406	-0.187
$a_o^\beta \rho_o$	0.501	0.415	-0.590	-0.478
Eigenvalue	47.2%	22.5%	19.6%	10.7 %

Table 6.7: Eigenvectors and Eigenvalues for $a_o^\beta \rho_o$

radio sources with a narrow range of radio luminosities (e.g. Pedelty et al., 1989) may be affected by the P_{151}-$a_o^\beta \rho_o$ correlation.

Hardcastle & Worrall (2000), Prestage & Peacock (1988) and Longair & Seldner (1979) found that low-z (hence low radio-luminosity) FRII sources do not live in rich environments. Yates, Miller & Peacock (1989); Crawford & Fabian (1989) and also Yee & Green (1987) find that the most powerful radio-galaxies inhabit rich environments, generally rich clusters. This is consistent with my results presented here. However, it is worth noting that all of the observational studies suffer from the redshift-radio luminosity degeneracy. Thus it is hard to determine whether the density of the source environment changes with redshift or radio-luminosity. A recent study by Blundell et al. (1999) found that when they modelled the radio-luminosity, size, redshift and spectral index plane of the 3CRR, 6C and 7C sample their models did not require any evolution of the source density with redshift to match the observations. This may indicate that any evolution of density with redshift is relatively unimportant.

Table 6.6 also shows that there is a weak anti-correlation of density with α_{high}. The Partial Spearman Rank results between α_{high}, $a_o^\beta \rho_o$ and p_{lobe} below, demonstrate that the apparent $a_o^\beta \rho_o$-α_{high} correlation vanishes at any given lobe pressure and is simply due to the $a_o^\beta \rho_o$-p_{lobe} correlation coupled with the p_{lobe}-α_{high} anti-correlation. This proves that the spectral index of a source is insensitive to direct changes in the environment. However, since density and lobe pressure are correlated, any change in the source density is reflected in a change in the lobe pressure and hence α_{high}.

$$r_{\alpha_{high}\ a_o^\beta \rho_o,\ p_{lobe}} = -0.128 \qquad D = 1.86$$

$$r_{\alpha_{high}\ p_{lobe},\ a_o^\beta \rho_o} = -0.177 \qquad D = 2.58$$

$$r_{p_{lobe}\ a_o^\beta \rho_o,\ \alpha_{high}} = 0.638 \qquad D = 10.92$$

6.4.7 Jet power, Q_o

Figure 6.12(a) shows that jet power, Q_o, and radio-luminosity are highly correlated, with a significance exceeding 99.99% (see Table 6.8). This is expected from the model as it predicts that the more luminous sources have a stronger jet driving them. However, the KDA model does not predict any relationship between jet-power and redshift. Table 6.8 shows that there is a strong correlation of jet-power with redshift. This strong correlation is evident in Figure 6.12(b). The PCA results in Table 6.9 are dominated by the Q_o-P_{151} correlation which only reverses in the final eigenvector. Conversely the correlation with redshift reverses in the second eigenvector and shows a much weaker correlation in comparison to the Q_o-P_{151} correlation. There is no significant trend with the size of the lobe.

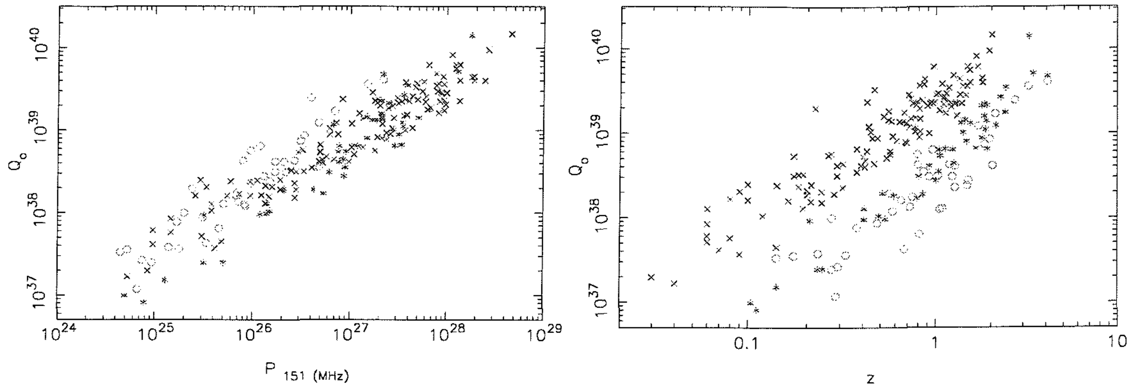

Figure 6.12: (a - left) Jet power against radio-luminosity and (b - right) against redshift. Symbols are as in Figure 6.5.

Parameters	rs value	t value
Q_o p_{lobe}	0.64330	12.18
Q_o D_{lobe}	-0.14354	-2.10
Q_o z	0.70195	14.28
Q_o P_{151}	0.92486	35.24
Q_o α_{high}	-0.30324	-4.61

Table 6.8: Spearman Rank values for the jet power

Parameter	1	2	3	4
z	0.501	0.156	0.829	0.912
P_{151}	0.578	-0.227	-0.455	0.638
D_{lobe}	-0.222	-0.927	0.291	0.079
Q_o	0.604	-0.254	-0.146	-0.741
Eigenvalue	58.3%	24.3 %	14.0%	3.4%

Table 6.9: Eigenvectors and Eigenvalues for jet power

By using the Partial Spearman Rank test, it is possible to disentangle the relationship between redshift and radio-luminosity and jet-power.

$$\begin{aligned} r_{z\,Q_\circ,\,P_{151}} &= 0.223 & D &= 3.26 \\ r_{z\,P_{151},\,Q_\circ} &= 0.162 & D &= 2.35 \\ r_{P_{151}\,Q_\circ,\,z} &= 0.854 & D &= 18.32 \end{aligned}$$

It is obvious that although the z-Q$_\circ$ correlation is significantly weaker than the P$_{151}$-Q$_\circ$ correlation it does not completely vanish at any given radio-luminosity. FRII radio sources are powered by jets created in the vicinity of the most massive black holes known in the universe. It is commonly assumed that the mass of the black hole determines the jet power. Lacy et al. (2001) find that for their sample of sources taken in the redshift range $0.3 < z < 0.5$ the black hole mass - 5 GHz radio luminosity relation can be described by $L_{5\,\mathrm{GHz}} \propto M_{\mathrm{bh}}^{1.9\pm0.2}$ whereas Dunlop et al. (2003) find $L_{5\,\mathrm{GHz}} \propto M_{\mathrm{bh}}^{2.5}$ between $0.1 < z < 0.25$. A recent study by McLure et al. (2004), at a narrow range of redshift ($z \approx 0.5$), find that to 3σ there is a trend between the low frequency luminosity, $L_{151\mathrm{MHz}}$, and black-hole mass. The fact that I also find a correlation between Q$_\circ$ and z suggests that the mass of the black-hole powering the radio sources changes with redshift as well as with the low-frequency radio-luminosity. This is evidence that the mass of a black-hole powering FRII sources is not constant with redshift. The difference in the findings of Lacy et al. (2001) and Dunlop et al. (2003) may be attributed to the slight difference in the cosmological epoch of their samples.

Table 6.8 shows that there is a weak α_{high}-Q$_\circ$ anti-correlation but, as the Partial Spearman Rank results show, this is simply due to the independent Q$_\circ$-p$_{lobe}$ correlation and p$_{lobe}$-α_{high} anti-correlation.

$$\begin{aligned} r_{p_{lobe}\,Q_\circ,\,\alpha_{high}} &= 0.603 & D &= 10.04 \\ r_{p_{lobe}\,\alpha_{high},\,Q_\circ} &= -0.198 & D &= 2.88 \\ r_{\alpha_{high}\,Q_\circ,\,p_{lobe}} &= -0.118 & D &= 1.71 \end{aligned}$$

6.5 Conclusions

I find no trend of the polarisation parameters DM$_z$ and σ_{RM_z} with the density of the lobe environment, $a_\circ^\beta \rho_\circ$. This provides further evidence that the polarisation trends do not map changes in the density of the source environment, but are indicators of the degree of disorder in the structure of the magnetic field in these environments evolving with redshift.

It was suggested in chapter 4 that many of the sources from the small sample show evidence of beaming. However, the density estimate from the KDA model disagreed with this finding, providing evidence instead that it is changes in the lobe environment that causes the observed changes in the minimum energy magnetic field. The lobe pressure and the minimum energy magnetic field are tightly correlated, since the pressure from the KDA models is directly related to estimates of the minimum energy magnetic field.

I find little evidence of any spectral ageing between 151 MHz and 1400 MHz. There is no trend of the lobe pressure with the low frequency spectral index, but a weak trend with the higher frequency spectral index which indicates, as expected, that radiative losses become more important at higher observing frequencies.

Unsurprisingly I find a strong correlation with lobe pressure and size. The lobe pressure of a source also shows a strong anti-correlation with radio-luminosity and a weaker correlation with redshift. The lobe pressure of a source was also found to correlate with the density of the source environment. However, density is found to show a strong trend with radio-luminosity but there is no corresponding trend with redshift. This indicates that although density and pressure are related, it is only the lobe pressure that is significantly affected by changes in redshift. There is no indication of any evolution of the source environment with cosmological epoch.

Finally, I find a very strong correlation between jet power and radio-luminosity with a much weaker correlation with redshift. This provides evidence of the evolution of black hole masses with low-frequency luminosity, but more importantly with redshift.

Chapter 7

Conclusions

I have presented a complete data set of three samples of radio galaxies and radio-loud quasars. The three samples were defined such that two of them overlap in redshift and two have similar radio luminosities, allowing a study into the trends of various properties with redshift and radio luminosity. The spectral index, the rotation measure and the depolarisation measure were derived directly from the radio observations.

The spectral index was found to be insensitive to the fundamental parameters (redshift, radio-luminosity and radio-size) and thus I can not confirm previous findings of a correlation of spectral index with redshift (Athreya & Kapahi, 1999), a trend of spectral index with radio luminosity (Veron et al., 1972; Onuora, 1989) nor a trend of spectral index with size (Blundell et al., 1999). This is most probably due to the comparatively small size of my sample.

All sources were found to have an external Faraday medium that was local to each source and is responsible for variations of RM on small angular scales. The observed rotation measure itself was insensitive to changes in any of the fundamental parameters which is consistent with a Galactic origin. This Galactic contribution dominates the RM properties of the sources on large scales. At small angular scales, e.g. σ_{RM_z} (rms variation of rotation measure) and DM_z (depolarisation measure), the Galactic contribution is effectively removed. The higher redshift sources display a greater variation in their rotation measures properties. Only the observed depolarisation shows any significant trend with radio-luminosity. My results are consistent with both Morris & Tabara (1973) and Kronberg et al. (1972), as I find both redshift and radio-luminosity to correlate with depolarisation.

The lack of any asymmetries in σ_{RM_z} and DM with the minimum energy magnetic field suggests that the environment has no direct impact on the depolarisation or σ_{RM_z} in a source, but it is the degree of disorder in the structure of the magnetic field that is changing with redshift. This is consistent with my findings that there is no strong correlation between the projected sizes of the sources and their depolarisation measure which agrees with the findings by Dennett-Thorpe (1996), but disagrees with findings by Strom (1973); Strom & Jägers (1988); Pedelty et al. (1989) and Ishwara-Chandra et al. (1998). The lack of any trend between σ_{RM_z} and DM_z and the density of the source environment (from the KDA models) adds further evidence against the assumption that depolarisation and density are related.

Asymmetries in spectral index show evidence of beaming in the majority of my sources. The results from the minimum energy magnetic field asymmetries are inconclusive and could also be explained by an environmental effect. The density estimates from the KDA model suggest that it is more likely that environmental differences and not beaming that causes the observed asymmetries.

In general all asymmetries were found to be insensitive to changes in the source redshift, or low frequency radio luminosity; suggesting that the environments of the high redshift and low redshift samples are similar and any asymmetries caused are due to localised changes in the environment.

I did not find any significant spectral ageing between 151 MHz and 1400 MHz for the sources in the 3CRR, 6CE and 7C III samples. The lobe pressure shows only a weak trend with the spectral index between 365 MHz and 1400 MHz. This indicates, as expected, that radiative losses are more important at higher observing frequencies.

The 3CRR, 6CE and 7C III sources also show that the density of the source environment correlates with radio-luminosity but seemed to be insensitive to changes in redshift. This is consistent with the findings of Longair & Seldner (1979); Prestage & Peacock (1988); Yates et al. (1989) and Yee & Green (1987) that there is no indication of any evolution of the source environment with cosmological epoch.

Finally, I find that jet power and radio-luminosity are tightly correlated. This is expected as the more luminous sources have larger black-holes and thus have stronger jets emerging from their accretion disk (Urry & Padovani, 1995; McLure et al., 2004; Wang et al., 2003; Lacy et al., 2001). However, I also find evidence of jet-power and hence black-hole mass evolution with cosmic epoch.

7.1 Evolution of the Faraday screen

The observational trends noted above are further complicated by the presence of an external Faraday screen. Using my observations of variations in the rotation measure and the Tribble (1991) models I was able to determine the effects and evolution of the Faraday screen with redshift, radio-luminosity and source size.

The observed depolarisation-redshift trend was found to be best explained in terms of the intrinsic rotation measure, σ_{RM}, varying as a function of redshift and a constant cell size, $s_\circ$. This is consistent with my earlier findings that it is the increasing disorder in the magnetic field and not density, that changes with redshift. A slight variation in the cell size, typically no more than ±50% around the best fit value, describes the scatter in the depolarisation results at any given redshift. In fact, it is generally the high redshift results that constrain the model. This suggests that to map the evolution of the Faraday screen, for all epochs, we must use samples containing sources from a large range of redshifts.

Although the Burn (1966) law over-estimates the degree of depolarisation, I find similar results using the Tribble (1991) models, which are more realistic. The simplistic Burn model however, can still be used to find the basic trends with depolarisation in a sample, with fewer assumptions about the underlying distribution. I find that linear polarisation is proportional to λ^{-1} best describes the data, compared to the widely used Burn result $p \sim \lambda^{-4}$.

This work indicates that there is no significant evolution of the density of the source environment with cosmic epoch. Almost all of the observed trends with redshift are directly related to the changes in the degree of disorder in the magnetic field with redshift. The weak trend noted between jet-power and redshift could be attributed to a difference in the formation of black-holes at higher redshifts, i.e. a higher rate of mergers at higher redshifts.

The significant parameter in determining source characteristics seems to be the radio-luminosity of the source. This is evident in both the small and large samples. This agrees with the findings of many other authors in different wavebands (e.g Alexander & Leahy, 1987; Yates et al., 1989; Prestage & Peacock, 1988; Inskip et al., 2003).

Thus in conclusion, I find that there is evidence for a relationship between radio-luminosity and the environment in which a given radio source lives, but there is no significant evolution of the source environment with redshift.

7.2 Further Work

As with any significant body of work there are many avenues in which to extend the research. Ideally I would like to make the same observations between 1.4 GHz and 4.8 GHz for all sources in the 3CRR, 6CE and 7C III. This is highly unrealistic and would also be too time consuming. A compromise would be to extend my small sample to lower-luminosities and higher redshifts. A sample of around 50-60 sources would be feasible and would represent a large cross section of the FRII population.

It would also be interesting to do a multi-waveband study of the sources already in my small sample. A X-ray study of each source could determine if the gas halo around each source was contributing to the depolarisation and if there was any interaction between the radio lobes and the gas detected due to its X-ray emission.

Several of the high redshift 7C sources show rather twisted morphologies and the signal-to-noise level was too low to get detailed depolarisation and rotation measure maps. Higher resolution and longer observations would show if there is any underlying physical reason for their distorted structure.

Appendix A

Sample A maps

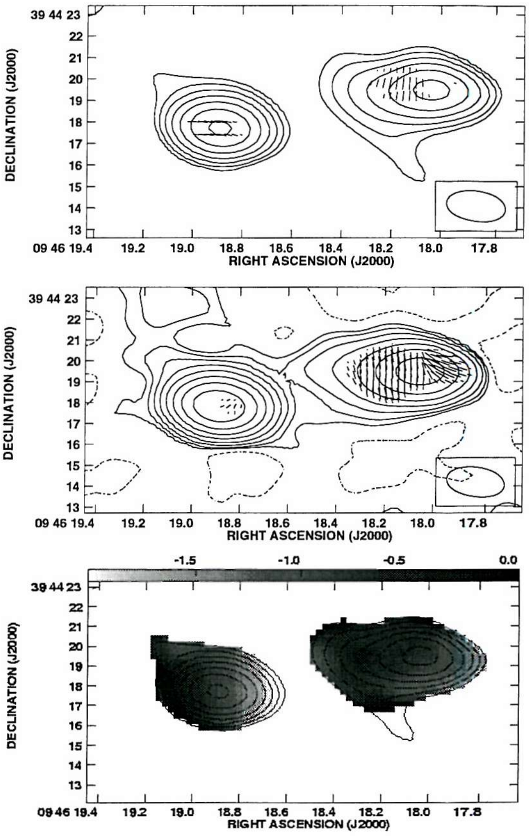

Figure A.1: Maps of the radio source **6C 0943+39** (a - top) 4710 MHz total intensity map with vectors of polarisation overlaid. 1 arc second corresponds to 1.7×10^{-3} Jy beam^{-1}. (b - middle) 1465 MHz total intensity map with vectors of polarisation overlaid. 1 arc second corresponds to 1.7×10^{-3} Jy beam^{-1}. (c - bottom) Map of the spectral index between 4710 MHz and 1465 MHz contours are at 5σ at 4710 MHz (0.5 mJy beam^{-1}) × (-1, 1, 2, 4...,1024). Beam size of 2.5" × 1.4".

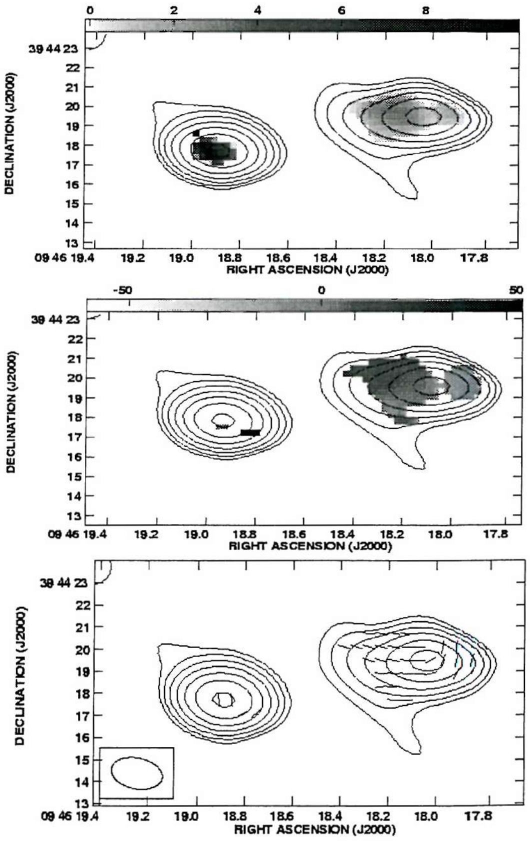

Figure A.1 continued. (d - top) Map of the depolarisation between 4710 MHz and 1465 MHz. (e - middle) Map of the rotation measure (rad m^{-2}) between 4710 MHz, 1665 MHz and 1465 MHz. (f - bottom) Map of the magnetic field direction (degrees). All contours are at 5σ at 4710 MHz (0.5 mJy beam^{-1}) × (-1, 1, 2, 4...,1024). Beam size of 2.5" ×1.4".

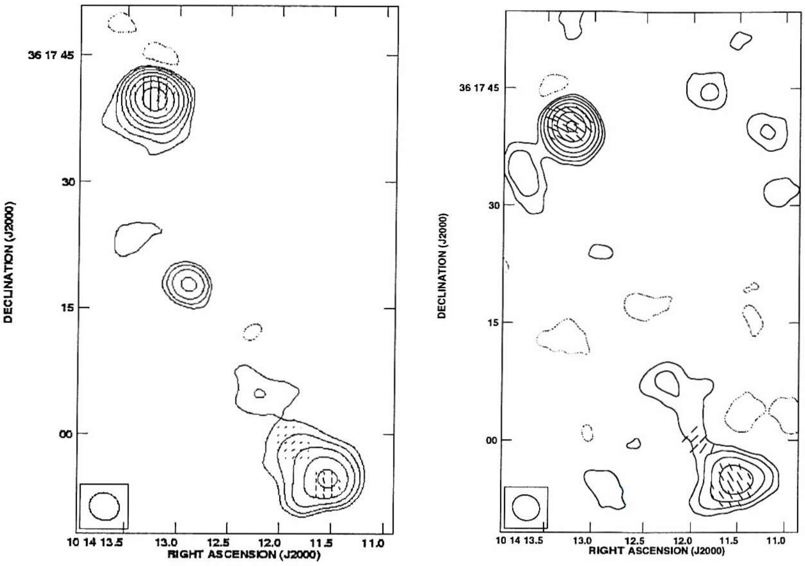

Figure A.2: Maps of the radio source **6C 1011+36**. (a - left) 4710 MHz total intensity map with vectors of polarisation overlaid. The contour levels are at 5σ (0.4 mJy beam^{-1}) $\times$ (-1, 1,2, 4...,1024). 1 arc second corresponds to 8.3×10^{-4} Jy beam^{-1}. (b - right) 1465 MHz total intensity map with vectors of polarisation overlaid. The contour levels are at 3σ (0.8 mJy beam^{-1}) $\times$ (-1, 1,2, 4,...,1024). 1 arc second corresponds to 1.7×10^{-3} Jy beam^{-1}.

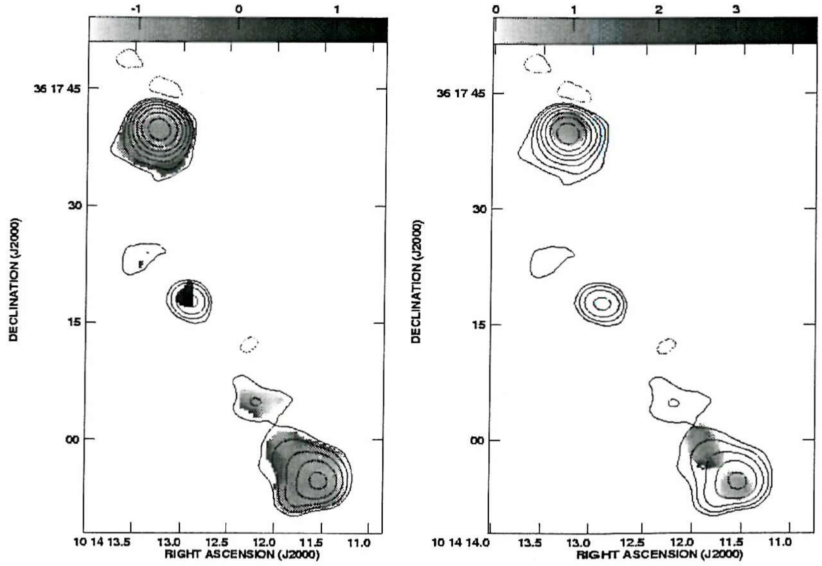

Figure A.2 continued (c - left) Map of the spectral index between 4535 MHz and 1465 MHz. (d - right) Map of the depolarisation between 4535 MHz and 1465 MHz. All contours are at 5σ at 4710 MHz (0.4 mJy beam^{-1}) $\times$ (-1, 1, 2, 4...,1024). Beam size of 3.5" $\times$ 3.2".

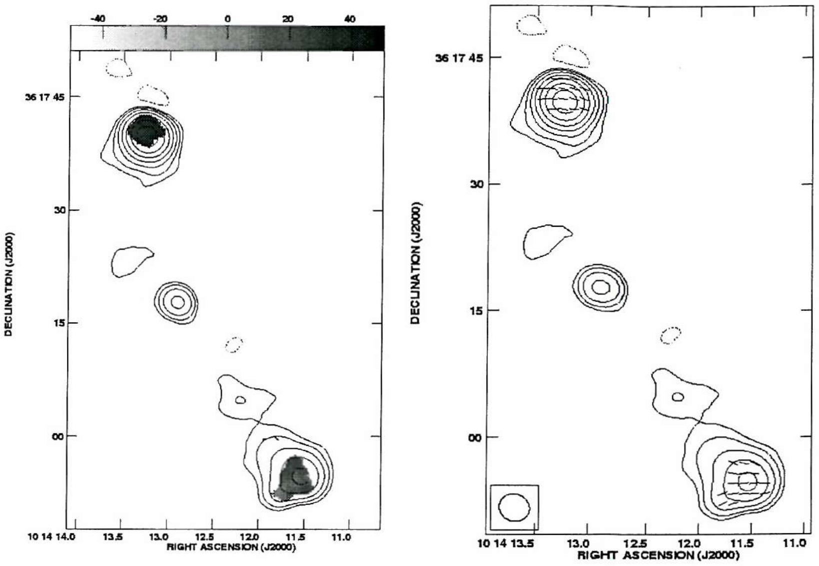

Figure A.2 continued (e - left) Map of the rotation measure (rad m^{-2}) between 4710 MHz, 1665 MHz and 1465 MHz. (f - right) Map of the magnetic field direction (degrees). All contours are at 5σ at 4710 MHz (0.4 mJy beam^{-1}) × (-1, 1, 2, 4...,1024). Beam size of 3.5"×3.2".

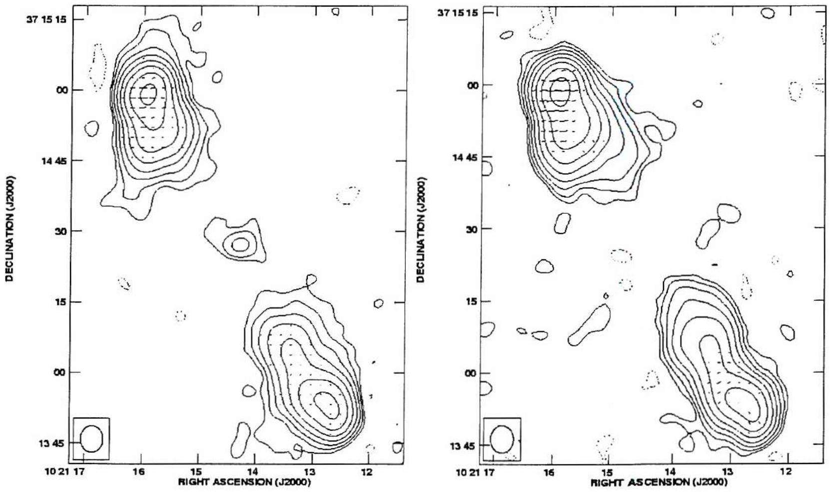

Figure A.3: Maps of the radio source **6C 1018+37**. (a - left) 4710 MHz total intensity map with vectors of polarisation overlaid. The contour levels are at 5σ (100 μJy beam^{-1}) × (-1, 1,2, 4...,1024). 1 arc second corresponds to 1.7×10^{-3} Jy beam^{-1}. (b - right) 1465 MHz total intensity map with vectors of polarisation overlaid. The contour levels are at 3σ (0.5 mJy beam^{-1}) × (-1, 1,2, 4,...,1024). 1 arc second corresponds to 1.7 × 10^{-3} Jy beam^{-1}.

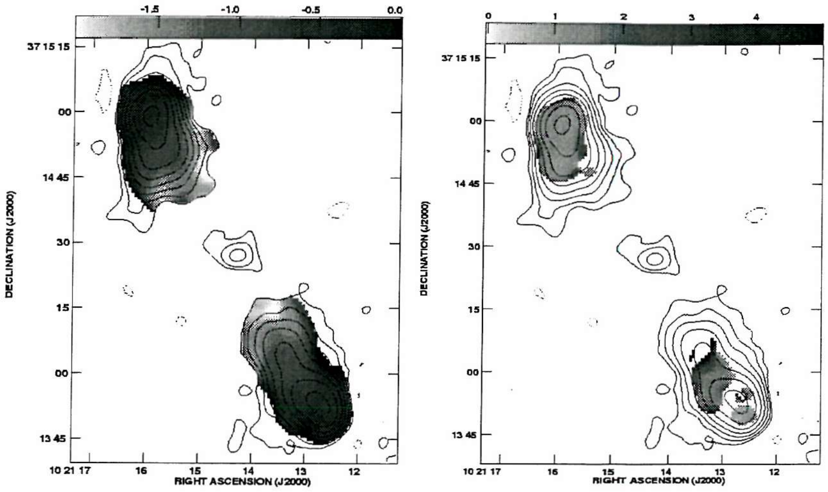

Figure A.3 continued (c - left) Map of the spectral index between 4710 MHz and 1465 MHz. (d - right) Map of the depolarisation between 4710 MHz and 1465 MHz. All contours are at 5σ at 4885 MHz (100 μJy beam^{-1}) × (-1, 1, 2, 4...,1024). Beam size of 4"×4".

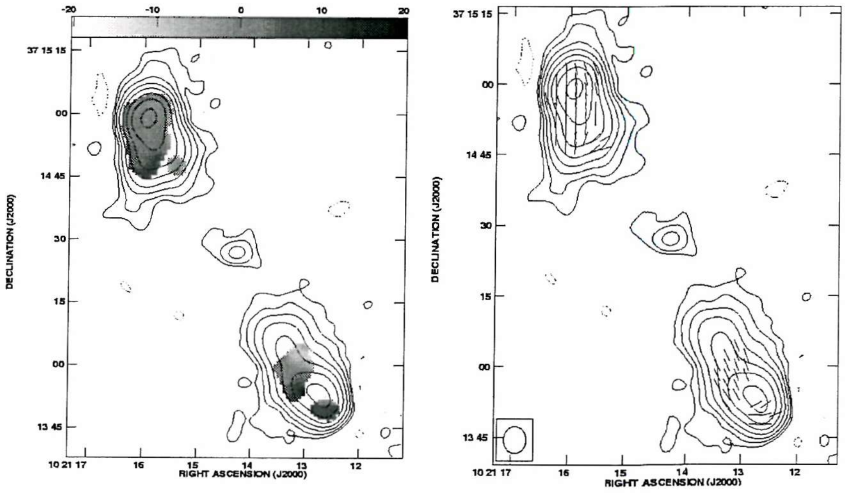

Figure A.3 continued (e - left) Map of the rotation measure (rad m^{-2}) between 4710 MHz, 1665 MHz and 1465 MHz. (f - right) Map of the magnetic field direction (degrees). All contours are at 5σ at 4885 MHz (100 μJy beam^{-1}) × (-1, 1, 2, 4...,1024). Beam size of 4"×4".

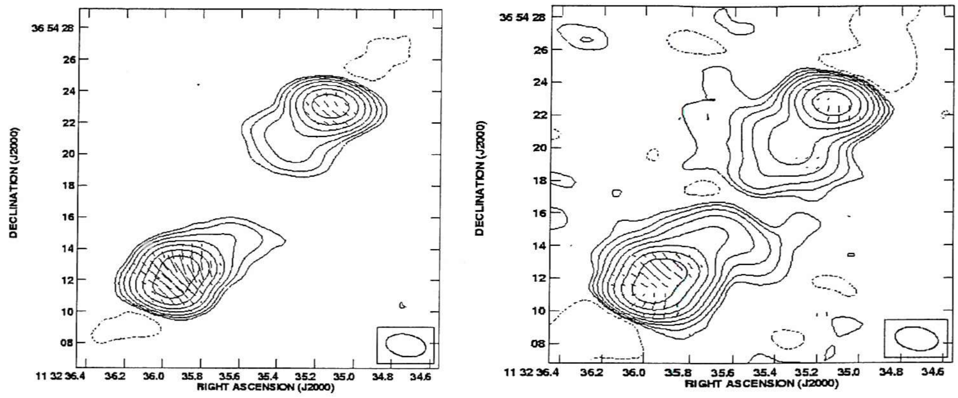

Figure A.4: Maps of the radio source **6C 1129+37**. (a - left) 4710 MHz total intensity map with vectors of polarisation overlaid. The contour levels are at 5σ (0.3 mJy beam)$^{-1}$) × (-1, 1,2, 4...,1024). 1 arc second corresponds to 1.7×10^{-3} Jy beam^{-1}. (b - right) 1465 MHz total intensity map with vectors of polarisation overlaid. The contour levels are at 3σ (0.4 mJy beam^{-1}) × (-1, 1,2, 4,...,1024). 1 arc second corresponds to 3.3×10^{-3} Jy beam^{-1}. Beam size of 2.5"×1.4".

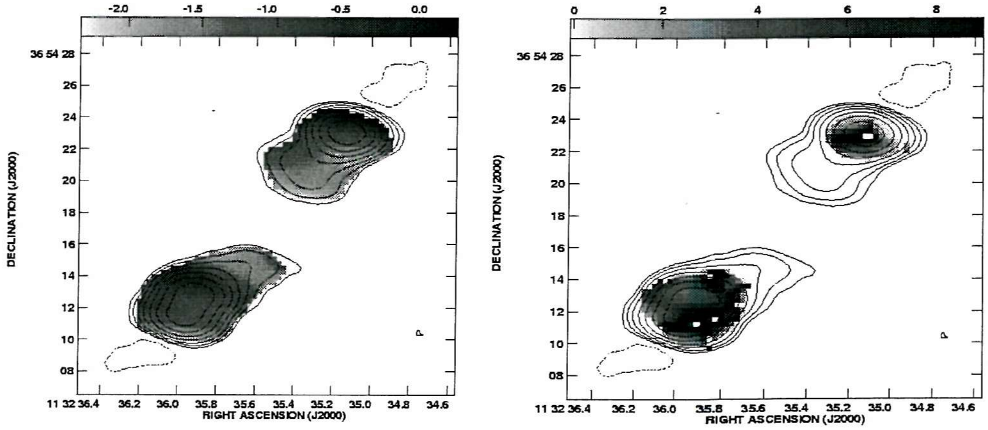

Figure A.4 continued. (c - left) Map of the spectral index between 4710 MHz and 1465 MHz. (d - right) Map of the depolarisation between 4710 MHz and 1465 MHz. All contours are at 5σ at 4710 MHz (0.3 mJy beam^{-1}) × (-1, 1, 2, 4...,1024). Beam size of 2.5"×1.4".

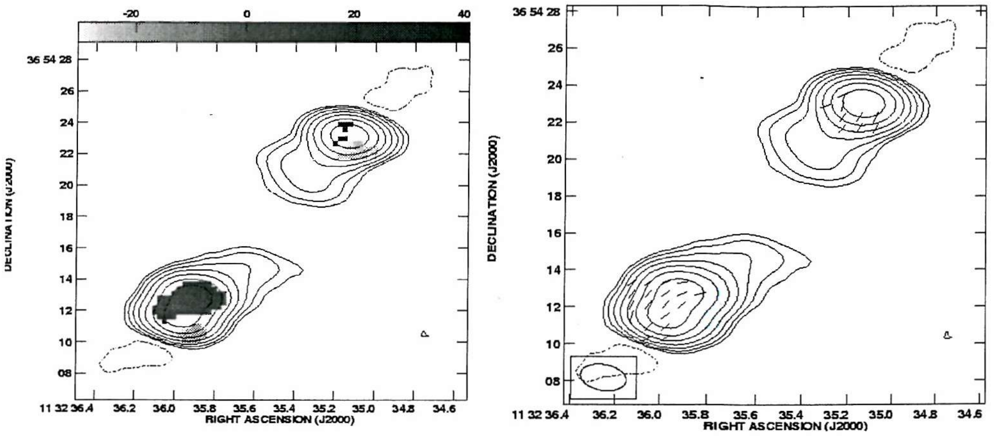

Figure A.4 continued. (e - left) Map of the rotation measure (rad m^{-2}) between 4710 MHz, 1665 MHz and 1465 MHz. (f - right) Map of the magnetic field direction (degrees). All contours are at 5σ at 4710 MHz (0.3 mJy beam^{-1}) × (-1, 1, 2, 4...,1024). Beam size of 2.5"×1.4".

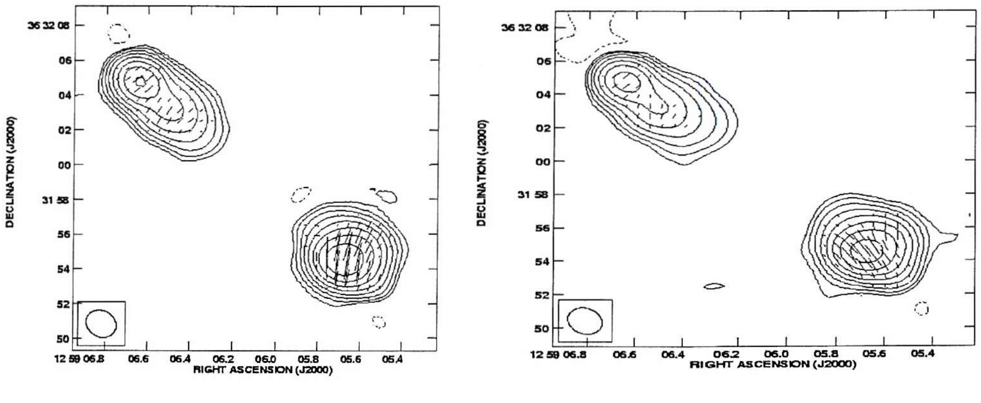

Figure A.5: Maps of the radio source **6C 1256+36**. (a - left) 4710 MHz total intensity map with vectors of polarisation overlaid. The contour levels are at 5σ (0.25 mJy beam^{-1}) × (-1, 1,2, 4...,1024). 1 arc second corresponds to 3.3×10^{-3} Jy beam^{-1}. (b - right) 1465 MHz total intensity map with vectors of polarisation overlaid. The contour levels are at 3σ (0.5 mJy beam^{-1}) × (-1, 1,2, 4,...,1024). 1 arc second corresponds to 8.3 × 10^{-3} Jy beam^{-1}. Beam size of 1.8"×1.5".

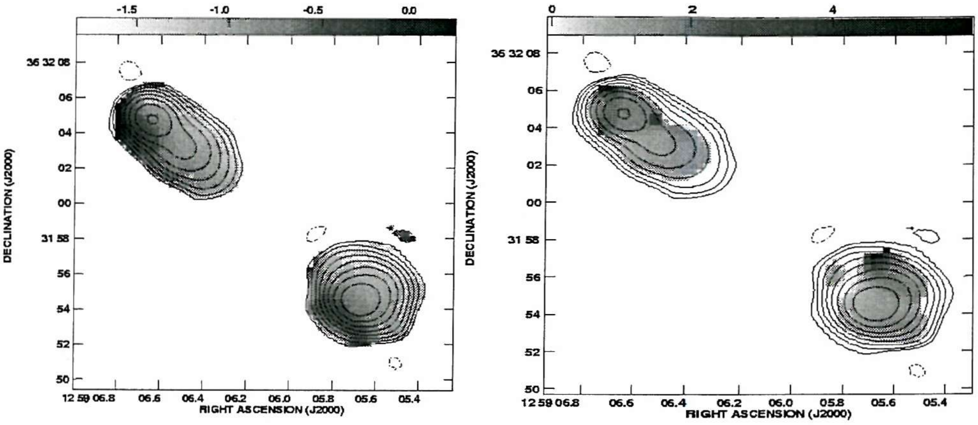

Figure A.5 continued. (c - left) Map of the spectral index between 4710 MHz and 1465 MHz. (d - right) Map of the depolarisation between 4710 MHz and 1465 MHz.All contours are at 5σ at 4710 MHz (0.25 mJy beam^{-1}) × (-1, 1, 2, 4...,1024). Beam size of 1.8"×1.5".

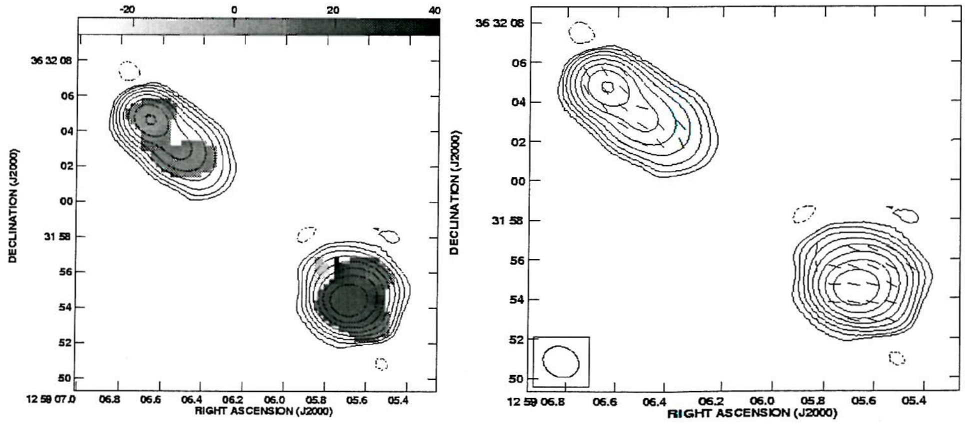

Figure A.5 continued. (e - left) Map of the rotation measure (rad m^{-2}) between 4710 MHz, 1665 MHz and 1465 MHz. (f - right) Map of the magnetic field direction (degrees). All contours are at 5σ at 4710 MHz (0.25 mJy beam^{-1}) × (-1, 1, 2, 4...,1024). Beam size of 1.8"×1.5".

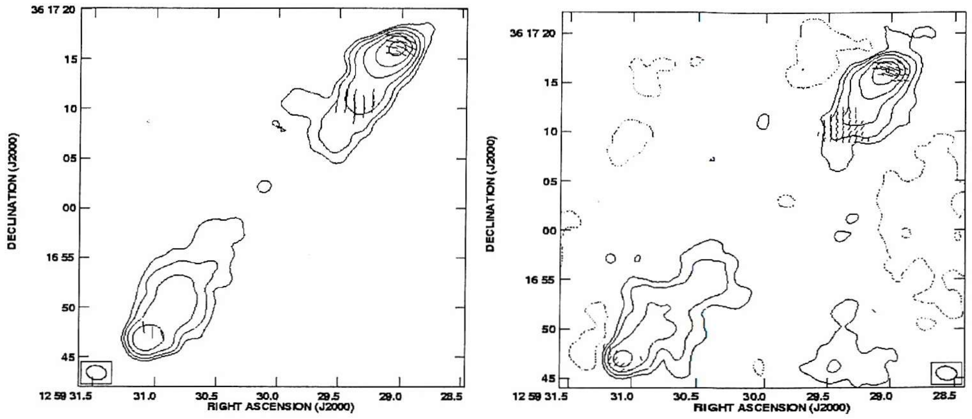

Figure A.6: Maps of the radio source **6C 1257+36**. (a - left) 4710 MHz total intensity map with vectors of polarisation overlaid. The contour levels are at 5σ (0.25 mJy beam^{-1}) × (-1, 1,2, 4...,1024). 1 arc second corresponds to 8.3$\times$10^{-4} Jy beam^{-1}. (b - right) 1465 MHz total intensity map with vectors of polarisation overlaid. The contour levels are at 3σ (0.7 mJy beam^{-1}) × (-1, 1,2, 4,...,1024). 1 arc second corresponds to 1.7 × 10^{-3} Jy beam^{-1}.

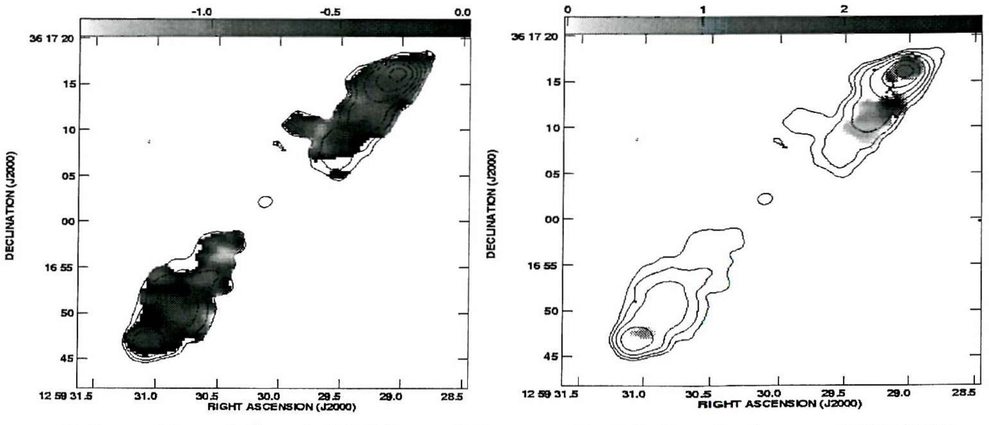

Figure A.6 continued (c - left) Map of the spectral index between 4860 MHz and 1465 MHz. (d - right) Map of the depolarisation between 4710 MHz and 1465 MHz. All contours are at 5σ at 4710 MHz (0.25 mJy beam^{-1}) × (-1, 1, 2, 4...,1024). Beam size of 2.0"×1.4".

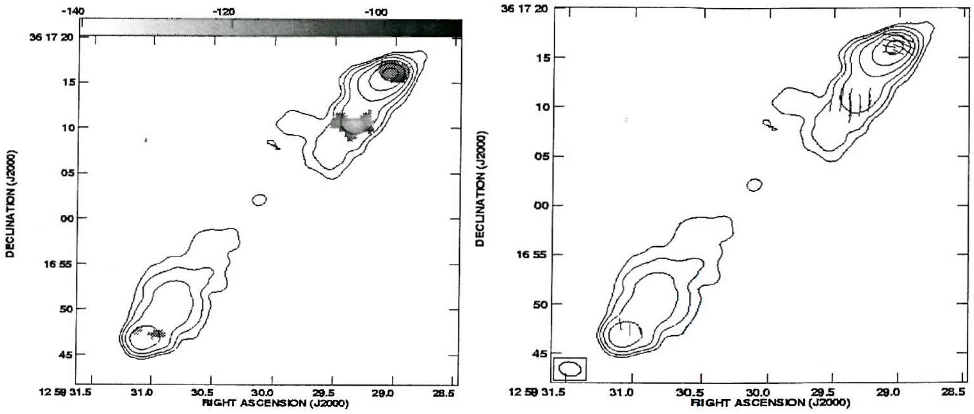

Figure A.6 continued (e - left) Map of the rotation measure (rad m^{-2}) between 4710 MHz, 1665 MHz and 1465 MHz. (f - right) Map of the magnetic field direction (degrees). All contours are at 5σ at 4710 MHz (0.25 mJy beam^{-1}) $\times$ (-1, 1, 2, 4...,1024). Beam size of 2.0" $\times$1.4".

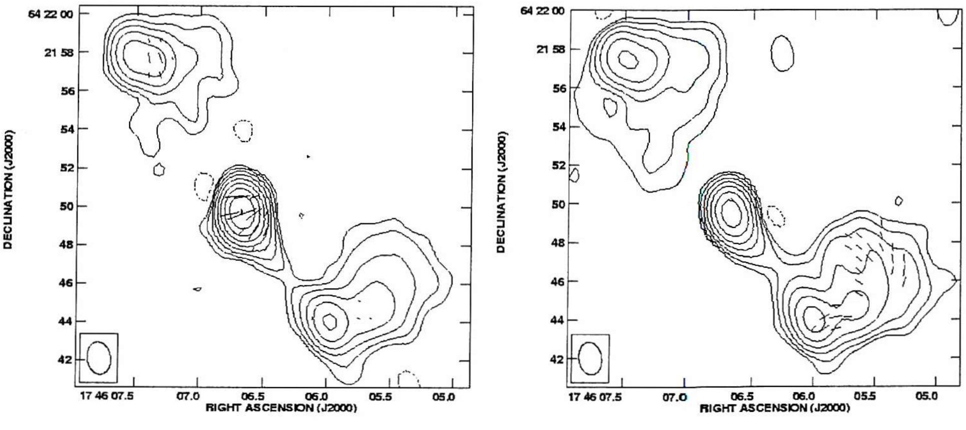

Figure A.7: Maps of the radio source **7C 1745+642**. (a - left) 4710 MHz total intensity map with vectors of polarisation overlaid. The contour levels are at 5σ (0.3 mJy beam^{-1}) $\times$ (-1, 1, 2, 4...,1024). 1 arc second corresponds to 1.7×10^{-3} Jy beam^{-1}. (b - right) 1465 MHz total intensity map with vectors of polarisation overlaid. The contour levels are at 3σ (0.6 mJy beam^{-1}) $\times$ (-1, 1, 2, 4...,1024). 1 arc second corresponds to 1.7×10^{-3} Jy beam^{-1}

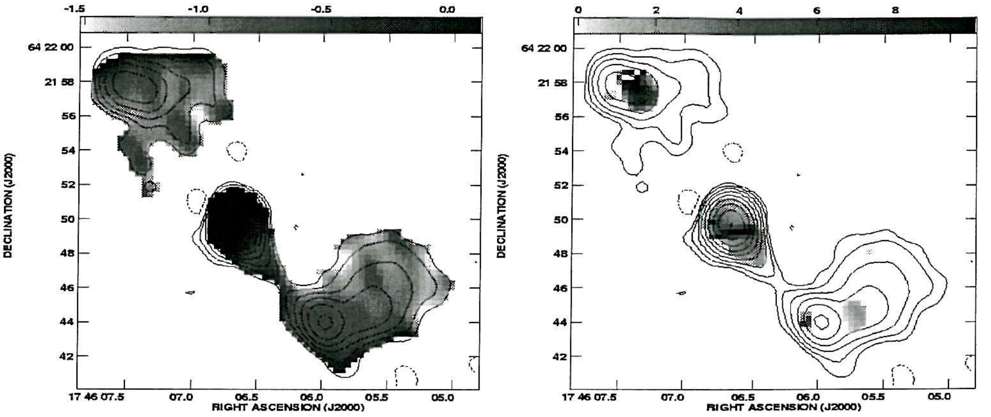

Figure A.7 continued. (c - left) Map of the spectral index between 4710 MHz and 1465 MHz. (d - right) Map of the depolarisation between 4710 MHz and 1465 MHz. All contours are at 5σ at 4710 MHz (0.3 mJy beam^{-1}) × (-1, 1, 2, 4...,1024). Beam size of 1.7" ×1.2".

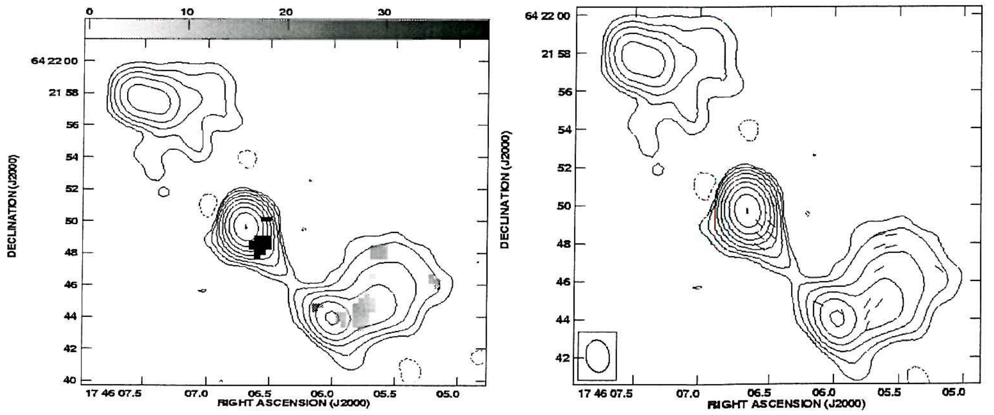

Figure A.7 continued. (e - left) Map of the rotation measure (rad m^{-2}) between 4710 MHz, 1665 MHz and 1465 MHz. (f - right) Map of the magnetic field direction (degrees). All contours are at 5σ at 4710 MHz (0.3 mJy beam^{-1}) × (-1, 1, 2, 4...,1024). Beam size of 1.7" ×1.2".

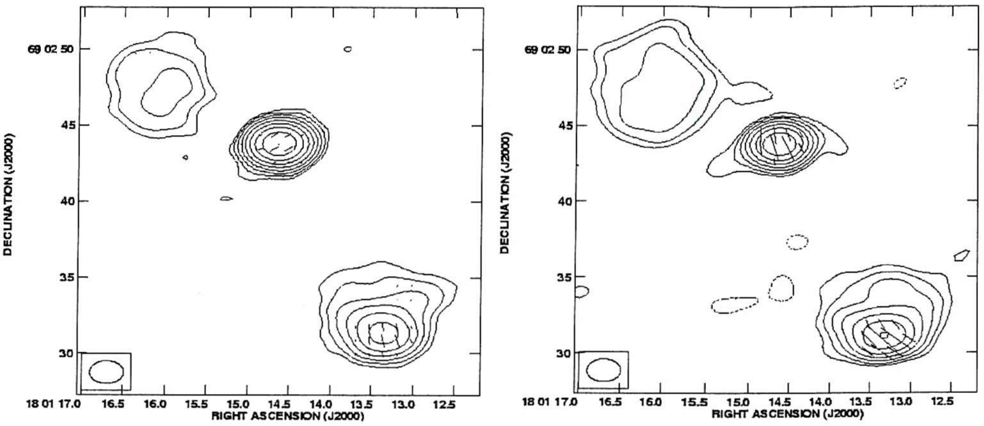

Figure A.8: Maps of the radio source **7C 1801+690**. (a - left) 4710 MHz total intensity map with vectors of polarisation overlaid. The contour levels are at 5σ (0.3 mJy beam^{-1}) × (-1, 1, 2, 4..., 1024). 1 arc second corresponds to 1.7 × 10^{-3} Jy beam^{-1}. (b - right) 1465 MHz total intensity map with vectors of polarisation overlaid. The contour levels are at 3σ (0.6 mJy beam^{-1}) × (-1, 1, 2, 4,..,1024). 1 arc second corresponds to 1.7 × 10^{-3} Jy beam^{-1}.

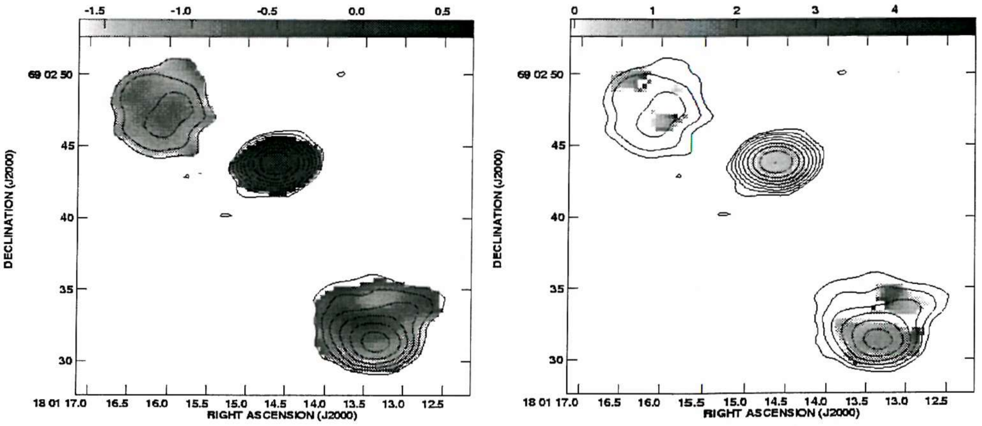

Figure A.8 continued. (c - left) Map of the spectral index between 4710 MHz and 1465 MHz. (d - right) Map of the depolarisation between 4710 MHz and 1465 MHz. All contours are at 5σ at 4710 MHz (0.30 mJy beam^{-1}) × (-1, 1, 2, 4...,1024). Beam size of 2.2" ×1.5".

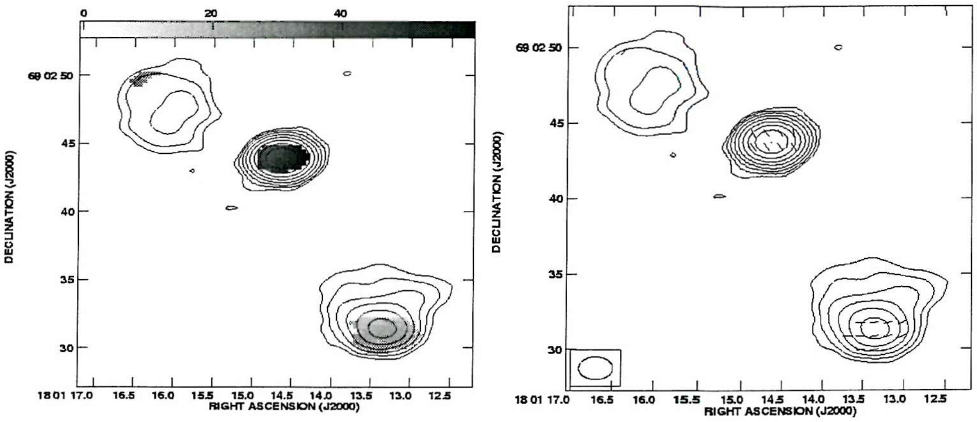

Figure A.8 continued. (e - left) Map of the rotation measure (rad m^{-2}) between 4710 MHz, 1665 MHz and 1465 MHz. (f - right) Map of the magnetic field direction (degrees). All contours are at 5σ at 4710 MHz (0.30 mJy $beam^{-1}$) × (-1, 1, 2, 4...,1024). Beam size of 2.2"×1.5".

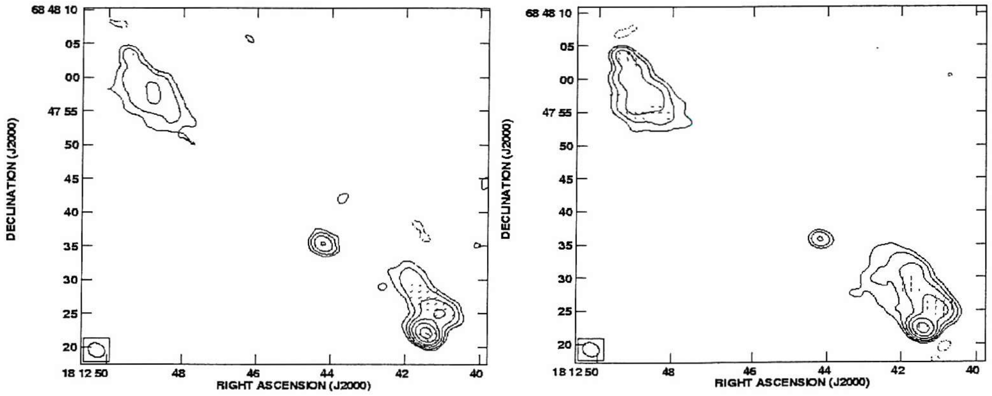

Figure A.9: Maps of the radio source **7C 1813+684**. (a - left) 4710 MHz total intensity map with vectors of polarisation overlaid. The contour levels are at 5σ (0.35 mJy $beam^{-1}$) × (-1, 1, 2, 4... ,1024). 1 arc second corresponds to 8.3×10^{-4} Jy $beam^{-1}$. (b - right) 1465 MHz total intensity map with vectors of polarisation overlaid. The contour levels are at 3σ (0.7 mJy $beam^{-1}$) × (-1, 1, 2, 4... ,1024). 1 arc second corresponds to 1.7×10^{-3} Jy $beam^{-1}$.

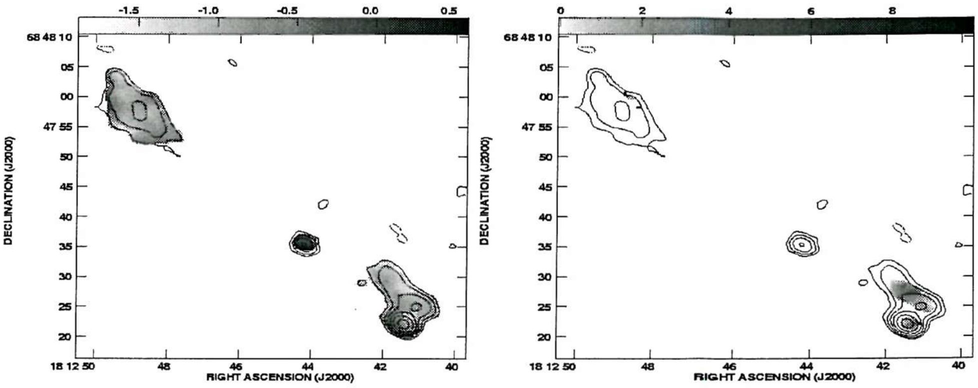

Figure A.9 continued. (c - left) Map of the spectral index between 4710 MHz and 1465 MHz. (d - right) Map of the depolarisation between 4710 MHz and 1465 MHz. All contours are at 5σ at 4710 MHz (0.35 mJy beam^{-1}) × (-1, 1, 2, 4...,1024). Beam size of 2.5"×2.0".

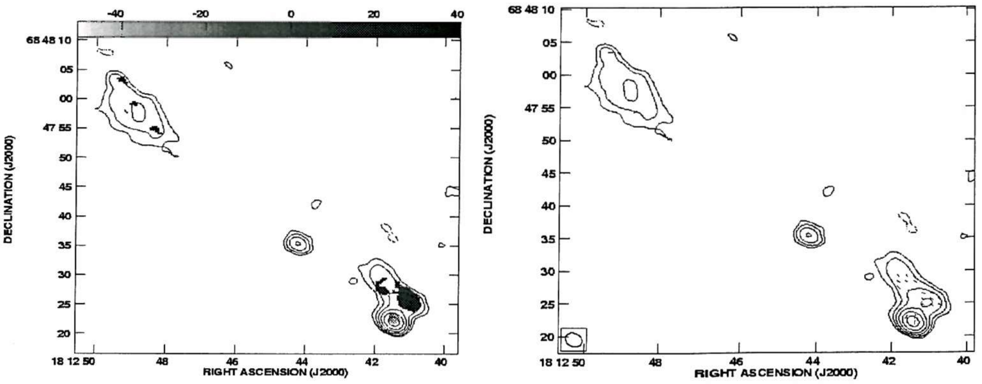

Figure A.9 continued. (e - left) Map of the rotation measure (rad m^{-2}) between 4710 MHz, 1665 MHz and 1465 MHz. (f - right) Map of the magnetic field direction (degrees). All contours are at 5σ at 4710 MHz (0.35 mJy beam^{-1}) × (-1, 1, 2, 4...,1024). Beam size of 2.5"×2.0"

Appendix B

Sample B maps

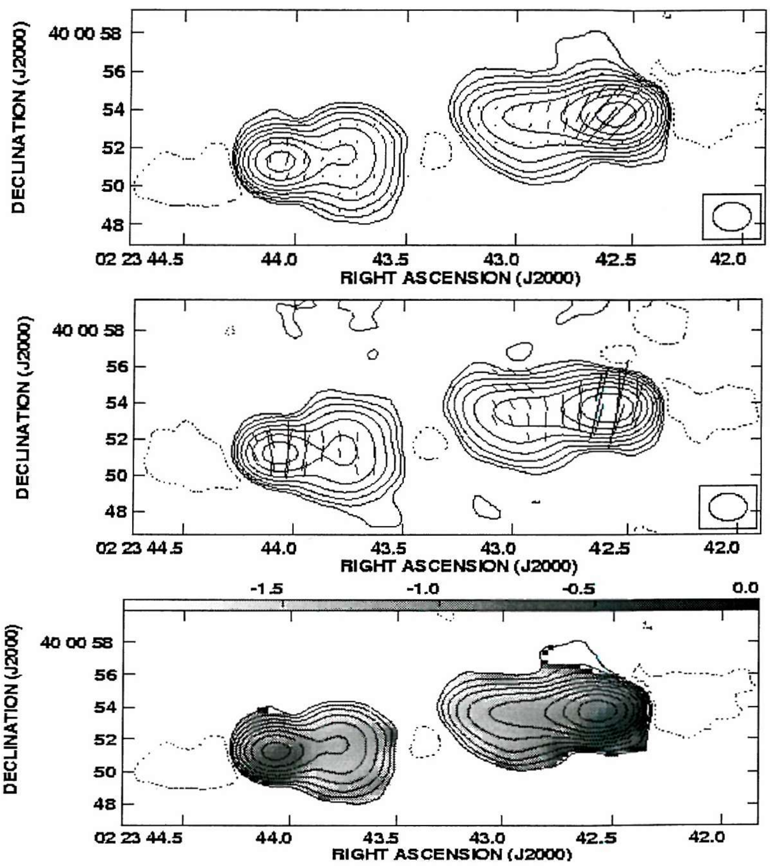

Figure B.1: Maps of the radio source **3C 65**. (a - top) 4710 MHz total intensity map with vectors of polarisation overlaid. The contour levels are at 5σ (0.8 mJy beam^{-1})$\times$ (-1, 1, 2, 4... ,1024). 1 arc second corresponds to 1.7×10^{-2} Jy beam^{-1}. (b - middle) 1465 MHz total intensity map with vectors of polarisation overlaid. The contour levels are at 3σ (3.0 mJy beam^{-1})$\times$ (-1, 1, 2, 4... ,1024). 1 arc second corresponds to 8.3×10^{-3} Jy beam^{-1}. (c - bottom) Map of the spectral index between 4710 MHz and 1465 MHz contours are as (a). Beam size of 2.0"$\times$1.5".

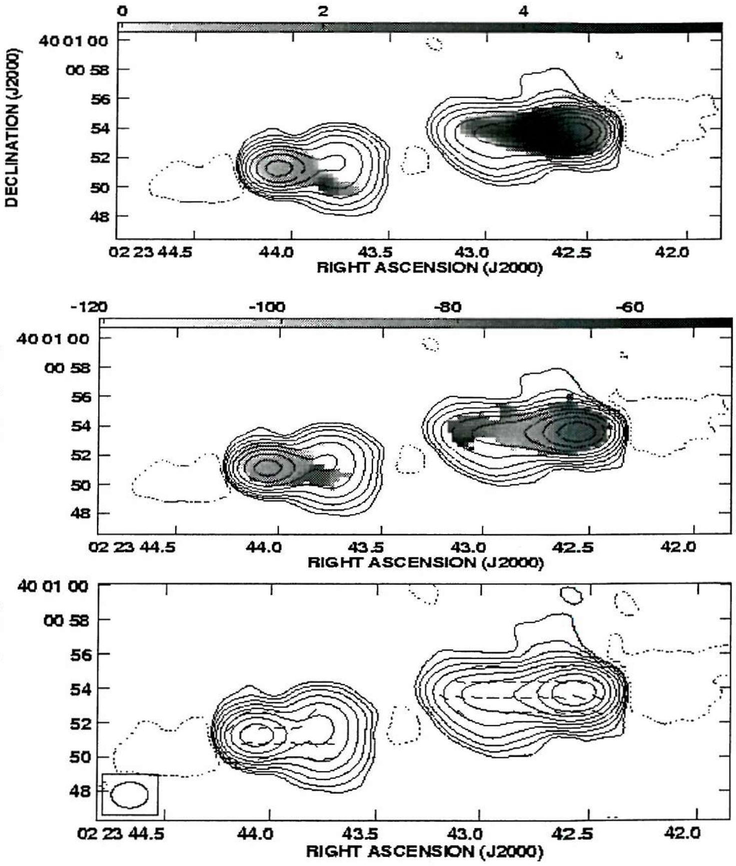

Figure B.1 continued. (d - top) Map of the depolarisation between 4710 MHz and 1465 MHz. (e - middle) Map of the rotation measure (rad m^{-2}) between 4710 MHz, 1665 MHz and 1465 MHz. (f - bottom) Map of the magnetic field direction (degrees). All contours are at 5σ at 4860 MHz (0.8 mJy beam^{-1})$\times$ (-1, 1, 2, 4...,1024). Beam size of 2.0"×1.5".

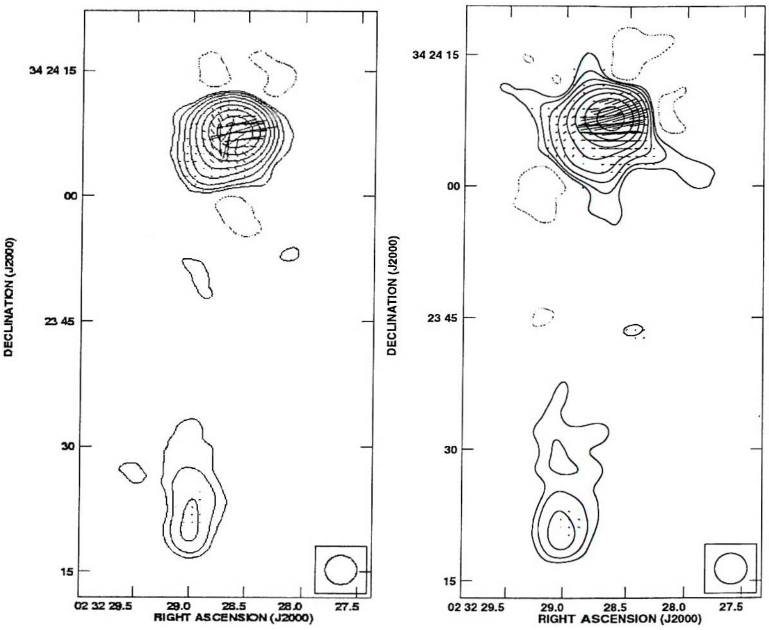

Figure B.2: Maps of the radio source **3C 68.1**. (a - left) 4710 MHz total intensity map with vectors of polarisation overlaid. The contour levels are at 5σ (2.0 mJy beam^{-1})$\times$ (-1, 1, 2, 4... ,1024). 1 arc second corresponds to 8.3×10^{-3} Jy beam^{-1}. (b - right) 1465 MHz total intensity map with vectors of polarisation overlaid. The contour levels are at 3σ (6.0 mJy beam^{-1})$\times$ (-1, 1, 2, 4... ,1024). 1 arc second corresponds to 1.67×10^{-3} Jy beam^{-1}.

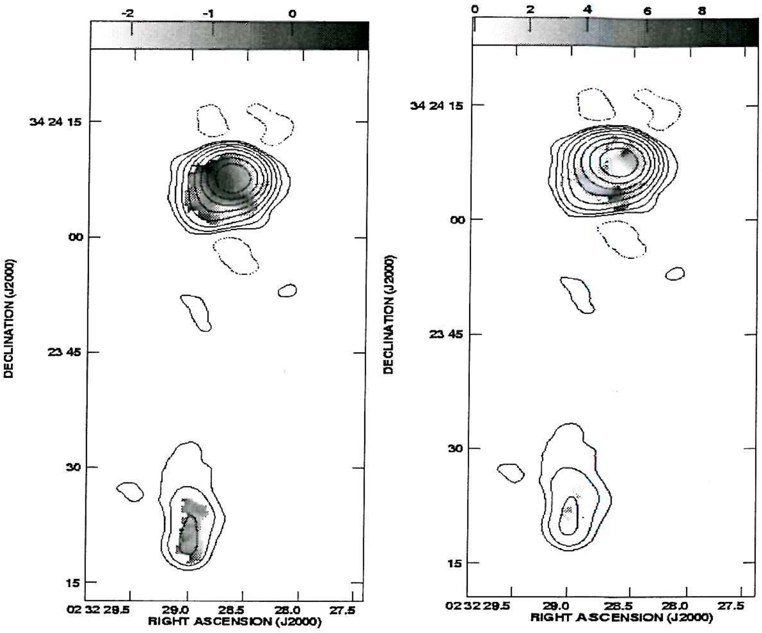

Figure B.2 continued. (c - left) Map of the spectral index between 4710 MHz and 1417 MHz. (d - right) Map of the depolarisation between 4710 MHz and 1417 MHz. All contours are at 5σ at 4710 MHz (2.0 mJy beam^{-1})× (-1, 1, 2, 4...,1024). Beam size of 3.5"×3.5".

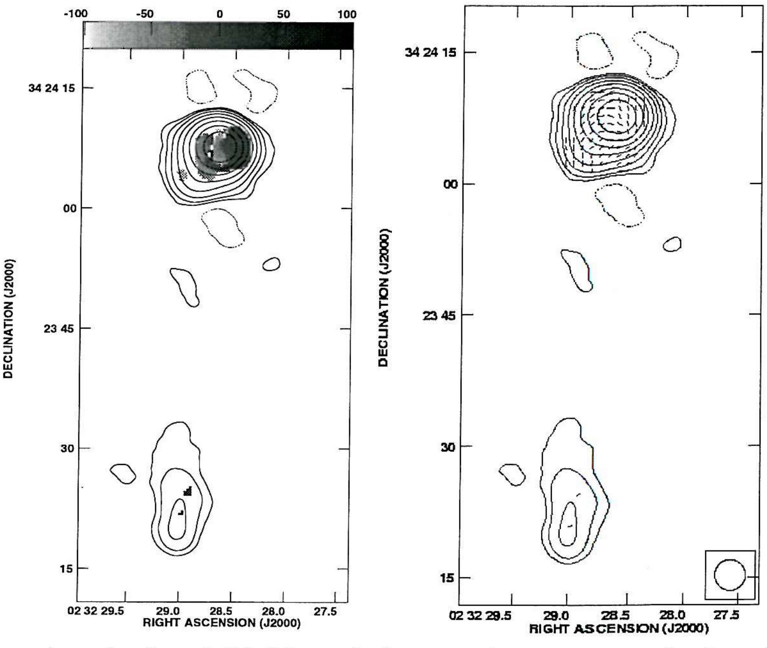

Figure B.2 continued. (e - left) Map of the rotation measure (rad m^{-2}) between 4710 MHz, 1662 MHz and 1417 MHz. (f - right) Map of the magnetic field direction (degrees). All contours are at 5σ at 4710 MHz (2.0 mJy beam^{-1})× (-1, 1, 2, 4...,1024). Beam size of 3.5"×3.5".

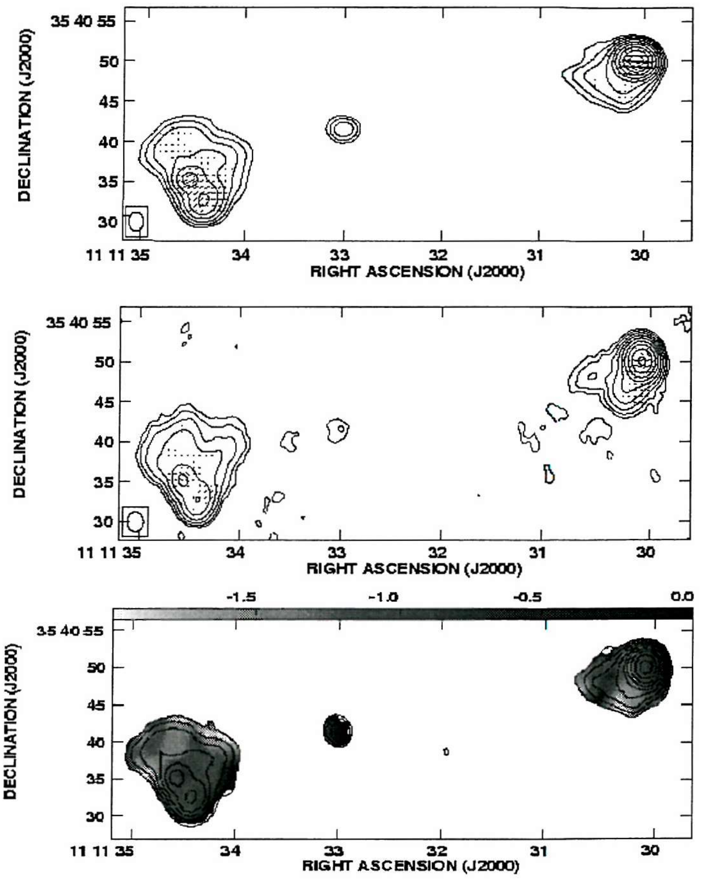

Figure B.3: Maps of the radio source **3C 252** . (a - top) 4710 MHz total intensity map with vectors of polarisation overlaid. The contour levels are at 5σ (0.4 mJy beam^{-1})$\times$ (-1, 1, 2, 4... ,1024). 1 arc second corresponds to 3.3×10^{-3} Jy beam^{-1}. (b - middle) 1465 MHz total intensity map with vectors of polarisation overlaid. The contour levels are at 3σ (1.0 mJy beam^{-1})$\times$ (-1, 1, 2, 4... ,1024). 1 arc second corresponds to 3.3×10^{-3} Jy beam^{-1}. (c - bottom) Map of the spectral index between 4710 MHz and 1465 MHz contours are as (a).

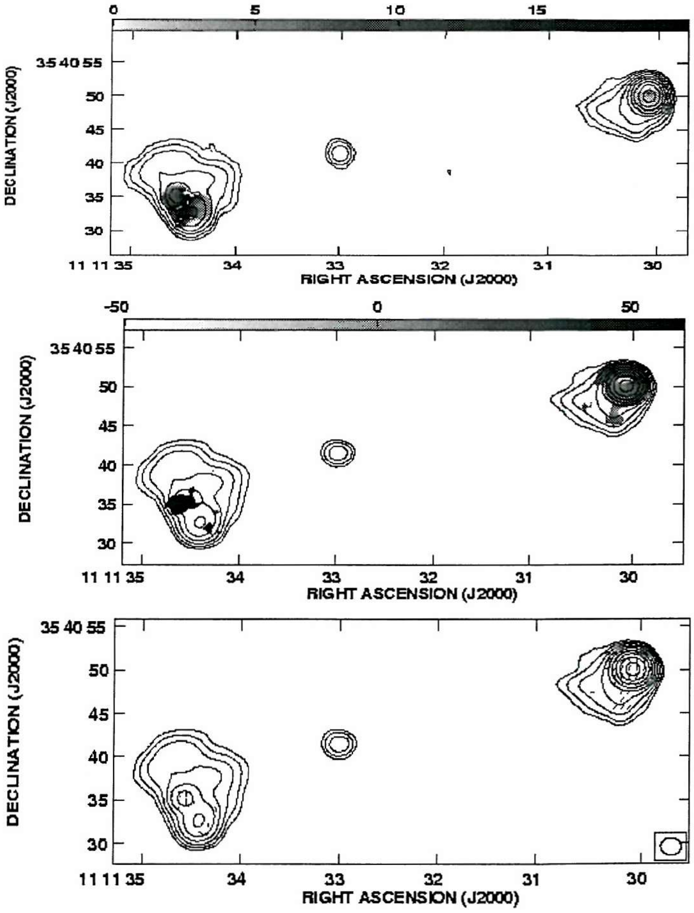

Figure B.3 continued. (d - top) Map of the depolarisation between 4710 MHz and 1465 MHz. (e - middle) Map of the rotation measure (rad m^{-2}) between 4710 MHz, 1665 MHz and 1465 MHz. (f - bottom) Map of the magnetic field direction (degrees). All contours are at 5σ at 4710 MHz (0.4 mJy beam^{-1})× (-1, 1, 2, 4...,1024). Beam size of 2.0" × 2.5".

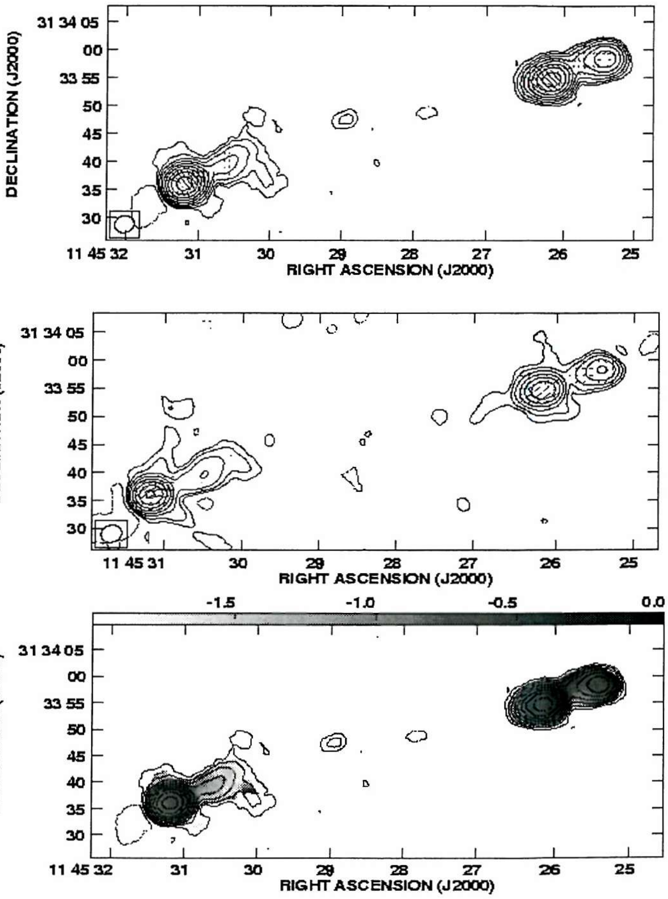

Figure B.4: Maps of the radio source **3C 265**. (a - top) 4848 MHz total intensity map with vectors of polarisation overlaid. The contour levels are at 5σ (0.7 mJy beam^{-1})$\times$ (-1, 1, 2, 4... ,1024). 1 arc second corresponds to 4.2×10^{-3}Jybeam^{-1}. (b - middle) 1417 MHz total intensity map with vectors of polarisation overlaid. The contour levels are at 3σ (1.4 mJy beam^{-1})$\times$ (-1, 1, 2, 4... ,1024). 1 arc second corresponds to 3.3×10^{-3}Jybeam^{-1}. (c - bottom) Map of the spectral index between 4848 MHz and 1417 MHz contours are as (a).

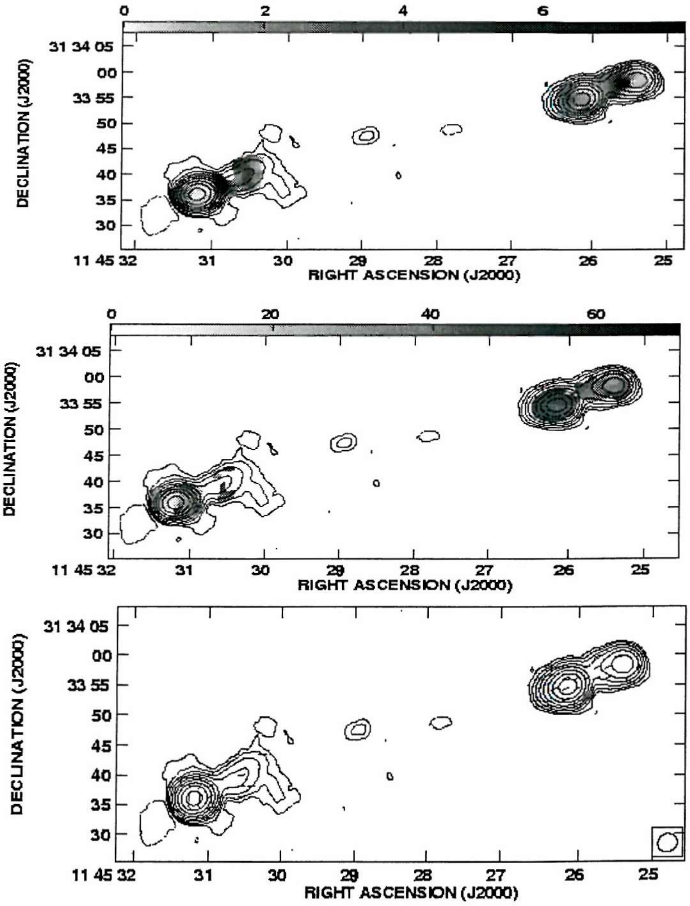

Figure B.4 continued. (d - top) Map of the depolarisation between 4848 MHz and 1417 MHz. (e - middle) Map of the rotation measure (rad m^{-2}) between 4848 MHz, 1662 MHz and 1417 MHz. (f - bottom) Map of the magnetic field direction (degrees) All contours are at 5σ at 4848 MHz (0.7 mJy beam^{-1})× (-1, 1, 2, 4...,1024). Beam size of 3.5"× 3.0".

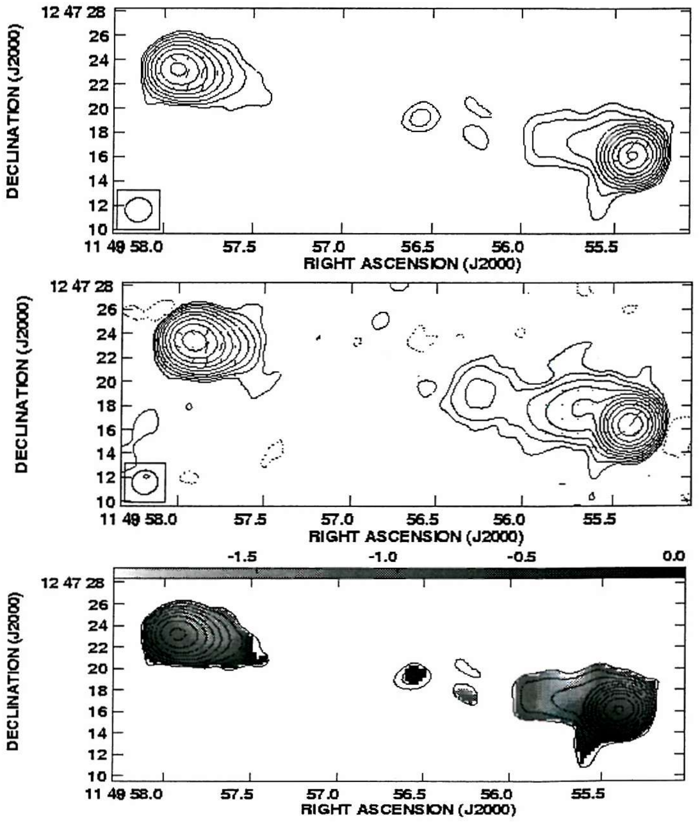

Figure B.5: Maps of the radio source **3C 267** . (a - top) 4848 MHz total intensity map with vectors of polarisation overlaid. The contour levels are at 5σ (0.8 mJy beam^{-1})$\times$ (-1, 1, 2, 4... ,1024). 1 arc second corresponds to 8.3×10^{-3} Jy beam^{-1}. (b - middle) 1465 MHz total intensity map with vectors of polarisation overlaid. The contour levels are at 3σ (1.3 mJy beam^{-1})$\times$ (-1, 1, 2, 4... ,1024). 1 arc second corresponds to 8.3×10^{-3} Jy beam^{-1}. (c - bottom) Map of the spectral index between 4848 MHz and 1465 MHz contours are as (a).

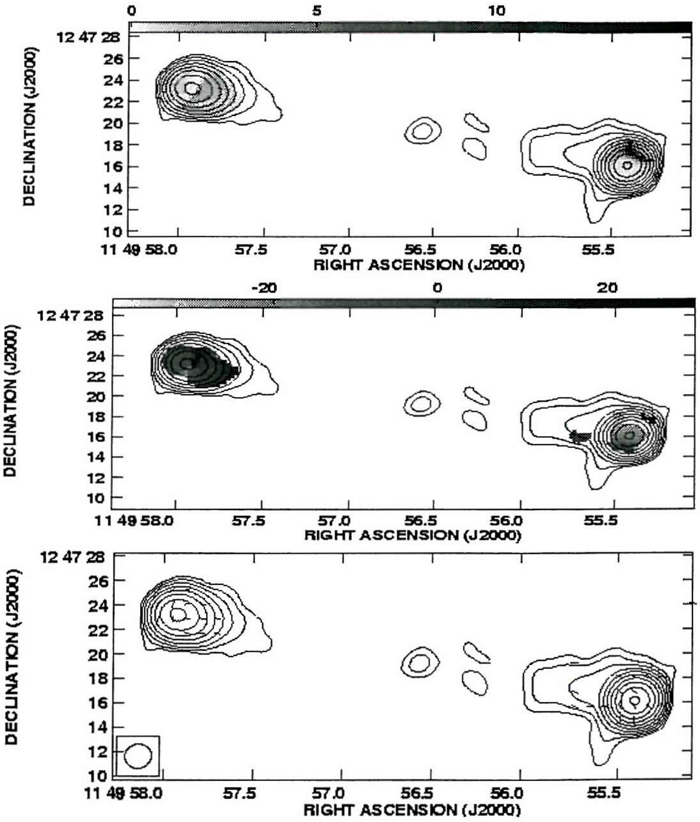

Figure B.5 continued. (d - top) Map of the depolarisation between 4848 MHz and 1465 MHz. (e - middle) Map of the rotation measure (rad m^{-2}) between 4848 MHz, 1665 MHz and 1465 MHz. (f - bottom) Map of the magnetic field direction (degrees). All contours are at 5σ at 4848 MHz (0.8 mJy $beam^{-1}$)× (-1, 1, 2, 4...,1024). Beam size of 2.2" ×2.0".

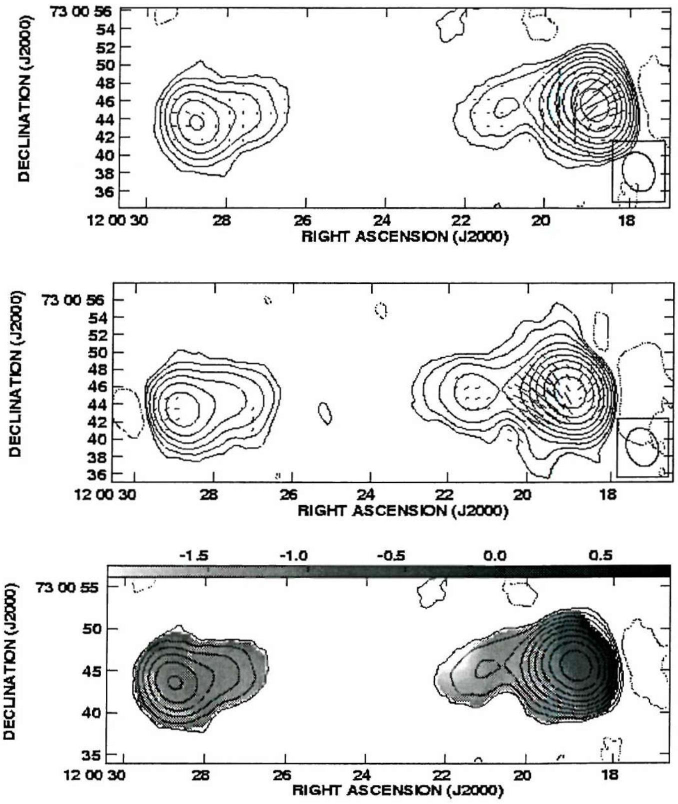

Figure B.6: Maps of the radio source **3C 268.1**. (a - top) 4848 MHz total intensity map with vectors of polarisation overlaid. The contour levels are at 5σ (5.2 mJy beam^{-1})$\times$ (-1, 1, 2, 4... ,1024). 1 arc second corresponds to 1.7×10^{-2} Jy beam^{-1}. (b - middle) 1417 MHz total intensity map with vectors of polarisation overlaid. The contour levels are at 3σ (7.0 mJy beam^{-1})$\times$ (-1, 1, 2, 4... ,1024). 1 arc second corresponds to 1.7×10^{-2} Jy beam^{-1}. (c - bottom) Map of the spectral index between 4848 MHz and 1417 MHz contours are as (a).

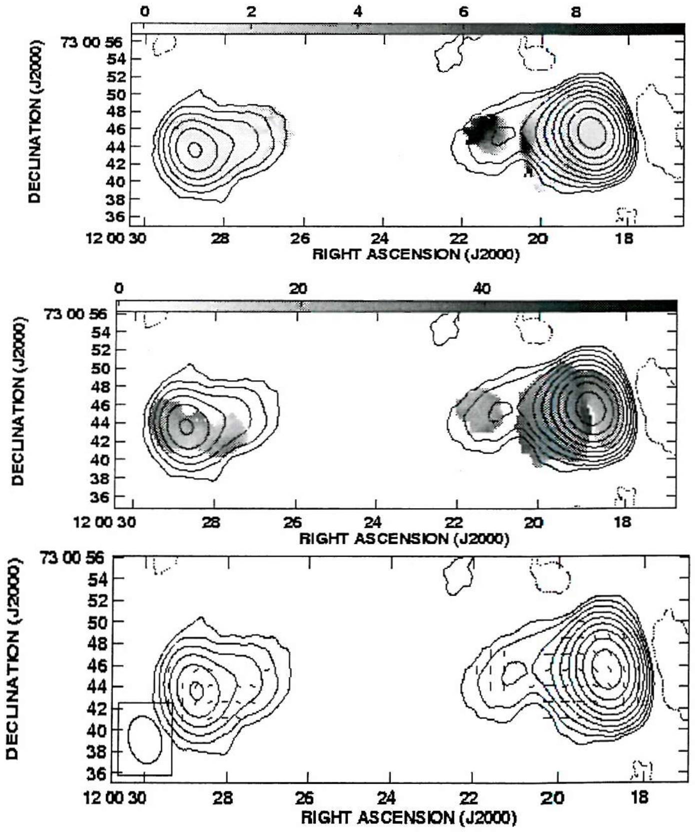

Figure B.6 continued. (d - top) Map of the depolarisation between 4848 MHz and 1417 MHz. (e - middle) Map of the rotation measure (rad m^{-2}) between 4848 MHz, 1662 MHz and 1417 MHz. (f - bottom) Map of the magnetic field direction (degrees). All contours are at 5σ (5.2 mJy beam^{-1})$\times$ (-1, 1, 2, 4...,1024). Beam size of 4.5"$\times$3.5".

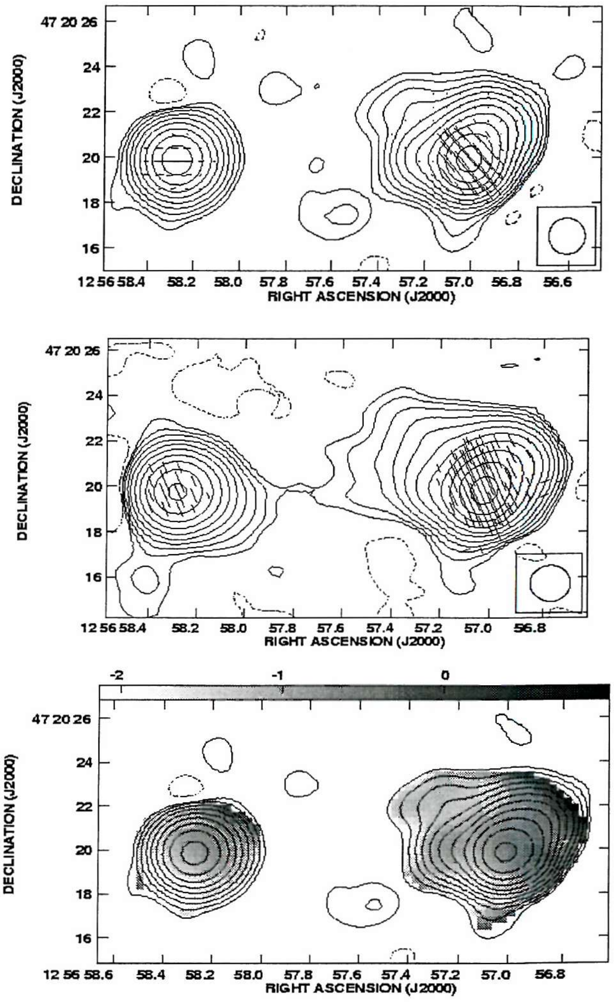

Figure B.7: Maps of the radio source **3C 280** . (a - top) 4848 MHz total intensity map with vectors of polarisation overlaid. The contour levels are at 5σ (0.8 mJy beam^{-1})$\times$ (-1, 1, 2, 4... ,1024). 1 arc second corresponds to 3.3×10^{-2} Jy beam^{-1}. (b - middle) 1465 MHz total intensity map with vectors of polarisation overlaid. The contour levels are at 3σ (1.6 mJy beam^{-1})$\times$ (-1, 1, 2, 4... ,1024). 1 arc second corresponds to 3.3×10^{-2} Jy beam^{-1}. (c - bottom) Map of the spectral index between 4848 MHz and 1465 MHz contours as (a).

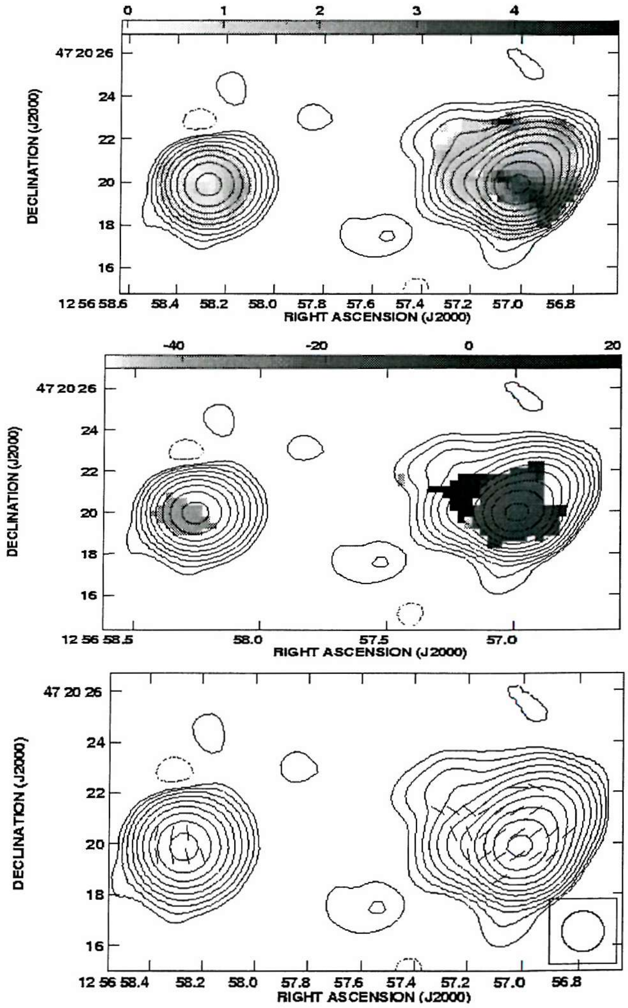

Figure B.7 continued. (d - top) Map of the depolarisation between 4848 MHz and 1465 MHz. (e - middle) Map of the rotation measure (rad m^{-2}) between 4848 MHz, 1665 MHz and 1465 MHz. (f - bottom) Map of the magnetic field direction (degrees). All contours are at 5σ at 4848 MHz (0.8 mJy $beam^{-1}$)× (-1, 1, 2, 4...,1024). Beam size of 1.6"×1.6".

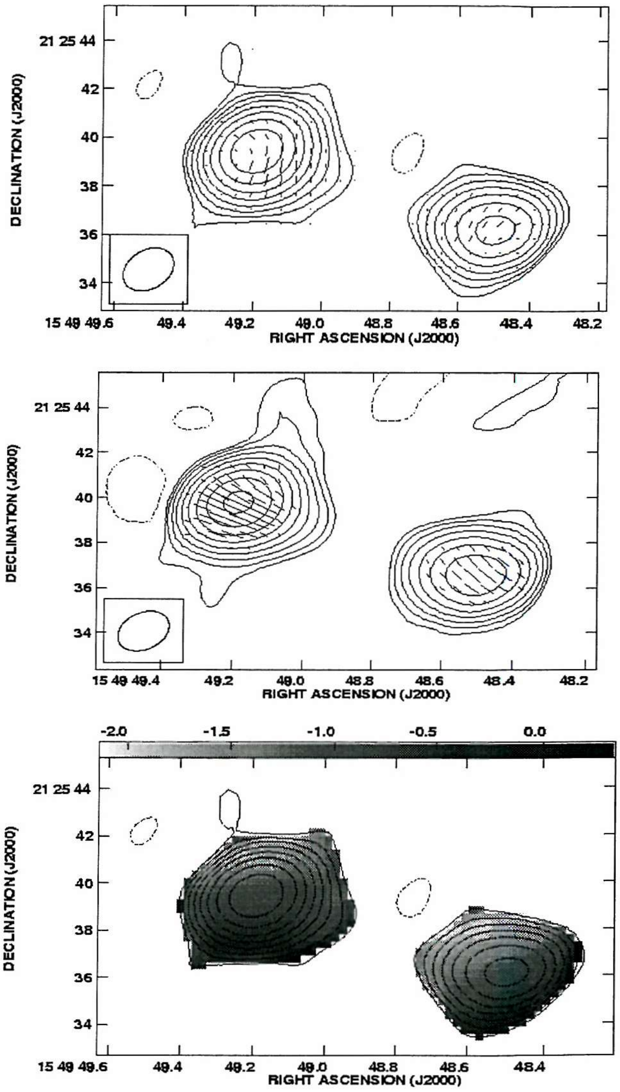

Figure B.8: Maps of the radio source **3C 324** . (a - top) 4848 MHz total intensity map with vectors of polarisation overlaid. The contour levels are at 5σ (1.5 mJy beam^{-1})$\times$ (-1, 1, 2, 4... ,1024). 1 arc second corresponds to 3.3×10^{-3} Jy beam^{-1}. (b - middle) 1465 MHz total intensity map with vectors of polarisation overlaid. The contour levels are at 3σ (3.5 mJy beam^{-1})$\times$ (-1, 1, 2, 4... ,1024). 1 arc second corresponds to 3.3×10^{-3} Jy beam^{-1}. (c - bottom) Map of the spectral index between 4848 MHz and 1465 MHz contours are as (a).

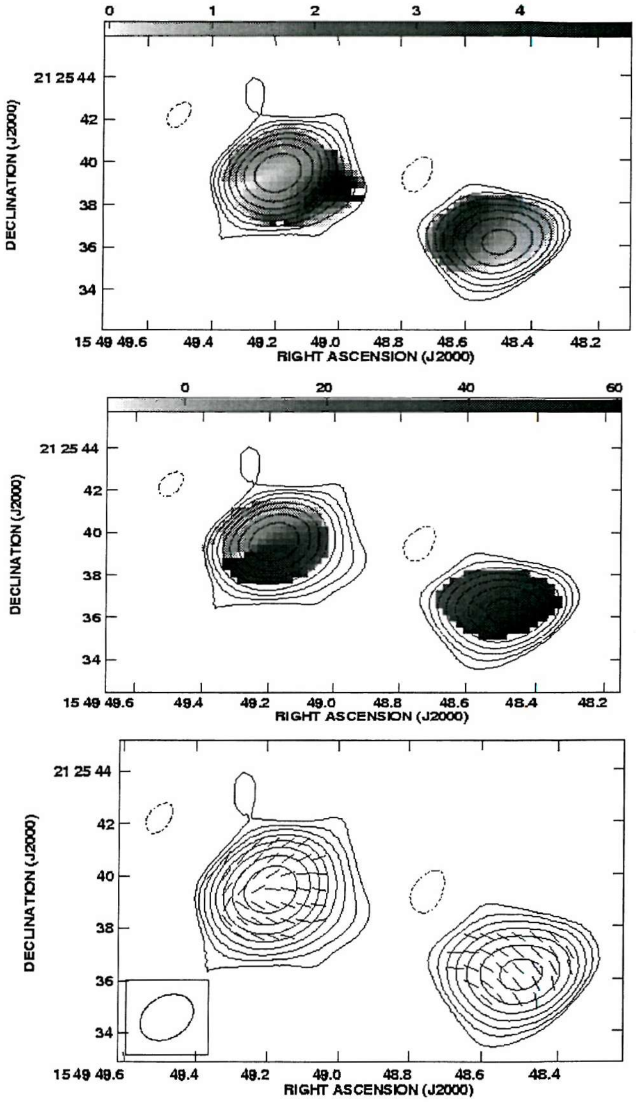

Figure B.8 continued. (d - top) Map of the depolarisation between 4848 MHz and 1465 MHz. (e - middle) Map of the rotation measure (rad m^{-2}) between 4848 MHz, 1665 MHz and 1465 MHz. (f - bottom) Map of the magnetic field direction (degrees). All contours are at 5σ at 4848 MHz (1.5 mJy beam^{-1})$\times$ (-1, 1, 2, 4...,1024). Beam size of 2.2" $\times$1.6".

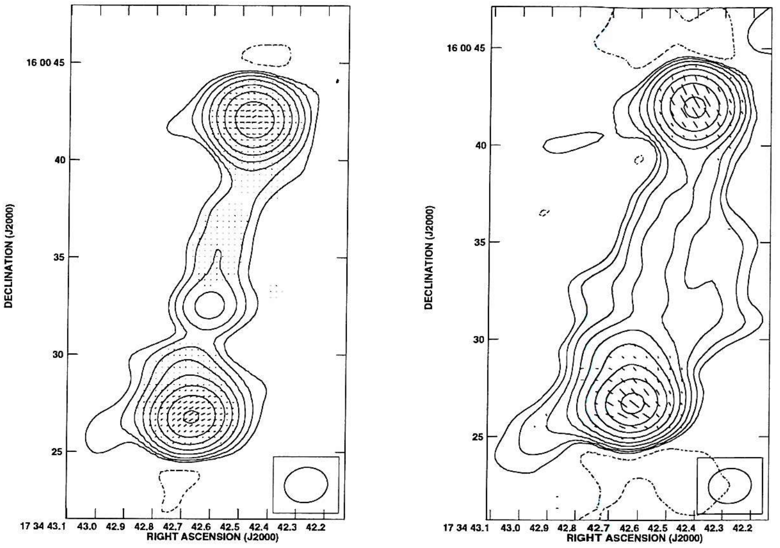

Figure B.9: Maps of the radio source **4C 16.49**. (a - left) 4710 MHz total intensity map with vectors of polarisation overlaid. The contour levels are at 5σ (0.8 mJy beam^{-1})$\times$ (-1, 1, 2, 4... ,1024). 1 arc second corresponds to 3.3×10^{-3} Jy beam^{-1}. (b - right) 1465 MHz total intensity map with vectors of polarisation overlaid. The contour levels are at 3σ (1.5 mJy beam^{-1})$\times$ (-1, 1, 2, 4... ,1024). 1 arc second corresponds to 3.3×10^{-3} Jy beam^{-1}.

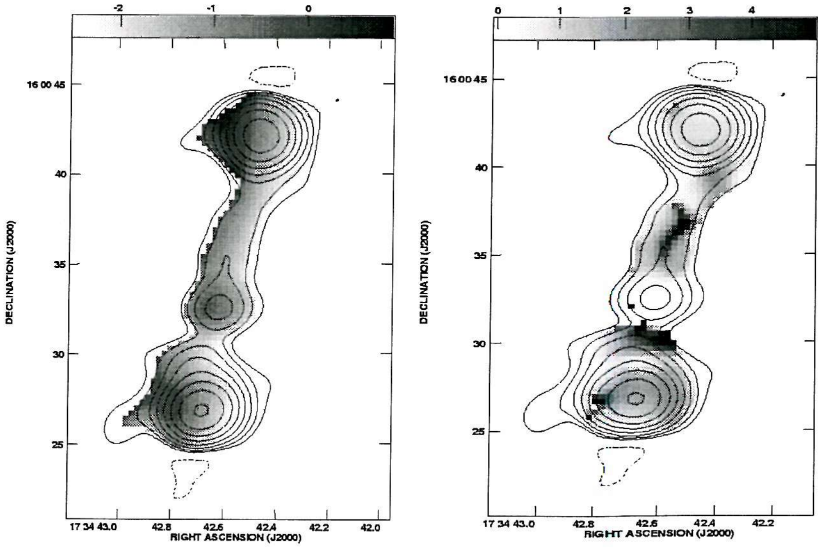

Figure B.9 continued. (c - left) Map of the spectral index between 4710 MHz and 1465 MHz. (d - right) Map of the depolarisation between 4710 MHz and 1465 MHz. All contours are at 5σ at 4710 MHz (0.8 mJy beam^{-1})$\times$ (-1, 1, 2, 4...,1024). Beam size of 2.2"$\times$1.8".

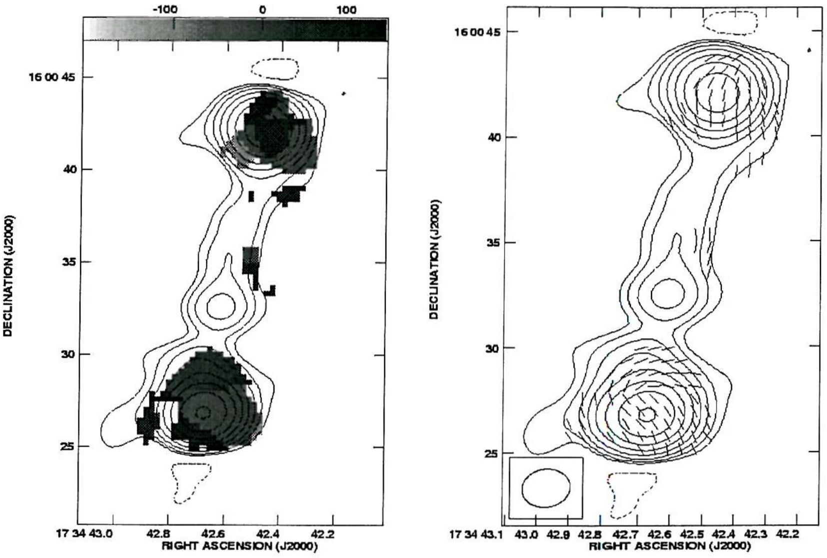

Figure B.9 continued. (e - left) Map of the rotation measure (rad m^{-2}) between 4710 MHz, 1665 MHz and 1465 MHz. (f - right) Map of the magnetic field direction (degrees). All contours are at 5σ at 4710 MHz (0.8 mJy beam^{-1})× (-1, 1, 2, 4...,1024). Beam size of 2.2"×1.8".

Appendix C

Sample C maps

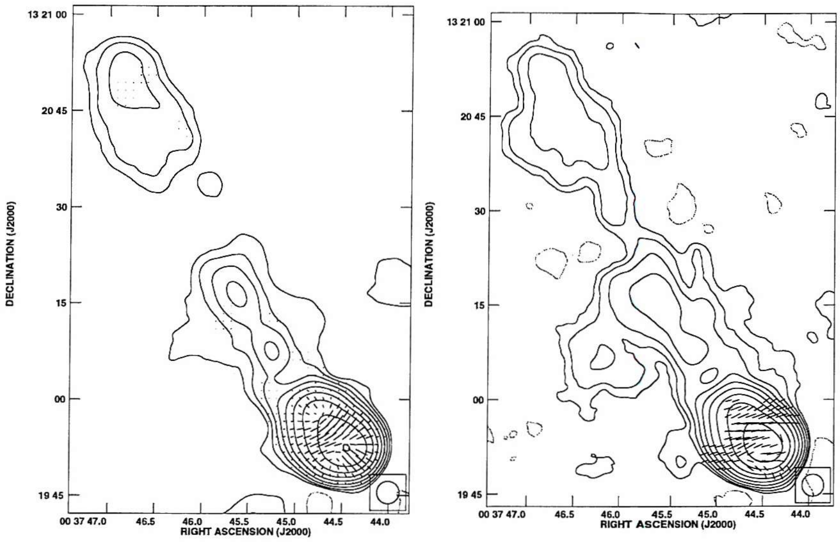

Figure C.1: Maps of the radio source **3C 16**. (a - left) 4710 MHz total intensity map with vectors of polarisation overlaid. The contour levels are at 5σ (0.4 mJy beam^{-1})$\times$ (-1, 1, 2, 4... ,1024). 1 arc second corresponds to 5.6×10^{-3} Jy beam^{-1}. (b - right) 1452 MHz total intensity map with vectors of polarisation overlaid. The contour levels are at 3σ (0.8 mJy beam^{-1})$\times$ (-1, 1, 2, 4... ,1024). 1 arc second corresponds to 5.6×10^{-3} Jy beam^{-1}.

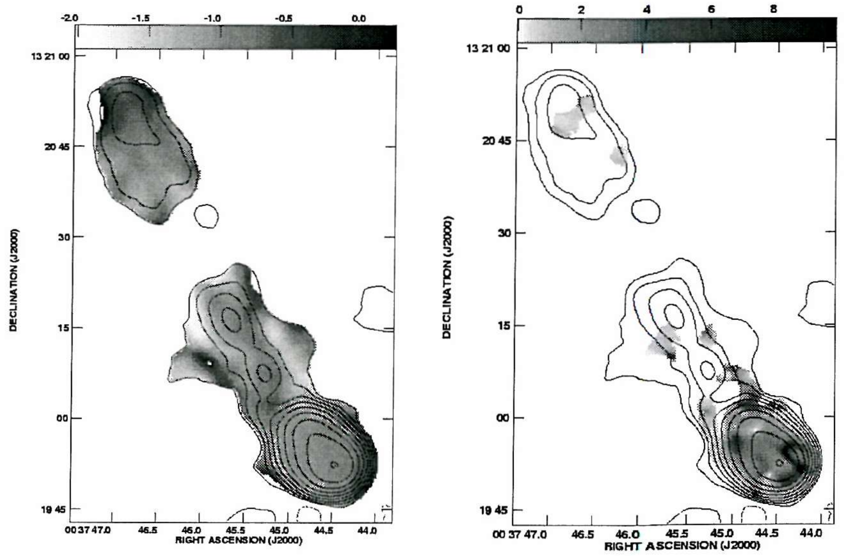

Figure C.1 continued. (c - left) Map of the spectral index between 4710 MHz and 1452 MHz. (d - right) Map of the depolarisation between 4710 MHz and 1452 MHz. All contours are at 5σ at 4710 MHz (0.40 mJy beam^{-1})$\times$ (-1, 1, 2, 4...,1024). Beam size of 3.5"$\times$3.5".

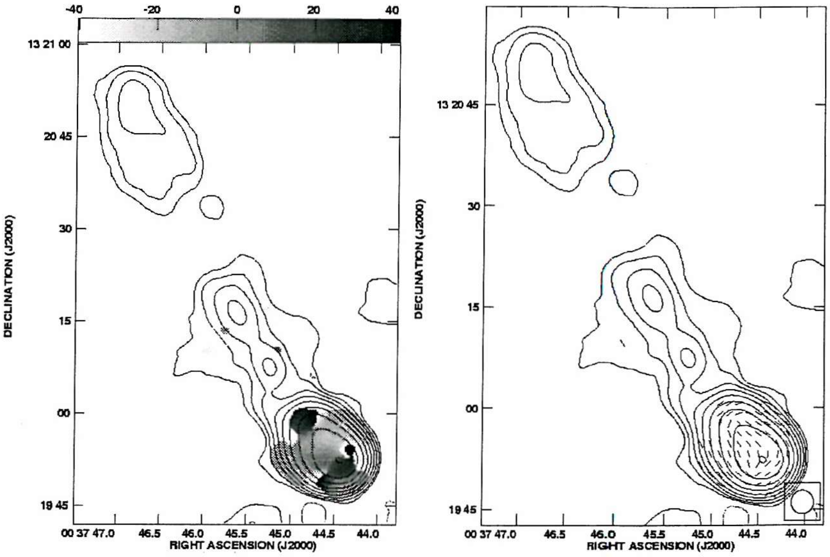

Figure C.1 continued. (e - left) Map of the rotation measure (rad m^{-2}) between 4885 MHz, 4535 MHz, 1502 MHz and 1452 MHz. (f - right) Map of the magnetic field direction (degrees). All contours are at 5σ at 4710 MHz (0.40 mJy beam^{-1})× (-1, 1, 2, 4...,1024). Beam size of 3.5"×3.5".

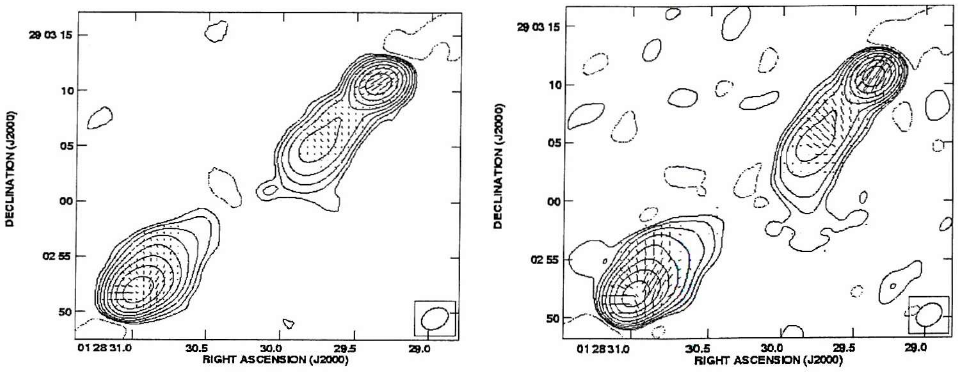

Figure C.2: Maps of the radio source **3C 42** . (a - left) 4710 MHz total intensity map with vectors of polarisation overlaid. The contour levels are at 5σ (1.0 mJy beam^{-1})× (-1, 1, 2, 4... ,1024). 1 arc second corresponds to 3.3×10^{-3} Jy beam^{-1}. (b - right) 1452 MHz total intensity map with vectors of polarisation overlaid. The contour levels are at 3σ (2.5 mJy beam^{-1})× (-1, 1, 2, 4... ,1024). 1 arc second corresponds to 3.3×10^{-3} Jy beam^{-1}

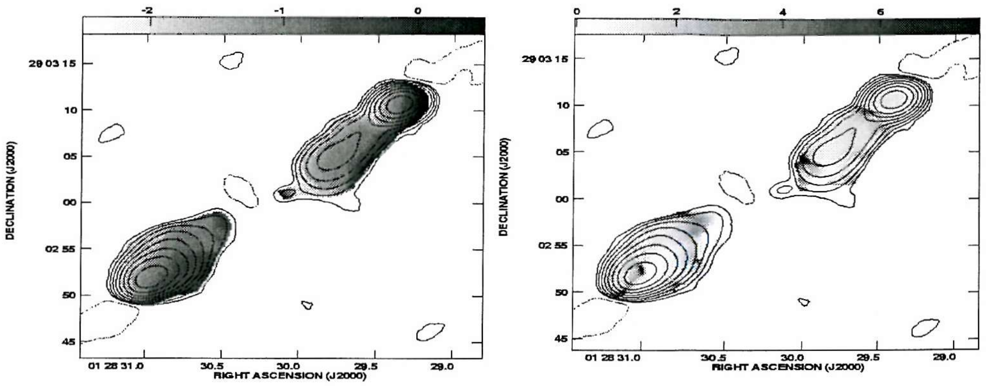

Figure C.2 continued. (c - left) Map of the spectral index between 4710 MHz and 1465 MHz. (d - right) Map of the depolarisation between 4710 MHz and 1452 MHz. All contours are at 5σ at 4710 MHz (1.0 mJy beam^{-1})$\times$ (-1, 1, 2, 4...,1024). Beam size of 2.5"$\times$1.8".

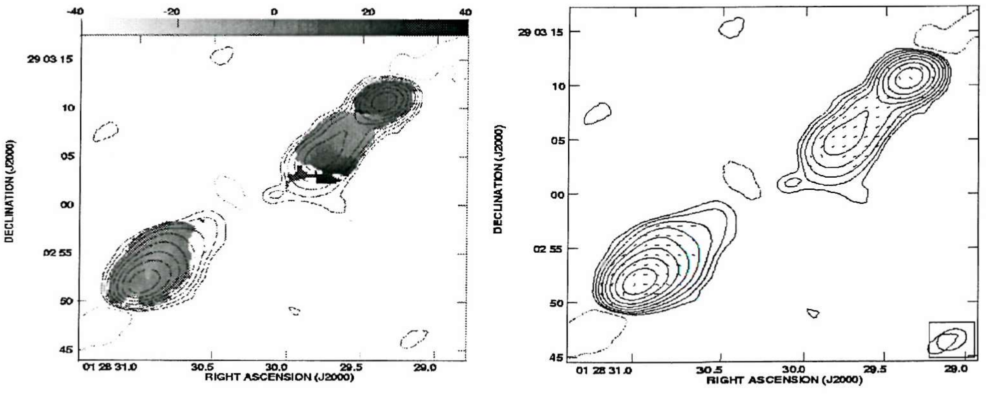

Figure C.2 continued. (e - left) Map of the rotation measure (rad m^{-2}) between 4885 MHz, 4535 MHz, 1502 MHz and 1452 MHz. (f - right) Map of the magnetic field direction (degrees). All contours are at 5σ at 4710 MHz (1.0 mJy beam^{-1})$\times$ (-1, 1, 2, 4...,1024). Beam size of 2.5"$\times$1.8".

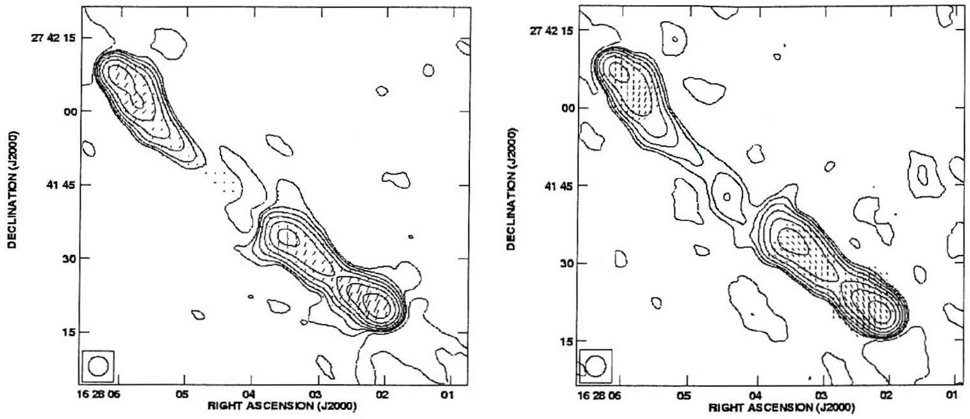

Figure C.3: Maps of the radio source **3C 341** . (a - left) 4710 MHz total intensity map with vectors of polarisation overlaid. The contour levels are at 5σ (0.7 mJy beam^{-1})$\times$ (-1, 1, 2, 4... ,1024). 1 arc second corresponds to 5.0×10^{-3} Jy beam^{-1}. (b - right) 1452 MHz total intensity map with vectors of polarisation overlaid. The contour levels are at 3σ (1.4 mJy beam^{-1})$\times$ (-1, 1, 2, 4... ,1024). 1 arc second corresponds to 1.3×10^{-2} Jy beam^{-1}.

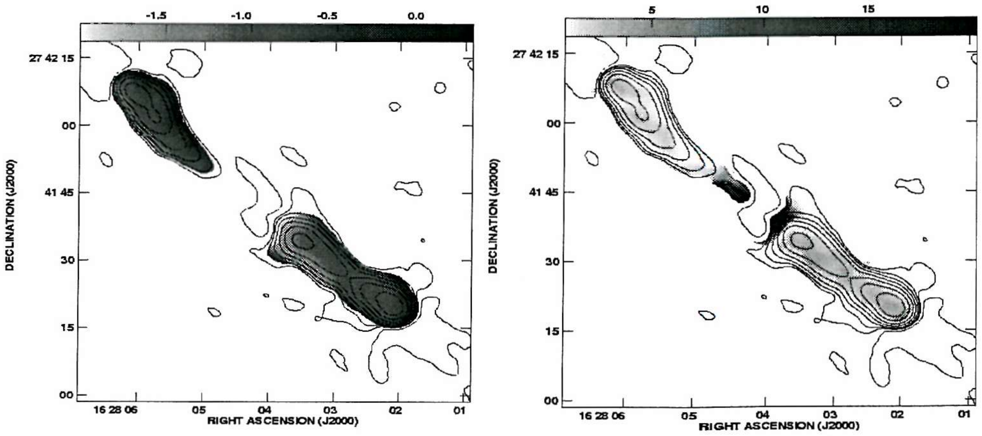

Figure C.3 continued. (c - left) Map of the spectral index between 4710 MHz and 1452 MHz. (d - right) Map of the depolarisation between 4710 MHz and 1452 MHz. All contours are at 5σ at 4710 MHz (0.7 mJy beam^{-1})$\times$ (-1, 1, 2, 4...,1024). Beam size of 4.0" $\times$ 4.0".

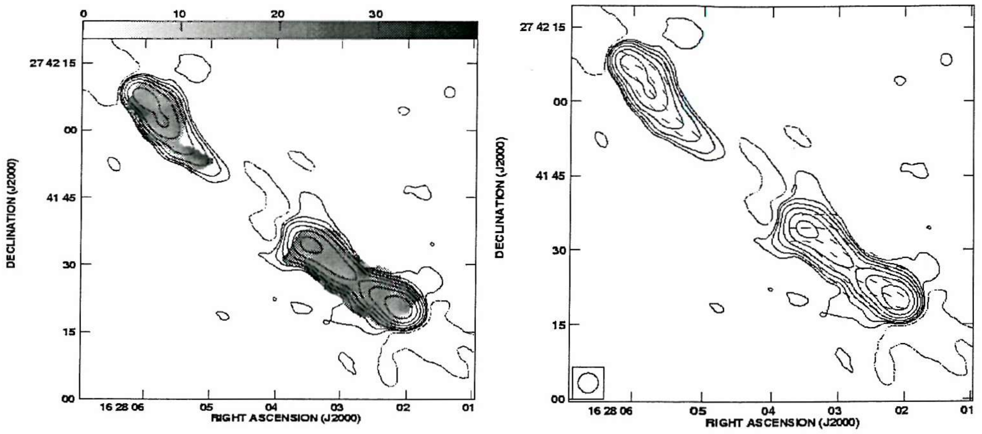

Figure C.3 continued. (e - left) Map of the rotation measure (rad m^{-2}) between 4885 MHz, 4535 MHz, 1502 MHz and 1452 MHz. (f - right) Map of the magnetic field direction (degrees).All contours are at 5σ at 4710 MHz (0.7 mJy beam^{-1})× (-1, 1, 2, 4...,1024). Beam size of 4.0"×4.0".

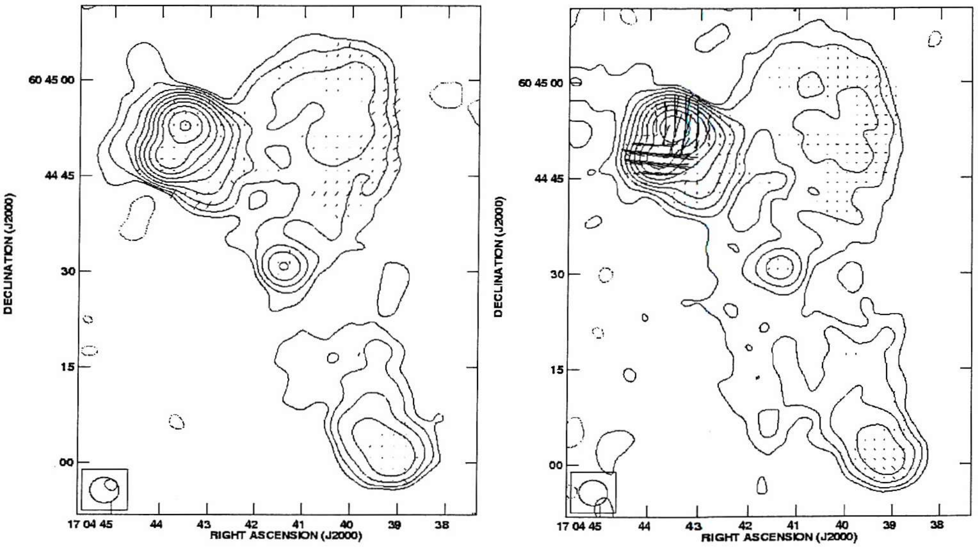

Figure C.4: Maps of the radio source **3C 351** . (a - left) 4810 MHz total intensity map with vectors of polarisation overlaid. The contour levels are at 5σ (1.0 mJy beam^{-1})× (-1, 1, 2, 4... ,1024). 1 arc second corresponds to 1.7×10^{-1} Jy beam^{-1}. (b - right) 1452 MHz total intensity map with vectors of polarisation overlaid. The contour levels are at 3σ (2.0 mJy beam^{-1})× (-1, 1, 2, 4... ,1024). 1 arc second corresponds to 8.3×10^{-3} Jy beam^{-1}.

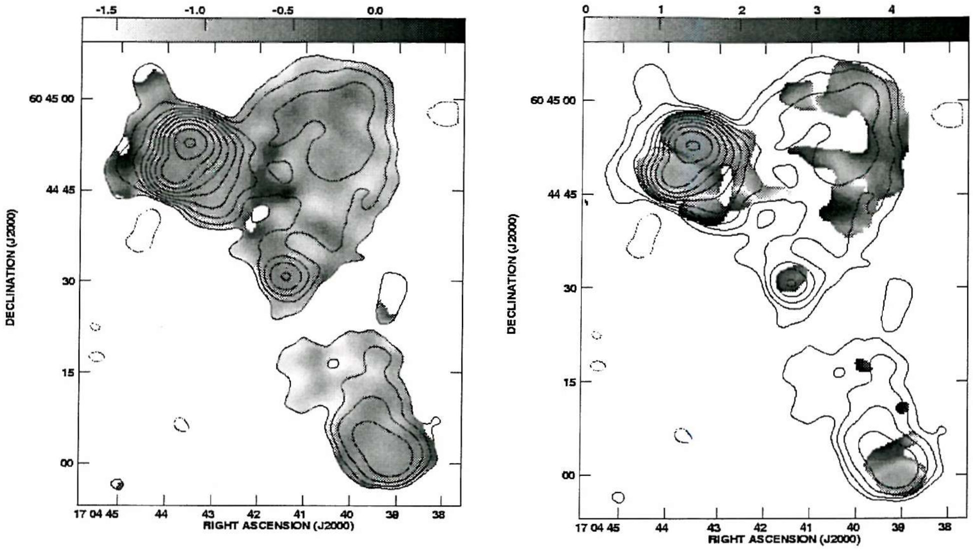

Figure C.4 continued. (c - left) Map of the spectral index between 4810 MHz and 1452 MHz. (d - right) Map of the depolarisation between 4810 MHz and 1452 MHz. All contours are at 5σ at 4810 MHz (1.0 mJy beam^{-1})× (-1, 1, 2, 4...,1024). Beam size of 4.5"×4.0".

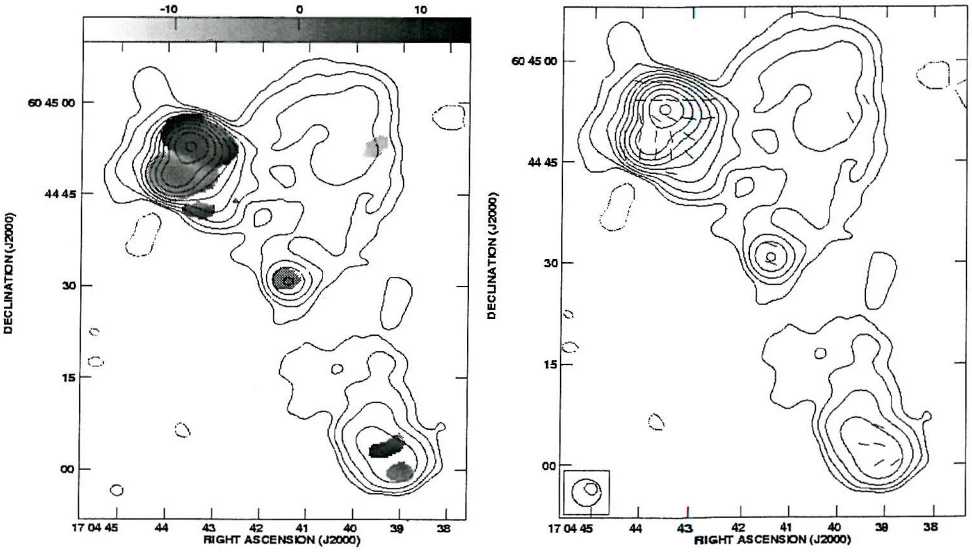

Figure C.4 continued. (e - left) Map of the rotation measure (rad m^{-2}) between 4810 MHz, 1502 MHz and 1452 MHz. (f - right) Map of the magnetic field direction (degrees). All contours are at 5σ at 4810 MHz (1.0 mJy beam^{-1})× (-1, 1, 2, 4...,1024). Beam size of 4.5"×4.0".

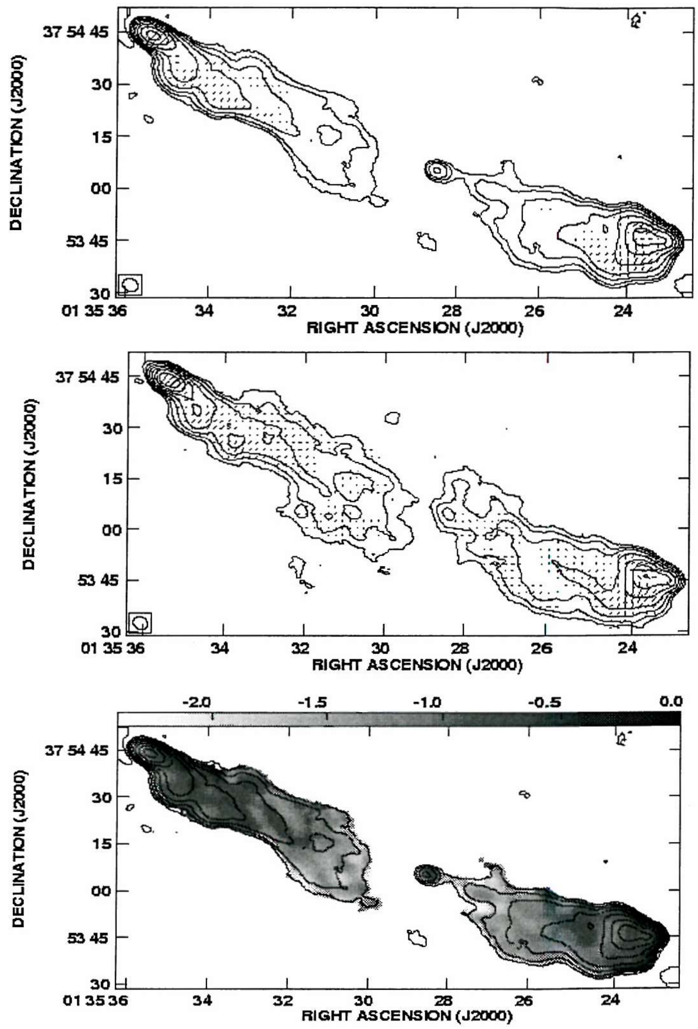

Figure C.5: Maps of the radio source **3C 46**. (a -top) 4710MHz total intensity map with vectors of polarisation overlaid. The contour levels are at 5σ (0.25 mJy beam^{-1})$\times$ (-1, 1, 2, 4..., 1024). 1 arc second corresponds to 1.7×10^{-3} Jy beam^{-1}. (b - middle) 1452MHz total intensity map with vectors of polarisation overlaid. The contour levels are at 3σ (1.0 mJy beam^{-1})$\times$ (-1, 1, 2, 4,..,1024). 1 arc second corresponds to 5.5×10^{-4} Jy beam^{-1}. (c - bottom) Map of the spectral index between 4710 MHz and 1452 MHz. Contours are as (a).

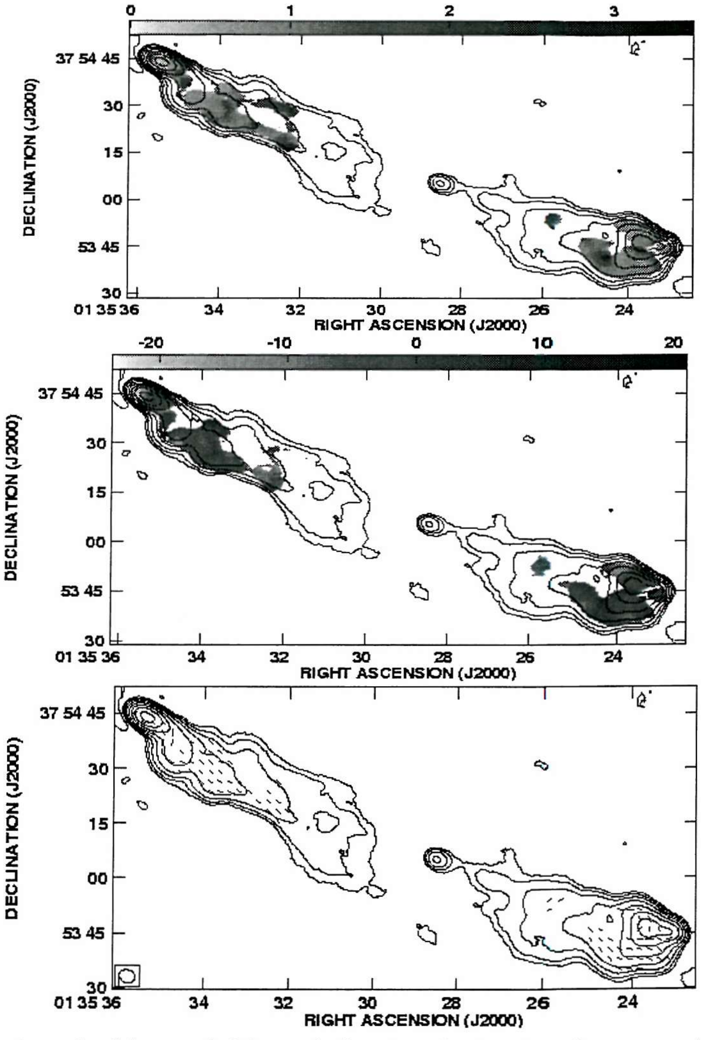

Figure C.5 continued. (d - top) Map of the depolarisation between 4710 MHz and 1452 MHz. (e - middle) Map of the rotation measure (rad m^{-2}) between 4885 MHz, 4535 MHz, 1502 MHz and 1452 MHz. (f - bottom) Map of the magnetic field direction (degrees). All contours are at 5σ at 4710 MHz (0.25 mJy $beam^{-1}$)× (-1, 1, 2, 4...,1024). Beam size of 4.5"×3.0".

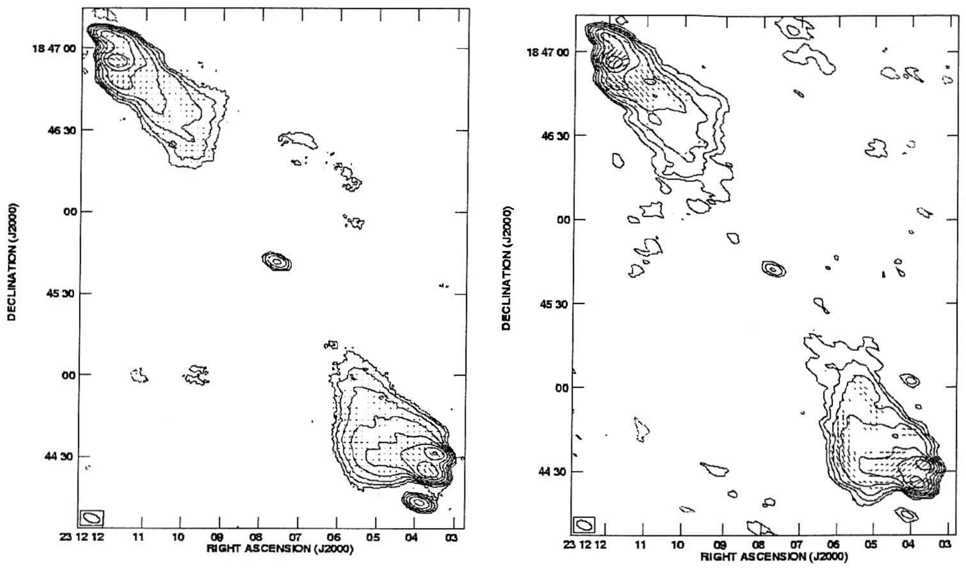

Figure C.6: Maps of the radio source **3C 457**. (a - left) 4710 MHz total intensity map with vectors of polarisation overlaid. The contour levels are at 5σ (0.3 mJy beam^{-1})$\times$ (-1, 1, 2, 4... ,1024). 1 arc second corresponds to 1.7×10^{-3} Jy beam^{-1}. (b - right) 1452 MHz total intensity map with vectors of polarisation overlaid. The contour levels are at 3σ (1.0 mJy beam^{-1})$\times$ (-1, 1, 2, 4... ,1024). 1 arc second corresponds to 1.7×10^{-3} Jy beam^{-1}.

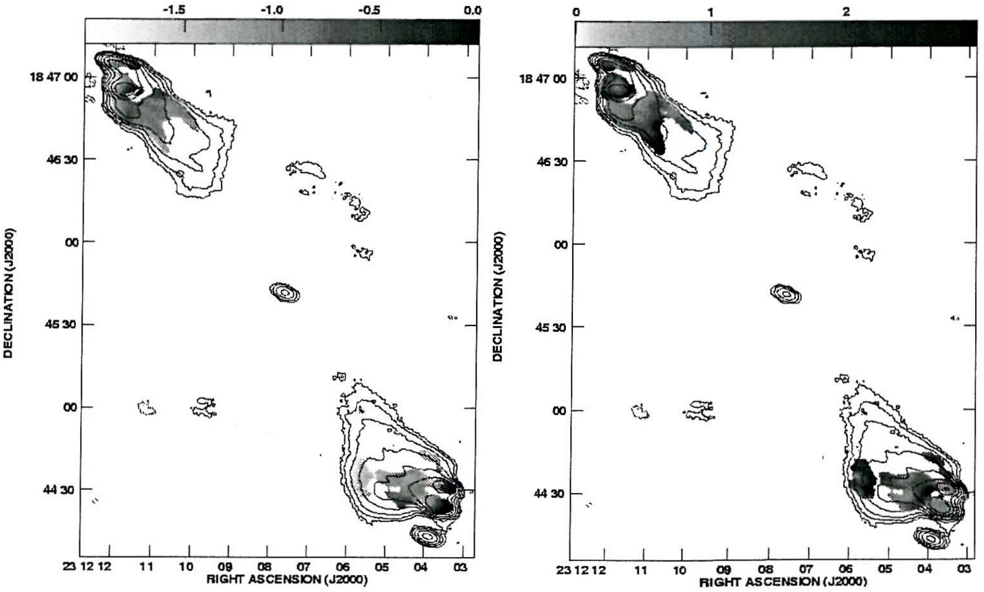

Figure C.6 continued. (c - left) Map of the spectral index between 4710 MHz and 1452 MHz. (d - right) Map of the depolarisation between 4710 MHz and 1452 MHz. All contours are at 5σ at 4710 MHz (0.3 mJy beam^{-1})$\times$ (-1, 1, 2, 4...,1024). Beam size of 6.0"$\times$3.0".

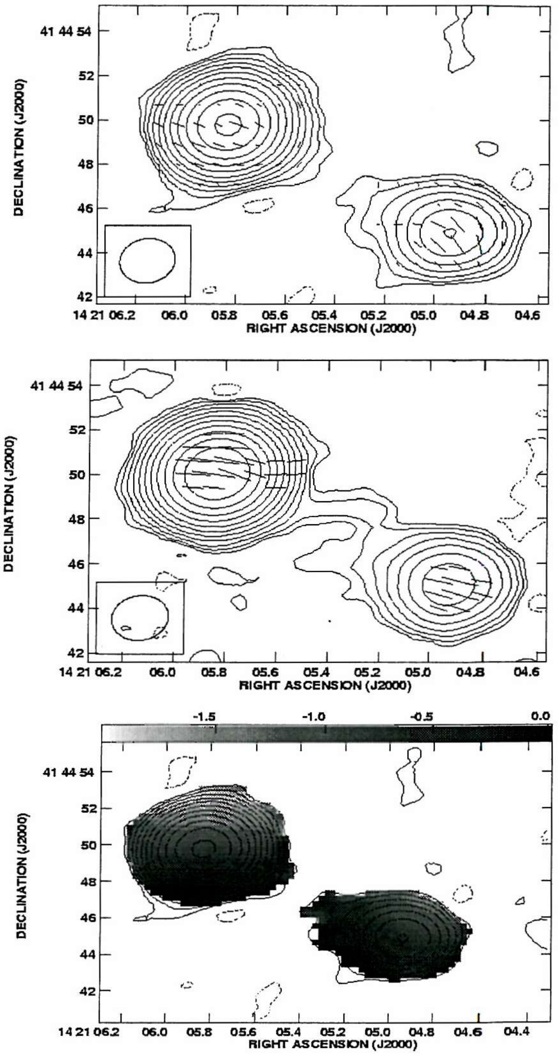

Figure C.7: Maps of the radio source **3C 299** . (a - top) 4770 MHz total intensity map with vectors of polarisation overlaid. The contour levels are at 5σ (0.7 mJy beam^{-1})$\times$ (-1, 1, 2, 4... ,1024). 1 arc second corresponds to 8.3×10^{-4} Jy beam^{-1}. (b - middle) 1452 MHz total intensity map with vectors of polarisation overlaid. The contour levels are at 3σ (1.0 mJy beam^{-1})$\times$ (-1, 1, 2, 4... ,1024). 1 arc second corresponds to 5.6×10^{-3} Jy beam^{-1}. (c - bottom) Map of the spectral index between 4770 MHz and 1452 MHz contours are as (a).

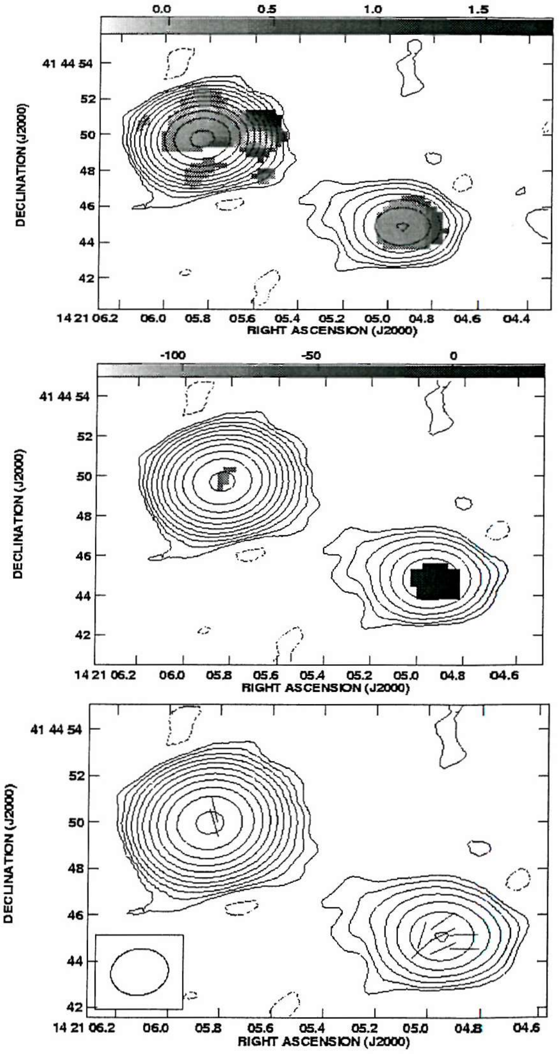

Figure C.7 continued. (d - top) Map of the depolarisation between 4770 MHz and 1452 MHz.(e - middle) Map of the rotation measure (rad m^{-2}) between 4770 MHz, 1502 MHz and 1452 MHz. (f - bottom) Map of the magnetic field direction (degrees). All contours are at 5σ at 4770 MHz (0.7 mJy $beam^{-1}$)× (-1, 1, 2, 4...,1024). Beam size of 2.5"×2.0".

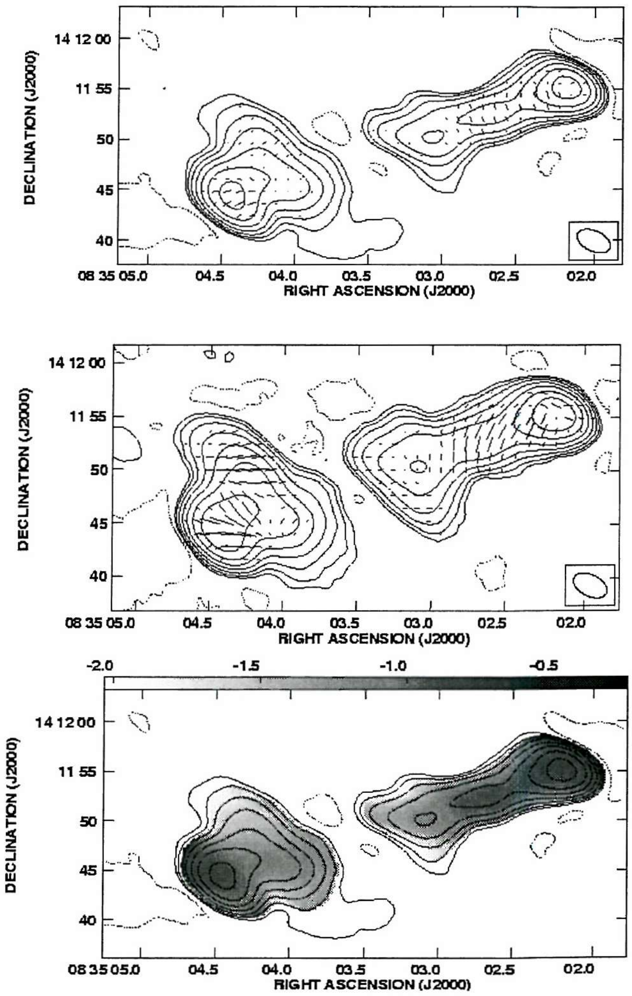

Figure C.8: Maps of the radio source **4C 14.27** . (a - top) 4710 MHz total intensity map with vectors of polarisation overlaid. The contour levels are at 5σ (0.4 mJy beam^{-1})$\times$ (-1, 1, 2, 4... ,1024). 1 arc second corresponds to 3.3×10^{-3} Jy beam^{-1}. (b - middle) 1452 MHz total intensity map with vectors of polarisation overlaid. The contour levels are at 3σ (1.0 mJy beam^{-1})$\times$ (-1, 1, 2, 4... ,1024). 1 arc second corresponds to 3.3×10^{-3} Jy beam^{-1}. (c - bottom) Map of the spectral index between 4710 MHz and 1452 MHz contours are as (a).

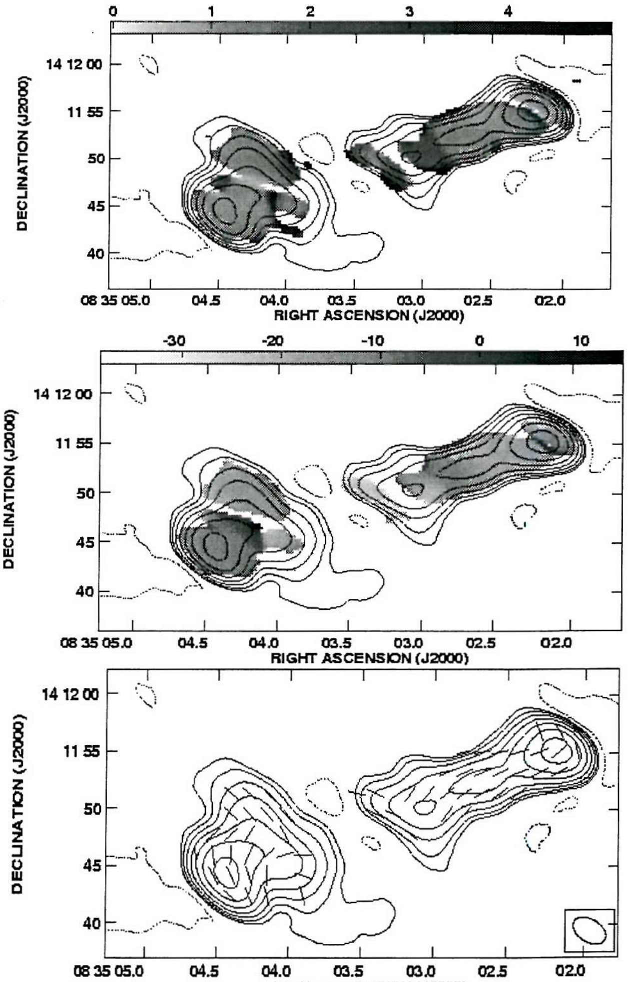

Figure C.8 continued. (d - top) Map of the depolarisation between 4710 MHz and 1452 MHz.(e - middle) Map of the rotation measure (rad m^{-2}) between 4885 MHz, 4535 MHz, 1502 MHz and 1452 MHz. (f - bottom) Map of the magnetic field direction (degrees). All contours are at 5σ at 4710 MHz (0.4 mJy beam^{-1})$\times$ (-1, 1, 2, 4...,1024). Beam size of 3.5"$\times$2.0".

Appendix D

Cosmology

D.1 Basic assumptions used

The frequency at which I observe my sources is redshift dependent,

$$\nu_{\text{emit}} = (1+z)\nu_{\text{observed}} \tag{D.1}$$

where ν_{emit} is the emitted frequency, ν_{observed} is the observed frequency and z is the redshift of the source. Although I observe at 1.4 GHz and 4.8 GHz the emitted frequency will be slightly different for each source. This is the reason why the polarisation observations are shifted to a common redshift, thus removing any residual redshift effects.

To convert from the angular size of a source on the sky, θ, to a physical size, D$_{source}$, I use the angular diameter distance formula,

$$\begin{aligned} D_{source} &= \frac{R_{\circ} s_r\, \theta}{1+z} && \text{(D.2)} \\ \text{where,}\quad R_{\circ} s_r &= \left(\frac{2c}{H_{\circ}}\right) \frac{\Omega z + (\Omega - 2)(\sqrt{1+\Omega z} - 1)}{\Omega^2 (1+z)}. && \text{(D.3)} \end{aligned}$$

where Ω is the density parameter of the Universe, c is the speed of light and $H_{\circ}$ is the Hubble constant.

The flux density of a source is also dependent on the redshift of a source,

$$S_{\nu} = \frac{P_{\nu}}{(1+z)(R_o s_r)^2} \tag{D.4}$$

where P_{ν} is the radio-luminosity at a specific frequency ν.

Appendix E

3CRR sample

Source	z	θ (arc sec.)	S_{178MHz} Jy	S_{365MHz} Jy	$S_{1400MHz}$ Jy	R	REF
4C 12.03	0.16	240	10.9	4.45^B	2.01^A	1.77	LP91
3C 6.1	0.84	26	14.9	9.98^D	3.56^C	1.73	NRH95
3C 9	2.01	14	19.4	9.50	2.18^E	3.34	F02
3C 13	1.35	28	13.1	7.72	1.87^E	1.50	LLA95
3C 14	1.47	24	11.3	6.83	1.98^E	1.31	ALB94
3C 16	0.41	78	12.2	6.15	1.88^C	2.62	G04
3C 19	0.48	7	13.2	8.98	3.22^E	3.27	DRAGN
3C 20	0.17	54	46.8	30.30	11.53^E	2.24	HPPR97
3C 22	0.94	24	13.2	8.58	2.25^C	2.51	BLR97
3C 33	0.06	255	59.3	20.42	13.65^C	1.70	LP91
3C 33.1	0.18	227	14.2	5.34^C	3.23^C	1.93	LCF01
3C 34	0.69	49	13.0	7.09	1.65^E	2.72	NRH99
3C 35	0.07	750	11.4	3.78^C	2.31^C	1.84	DRAGN
3C 41	0.79	25	11.6	7.53^G	3.71^E	1.81	NRH99
3C 42	0.40	29	13.1	8.92	2.89^E	2.22	G04
3C 46	0.44	158	11.1	2.16^C	1.17^C	3.70	G04
3C 47	0.43	77	28.8	13.02	$3.85\ ^G$	1.22	HLL94
3C 49	0.62	1	11.2	7.74	2.74^C	0.78	PPR85
3C 55	0.74	72	23.4	11.98	2.69^C	3.34	FBB93
3C 61.1	0.19	186	34.0	20.54^D	$6.00\ ^G$	2.69	LP91
3C 65	1.18	17	16.6	10.43	3.11^E	1.50	G04
3C 67	0.31	3	10.9	8.01	3.02^E	1.72	AG95
3C 68.1	1.24	53	14.0	8.87	2.49^C	1.88	HLL94
3C 79	0.26	89	33.2	13.30	4.943^G	2.25	HPPR97
3C 98	0.03	310	51.4	$26.67\ ^G$	$10.20\ ^G$	1.95	DRAGN
3C 109	0.31	103	23.5	13.47	4.103^G	2.05	G04
4C 14.11	0.21	116	12.1	4.67	2.10^A	1.62	HPPR97

Source	z	θ (arc sec.)	$S_{178\mathrm{MHz}}$ Jy	$S_{365\mathrm{MHz}}$ Jy	$S_{1400\mathrm{MHz}}$ Jy	R	REF
3C 123	0.22	38	206.0	122.53^G	47.96^G	1.98	HPPR97
3C 132	0.21	22	14.9	10.54	3.43^E	1.97	HPPR97
3C 153	0.28	9	16.7	11.25	4.13^G	1.53	HPPR97
3C 171	0.24	33	21.3	12.69	3.68^E	1.64	HPPR97
3C 172	0.52	121	16.5	8.40	2.89^H	1.88	SC85
3C 173.1	0.29	61	16.8	9.52^D	2.60^C	1.78	HPPR97
3C 175	0.77	52	19.2	10.22	2.44^C	1.71	HLL94
3C 175.1	0.92	7	12.4	5.64	1.93^E	1.39	NRH99
3C 181	1.38	6	15.8	7.62	2.33^C	0.93	PH74
3C 184	0.99	5	14.4	9.08	2.58^E	2.06	LP91
3C 184.1	0.12	182	14.2	9.57^D	3.30^G	2.84	LP91
3C 186	1.06	3	15.4	6.58	1.24^E	2.00	AG95
DA 240	0.04	2109	23.2	130.00^I	0.19^E	1.48	T82
3C 190	1.20	7	16.4	9.09	2.73^E	1.21	AG95
3C 191	1.95	5	14.2	7.49	1.85^E	2.62	AG95
3C 192	0.06	200	23.0	14.39^G	4.80^G	3.18	BHB88
3C 196	0.87	6	74.3	49.02	15.01^E	0.75	ASZ91
3C 200	0.46	25	12.3	6.41	2.04^H	1.90	DRAGN
4C 14.27	0.39	36	11.2	4.41	1.03^A	2.30	G04
3C 204	1.11	37	11.4	5.49	1.38^A	2.92	HLL94
3C 205	1.53	18	13.7	9.27	2.26^E	1.29	BMS88
3C 207	0.69	13	14.8	8.92	2.61^E	1.37	PH74
3C 208	1.11	14	18.3	10.33	2.36^C	1.91	HLL94
3C 212	1.05	9	16.5	8.34	2.37^E	1.50	ASZ91
3C 215	0.41	56	12.4	6.30^C	1.59^C	1.52	HLL94
3C 216	0.67	30	22.0	13.93	4.23^E	1.70	AG95
3C 217	0.90	12	12.3	8.37	2.16^C	2.88	BLR95
3C 219	0.17	190	44.9	14.00^H	8.46^C	1.50	NRH99
3C 220.1	0.61	35	17.2	9.23^D	2.24^E	2.29	JPR77
3C 220.3	0.69	10	17.1	11.59	2.89^C	1.19	JPR77
3C 223	0.14	306	16.0	8.51^G	3.58^C	2.95	LP91
3C 225B	0.58	5	23.2	10.17	3.34^E	1.98	-
3C 226	0.82	35	16.4	9.34	2.39^C	1.80	BLR97
4C 73.08	0.06	1004	15.6	24.20^J	2.65^A	1.33	DRAGN
3C 228	0.55	46	23.8	10.44	3.69^A	2.40	JLG95
3C 234	0.18	112	34.2	15.78	5.38^G	3.29	HPPR97
3C 236	0.10	2478	15.7	7.60	3.28^K	1.13	ALB94
3C 239	1.78	11	14.4	7.37	1.46^C	1.38	BLR94
4C 74.16	0.81	40	12.8	25.90^J	2.30^A	1.98	-
3C 241	1.62	1	12.6	7.18	1.69^C	0.80	PPR85
3C 244.1	0.43	51	22.1	13.89	3.94^C	4.32	F02

Source	z	θ (arc sec.)	S_{178MHz} Jy	S_{365MHz} Jy	$S_{1400MHz}$ Jy	R	REF
3C 245	1.03	9	15.7	9.45	3.31^E	1.98	-
3C 247	0.74	15	11.6	7.61	2.88^E	4.15	ALB94
3C 249.1	0.31	47	11.7	7.55^D	2.34^A	1.59	HLL94
3C 252	1.11	60	12.0	6.56	1.21^C	1.12	G04
3C 254	0.73	15	21.7	12.57	3.13^E	1.98	-
3C 263	0.66	51	16.6	11.12	3.00^G	1.98	-
3C 263.1	0.82	7	19.8	16.96	3.13^E	0.98	NRH99
3C 265	0.81	78	21.3	12.18	2.84^C	2.95	G04
3C 266	1.28	5	12.1	6.91	1.43^E	1.98	AG95
3C 267	1.14	38	15.9	9.07	2.16^C	1.77	G04
3C 268.1	0.97	46	23.3	10.02^C	6.80^G	1.87	G04
3C 268.3	0.37	1	11.7	11.27	3.72^E	1.56	AG95
3C 268.4	1.40	10	11.2	6.59	1.98^E	1.98	-
3C 270.1	1.52	12	14.8	9.74	2.85^E	1.69	ALB94
3C 274.1	0.42	150	18.0	5.12^C	2.78^C	3.56	AL87
3C 275.1	0.56	16	19.9	9.31^B	2.90^E	1.29	ALB94
3C 277.2	0.77	55	13.1	7.09	1.85^C	1.67	PRL97
3C 280	1.00	15	25.8	14.94	5.10^E	0.98	G04
3C 284	0.24	178	12.3	7.07	1.93^A	3.14	HPPR97
3C 285	0.08	180	12.3	3.14^C	2.04^C	1.25	AL87
3C 289	0.97	10	13.1	8.10	2.40^E	2.34	BLR97
3C 292	0.71	140	11.0	5.34	2.07^H	3.82	AL87
3C 294	1.78	15	11.2	6.12	1.32^E	1.98	-
3C 295	0.46	6	91.0	65.44^G	22.82^C	1.73	AL87
3C 299	0.37	11	12.9	8.17	3.15^E	1.17	G04
3C 300	0.27	101	19.5	10.47	3.70^G	3.23	HPPR98
3C 303	0.14	47	12.2	7.24	2.67^C	1.14	HPPR98
3C 318	1.57	1	13.4	9.21	2.69^E	1.25	AG95
3C 319	0.19	105	16.7	7.66	2.50^C	2.49	HPPR97
3C 321	0.10	307	14.7	9.31^G	3.50^G	2.04	BHB88
3C 322	1.68	33	11.0	6.94	1.98^C	1.53	LLA95
3C 324	1.21	10	17.2	8.91	2.44^C	1.07	G04
3C 326	0.09	1206	22.2	6.60^F	3.10^F	3.23	DRAGN
3C 325	0.86	16	17.0	12.12	3.56^E	3.70	FBP97
3C 330	0.55	60	30.3	21.88	7.10^G	1.20	F02
3C 334	0.56	58	11.9	6.80	2.15^C	1.58	HLL94
3C 336	0.93	28	12.5	7.88	2.74^C	1.65	HLL94
3C 341	0.45	74	11.8	6.35	2.15^C	3.14	HLL94
3C 340	0.78	46	11.0	7.79	2.49^C	2.10	JPR97
3C 337	0.63	46	12.9	9.98	2.94^C	2.07	BLR97
3C 343.1	0.75	0.3	12.5	8.00^C	4.83^C	0.89	AG95

Source	z	θ (arc sec.)	S_{178MHz} Jy	S_{365MHz} Jy	$S_{1400MHz}$ Jy	R	REF
3C 349	0.21	86	14.5	9.95	3.30^G	2.77	HPPR97
3C 351	0.37	74	14.9	8.37	3.27^G	1.34	G04
3C 352	0.81	13	12.3	7.85	1.87^E	1.57	ALB94
3C 356	1.08	75	12.3	6.39	1.41^C	3.00	FBB93
4C 16.49	1.30	16	11.4	6.27	1.46^E	1.10	G04
4C 13.66	1.45	6	12.3	6.95	1.70^E	1.49	LGS98
3C 368	1.13	8	15.0	7.40	1.11^C	2.67	BLR95
3C 381	0.16	73	18.1	8.71	3.910^G	2.11	HPPR97
3C 382	0.06	185	21.7	6.55	5.83^C	0.86	F02
3C 388	0.09	50	26.8	16.04	5.74^C	1.21	PH74
3C 390.3	0.06	229	51.8	30.19^D	11.90^G	1.40	F02
3C 401	0.20	24	22.8	14.34	5.07^E	1.49	HPPR97
3C 427.1	0.57	27	29.0	15.52^D	3.80^G	2.78	NRH95
3C 432	1.81	15	12.0	6.48	1.58^E	1.33	BHL94
3C 433	0.10	68	61.3	31.27	11.80^G	1.98	-
3C 436	0.21	109	19.4	5.74^C	3.40^C	2.75	HPPR97
3C 437	1.48	34	15.9	8.68	2.76^C	1.94	BLR97
3C 438	0.29	23	48.7	26.40	6.37^E	1.81	HPPR97
3C 441	0.71	37	13.7	8.34	2.52^C	1.58	FBP97
3C 452	0.08	280	59.3	32.67^G	10.54^C	2.16	DRAGN
3C 455	0.54	4	14.0	9.18	2.89^C	1.46	AG95
3C 457	0.43	210	14.3	5.68	1.75^A	2.45	G04
3C 469.1	1.34	74	12.1	6.46^D	1.76^C	1.98	-
3C 470	1.65	24	11.0	5.98	1.94^E	3.35	BLR97

Table E.1: Parameters used in the fitting on the KDA model in chapter 6. Column 1: 3CRR source name. Column 2: redshifts. Column 3: Angular size in arcseconds. Column 4: Flux density at 178 MHz. Column 5: Flux density at 365 MHz taken from Douglas et al. (1996) unless otherwise noted. Column 6: Flux density at 1400 MHz and Column 7: Average source lobe ratio. Columns 2, 3 and 4 use data taken from Willot (2003). Sources with no high quality maps have lobe ratios which are the average for the 3CRR sample. See Table E.2 for an explanation of the reference codes used.

Listing	Full Reference
A	White & Becker (1992)
B	Large et al. (1981)
C	Laing & Peacock (1980)
D	WENSS COLLABORATION (1998)
E	Condon et al. (1998)
F	Kellermann et al. (1969)
G	Kuehr et al. (1981)
H	Pauliny-Toth et al. (1966)
I	Viner & Erickson (1975)
J	Hales et al. (1995)
K	Becker et al. (1995)
LP91	Leahy & Perley (1991)
G04	Goodlet et al. (2004)
LLA95	Law-Green et al. (1995)
NRH95	Neff et al. (1995)
F02	Fernini (2002)
ALB94	Akujor et al. (1994)
DRAGN	Leahy et al. (2000)
HPPR97	Hardcastle et al. (1997)
HPR98	Hardcastle et al. (1998)
HLL94	Bridle et al. (1994)
ASZ91	Akujor et al. (1991)
BLR97	Best et al. (1997)
LCF01	Lara et al. (2001)
PPR85	Pearson et al. (1985)
FBB93	Fernini et al. (1993)
AG95	Akujor & Garrington (1995)
SC85	Strom & Conway (1985)
PH74	Pooley & Henbest (1974)
T82	Tsien (1982)
BHB88	Baum et al. (1988)
JPR77	Jenkins et al. (1977)
BMS88	Barthel et al. (1988)
JLG95	Johnson et al. (1995)
AL87	Alexander & Leahy (1987)
FBP97	Fernini et al. (1997)
LGS98	Ludke et al. (1998)

Table E.2: Reference table

Appendix F

6CE sample

Source	z	θ (arc sec.)	$S_{151\mathrm{MHz}}$ Jy	$S_{365\mathrm{MHz}}$ Jy	$S_{1400\mathrm{MHz}}$ mJy	R	REF
6C 0820+364	1.86	24	2.39	1.15	213^{A}	1.58	
6C 0822+341	0.41	18	3.06	1.77	552^{A}	1.83	-
6C 0822+343	0.77	21	2.93	1.03	111^{A}	1.64	
6C 0823+375	0.21	81	3.35	1.42	425^{A}	1.41	
6C 0824+353	2.25	8	2.42	1.83	$958\ ^{E}$	1.80	NAR92
6C 0825+345	1.47	7	2.10	1.22	284^{A}	1.95	
6C 0847+375	0.41	33	3.07	1.43	614^{A}	2.67	MMC97
6C 0857+390	0.23	24	2.71	1.51	503^{A}	1.83	-
6C 0901+355	1.90	4	2.07	1.08	219^{K}	1.24	NAR92
6C 0902+341	3.40	5	2.14	1.12	298^{K}	2.42	COM94
6C 0905+395	1.88	5	2.82	0.94^{L}	233^{A}	2.85	LEL95
6C 0908+373	0.11	39	2.33	1.33	614^{A}	1.08	PRF86
6C 0913+390	1.25	9	2.27	1.80	1005^{E}	0.80	HBW95
6C 0919+380	1.65	10	2.72	1.05^{L}	65^{N}	1.84	NAR92
6C 0922+364	0.11	17	3.27	1.09	725^{K}	1.85	MPC97
6C 0930+385	2.40	5	2.21	1.06	278^{A}	1.84	FPD01
6C 0943+395	1.04	12	2.31	1.20	323^{A}	2.01	G04
6C 0955+384	1.41	22	3.45	1.75	388^{A}	1.66	
6C 1011+363	1.04	66	2.10	1.07	374^{A}	2.07	
6C 1016+363	1.89	31	2.28	1.39	$528\ ^{E}$	1.61	
6C 1017+371	1.05	9	2.68	1.44	359^{A}	1.83	
6C 1018+372	0.81	83	2.52	0.97	271^{A}	2.07	
6C 1019+392	0.92	9	2.99	1.76	392^{A}	2.05	BEL99
6C 1025+390	0.36	1	2.97	1.98	659^{E}	2. 6	NAR92
6C 1031+340	1.83	3	2.33	1.55	478^{A}	2.72	
6C 1042+391	1.77	11	2.68	1.96	655^{E}	1.57	NAR92
6C 1043+371	0.79	5	2.62	1.18	249^{K}	1.07	NAR92

Source	z	θ (arc sec.)	$S_{151\mathrm{MHz}}$ Jy	$S_{365\mathrm{MHz}}$ Jy	$S_{1400\mathrm{MHz}}$ mJy	R	REF
6C 1045+340	1.83	22	2.00	1.20	266^{A}	1.98	
6C 1045+355	0.85	9	2.07	1.26	267^{K}	1.44	NAR92
6C 1045+351	1.60	0.1	3.03	2.44	1035^{E}	1.83	-
6C 1100+350	1.44	14	2.26	1.18	304^{A}	4.25	
6C 1108+395	0.59	16	2.10	2.01	390^{A}	1.83	-
6C 1113+345	2.41	17	2.33	1.39	440^{A}	2.80	
6C 1123+340	1.25	0.2	3.40	3.80	1378^{E}	0.98	NAR92
6C 1125+374	1.23	18	2.07	1.06	325^{K}	1.83	-
6C 1129+371	1.06	19	2.36	1.42	416^{K}	1.72	
6C 1130+345	0.51	78	3.20	2.10^{M}	524^{K}	2.31	
6C 1134+365	2.13	17	2.07	1.10	235^{K}	1.27	
6C 1141+352	1.78	12	2.40	1.13	290^{K}	1.65	
6C 1143+370	1.96	0.1	2.06	1.51	448^{K}	1.83	-
6C 1148+363	0.14	27	3.21	1.41	550^{A}	1.83	-
6C 1148+384	1.30	10	3.83	2.20	652^{E}	2.22	NAR92
6C 1158+343	0.53	40	2.12	1.30	314^{K}	1.83	-
6C 1159+365	1.40	2	2.20	1.40	352^{K}	1.28	
6C 1204+351	1.38	63	3.43	1.96	505^{A}	1.49	
6C 1205+391	0.24	24	3.83	1.61	634^{A}	1.55	MMC82
6C 1212+380	0.95	0.6	2.14	1.27	287^{K}	1.20	NAR92
6C 1213+350	0.86	0.1	2.39	2.32	1507^{E}	1.25	XRP95
6C 1217+364	1.09	0.5	2.40	1.32	396^{K}	0.93	
6C 1220+372	0.49	36	2.52	1.44	463^{A}	1.83	-
6C 1230+345	1.53	12	2.90	1.89	424^{A}	2.30	
6C 1232+394	3.22	51	3.27	1.47	1130^{L}	1.70	NAR92
6C 1255+370	0.71	0.6	3.66	2.33	759^{E}	1.83	-
6C 1256+364	1.13	18	2.88	1.61	527^{E}	1.53	
6C 1257+363	1.00	40	2.40	1.07	196^{A}	1.80	
6C 1301+381	0.47	28	3.46	2.01	536^{A}	1.83	-

Table F.1: Parameters used in the fitting on the KDA model in chapter 6. Column 1: 6CE source name. Column 2: redshifts. Column 3: Angular size in arcseconds. Column 4: Flux density at 151 MHz. Column 5: Flux density at 365 MHz taken from Douglas et al. (1996) unless otherwise stated. Column 6: Flux density at 1400 MHz and Column 7: Average source lobe ratio, high resolution maps taken from Law-Green et al. (1995) unless otherwise stated. Columns 2, 3 and 4 use data taken from Rawlings et al. (2001). See Table F.2 for explanation of reference codes.

Listing	Full Reference
A	White & Becker (1992)
E	Condon et al. (1998)
I	Viner & Erickson (1975)
J	Hales et al. (1995)
K	Becker et al. (1995)
L	Ficarra et al. (1985)
M	Pilkington & Scott (1965)
N	Becker et al. (1991)
G04	Goodlet et al. (2004)
HBW95	Henstock et al. (1995)
PRF86	Parma et al. (1986)
COH94	Carilli et al. (1994)
LEL95	Law-Green et al. (1995)
MPC97	Morganti et al. (1997)
FPD01	Fanti et al. (2001)
BEL99	Best et al. (1999)
NAR92	Naundorf et al. (1992)
MMC82	Machalski et al. (1982)
XRP95	Xu et al. (1995)

Table F.2: 6CE Reference table

Appendix G

7C III sample

	Source	z	θ	S_{151MHz}	S_{327MHz}	$S_{1490MHz}$	R
			(arc sec.)	Jy	mJy	mJy	
7C	1732+6535	0.86	20	6.17	2979	1058	1.80
7C	1733+6719	1.84	3	1.84	966	247	1.80
7C	1741+6704	1.05	4	0.73	366	80	1.80
7C	1742+6346	1.27	51	0.62	290	68	1.80
7C	1743+6344	0.32	14	1.33	685	214	3.16
7C	1743+6431	1.70	45	1.89	948	247	1.25
7C	1743+6639	0.27	50	1.97	1238	433	1.51
7C	1745+6415	0.67	6	0.64	399	148	1.50
7C	1745+6422	1.23	16	1.51	823	237	1.07
7C	1747+6533	1.52	0.7	2.92	1605	375	1.80
7C	1748+6703	3.20	14	2.29	1199	217	1.94
7C	1748+6657	1.05	0.3	1.21	1523	530	1.80
7C	1748+6731	0.56	108	0.64	376	118	2.75
7C	1751+6809	1.54	2	0.74	480	134	1.80
7C	1751+6455	0.29	43	0.65	421	130	1.19
7C	1753+6311	1.96	17	1.09	536	138	2.35
7C	1753+6543	0.14	84	1.62	1072	461	1.64
7C	1754+6420	1.09	15	0.42	255	57	2.11
7C	1755+6830	0.74	9	1.11	654	211	1.80
7C	1756+6520	1.48	5	0.73	465	171	1.15
7C	1758+6535	0.80	106	1.13	739	226	2.50
7C	1758+6553	0.17	115	1.30	715	210	1.80
7C	1758+6307	1.19	4	1.94	1174	304	1.50
7C	1758+6719	2.70	45	0.76	400	98	2.19
7C	1801+6902	1.27	21	1.37	673	203	1.40
7C	1802+6456	2.11	26	1.97	857	211	1.71
7C	1804+6313	1.50	29	0.62	333	66	1.80

Source		z	θ	S_{151MHz}	S_{327MHz}	$S_{1490MHz}$	R
			(arc sec.)	Jy	mJy	mJy	
7C	1805+6332	1.84	14	1.08	569	137	2.08
7C	1807+6831	0.58	29	2.12	1216	334	1.44
7C	1807+6841	0.81	12	0.63	359	115	1.38
7C	1811+6321	0.27	52	0.95	452	129	2.56
7C	1813+6439	2.04	38	0.5	237	41	2.00
7C	1813+6846	1.03	52	1.51	754	209	1.93
7C	1814+6529	0.96	126	1.22	629	125	1.80
7C	1815+6805	0.23	50	1.96	1188	381	1.70
7C	1815+6815	0.79	200	1.37	725	181	2.00
7C	1816+6710	0.92	27	2.44	1476	456	1.67
7C	1816+6605	0.92	2	1.29	723	162	1.92
7C	1819+6550	0.72	9	1.21	772	257	1.19
7C	1822+6601	0.37	52	0.97	607	178	1.45
7C	1826+6602	2.38	3	1.63	605	144	1.10
7C	1826+6510	0.65	34	1.39	852	240	1.83
7C	1826+6704	0.29	19	0.61	355	108	1.19
7C	1827+6709	0.48	17	1.10	614	155	2.15
7C	1814+6702	4.05	18	2.32	1097	223	1.34

Table G.1: Parameters used in the fitting on the KDA model in chapter 6. Column 1: 7C III source name. Column 2: redshifts taken from Lacy (1999). Column 3: Angular size in arcseconds taken from Lacy et al. (1992). Column 4: Flux density of 151 MHz. Column 5: Flux density of 327 MHz. Column 6: Flux density of 1490 MHz and Column 7: Average source lobe ratio. Sources with a lobe ratio of 1.8 do not have high enough quality maps. All other lobe ratios use maps taken from Lacy et al. (1992). Columns 4-6 are taken from Lacy (1999).

Bibliography

Akujor C. E., Garrington S. T., 1995, A&A Supp., 112, 235

Akujor C. E., Luedke E., Browne I. W. A., Leahy J. P., Garrington S. T., 1994, A&A Supp., 105, 247

Akujor C. E., Spencer R. E., Zhang F. J., Davis R. J., Browne I. W. A., Fanti C., 1991, MNRAS, 250, 215

Alexander P., 2000, MNRAS, 319, 8

Alexander P., 2002, MNRAS, 335, 610

Alexander P., Leahy J. P., 1987, MNRAS, 225, 1

Almaini O., Lawrence A., Boyle B. J., 1999, MNRAS, 305, L59

Athreya R. M., Kapahi V. K., 1999, in Röttgering H. J. A., Best P. N., Lehnert H. D., eds, The Most Distant Radio Galaxies Radio Galaxies from the MRC/1Jy sample. Royal Netherlands Acad. Arts, the Netherlands, p. 453

Baars J. W. M., Genzel R., Pauliny-Toth I. I. K., Witzel A., 1977, A&A, 61, 99

Barkhouse W. A., Hall P. B., 2001, AJ, 121, 2843

Barthel P., 1989a, Scientific American, 260, 20

Barthel P. D., 1989b, ApJ, 336, 606

Barthel P. D., Miley G. K., 1988, Nat., 333, 319

Barthel P. D., Miley G. K., Schilizzi R. T., Lonsdale C. J., 1988, A&A Supp., 73, 515

Baum S. A., Heckman T. M., Bridle A., van Breugel W. J. M., Miley G. K., 1988, ApJ Supp., 68, 643

Becker R. H., White R. L., Edwards A. L., 1991, ApJ Supp., 75, 1

Becker R. H., White R. L., Helfand D. J., 1995, ApJ, 450, 559

Bennett A. S., 1962, MmRAS, 68, 163

Best P. N., 2000, MNRAS, 317, 720

Best P. N., Carilli C. L., Garrington S. T., Longair M. S., Röttgering H. J. A., 1998, MNRAS, 299, 357

Best P. N., Eales S. A., Longair M. S., Rawlings S., Röttgering H. J. A., 1999, MNRAS, 303, 616

Best P. N., Longair M. S., Röttgering H. J. A., 1996, MNRAS, 280, L9

Best P. N., Longair M. S., Röttgering H. J. A., 1997, MNRAS, 292, 758

Best P. N., Röttgering H. J. A., Longair M. S., 2000a, MNRAS, 311, 1

Best P. N., Röttgering H. J. A., Longair M. S., 2000b, MNRAS, 311, 23

Best P. N., Röttgering H. J. A., Bremer M. N., Cimatti A., Mack K. H., Miley G. K., Pentericci L., Tilanus R. P. J., van der Werf P. P., 1998, MNRAS, 301, L15

Blandford R. D., Rees M. J., 1974, MNRAS, 169, 395

Blundell K. M., Rawlings S., 2001, in ASP Conf. Ser. 250: Particles and Fields in Radio Galaxies Conference Spectral ageing: a new age perspective. p. 363

Blundell K. M., Rawlings S., Willott C. J., 1999, ApJ, 117, 677

Bowyer C. S., Lampton M., Mack J., de Mendonca F., 1970, ApJ Lett., 161, L1

Bremer M. N., Crawford C. S., Fabian A. C., Johnstone R. M., 1992, MNRAS, 254, 614

Bridle A. H., Hough D. H., Lonsdale C. J., Burns J. O., Laing R. A., 1994, AJ, 108, 766

Burn B. J., 1966, MNRAS, 133, 67

Carilli C. L., Barthel P. D., 1996, A&A Review, 7, 1

Carilli C. L., Owen F. N., Harris D. E., 1994, AJ, 107, 480

Chambers K. C., Miley G. K., van Breugel W., 1987, Nat., 329, 604

Condon J. J., Cotton W. D., Greisen E. W., Yin Q. F., Perley R. A., Taylor G. B., Broderick J. J., 1998, AJ, 115, 1693

Cornwell T., Braun R., Briggs D. S., 1999, Synthesis Imaging in Radio Astronomy II. Astronomical Society of the Pacific Conference Series Volume 180, pp 151–170

Crawford C. S., Fabian A. C., 1989, MNRAS, 239, 219 de Vries W. H., van Breugel W. J. M., Quirrenbach A., Roberts J., Fidkowski K., 2000, A&A Supp., 197, 2003

Deeming T. J., 1964, MNRAS, 127, 493

Dennett-Thorpe J., 1996, Ph.D. Thesis, Cambridge University

Dennett-Thorpe J., Bridle A. H., Laing R. A., Scheuer P. A. G., 1999, MNRAS, 304, 271

Dennett-Thorpe J., Bridle A. H., Scheuer P. A. G., Laing R. A., Leahy J. P., 1997, MNRAS, 289, 753

Dey A., van Breugel W., Vacca W. D., Antonucci R., 1997, ApJ, 490, 698

Douglas J. N., Bash F. N., Bozyan F. A., Torrence G. W., Wolfe C., 1996, AJ, 111, 1945

Dunlop J. S., McLure R. J., Kukula M. J., Baum S. A., O'Dea C. P., Hughes D. H., 2003, MNRAS, 340, 1095

Eales S., Rawlings S., Law-Green D., Cotter G., Lacy M., 1997, MNRAS, 291, 593

Efstathiou G., Fall S. M., 1984, MNRAS, 206, 453

Elvis M., Maccacaro T., Wilson A. S., Ward M. J., Penston M. V., Fosbury R. A. E., Perola G. C., 1978, MNRAS, 183, 129

Enßlin T. A., Vogt C., 2003, A&A, 401, 835

Fanaroff B. L., Riley J. M., 1974, MNRAS, 167, 31P

Fanti C., Pozzi F., Dallacasa D., Fanti R., Gregorini L., Stanghellini C., Vigotti M., 2001, A&A, 369, 380

Fernini I., 2002, AJ, 123, 132

Fernini I., Burns J. O., Bridle A. H., Perley R. A., 1993, AJ, 105, 1690

Fernini I., Burns J. O., Perley R. A., 1997, AJ, 114, 2292

Ficarra A., Grueff G., Tomassetti G., 1985, A&A Supp., 59, 255

Fomalont E. B., Ebneter K. A., van Breugel W. J. M., Ekers R. D., 1989, ApJ, 346, L17

Fomalont E. B., Perley R. A., 1999, Synthesis Imaging in Radio Astronomy II. Astronomical Society of the Pacific Conference Series Volume 180, p. 105

Garrington S. T., Conway R. G., 1991, MNRAS, 250, 198

Garrington S. T., Conway R. G., Leahy J. P., 1991, MNRAS, 250, 171

Garrington S. T., Leahy J. P., Conway R. G., Laing R. A., 1988, Nat., 331, 147

Giovannini G., Feretti L., Gregorini L., Parma P., 1988, A&A, 199, 73

Goodlet J. A., Kaiser C. R., Best P. N., Dennett-Thorpe J., 2004, MNRAS, 347, 508

Gregorini L., Padrielli L., Parma P., Gilmore G., 1988, A&A Supp., 74, 107

Gregory P. C., Condon J. J., 1991, ApJ Supp., 75, 1011

Hales S. E. G., Masson C. R., Warner P. J., Baldwin J. E., 1990, MNRAS, 246, 256

Hales S. E. G., Waldram E. M., Rees N., Warner P. J., 1995, MNRAS, 274, 447

Hardcastle M. J., Alexander P., Pooley G. G., Riley J. M., 1997, MNRAS, 288, 859

Hardcastle M. J., Alexander P., Pooley G. G., Riley J. M., 1998, MNRAS, 296, 445

Hardcastle M. J., Worrall D. M., 2000, MNRAS, 319, 562

Harvanck M., Hardcastle M. J., 1998, ApJ Supp., 119, 25

Harvanek M., Stocke J. T., 2002, AJ, 124, 1239

Henstock D. R., Browne I. W. A., Wilkinson P. N., Taylor G. B., Vermeulen R. C., Pearson T. J., Readhead A. C. S., 1995, ApJ Supp., 100, 1

Herbig T., Readhead A. C. S., 1992, ApJ Supp., 81, 83

Hewitt A., Burbidge G., 1991, ApJ Supp., 75, 297

Hill G. J., Lilly S. J., 1991, ApJ, 367, 1

Hill G. J., Rawlings S., 2003, New Astronomy Review, 47, 373

Högbom J., 1974, A&A Supp., 15, 417

Inskip K. J., Best P. N., Longair M. S., Rawlings S., Röttgering H. J. A., Eales S., 2003, MNRAS, 345, 1365

Inskip K. J., Best P. N., Rawlings S., Longair M. S., Cotter G., Röttgering H. J. A., Eales S., 2002, MNRAS, 337, 1381

Ishwara-Chandra C. H., Saikia D. J., Kapahi V. K., McCarthy P. J., 1998, MNRAS, 300, 269

Ishwara-Chandra C. H., Saikia D. J., McCarthy P. J., van Breugel W. J. M., 2001, MNRAS, 323, 460

Jenkins C. J., Pooley G. G., Riley J. M., 1977, MmRAS, 84, 61

Johnson R. A., Leahy J. P., Garrington S. T., 1995, MNRAS, 273, 877

Kaiser C., Alexander P., 1997, MNRAS, 286, 215

Kaiser C. R., Dennett-Thorpe J., Alexander P., 1997, MNRAS, 292, 723

Kapahi V. K., 1989, AJ, 97, 1

Kellermann K. I., Pauliny-Toth I. I. K., Williams P. J. S., 1969, ApJ, 157, 1

Krolik J. H., 1999, From the Central Black Hole to the Galactic Environment. Princeton Series in Astrophysics, pp 3–42

Kronberg P. P., Conway R. G., Gilbert. J. A., 1972, MNRAS, 156, 275

Kuehr H., Witzel A., Pauliny-Toth I. I. K., Nauber U., 1981, A&A Supp., 45, 367

Lacy M., 1999, in Flux-limited samples of radio sources in the North Ecliptic Cap. Available ONLINE from Caltech University: *http://www.its.caltech.edu/~mlacy/nec.html.* Accessed 10/10/03

Lacy M., Laurent-Muehleisen S. A., Ridgway S., Becker R. H., White R. L., 2001, ApJ Lett., 551, L17

Lacy M., Rawlings S., Hill G. J., Bunker A. J., Ridgway S., Stern D., 1999, MNRAS, 308, 1096

Lacy M., Rawlings S., Warner P. J., 1992, MNRAS, 256, 404

Laing R. A., 1980, MNRAS, 193, 439

Laing R. A., 1981, MNRAS, 195, 261

Laing R. A., 1984, Physics of energy transport in extragalactic radio sources. NRAO: Greenbank, p. 90

Laing R. A., 1988, Nat., 331, 149

Laing R. A., Peacock J. A., 1980, MNRAS, 190, 903

Laing R. A., Riley J. M., Longair M. S., 1983, MNRAS, 204, 151

Lara L., Cotton W. D., Feretti L., Giovannini G., Marcaide J. M., Márquez I., Venturi T., 2001, A&A, 370, 409

Large M. I., Mills B. Y., Little A. G., Crawford D. F., Sutton J. M., 1981, MNRAS, 194, 693

Law-Green J. D. B., Eales S. A., Leahy J. P., Rawlings S., Lacy M., 1995, MNRAS, 277, 995

Law-Green J. D. B., Leahy J. P., Alexander P., Allington-Smith J. R., van Breugel W. J. M., Eales S. A., Rawlings S. G., Spinrad H., 1995, MNRAS, 274, 939

Leahy J. P., 1987, MNRAS, 226, 433

Leahy J. P., Bridle A. H., Storm R. G., 2000, in 3CRR Atlas: Home Page Available ONLINE from Jodrell Bank, Manchester: *http://www.jb.man.ac.uk/atlas.* Accessed 08/10/03

Leahy J. P., Muxlow T. W. B., Stephens P. W., 1989, MNRAS, 239, 401

Leahy J. P., Perley R. A., 1991, AJ, 102, 537

Leahy J. P., Williams A. G., 1984, MNRAS, 210, 929

Liu R., Pooley G., 1991a, MNRAS, 249, 343

Liu R., Pooley G., 1991b, MNRAS, 253, 669

Longair M. S., 1994, High Energy Astrophysics Volume 2. Cambridge University Press, pp 292–296

Longair M. S., Riley J. M., 1979, MNRAS, 188, 625

Longair M. S., Seldner M., 1979, MNRAS, 189, 433

Lonsdale C. J., Barthel P. D., Miley G. K., 1993, ApJ Supp., 87, 63

Ludke E., Garrington S. T., Spencer R. E., Akujor C. E., Muxlow T. W. B., Sanghera H. S., Fanti C., 1998, MNRAS, 299, 467

McCarthy P. J., Spinrad H., van Breugel W., 1995, ApJ Supp., 99, 27

Machalski J., Maslowski J., Condon J. J., Condon M. A., 1982, AJ, 87, 1150

Macklin J. T., 1982, MNRAS, 199, 1119

McLure R. J., Willott C. J., Jarvis M. J., Rawlings S., Hill G. J., Mitchell E., Dunlop J. S., Wold M., 2004, MNRAS, 351, 347

McCarthy P. J., van Breugel W., Kapahi V. K., 1991, ApJ, 371, 478

Miller L., Longair M. S., Fabbiano G., Trinchieri G., Elvis M., 1985, MNRAS, 215, 799

Mills B. Y., Slee O. B., 1957, Australian Journal of Physics, 10, 162

Morganti R., Parma P., Capetti A., Fanti R., de Ruiter H. R., Prandoni I., 1997, A&A Supp., 126, 335

Morris D., Tabara H., 1973, PAsJ, 25, 295

Naundorf C. E., Alexander P., Riley J. M., Eales S. A., 1992, MNRAS, 258, 647

Neff S. G., Roberts L., Hutchings J. B., 1995, ApJ, 99, 349

Onuora L. I., 1989, Ap. & Sp. Sci., 162, 349

Owen F. N., Ledlow M. J., 1994, in The First Stromlo Symposium: The Physics of Active Galaxies. ASP Conference Series The FRI/II Break and the Bivariate Luminosity Function in Abell Clusters of Galaxies. p. 319

Owen F. N., Ledlow M. J., Morrison G. E., Hill J. M., 1997, ApJ Lett., 488, L15

Parma P., de Ruiter H. R., Fanti C., Fanti R., 1986, A&A Supp., 64, 135

Pauliny-Toth I. I. K., Wade C. M., Heeschen D. S., 1966, ApJ Supp., 13, 65

Peacock J. A., 1987, in NATO ASIC Proc. 208: Astrophysical Jets and their Engines. Unified beaming models and compact radio sources. pp 185–196

Pearson T. J., Readhead A. C. S., Perley R. A., 1985, AJ, 90, 738

Pedelty J. A., Rudnick L., McCarthy P. J., Spinrad H., 1989, AJ, 97, 647

Pentericci L., van Reeven W., Carilli C. L., Röttgering H. J. A., Miley G. K., 2000, A&A Supp., 145, 121

Pilkington J. D. H., Scott P. F., 1965, MmRAS, 69, 183

Polatidis A. G., Wilkinson P. N., Xu W., Readhead A. C. S., Pearson T. J., Taylor G. B., Vermeulen R. C., 1995, ApJ Supp., 98, 1

Pooley D. M., Waldram E. M., Riley J. M., 1998, MNRAS, 298, 637

Pooley G. G., Henbest S. N., 1974, MNRAS, 169, 477

Press W. H., Teukolsky S. A., Vetterling W. T., Flannery B. P., 1997, Numerical reciepes in fortran 77. Second edition. Cambridge University Press, p. 402

Prestage R. M., Peacock J. A., 1988, MNRAS, 230, 131

Rawlings S., 2002, in IAU Symposium Cosmological Studies from Radio Source Samples. p. 34

Rawlings S., Eales S., Lacy M., 2001, MNRAS, 322, 523

Ridgway S. E., Stockton A., Lacy M., 2004, ApJ, 600, 70

Riley K. F., Hobson M. P., Bence S. J., 1997, Mathematical methods for physics and engineering. Cambridge University Press, pp 898–902

Roche N., Eales S., Hippelein H., 1998, MNRAS, 295, 946

Rudnick I., Zukowski E., Kronberg P. P., 1983, A&A Supp., 52, 317

Rupen M. P., 1997, in VLA Scientific Memorandum No. 172: A Test of the CS (Shortened C) Configuration.

Scheuer P. A. G., 1974, MNRAS, 166, 513

Scheuer P. A. G., 1987, in Superluminal Radio Sources Tests of beaming models. pp 104–113

Simard-Normandin M., Kronberg P. P., Button S., 1981, ApJ Supp., 45, 97

Singal A. K., 1993, MNRAS, 263, 139

Spinrad H., Marr J., Agiular L., Djorgovski S., 1985, PASP, 97, 932

Stevens J. A., Ivison R. J., Dunlop J. S., Smail I. R., Percival W. J., Hughes D. H., Röttgering H. J. A., van Breugel W. J. M., Reuland M., 2003, Nat., 425, 264

Storrie-Lombardi L. J., McMahon R. G., Irwin M. J., 1996, MNRAS, 283, L79

Strom R. G., 1973, A&A, 25, 303

Strom R. G., Conway R. G., 1985, A&A Supp., 61, 547

Strom R. G., Jägers W. J., 1988, A&A, 194, 79

Tabara H., Inoue M., 1980, A&A Supp., 39, 379

Tadhunter C. N., Morganti R., Robinson A., Dickson R., Villar-Martin M., Fosbury R. A. E., 1998, MNRAS, 298, 1035

Tribble P. C., 1991, MNRAS, 250, 726

Tsien S. C., 1982, MNRAS, 200, 377

Urry C. M., Padovani P., 1995, PASP, 107, 803

Veron M. P., Veron P., Witzel A., 1972, A&A, 18, 82

Viner M. R., Erickson W. C., 1975, AJ, 80, 931

Wang J.-M., Ho L. C., Staubert R., 2003, A&A, 409, 887

Welter G. L., Perry J. J., Kronberg P. P., 1984, ApJ, 279, 19

WENSS COLLABORATION 1998, in WENSS POLAR CATALOGUE (sources above 72 degress) version: 1.0. Avaliable ONLINE from Leiden University: *http://www.strw.leidenuniv.nl/WENSS/*. Accessed 10/10/03

White R. L., Becker R., 1992, ApJ Supp., 79, 331

Willot C. J., 2003, in 3CRR sample of radio sources Avaliable ONLINE from Oxford University: *http://www-astro.physics.ox.ac.uk/∼cjw/3crr/3crr.html.* Accessed 9/10/03

Willott C. J., McLure R. J., Jarvis M. J., 2003, ApJ Lett., 587, L15

Wold M., Lacy M., Lilje P. B., Serjeant S., 2001, MNRAS, 323, 231

Xu W., Readhead A. C. S., Pearson T. J., Polatidis A. G., Wilkinson P. N., 1995, ApJ Supp., 99, 297

Yates M. G., Miller L., Peacock J. A., 1989, MNRAS, 240, 129

Yee H. K. C., Green R. F., 1987, ApJ, 319, 28

Young A. J., Wilson A. S., Mundell C. G., 2001, Bulletin of the American Astronomical Society, 33, 1413

Zwicky F., Herzog E., Wild P., 1968, in CGCG1 "Catalogue of Galaxies and of Clusters of Galaxies", 1961-68, Pasadena: California Institute of technology

Index